PAUL THOMAS GOODALL

New College

INTERACTIONS OF THE MICROQUASAR SS 433 WITH THE MILKY WAY

A thesis submitted in candidature for the degree of
Doctor of Philosophy
at the
University of Oxford

Trinity Term 2010

To my dear family "of the mountains"...

Declaration

All of the work described in this thesis is believed to be original, except where explicit references are made to the work of other authors. It is the result of my own research, and includes nothing which is the outcome of work done in collaboration, except where specifically indicated. No part of this thesis has been, or is being, submitted for any other qualification other than the degree of Doctor of Philosophy at the University of Oxford.

Paul Goodall

July 2010
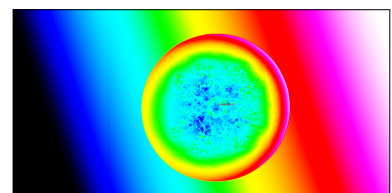
Interactions of the Microquasar SS 433 with the Milky Way

Paul Thomas Goodall
New College

Astrophysics
University of Oxford

Abstract

This thesis investigates the peculiar and somewhat unique[1] nature of the connection between the Microquasar SS 433 and its environs. This environment features the prominent nebula and candidate supernova remnant W 50, and jet interactions from SS 433 are evident on large scales of more than one hundred parsecs from the black hole powerhouse. The extent of the large scale structure surrounding SS 433 is such that it spans several scale heights (z) of the Galaxy in the direction perpendicular to the Galactic Disc.

In order to understand the formation of W50, several models from the literature are contested, along with a few new ones devised in this thesis. The many possible modes for interactions of SS 433 and W50 and consequent evolutions are investigated in turn via high resolution hydrodynamical simulations. The aim of the simulations is to compose a clear picture of the formation of this complex system, using all available observational data relevant to this system. A high resolution kinematic study of the nebula W50 involving radio interferometric data from the VLA archives spanning over a decade is also presented herein, and this provides useful constraints upon and comparisons with my numerical models. The successful model(s) have potential applications to other similar systems upon their discovery.

There are several very interesting results that have emerged from this thesis work, namely:

1. The kinematic study of W 50 unveils evidence that suggests that SS 433's jets have undergone a series of intermittent jet outbursts with varying jet characteristics, in contrast to SS 433's reputation as a constant jet source.

2. Jet simulations reveal that conical jets (i.e. precessing jets with non-zero precession cone angle) are unable to produce sufficiently collimated jet lobes to be in agreement with observation of W 50. This is consistent with (1) above, since SS 433's current jet undergoes precession and hence a previous jet state with zero (or close to zero) precession angle would be required in order to produce the lobes seen in W 50.

---

[1]This system is, to our knowledge, unique at the time of writing, although investigations are underway even now to search for similar objects within our Galaxy.
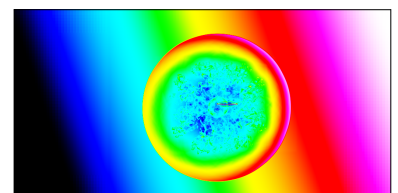
3. The east-west asymmetry in W 50 is used as an independent constraint upon the Galaxy disc scale height Z_d and density normalisation n_0 at the location of SS 433. Simulations suggest that the parameter combinations ($n_0 = 0.2\,\mathrm{cm}^{-3}$, $Z_d = 40\,\mathrm{pc}$) and ($n_0 = 0.1\,\mathrm{cm}^{-3}$, $Z_d = 30\,\mathrm{pc}$) describe SS 433's environment equally well.

This thesis begins with an overview of the microquasar field, including the relevant physics, both observational and theoretical, which necessarily constitute the microquasar toolkit. A short biography of SS 433's discovery is included as a point of interest. Observational data spanning thirty years are included in the simulations and the preceding investigations, from the year of SS 433's discovery in 1979 to present day. The radio interferometer theory, reduction and analyses relevant to the imaging and transverse proper motion study of W 50 are detailed in chapters 4 and 5 respectively. The theory, method and results relevant to high resolution hydrodynamic simulations using AMR are presented in the final chapters of this thesis, and the conclusions of the final chapter draw upon my findings through both simulations and observation.

Thesis submitted for the degree of Doctor of Philosophy
at the University of Oxford

Trinity 2010

Acknowledgements

I could fill the pages of this thesis many times over with gratitude to the many exceptionally talented individuals who have profoundly influenced and inspired me during my Doctorate degree. I feel very fortunate that I cannot hope to do justice in acknowledging everyone here.

First and foremost I would like to thank my supervisors Professor Katherine Blundell and Professor Dame Jocelyn Bell Burnell for their unwavering support and encouragement. To Katherine for her endless enthusiasm, creativity and expertise in seemingly any topic one wishes to engage. To Jocelyn for her invaluable wisdom in and around astrophysics. Thanks to each for their contagious tenacity in all endeavours, and valued friendship.

I'm also very grateful to all Oxford Astrophysics faculty who have helped with my Astrophysics training and development during my D.Phil. Thanks to PerlMonk Sebastián Pérez for teaching me Unix power-user tricks, and generally always being supportive and making time to talk about astrophysics. I am extremely lucky to work with Fathallah Alouani Bibi who has successfully educated a poor astronomer in the finer points of computational plasma physics. Particular thanks to Katrien Steenbrugge, Ian Heywood, James Binney, Stephen Justham, Hans Rainer-Klockner, Philipp Podsiadlowski, Adrianne Slyz, Martin Beaureu, Aprajita Verma, and Tony Lynas-Gray who have been directly helpful to me on many occasions.

I am grateful for all the wonderful friends I've made whilst at Oxford, who have made this experience unforgettable both professionally and socially. I'm honoured to have worked alongside the Oxford *AstroGrads* [2], and particularly the founding members of *"The Hitchhiker's guide to Grad-school"* - a better bunch there could not be. I am extremely grateful to the New College graduates and MCR for keeping my sanity and morale in-check during stressful times by adding flavour to my graduate life. Thanks to all the not-so-secret[3] societies who kept me amused.

---

[2]Special thanks to: Sebastián Pérez, Millie Maier, James Allison, Alison Crocker, Oliver King, Emma Walker, Lisa Fogarty, Cristina Fernandes, Ben Burnett, David Sutton, Teeraparb Chantravat, Graeme Salter, Sam Doolin, Emma Curtis-Lake, Calum Brown, Boon Kok Tan, Sam Geen, Ben Fitzpatrick, Sarah Blake, Renee Hlojek, Sarah Miller, Tim Davis, Richard Armstrong, Richard Masters, Natalie Christopher.

[3]HouseX, SMOF, Frisbeedials, New-Crew, Ma-Boogies.
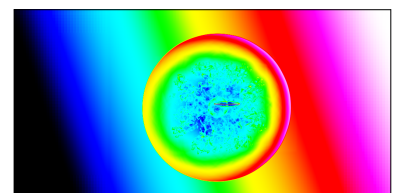
I am especially grateful to Emma Curtis-Lake, Eric Greveson, Sophie Boldon and Sarah Rudebeck for their support during my write-up, and to Shannah Moran for keeping me laughing!

Most of all, I would like to thank my loving parents Jean and Paul and brother Lee, whose footprints were, and are, always in the sand.
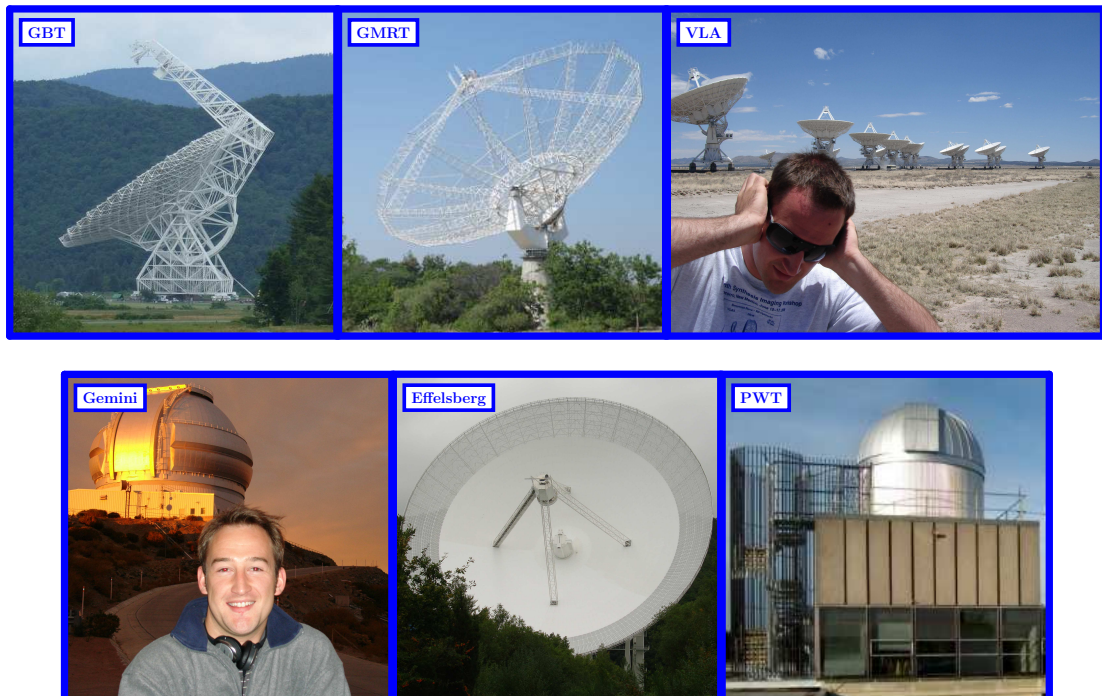
Figure 1: Telescopes I have visited during my D.Phil.

Resources

Contents

List of Figures

"To infinity,

and beyond!..."

Chapter 1

Introduction

This thesis is focused on the effects of the jets from a rather exotic object in our Galaxy called SS 433, upon its local (and not so local) environment. The investigation is carried out primarily through numerical simulations, and by comparing the numerical results with observations to constrain the parameters of the system. Although microquasar jets are central to the research of this thesis (and will be discussed in more detail throughout), it is useful to briefly introduce the topic in a broader context, as the models developed in this thesis have potential for application to other interesting astrophysical phenomena featured in this introduction.

1.1   Jets and Outflows - the big picture

Seemingly ubiquitous, astrophysical outflows have been observed in vastly different classes of objects throughout the universe. Jets are a special case of outflow with a high degree of collimation, such that the outflow length is at least 4 times its width (Bridle & Perley, 1984), constraining the opening angle of collimation to less than $\arctan(\frac{1}{4}) \approx 14°$. Jets have been observed to emit radiation across the entire electromagnetic spectrum, via direct observations from radio (Perley et al., 1984) through to X-rays (Marshall et al., 2002), and also indirectly via intense bursts of
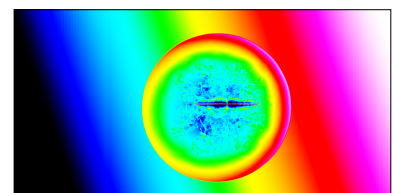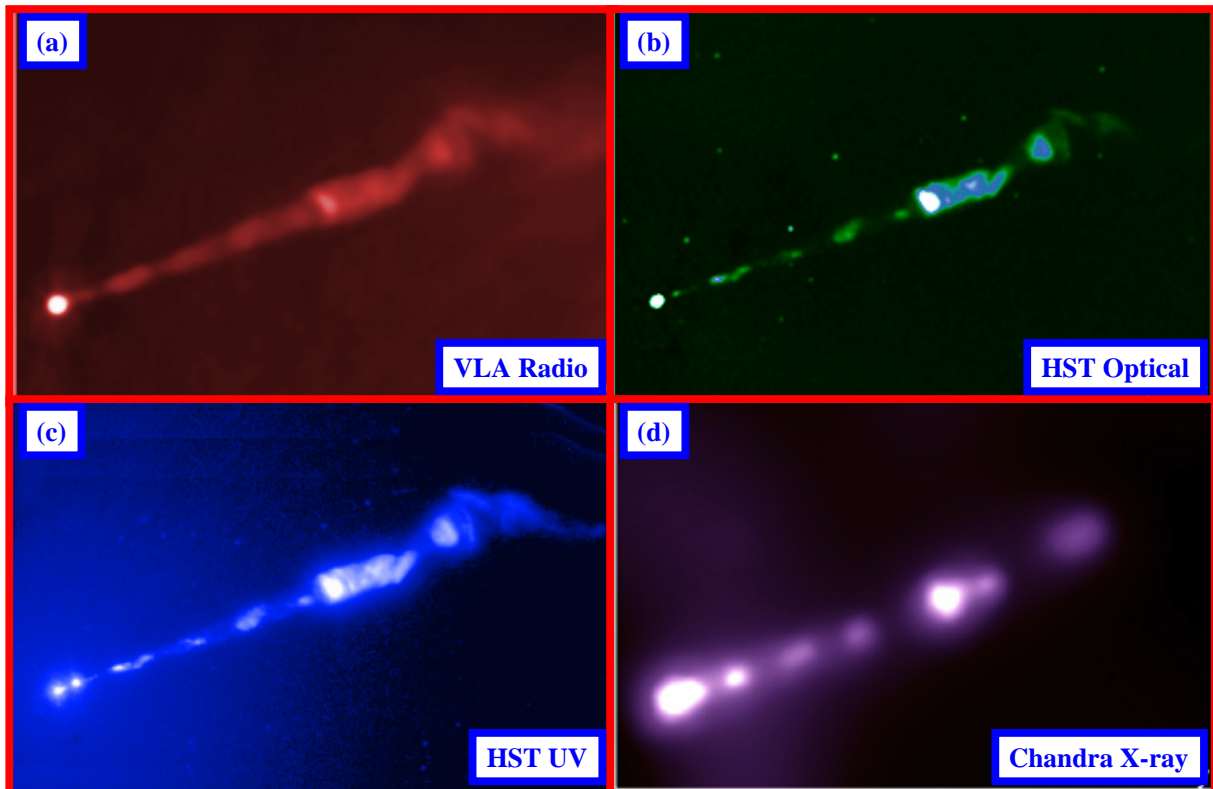
Figure 1.1: The approaching jet emanating from the core of M87 is visible across the electromagnetic spectrum. **(a) VLA Radio image**, credit: Biretta et al. (1995), **(b) Hubble Optical image**, credit: Capetti et al. (1997), **(c) Hubble UV image**, credit: Madrid et al. (2007), **(c) Chandra X-ray image**, credit: Marshall et al. (2002)

$\gamma-$ray emission (c.f. $\gamma-$ray bursts). Figure 1.1 shows the jet of M87 in four wavebands, which also happens to be the first jet to be discovered (Curtis, 1918).

Figure 1.2 shows a diverse group of objects that exhibit outflows or jets with varying degrees of collimation, however each of these objects comes from a very different class of astrophysical phenomenon. The radio galaxy Cygnus$-$A of Figure 1.2a and the massive elliptical galaxy M87 of Figure 1.1 are of particular relevance to this thesis as each hosts an Active Galactic Nucleus (AGN), which are thought to be much larger analogues of microquasars, as detailed in §1.4. The bright central spot in Figure 1.2a comes from the core of the host radio galaxy Cygnus$-$A containing the AGN, wherein a supermassive black hole (SMBH) of several billion times the mass of the Sun (Tadhunter et al., 2003) is in an "active" state, as evident from the jet ejecta
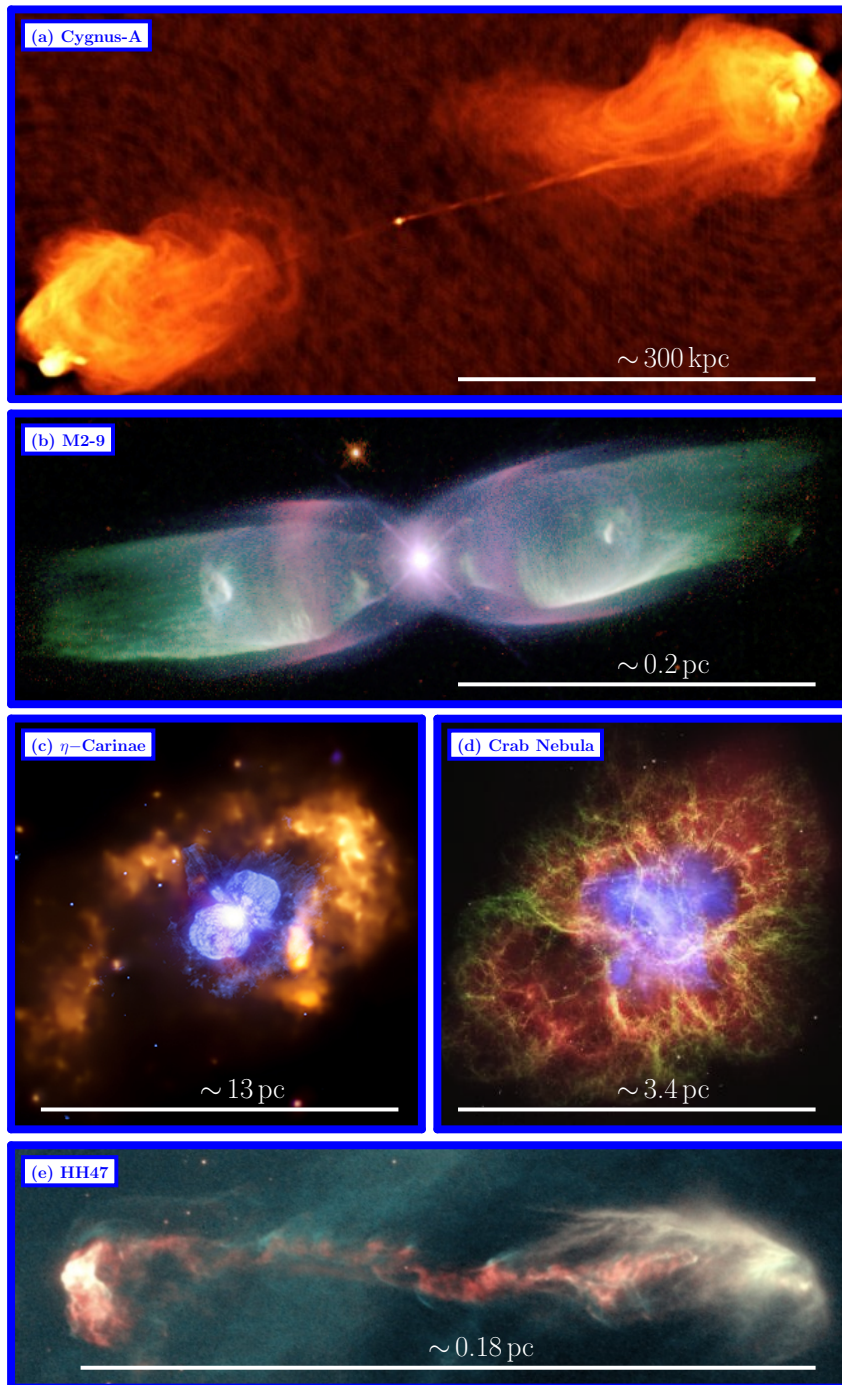
Figure 1.2: A selection of very different objects that exhibit outflows. **(a) Active Galaxy Cygnus-A in radio wavelengths**, credit: Perley et al. (1984) **(b) Planetary Nebula M2-9**, credit: Smith et al. (2005), and composite images: **(c) η-Carinae**, credit: X-ray: NASA/CXC/GSFC/M.Corcoran et al.; Optical: NASA/STScI, and **(d) Crab Pulsar Wind Nebula**, credit: X-ray: NASA/CXC/ASU/J.Hester et al.; Optical: NASA/ESA/ASU/J.Hester & A.Loll; Infrared: NASA/JPL-Caltech/Univ. Minn./R.Gehrz, **(e) Herbig$-$Haro 47**, credit: Hartigan et al. (2005)
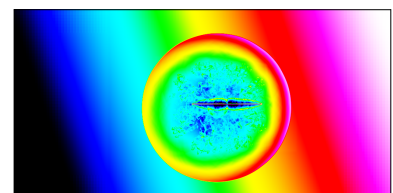
extending all the way back to the core.

The planetary nebula M2−9 of Figure 1.2b is the result of the interaction of two stars of comparable mass to the Sun. The primary (more evolved) star reached the end of its main sequence lifetime a long time ago and underwent a transition through the asymptotic giant branch (AGB) phase, in which the star becomes quite unstable to pulsations and ejects a large fraction of its mass into its surroundings. This phase in which the star is a red giant is relatively short-lived, and the star contracts unto a white dwarf star. This in itself is unlikely to result in a collimated outflow, however the secondary star in this system has also begun the AGB phase, and is believed to be transferring mass unto the white dwarf star (Livio & Soker, 2001). It is interesting to note, that had the primary star been massive enough to form a more compact object (either a neutron star or a black hole), then it is possible that this system might have become a microquasar.

The Homunculus nebula of Figure 1.2c is thought to have formed through an enormous eruption from the extremely massive star $\eta−$Carinae and its companion, both of which have very strong outflows in the form of powerful stellar winds, although these are less collimated.

The Crab nebula of Figure 1.2d is a supernova remnant associated with a rapidly rotating neutron star, or "pulsar". The Crab pulsar also features well collimated jets, which are inflating the surrounding plerionic nebula. Finally, Figure 1.2e shows a Herbig-Haro (HH47) system containing a newly forming protostar in the bright region in the far right of the image, which is ejecting material (from right to left) in the form of a protostellar jet.

Remarkably, all of the objects in Figure 1.2 that have well-collimated outflows (i.e. excluding $\eta−$Carinae) have two very significant attributes in common. Firstly, the most highly collimated outflows arise from systems that contain a compact object or star, either a white dwarf, a neutron star, or most impressively a black hole. Secondly, from the unfathomably powerful jets of Cygnus−A to the comparatively feeble ejecta of HH47, these systems all contain *accretion discs*.

1.2   Accretion discs

Gravity produces discs. A cloud of gaseous particles, without the influence of any external forces, will naturally begin to collapse due to its own self-gravity. However, clouds of particles in nature are never completely at rest with respect to their centres of mass, or indeed with respect to each other (in the latter case the pressure would tend towards zero). Such a cloud of gas will have some net rotation, or more importantly, non-zero angular momentum. It is this angular momentum that prevents a test particle from moving radially inwards towards the centre of mass of the cloud. Thus, the contraction process continues, causing the gas pressure to increase as the cloud volume decreases until eventually the thermal pressure becomes significant and resists further collapse. The rate of collapse is limited by the rate at which the cloud can thermally radiate away its internal energy, which is of course a function of its opacity. To a first approximation this is true for molecular clouds in star forming regions (however I have neglected the effects of molecular changes of state). The gravitational attraction to the centre of mass for a particle at some point (r, θ, z) in cylindrical coordinates about the rotation axis, has components in the radial $\hat{r}$ and axial $\hat{z}$ directions, whereas for the simplest case of a co-rotating body, the angular momentum is only a function of the radial distance from the axis of rotation. As a consequence, particles have a tendency to condense into a disc about the rotation axis with the protostar at the centre of mass. It is believed that viscous dissipation within the disc (and radiation from its surface) allows the angular momentum to be redistributed such that material close to the centre of mass can be accreted onto the protostar, whilst co-rotating material that gains angular momentum must therefore move outwards to larger radii. It is probably at this point when the protostar begins to eject material in the form of jets, as in Figure 1.2e. The disc formation process can reasonably explain why the orbits of the planets in the solar system lie approximately in the same plane, as their formation would follow from coagulation of dust grains in the disc, followed by coalescence of planetessimals, until eventually they are massive enough that accretion occurs onto the
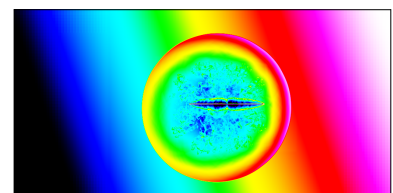
protoplanets themselves. Although only a qualitative outline is given here, it is thought that this same mechanism for redistributing angular momentum through a disc may also be responsible for the flatness of spiral galaxies, and the planetary rings of Saturn and Uranus, but by far the most exotic example of the role of discs is the accretion of matter onto compact objects, through matter stored in their accretion discs.

Accretion power is probably the most awesome and terrifying aspect of astrophysics, considering that it is the fuelling mechanism by which the jets of microquasars and AGN reach relativistic speeds, and the impact that these jets have upon their environments (Figure 1.2a). A simple description of the energy available through accretion can be briefly summarised by considering a test particle of mass m coming from $r = \infty$ to the effective surface of the accretor at $r = R$ of mass M. If the radiated energy can be attributed to the change in the gravitational potential energy of the system $\Delta U = GMm/R$, then this can be neatly rearranged with the addition of the factor c^2 such that:

$$E_{\rm rad} = \Delta U = \left(\frac{GM}{R\,c^2}\right) mc^2 \qquad (1.1)$$

where G is Newton's constant of gravitation, and c is the speed of light. Now supposing that we change the meaning of m from the mass of a particle, to a small mass of accreted gas m that is negligible compared to M, such that the latter can be considered constant. The time derivative of (1.1) then describes the radiated power or luminosity of the system:

$$L_{\rm rad} = \dot{E}_{\rm rad} = \eta\,\dot{m}\,c^2 \qquad (1.2)$$

where $\eta = GM/(R\,c^2)$ is a constant for a given accretor, and describes the efficiency of the accretion process. The *accretion rate* $\dot{m}$ is a variable for any given accretor. The *accretion efficiency* η increases with the ratio M/R which describes the "compactness" of a given accretor, and so *compact objects* such as white dwarfs, neutron stars, and particularly black holes make

for very efficient conversion of accreted matter into radiation. A quick calculation, based upon a white dwarf with of $1 M_\odot$ and R=10,000 km shows that $\eta \approx 10^{-4}$, whilst a neutron star with the same mass and a radius of R=15 km has a much greater efficiency of $\eta \sim 0.1$. The calculation is a bit more difficult for a black hole, since BH masses can vary dramatically and they have no solid surface. In this case matter is deemed to have been accreted once it passes the last stable orbit of $3 R_S$, where I have introduced the *Schwarzschild radius*

$$R_{\mathrm{S}} = \frac{2\, G\, M}{c^2} \tag{1.3}$$

which depends only upon the mass of the accretor. Further complications arise due to the meddling of magnetic fields and rotation of the black hole, and ultimately a *General Relativistic* treatment is necessary. A "spherical" black hole is thought to have an efficiency of $\eta \sim 0.06$, however rotating *Kerr* BH's cause more of the potential energy of the in-falling matter to be dissipated, and hence radiated, on the path towards $3 R_S$, in which case the efficiency is thought to reach as high as $\eta \sim 0.4$. This is astonishing when compared to the efficiency with which mass is converted into energy via the proton−proton chain in the cores of main sequence stars, of $\eta = 7 \times 10^{-3}$, underlining the true power of accretion.

In summary, the efficiency factor η described in this section, is a measure of how much of the potential energy of the accreted material is converted to radiation, via frictional heating of the viscous accretion disc. The accretion disc is heated to temperatures well above a million degrees Kelvin, and so the disc radiates very efficiently in the X-rays as a black body. Actually, for the case of a non-rotating black hole, the black-body temperature of the accretion disc was estimated by Rees (1984) according to: $T \simeq 5 \times 10^7 (M/M_\odot)^{-1/4}$ Kelvin.

For a more detailed account of the physics governing the accretion process, I refer the reader to the early works of Fred Hoyle, Hermann Bondi and Raymond Lyttleton (Hoyle & Lyttleton, 1941; Bondi & Hoyle, 1944; Bondi, 1952). Probably the most credible description of the for-

mation of collimated and relativistic jets emanating from accreting compact objects, comes from the theoretical *Blandford−Znajek* process (Blandford & Znajek, 1977) relating to *Kerr* (rotating) black holes, but alas details of which are beyond the scope of this thesis.
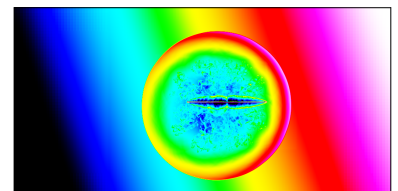
1.3   X-ray binary systems

An X-ray binary consists of a pair of gravitationally bound stars in quite close orbit around their common centre of mass, whereby the primary star (the more massive of the two) has evolved off the main sequence and formed a compact object (either a neutron star or black hole). Material from the secondary star is accreted onto the compact object, generating vast amounts of X-rays via the accretion mechanism described in §1.2, thus earning their name *X-ray binary*. X-ray binaries are usually sub-categorised according to the mass of the companion (the donor star) according to the approximate guidelines:

- Low Mass X-ray Binaries (LMXB) : $M_{donor} \leq 1\,M_\odot$

- Intermediate Mass X-ray Binaries (IMXB) : $1 < M_{donor} < 10\,M_\odot$

- High Mass X-ray Binaries (HMXB) : $M_{donor} \geq 10\,M_\odot$

and the third category (HMXBs) is central to this thesis, because SS 433 belongs to this group.

Although about 50% of stars are found in binary systems, only a small fraction of these evolve into X-ray binary systems. There are many reasons for this, for example the binary may have to survive the supernova explosion of the primary star without dissociating from each other, and yet the primary and secondary must also be in close enough orbit with one another that material is transferable from the primary to the secondary (and vice-versa, as indicated in Figure 1.3), via strong winds/envelope ejecta, or Roche lobe overflow. However, it is possible that in some cases the binary separation will decrease as the system evolves, via gravitational radiation or through loss of orbiting angular momentum through interactions with ejected envelope. The latter could

feasibly create a dampening effect upon the orbital motion, due to an increase in the ambient density (from winds or ejecta), or even through asymmetric ejections/accretion on the surface of one or both of the stars. Figure 1.3 gives an overview of the chain of events that leads to the formation of a HMXB from a HMB (high mass binary) where both stars are initially on the main sequence.

Firstly, the primary star (M_1, on the left of Figure 1.3) is in its post main sequence phase of evolution, with a contracting core that heats up, and fuses heavier and heavier elements, whilst fusion of lighter elements occurs in a sequence of shells around the core. The electrons in the core are degenerate, and as such the pressure is only a function of the core density rather than temperature. The outer envelope is not degenerate however, and via the ideal gas law an increase in temperature due to heating from the core leads to increased pressure in the surrounding envelope, such that the outer layers of the star expand and may completely fill the Roche lobe of the primary as shown in Figure 1.3b. In very massive stars (such as those in Figure 1.3), the outer envelope of hydrogen of the primary star can be completely stripped-off, leaving behind a hot Wolf-Rayet (Figure 1.3c) whose surface has a deficit of hydrogen, but is instead rich in processed materials such as helium, or even metals such as carbon and nitrogen. If the binary is sufficiently close, most of the envelope will be acquired by the companion (secondary) star. In turn, this extra mass accelerates the evolution of the companion, which soon (in astronomical terms) follows the trend set by the primary, and expands such that it's outer envelope is relatively loosely bound. Meanwhile (in this scenario), the primary star has reached the point by which it can no longer sustain fusion reactions of the heavier elements, and has succumbed to gravity, creating a compact object following a violent supernova explosion[1]. The strong stellar winds produced when the now-evolved companion star begins to eject its envelope, can be accreted by the compact object, bringing about the onset of the X-ray emitting phase (Figure 1.3e). Once

---

[1]It is interesting to note at this stage, that if no companion star is present to accept the envelope of hydrogen ejected by the primary (or indeed if the binary separation is too great), then the surrounding envelope around the contracting core of the primary star is a necessary ingredient in the *Hypernova* model for long-duration $\gamma-$ray bursts from Wolf-Rayet progenitors.

Birth of an X-ray Binary

(a) t = 0 yr
$M_1 = 25\,M_\odot, M_2 = 10\,M_\odot$

(b) t = 4.71×10⁶yr
$M_1 = 25\,M_\odot, M_2 = 10\,M_\odot$

Helium Star

(c) t = 4.72×10⁶yr
$M_1 = 8.5\,M_\odot, M_2 = 26.5\,M_\odot$

Compact Star   Weak wind

(d) t = 5.2×10⁶yr
$M_1 = 1.4\,M_\odot, M_2 = 26.5\,M_\odot$

X-rays begin

Strong wind

(e) t = 9.0×10⁶yr
$M_1 = 1.4\,M_\odot, M_2 = 26.5\,M_\odot$

X-rays + Jets(?)

Roche lobe overflow

(f) t = 9.01×10⁶yr
$M_1 = 1.4\,M_\odot, M_2 = 26.5\,M_\odot$
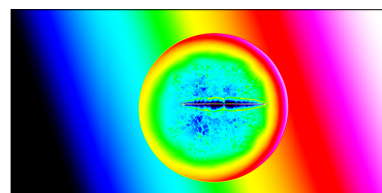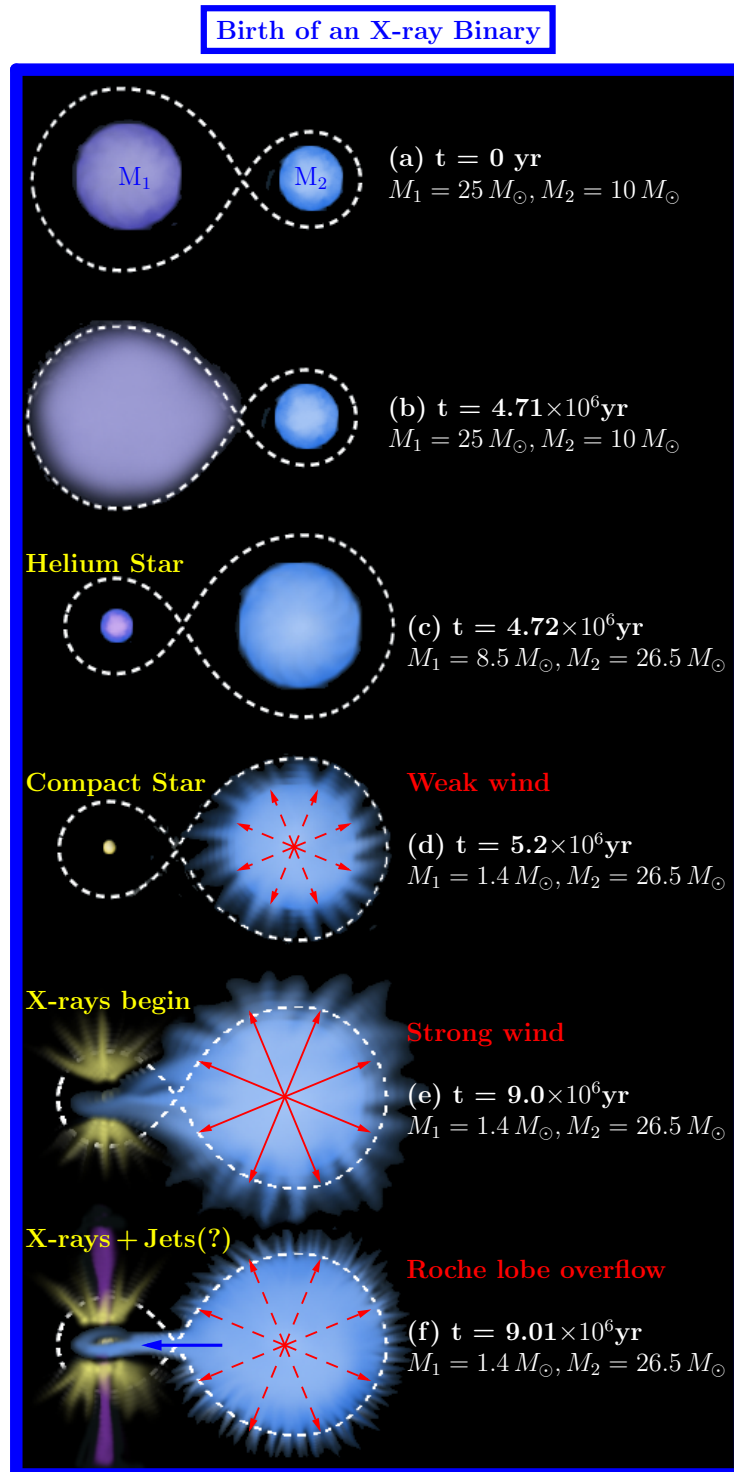
Figure 1.3: This cartoon is entirely based upon Fig. 1 of van den Heuvel (1977), with a few minor adjustments. The jets in the last step would designate the binary a microquasar. See text in §1.3 for a more detailed description of this figure.

the companion star has expanded to fill its Roche lobe, it then provides a sustained flow of gas via the inner Lagrangian point L_1 (intersected by the blue arrow in Figure 1.3f) to be stored in the accretion disc of the compact object, until it reaches the surface of the neutron star or the last stable circular orbit of the black hole. The formation of relativistic jets presumably follows some time after the accretion process has begun, thus promoting the X-ray binary to the rank of *microquasar*.

The term "Microquasar" (introduced by Mirabel et al. (1992)) was brought about by the discovery of several relativistic jet sources in the galaxy within the last few decades, to highlight their similarities in appearance with quasars (a subset of active galaxies). Microquasars and X-ray binaries are essentially synonymous, with the only difference being that microquasars have relativistic jets that have been confirmed observationally, usually at radio wavelengths.

1.4   Microquasars, and the AGN connection

It is now believed that almost every galaxy hosts a supermassive black hole (SMBH) at its centre. If the SMBH shows observational signs of accretion by way of one or two jets (the receding jet is not always visible) then it is termed an *active galaxy* because its nucleus is an AGN. When SMBH's are not launching relativistic jets for us to observe, they are said to be "dormant". Our own galaxy falls under the latter category, for observations monitoring the stellar orbits nearest the centre of our galaxy over the last 16 years indicate a common locus for the stellar orbits around an invisible object. The mass of the central object has been inferred through Keplerian mechanics to be $\gtrsim 4 \times 10^6 M_\odot$ (Gillessen et al., 2009) inside a region (confined by the orbits) so compact that a black hole seems to be the only viable explanation. This supermassive black hole at the centre of the Milky Way is called *Sagittarius A** (or Sgr$-$A* for short), and for the time being at least, it is not active.

It seems that it is only a matter of time before those stars on close orbits around the centre of
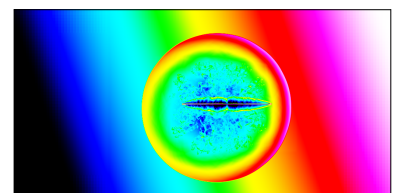
the galaxy, meet their doom. But how much time? It can take millions of years for material from the parent galaxy, whether that be gas or individual stars, to be gravitationally captured into an accretion disc around a SMBH. It also takes time for material in the accretion disc to move past the last stable orbit of $3R_\mathrm{S}$ and actually be accreted. Thus, it may be the case that AGN change from one state (active/inactive) to the other every few million years or so in between refuelling. This temporal variability, such that AGN can be in a state of activity or quiescence, could explain why some galaxies are seen to be active, and others not, and this is one of the many questions which microquasars could be particularly helpful with.

Microquasars typically also show signs of intermittent jet activity (see chapter 2 for more details on this), whereby the jets become observable during periods of outburst, and then disappear below telescope sensitivity thresholds[2]. Hence, a more befitting name might be "Active binary nuclei" rather than microquasars, since this emphasises the similarity with active galaxies, whereas X-ray binaries that are not "active" are likened to galaxies that are not active.

The exact physics governing accretion processes, extraction of energy, jet-launch, and jet collimation, so far remain theoretical. In order to provide adequate tests for these theories, we require data from observations. This can prove difficult with AGN since the timescales related to their activity can be of order 10^6 years or more, in other words it takes a long time for AGN to change their behaviour and therefore provide evidence that conclusively distinguishes between the proposed models. This underlines the importance of microquasars, which might provide the key to unlocking the secrets of the elusive black hole, and the truth as to the mode of jet formation.

The stellar mass black holes present in microquasars undergo the same physical mechanisms of accretion, jet-launch and so on, as do AGN, and the key similarities and differences in these two classes of object are depicted in Figure 1.4. The principle difference is that stellar-mass black holes are observed to vary on timescales of weeks, days, hours, or in some cases even

---

[2]For a given exposure time, obviously.
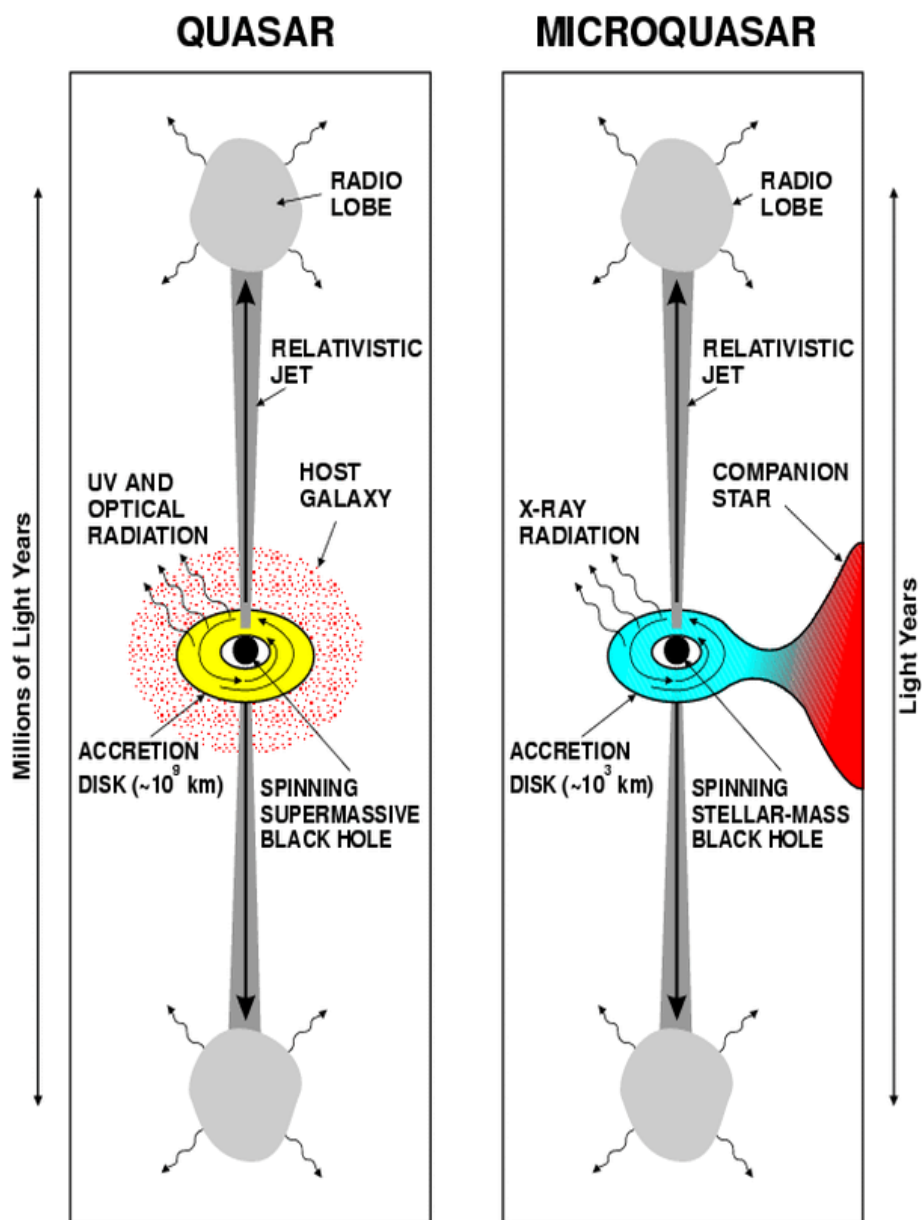
Figure 1.4: A graphical summary of the similarities between microquasars and AGN from Mirabel & Rodríguez (1998). Both of these systems share striking featurs in common, such as accretion unto a compact object resulting in very high luminosities and the ejection of relativistic plasma in the form of jets. The main differences are: (i) obviously the system sizes, for example accretion disc radius and jet extents, (ii) the source of fuel, which is usually a companion star for a microquasar, or ambient gas and nearby stars for the AGN, (iii) microquasars emit much of their radiation in the X-ray region of the electromagnetic spectrum, whereas AGN emit most strongly in the optical.
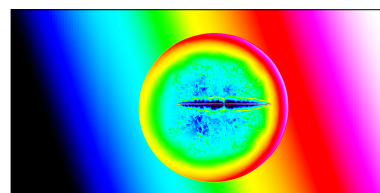
minutes. It is therefore humanly possible (i.e. within a lifetime) to generate models of the behaviour of microquasar systems based upon observational data, and then re-observe one year or so later to test the model(s). From the wealth of data obtained in the last few decades pertaining to Galactic microquasars, it seems that some microquasars (misbehave) undergo episodes of activity more frequently than others, and one field that has been particularly successful in studying microquasars, is radio astronomy (more details in chapter 3).

1.5   The structure of this thesis

This thesis presents a study of the interactions of the jets from SS 433 with its environs. This has been done via a radio study of the surrounding interstellar medium spanning 12 years from 1984 to 1996, and via a series of high resolution hydrodynamical simulations of the system. Chapter 2 briefly describes the wealth of observational and theoretical work that has contributed to our current understanding of the system. It also describes some of the pitfalls in our understanding, and poses some of the most puzzling questions regarding the large scale structure around SS 433, which I will attempt to address in this thesis. Chapter 3 presents a brief overview of radio interferometry and synthesis imaging, and describes some of the radio data reduction techniques I used to reduce VLA data. Chapter 4 describes an analysis of multi-epoch radio data to constrain the kinematics of the galactic environment at the locality of SS 433. Chapter 5 introduces the esoteric art of computational hydrodynamics and the difficulties therein, before describing the numerical model I devised to describe SS 433's background environment. Chapter 6 gives details of my numerical model for simulating a supernova explosion appropriate to that experienced by the progenitor of SS 433. In Chapter 7 I describe the models used to emulate the behaviour of SS 433's jets. Chapter 8 presents the results of the interaction of various kinds of jets described in the models of Chapter 7 with an evolved supernova remnant from Chapter 8. Finally, Chapter 9 summarises the ideas presented in this thesis and their conclusions, along with my ideas for further research in this field and its extension to relevant others.

Chapter 2

Concerning SS 433 and other Microquasars

This thesis is primarily concerned with the interaction of the microquasar SS 433 with its environment. In this section I endeavour to set the scene for the investigations that follow, by briefly introducing the facts derived from observations of SS 433, and then by drawing some relevant comparisons with other microquasar systems.

2.1 A brief history of SS 433

In 1976 Stephenson and Sanduleak conducted a survey of bright H_α stars in the Milky Way (Stephenson & Sanduleak, 1977), and the 433rd object in this survey was originally assumed to be an ordinary O-class star with strange Hydrogen and Helium emission lines. Two years later came the realisation that this was not an entirely accurate description of this particular object, and the first insight as to the true complexity of the system came from the "bizzare" moving emission lines in its optical spectra (Margon et al., 1979a). The H_α emission line was seen to be flanked by two unknown emission lines which shifted periodically and in contrary motion. Later that same year, several astrophysicists (Milgrom, 1979; Margon et al., 1979b; Fabian & Rees, 1979) realised that the behaviour of these strange emission lines could be explained by
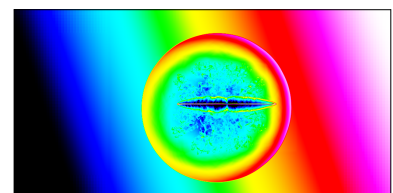
the precession of two oppositely directed relativistic beams of emission. The latter was very successful in describing the bulk changes in the observed Doppler shifts with time, and was dubbed "the kinematic model" of SS 433 and is described in §2.2. This news was extremely exciting, and SS 433 became widely known as the first stellar source of relativistic jets to be discovered within our Galaxy.

Three decades later, the quest to understand SS 433 continues. A lot of headway has been made since its discovery, and SS 433 has already contributed greatly to our understanding of X-ray binaries and jets. Still, some very important questions remain, and a few of these are outlined in §2.5.

2.2   The Kinematic Model

The interesting emission line characteristics in SS 433's spectra are a consequence of its orientation with respect to our line of sight. To the nearest degree, one period of SS 433's jet precession sweeps out a cone of semi-angle $\sim 21°$, and the axis of the cone is at an inclination to our line of sight of $78°$, such that each jet spends some time in redshift and some time in blueshift. The kinematic model of SS 433 (Milgrom, 1979; Margon et al., 1979b) roughly describes the bulk kinematics of the system, where the component of the jet velocity along our line-of-sight is given as:

$$\beta_{\mathrm{radial}}(t) = \frac{\mathbf{v}_{\mathrm{Jet}}}{c} \cdot \hat{n} = \beta_0 [\sin i \, \sin \theta \, \cos(\omega t + \delta) + \cos i \cos \theta] = \beta_0 [a \, \cos(\omega t + \delta) + b] \quad (2.1)$$

where β_0 is the bulk jet speed, θ is the opening angle of the jet precession cone, i is the inclination to our line of sight, δ is a phase offset (depending on the definition of phase-zero), and ω is the angular frequency of precession. In this case, $\hat{n}$ is used to denote a unit vector along the observer's line-of-sight to SS 433. The most sensible definition for phase-zero specifies that the
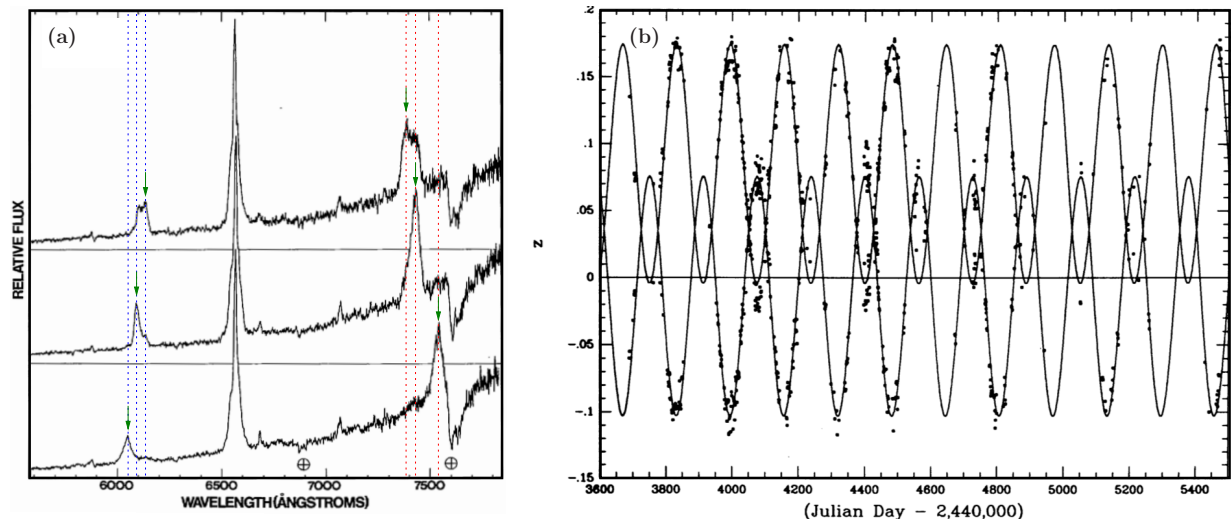
Figure 2.1: (a) An early observation of SS 433's spectrum (Margon et al., 1979a). The rest-frame H_α emission is shown by the strong emission peak at ≈ 6563Å. In each panel (top, middle and bottom), the central H_α peak is flanked by a single redshifted H_α emission line (red dashed line) and a single H_α blueshifted emission line (blue dashed line). The upper, middle, and lower panels correspond to the observations of 23rd, 24th, and 26th October, 1978. (b) The fit of the kinematic model to 10 years (1978-1988) of spectroscopic data from SS 433 (Margon & Anderson, 1989).

receding jet is maximally redshifted at t=0, requiring that $(\omega t + \delta) = 0$ and hence $\delta = 0$. The observed Doppler effect as a function of time, due to the jet radial velocity described above, can be written as:

$$\lambda_{\mathrm{red}}(t) = \gamma \left(1 + \beta_0 \left[a \, \cos \omega t \, + \, b \right] \right) \lambda_0 \tag{2.2}$$

$$\lambda_{\mathrm{blue}}(t) = \gamma \left(1 - \beta_0 \left[a \, \cos \omega t \, + \, b \right] \right) \lambda_0 \tag{2.3}$$

for the red and blue shifted lines respectively.

2.2.1 Beyond the Kinematic Model

It is worth briefly mentioning the additional kinematic components within SS 433 that are not described by the kinematic model above. The emission lines also show variations on smaller timescales than the precession period. The binary orbital period is one example, with a period of
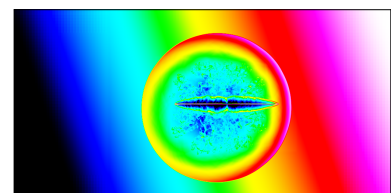
~ 13 days. The disc-jet system is also seen to nutate with a period of ~ 6.5 days, corresponding to the beat-frequency through the interference of the precessional and orbital periodicities. There are some small but notable deviations from the kinematic model at the maxima and minima of the Doppler shifting in each precessional period, but it is worth noting that the jet speed isn't exactly constant and varies slightly about the mean value, with a standard deviation of $\sim 1\%$.

2.3   Observational parameters of SS 433

After three decades of research[1], the system has been widely identified as a high mass X-ray binary (HMXB) system. The masses of the constituent bodies have been estimated using a variety of techniques (Crampton & Hutchings, 1981; D'Odorico et al., 1991; Collins & Scher, 2002; Gies et al., 2002; Hillwig et al., 2004; Fuchs et al., 2006; Lopez et al., 2006; Blundell et al., 2008) yielding some varied results. In general the observations seem to favour the scenario of a black hole in orbit around a more massive companion star (Fabrika, 2004). Recently, the presence of a circumbinary ring around SS 433 has been observed via optical spectroscopy (Blundell et al., 2008) and also near infra-red spectroscopy (Perez M. & Blundell, 2009), and these observations determine the mass internal to the ring to be $40 M_\odot$, of which $16 M_\odot$ is attributable to the compact object and its accretion disc. Thus, it is believed that SS 433 hosts a black hole (BH) rather than a neutron star. The BH's accretion disc is presumably fed by gas from a strong stellar wind or Roche-lobe-like overflow from the companion star with a rate of $7 \times 10^{-6} \lesssim \dot{M}_{\text{transfer}} \lesssim 4 \times 10^{-4} \, \text{M}_\odot \, \text{year}^{-1}$ (King et al., 2000), accompanied by two oppositely directed relativistic jets which are thought to eject material at a rate $\dot{M}_{\text{jet}} \gtrsim 10^{-6} \, \text{M}_\odot \, \text{year}^{-1}$ (Begelman et al., 1980) into the surrounding interstellar medium. The disc-jet system exhibits precessional motion, which is roughly described by the kinematic model of SS 433 (§2.2, Milgrom (1979); Margon et al. (1979b)) and is readily observed via the periodic Doppler shifting of

---

[1]At the time of writing, of order 10^3 research articles have been devoted to the study of SS 433 and its environs.

optical emission lines from the jets. By fitting the kinematic model to spectroscopic data spanning 20 years, Eikenberry et al. (2001) determined the following best-fit kinematic parameters: $t_{\mathrm{prec}} = (162.375 \pm 0.011)$ days for the precession period, $\beta_{\mathrm{jet}} = (0.2647 \pm 0.0008)$ for the jet speed as a fraction of the speed of light, $\theta_{\mathrm{prec}} = (20°.92 \pm 0°.08)$ for the precession cone half-angle, and $\theta_{\mathrm{inc}} = (78°.05 \pm 0°.05)$ for the inclination of the mean jet axis to our line of sight. Goranskii et al. (1998) conducted a multi-colour photometric study of SS 433 over a similar time period of 20 years, and used Fourier analysis to extract the orbital period of $P_{\mathrm{orb}} = 13.082$ days, and a nutation period of $P_{\mathrm{nut}} = 6.28$ days.

In the radio regime, more than two complete precessional cycles of the jets have been spatially resolved (Blundell & Bowler, 2004), providing confirmation of the jet speed as $\sim 0.26c$ and enabling an independent calculation of the distance to SS 433 as $d_{\mathrm{SS433}} = 5.5 \pm 0.2$ kpc. Using Very Long Baseline Interferometry (VLBI), the jet has been resolved at milliarcsec scales into individual fireballs of ejecta (Vermeulen et al., 1987; Paragi et al., 1999b), and the presence of an equatorial *"ruff"* outflow[2] from the accretion disc has become apparent (Paragi et al., 1999a; Blundell et al., 2001). Furthermore, recent optical spectroscopic studies have revealed that these discrete fireballs of jet ejecta (also referred to as bolides) are optically thin, and expanding in their own rest frame at approximately 1% of the jet speed (Blundell et al., 2007).

2.3.1 Mass Transfer

As described in the text of the preceding sections, and summarised in Figure 2.2e, there are a number of modes of mass transfer in effect in SS 433. The Wolf-Rayet companion star is thought to be ejecting its outer envelope at an alarming rate (as typical of Wolf-Rayets) via a strong stellar wind and is believed to be overfilling its Roche lobe, thus transferring mass to the accretion disc by multiple means. The accretion disc itself also has an incredibly strong wind,

---

[2]So called due to the shape of the outflow, which resembles that of an Elizabethan ruff about the accretion disk. See for example: $http : //en.wikipedia.org/wiki/Ruff\_(clothing)$.
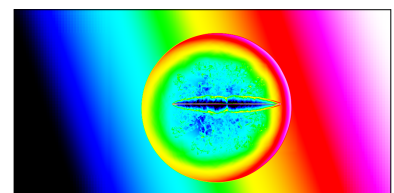
All scales of the SS 433−W 50 system
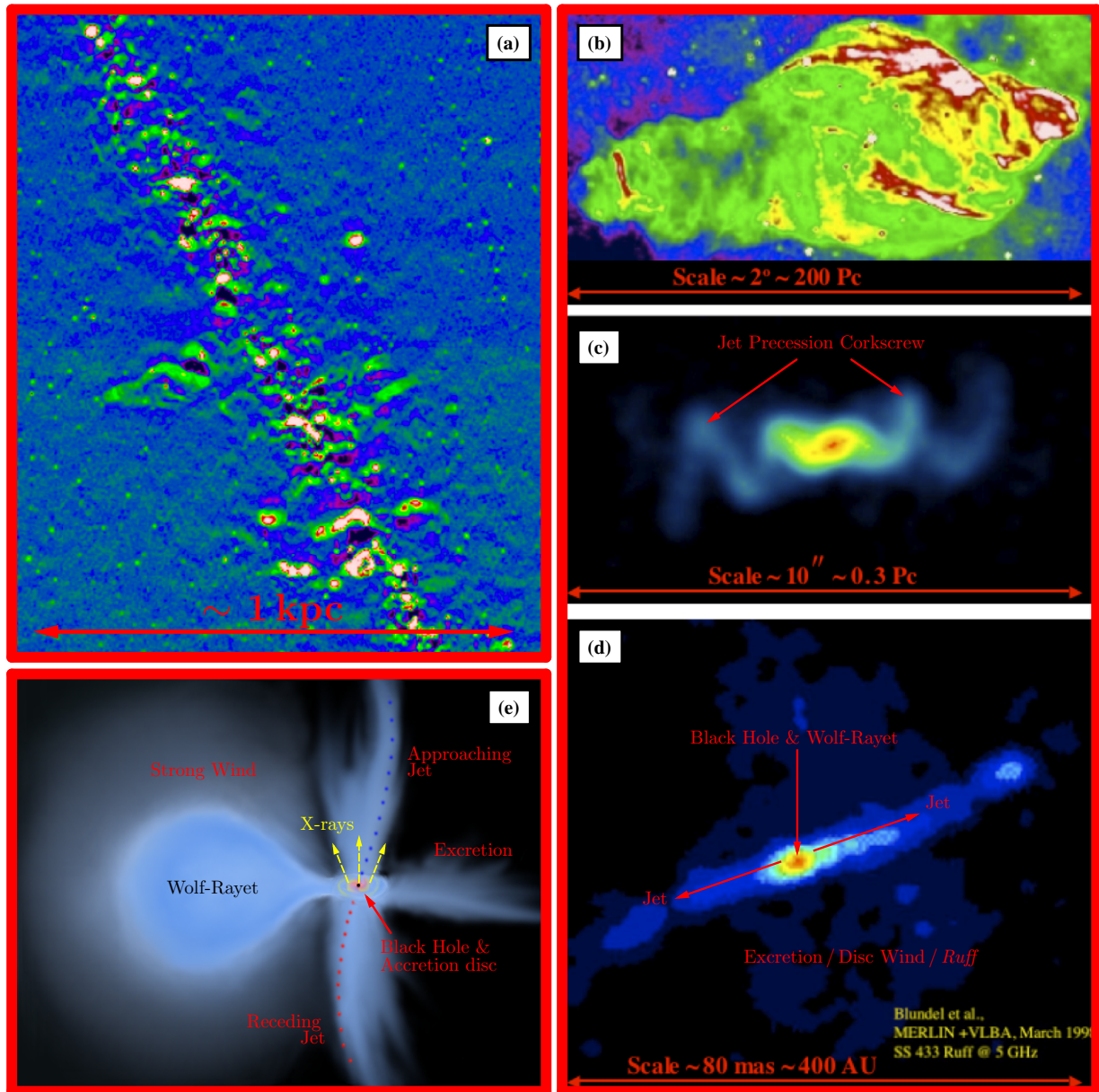
Figure 2.2: The impact of SS 433 upon its environment is shown on all scales, with increasing magnification from (a) to (e). Description: (a) 5GHz radio image of W 50 and SS 433 as located in the Milky Way, credit: GB6 survey (Gregory et al., 1996). (b) VLA (D-array) mosaic of W 50 at 1.4GHz, credit: (Dubner et al., 1998). (c) VLA (A-array) image of SS 433's precession "corkscrew" at 5GHz, credit: (Blundell & Bowler, 2004). (d) VLBI image of the central engine in SS 433, credit: (Blundell et al., 2001). (e) A cartoon of what I think SS 433 looks like as an X-ray binary system, with the key components labeled, credit: ptg.

and recent calculations based in infra-red spectroscopy (Perez M. & Blundell, 2009) reveal a (poloidal) mass loss of $\dot{M}_{\mathrm{disc}} = 10^{-4} \mathrm{M}_\odot \, \mathrm{yr}^{-1}$ with a disc-wind velocity of $v_{\mathrm{DW}} = 1500 \mathrm{km} \, \mathrm{s}^{-1}$.

2.4   Introducing the SS 433 − W 50 Complex

As shown in Figure 2.2, the central engine of the microquasar SS 433 is embedded deep within the W 50 nebula, where the features of the W 50 nebula itself are well displayed in the radio mosaic of Dubner et al. (1998) (Figure 2.2b). The remarkable phenomenology of W 50 (Figure 2.3b) spans 208 pc along its major axis, featuring a circular region which is believed to be the remains of an expanding supernova remnant (SNR) shell, with two elongated lobes to the east and west of the circular shell. The circular shell is centred upon the position of SS 433 with an offset of just 5 arcminutes (Lockman et al., 2007). The distance to W 50 is difficult to constrain using the kinematics of the HI gas within the nebula because of its extent and inhomogeneity, and due to the high level of turbulent confusion along the line of sight near the Galactic plane. However, recent radio observations of HI in absorption and emission now confirm that the distance to W 50 is consistent with 5.5 kpc (Lockman et al., 2007), which places it at the locality of SS 433. We consider the details of the local environments of SS 433 and W 50, as Dubner et al. (1998) did, that they are equidistant from us and that their mutual evolutions are connected.

2.5   Prevalent questions concerning the SS 433-W 50 system

The incredible detail revealed by the famous radio mosaic of W 50 (Dubner et al., 1998) presented a number of puzzling questions concerning its formation. We endeavour to address these issues through our models and will later discuss each one (see chapter 9).
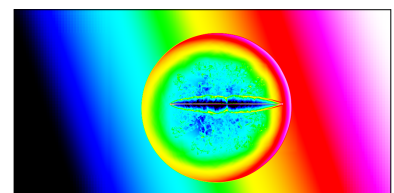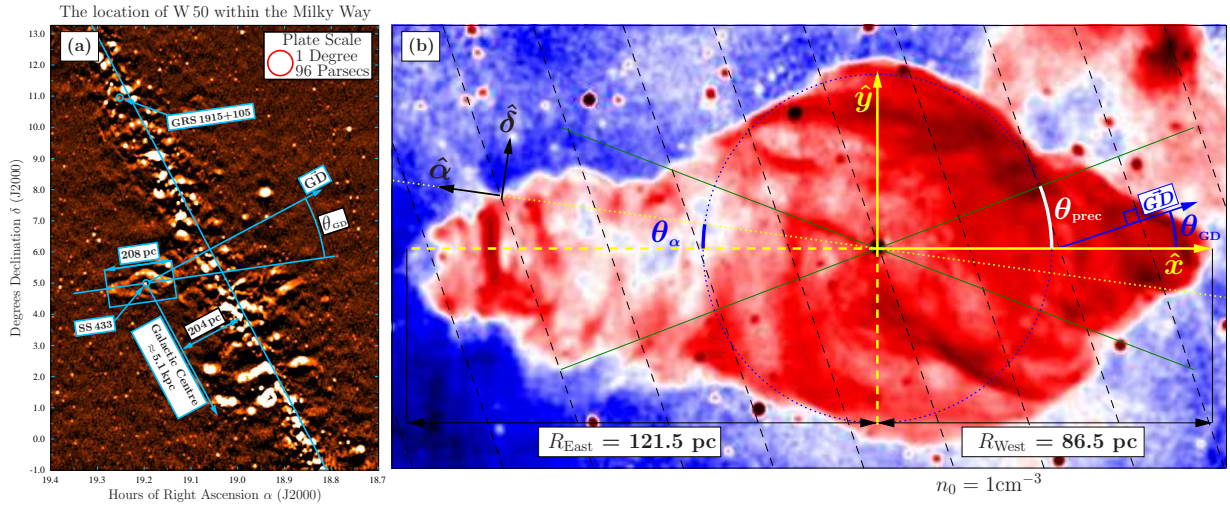
Figure 2.3: This figure describes the geometry of the SS 433-W 50 system. (a) This mosaic was created using archival data from the GBT6 survey (Gregory et al., 1996), showing the location of W 50 with respect to the Milky Way Galaxy plane. The vector **GD** points normally towards the Galactic disc, and $\theta_{\mathrm{GD}} = 19.7°$ is the angle this vector subtends with the mean jet axis. The plate scale in (a) applies to objects at the same distance as SS 433 of 5.5kpc (1 arcmin $\simeq 1.6$ pc). (b) The famous VLA mosaic of W 50 provided by Dubner et al. (1998) has been rotated here such that the x-axis is coincident with the mean axis of SS 433's jet precession cone. SS 433's western jet-cone points in the direction $+\hat{x}$, and the eastern jet-cone in $-\hat{x}$. In this frame the Right-Ascension ordinate $\hat{\alpha}$ makes an angle of 172° with the x-axis ($\theta_{\alpha} = 8°$). The dashed black lines indicate changes in the ISM density by a factor of 2 due to an exponential Galactic density profile with scale-height $z = 40$pc, and normalised to $n_0 = 1$ particles cm^{-3} at SS 433 (the seperation between adjacent dashed black lines corresponds to $40\ln 2$ pc). Another microquasar, GRS 1915+105 is also present in the field of view of (a) and its coordinates are indicated. However, GRS 1915+105 does not seem to be encapsulated within a well defined large-scale nebulous structure in the way that SS 433 is with W 50, and more details about this are given in §2.6.2.

2.5.1   East-west lobe asymmetry and annular structure

The lobes (or *ansae*) share an axis of symmetry with SS 433's mean jet axis (the $\hat{x}$ axis in Figure 2.3b), and exhibit a fascinating annular structure, which is most noticeable in the eastern lobe. The coincidence of W 50's axis of symmetry with SS 433's mean jet axis has led to the hypothesis that SS 433's jets are responsible for the formation of W 50's elongated lobes.

There is a noticeable asymmetry about the $\hat{y}$ axis in Figure 2.3b, that is, in the extents of the

east and west lobes of W 50. The east-west asymmetry can be characterised by the ratio of the lobe extents:

$$R_{\mathrm{ratio}} = \frac{R_{\mathrm{East}}}{R_{\mathrm{West}}} = 1.40. \tag{2.4}$$

The gas density in the Milky Way disc decays exponentially with perpendicular distance from the plane of the disc, with a scale-height of approximately 40 pc (Dehnen & Binney (1998) and §5.11). At 208 pc, the east-west length of W 50 is several times greater than the scale-height of the disc in the direction normal to the Milky Way disc (see Figure 2.3b and also §5.11 for more details on this). The galaxy ISM near the western edge of W 50 (being closer to the plane of the disc) is much denser than that near the eastern edge of W 50. Consequently, SS 433's west jet experiences greater resistance from an increasingly dense ISM as it nears the Galaxy disc. In contrast, the east jet experiences ever lower resistance from an ISM which is decreasing in density with increasing distance from the Galaxy disc. It is thought that the east-west lobe extent asymmetry about the $\hat{y}$ axis in Figure 2.3b is a result of this density gradient, and the validity of this theory is explored in §7.7 of this thesis.

Due to the inclination of the jet-axis with respect to our line of sight, a small geometrical correction $\sin\theta_{\mathrm{inc}} \approx 1$ is implicit in the measured values R_{East} and R_{West} (but not in the ratio R_{ratio}), where $\theta_{\mathrm{inc}} \approx 80°$ (Hjellming & Johnston, 1981; Eikenberry et al., 2001). As a result the physical extent of each lobe is larger than measured, by a factor $1/\sin\theta_{\mathrm{inc}} \approx 1$.

2.5.2   SS 433's latency period

We can calculate an *in vacuo* jet travel time required for the extent of the eastern lobe to reach R_{East} based on the jet speed:

$$t_{\mathrm{vacuo}} = \frac{R_{\mathrm{East}}}{\beta_{\mathrm{jet}}\, c} \simeq 1500 \text{ years} \tag{2.5}$$
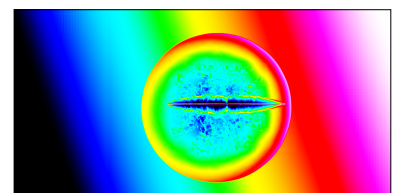
where t_{vacuo} is only a lower-limit estimate for the actual jet travel time, due to retardation of the jets in the presence of the ISM. This estimate is noticeably smaller than the time taken for a typical SNR to reach a radius of 45 parsecs (the radius of the circular region in Figure 2.3b), where the SNR expansion time can vary between $\sim 10^4 - 10^6$ years depending on the explosion blast energy and the background density. This suggests that SS 433's jets were initiated relatively recently in the history of W 50. We refer to the period after the supernova explosion of SS 433's progenitor and before the ignition of jets, as SS 433's "latency" period. The reason for this latency period is currently not well understood, and we endeavour to estimate the duration of this period in chapter 8 in order to constrain the possible scenarios.

2.5.3   SS 433's jet persistence and precession-cone angle

SS 433 is often noted as being somewhat unique among the microquasar class due to the apparent persistency of its radio jets. Other microquasars typically exhibit a more intermittent behaviour, temporarily increasing in luminosity with each episodic jet outburst, before returning to a state of relative quiescence. These jet ejection episodes in microquasars characteristically last for one or more weeks, and recur every one or more years. Successive jet outbursts can be observed to happen with substantially different properties, for example in 1997 a flare from the microquasar Cygnus X-3 was observed with jet speed $v_{1997} \geq 0.81c$ and precession cone angle $\psi_{1997} \lesssim 12°$ (Mioduszewski et al., 2001), while a subsequent flare was observed in 2001 with jet speed $v_{2001} = 0.63c$ and precession cone angle $\psi_{2001} = 2.4°$ (Miller-Jones et al., 2004). We must consider the possibility that SS 433's jets are not constantly active, but rather that they also exhibit jet outburst episodes of a much longer duration[3] than other known microquasars.

---

[3]In other words, we are currently (and have been since SS 433's discovery,) witnessing the most recent outburst of jet activity.

2.5.4   Radio and X-ray correlation

The X-ray emission from W 50 has been mapped using a number of telescopes (ROSAT, ASCA, RXTE, XMM-Newton, Chandra) covering three orders of magnitude in X-ray energies (Yamauchi et al., 1994; Brinkmann et al., 1996; Safi-Harb & Petre, 1999; Moldowan et al., 2005; Brinkmann et al., 2007), and it is generally noted that the X-ray emission from W 50 is seen to be confined to a region much closer to the mean jet axis than the precession cone of SS 433's jets would indicate. This has led to further questions about the possible refocusing of SS 433's jets.

The X-ray data from the observations described by Brinkmann et al. (1996), where kindly donated to me by W. Brinkmann (private communication) for comparison with my hydrodynamic simulations. By compiling a list of point-sources and their coordinates from both X-ray and radio surveys of the region $2° \times 2°$ centred upon SS 433, it was possible to see which point sources were coincident in both the X-ray and radio images of W 50. Using the coordinates of these point sources enabled me to calculate accurate coordinate systems for each image (by amending the header information in each FITS file), such that the radio and X-ray maps could be overlaid upon each other for comparison. The result are shown in Figure 2.4, and it is clear that the X-ray and radio maps of W 50 are remarkably similar. Note that the images shown in Figure 2.4 have both been rotated such that the mean jet axis in SS 433 is along the horizontal, so that these images can be easily compared with simulation results later in this thesis. It has been suggested in many of the X-ray publications that the X-ray emission comes from the central axis of W 50 only and does not fill the entirety of the wide lobes of W 50's shell as shown in the radio. However, Figure 2.4 shows the log of the flux in each image with the contrast levels adjusted to bring out the background emission, and this is necessary because SS 433 completely overpowers the emission from the rest of the nebula. This being done, Figure 2.4 clearly shows that extended X-ray emission that is too-well aligned with the radio nebula contours to be coincidental Poisson counting noise that one might expect from a noisy background. In other words, the blue emission regions in the lower panel of Figure 2.4 are more or less confined by the white radio contours,
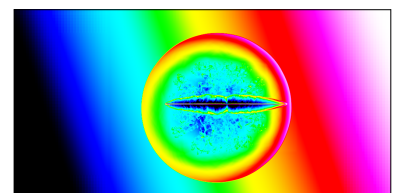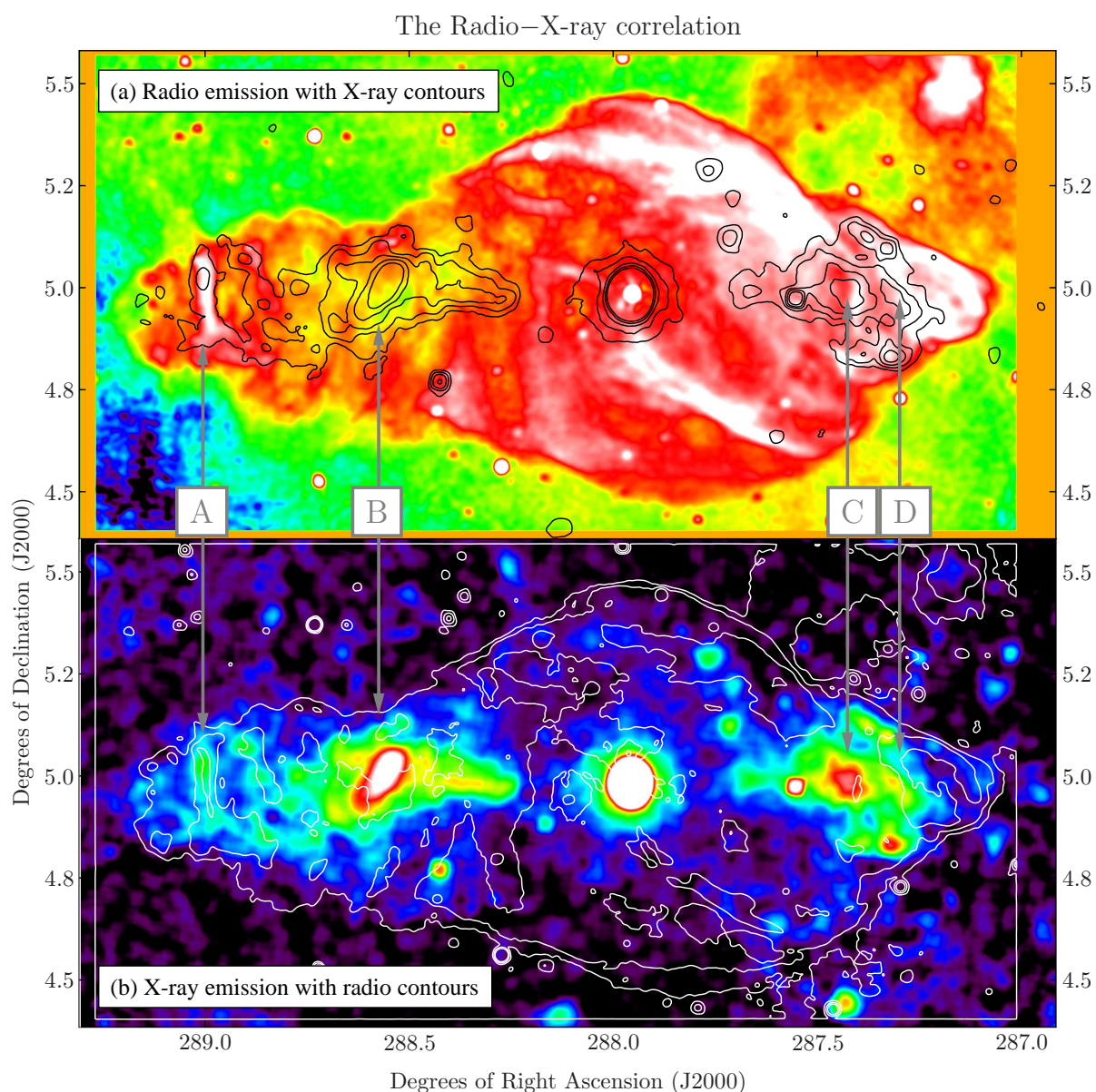
Figure 2.4: Comparing the X-ray and radio emission from W 50. The colour maps correspond to (a) radio emission at 1.4GHz from the VLA (Dubner et al., 1998), as compared to (b) X-ray emission in the range 0.9−2keV as detected by ROSAT (Brinkmann et al., 1996). The contours from the X-ray image in (b) are overlaid upon the radio image in (a), and the contours from the radio image in (a) are overlaid upon the X-ray image in (b). Note the striking correspondence in the lower figure between the low-level (blue) emission and the outline of the contour from the radio nebula. Furthermore, the bright filament at point **A** on the far west of W 50 is coincident in both X-rays and radio. Equally striking: the brightest parts of the X-ray lobes (emission from the jets) at points **B** and **C** are almost exactly coincident with regions where the radio emission becomes dimmer than its surroundings (i.e. a radio cavity where the X-ray lobes are brightest). Finally, the point labeled **D** shows an abrupt end to the eastern X-ray jet lobe, and the beginning of the brightest part of the radio jet lobe.

with the exception of a few foreground/background point sources that are not associated with
W 50. The caption of Figure 2.4 describes the correlation between radio and X-rays in more
detail. It should be noted that there are regions where the X-rays and radio flux are spatially
coincident, such as SS 433 and the bright eastern filament labelled "A".

2.6 Prevalent questions concerning Microquasars in general

2.6.1 Discovering new Microquasars

Although several hundred X-ray binaries have been observed and are documented in the literature
(Liu et al., 2006, 2007), only a handful of these are recognised as microquasars. This in itself
tells us something significant about the longevity of a microquasar's lifetime.

The microquasar stage in X-ray binary evolution is probably relatively short-lived; the com-
panion star in a HMXB (Figure 1.3) is also destined to undergo a supernova explosion[4], thereby
ejecting a lot of potential "fuel" out of the system. Furthermore, most microquasars exhibit
episodic, rather than persistent jet activity. Hence, if the jets of a given microquasar are not
active when a telescope is pointed towards it, it is less likely to show up as a point source in
the telescope survey (unless it is intrinsically bright in radio wavelengths). It therefore seems
plausible that the intermittency of jet activity in microquasars plays a significant role in their
discovery.

One can speculate as to the possible reasons for compact objects being inactive. Perhaps the
accretion process is being hindered in some way, by the lack of available "fuel" in the vicinity
for example. The nature of the outflow from the donor star could feasibly be responsible. If the
companion star is unstable to pulsations as massive stars can be (Cepheid variables and AGB
stars for example), then material in the star's outer envelope may only escape past the Roche

---

[4]The famous film "Knock on any door" in 1949 starring Humphrey Bogart features the quote "*Live fast, die
young, and leave a good-looking corpse.*". Whilst crude, this is seemingly very appropriate to high mass stars.
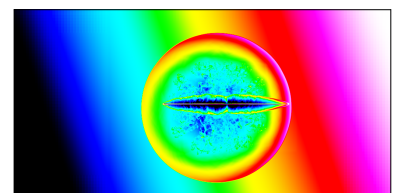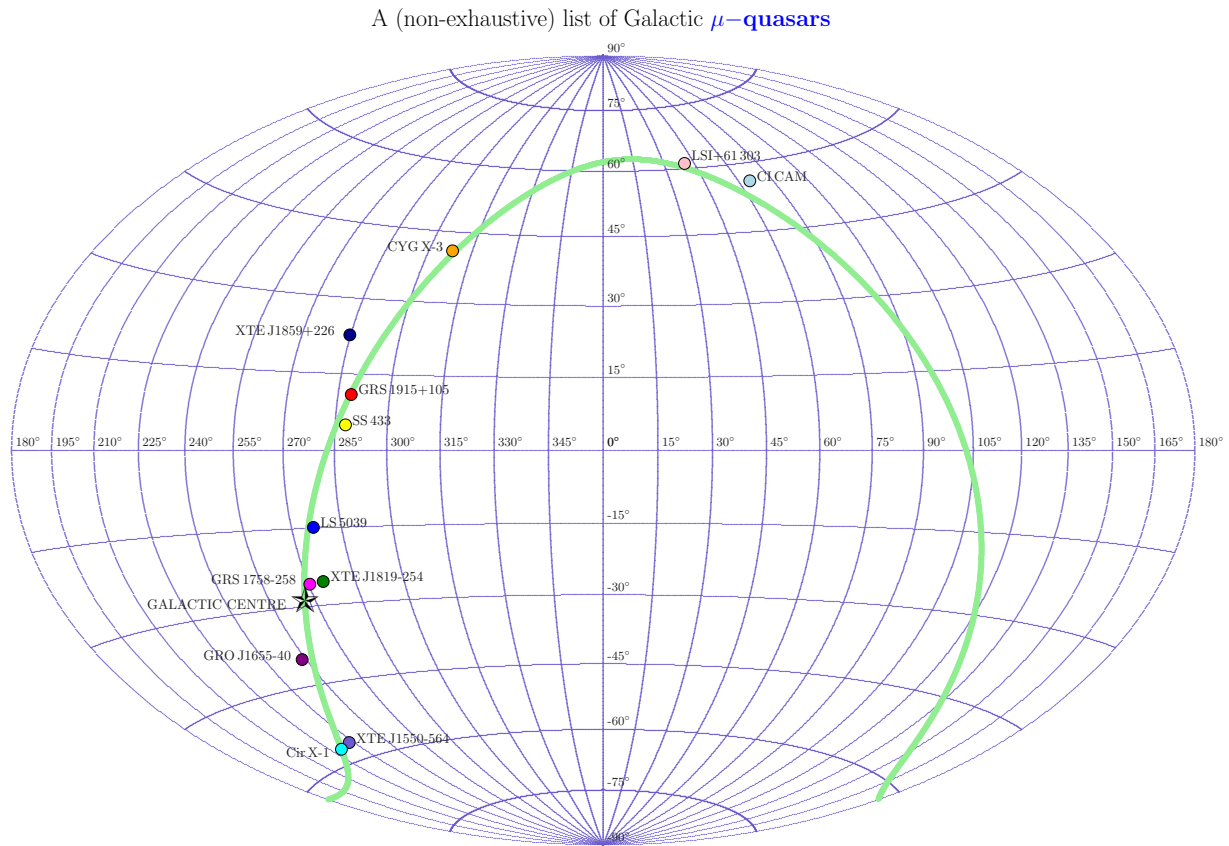
Figure 2.5: Some of the more famous microquasars are plotted here atop a Hammer-Aitoff projection of the celestial grid. The Milky Way disc is traced out by the green line.

lobe during a pulsation. If this was the case, then the accretion process would cease for a time in between pulsations, thus starving the compact object of its source of fuel. Maybe magnetic fields play a dominant role, in much the same way that magnetic reconnection is responsible for solar flaring. These are a few of the exciting questions that have yet to be solved, within the realm of microquasars.

2.6.2   On the dwelling places of Microquasars

Figure 1.2 of chapter 1 shows how collimated outflows can have profound effects upon their surroundings in many classes of objects outside the microquasar realm. As detailed in §2.3.1 there are several modes by which the microquasar SS 433 ejects material and shapes its surroundings.

Figure 2.5 shows the distribution of a sample of famous microquasars within our galaxy, and this section discusses the impact that microquasars like these should have upon their environment, in a similar manner to SS 433.

The most dramatic stage in the birth of an X-ray binary (refer back to Figure 1.3d) is the formation of a compact object, which later develops an accretion disc. The formation of a compact object is accompanied by a supernova explosion that can be devastating to the surrounding environment at the location of the progenitor. The fingerprints of supernovae explosions are present throughout our Galaxy in the form of supernova remnants (SNR) of varying shapes and sizes, which can be shell-like or plerionic (filled, usually containing a source that inflates the SNR, such as the crab pulsar in the crab nebula). Supernova remnants contain fast moving ionised plasmas and strong magnetic fields, and as a result SNRs emit synchrotron radiation and are often readily observed by radio telescopes. It is therefore not unreasonable to expect that a microquasar might be embedded within one of these remnants when observed at radio wavelengths, in the same way that SS 433 is located at the centre of W 50. To investigate this possibility, a group of well-known microquasars that are distributed throughout the Milky Way were examined (see Figure 2.5). Radio continuum maps of the field of view surrounding these microquasars were retrieved from three well-known radio sky surveys:

- The 6th Green Bank Telescope Survey (GB6, Gregory et al. (1996)) at 4850 MHz

- The Westerbork Northern Sky Survey (WENSS, Rengelink et al. (1997)) at 325 MHz

- The NRAO VLA Sky Survey (NVSS, Condon et al. (1998)) at 1400 MHz.

- The Sydney University Mongolo Sky Survey (SUMSS, Bock et al. (1999)) at 843 MHz.

Figures 2.6 and 2.7 show radio continuum images $8° \times 8°$ centred on the coordinates of each microquasar using either the GB6, SUMSS or WENSS surveys, depending on the quality of sky-coverage at the respective coordinates (there are gaps in some of the images, which are at
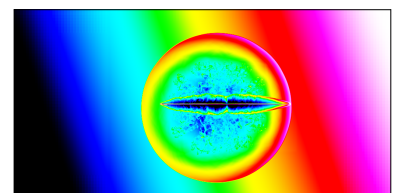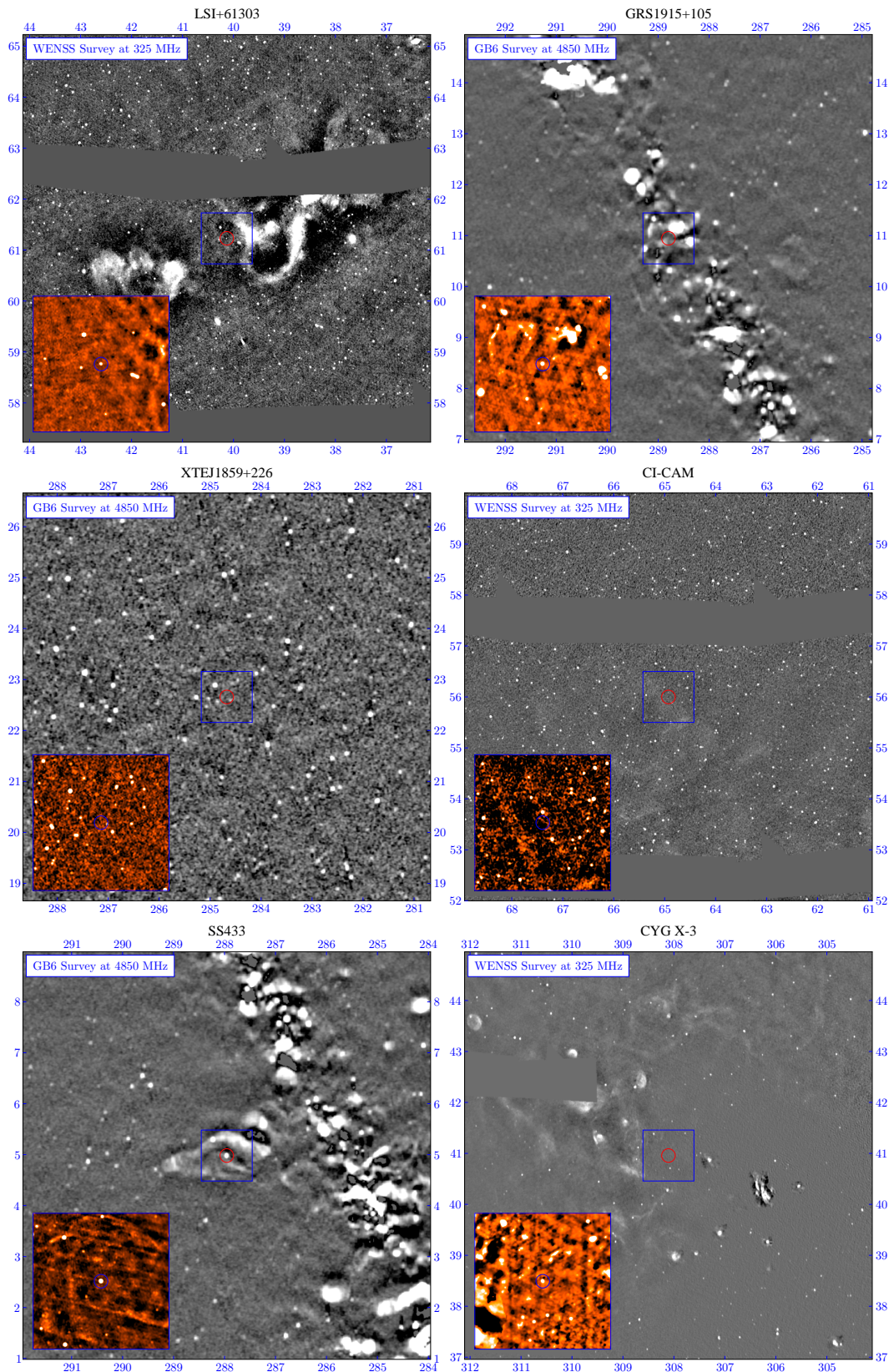
Figure 2.6: Using NVSS, WENSS, GB6 and SUMSS radio surveys to search for extended SNR structures around known microquasars (part1). The inlays are zoomed-in sections of the sky indicated by the blue boxes in each panel. The red and blue circles indicate the coordinates of a microquasar in the main panels and inlays respectively.
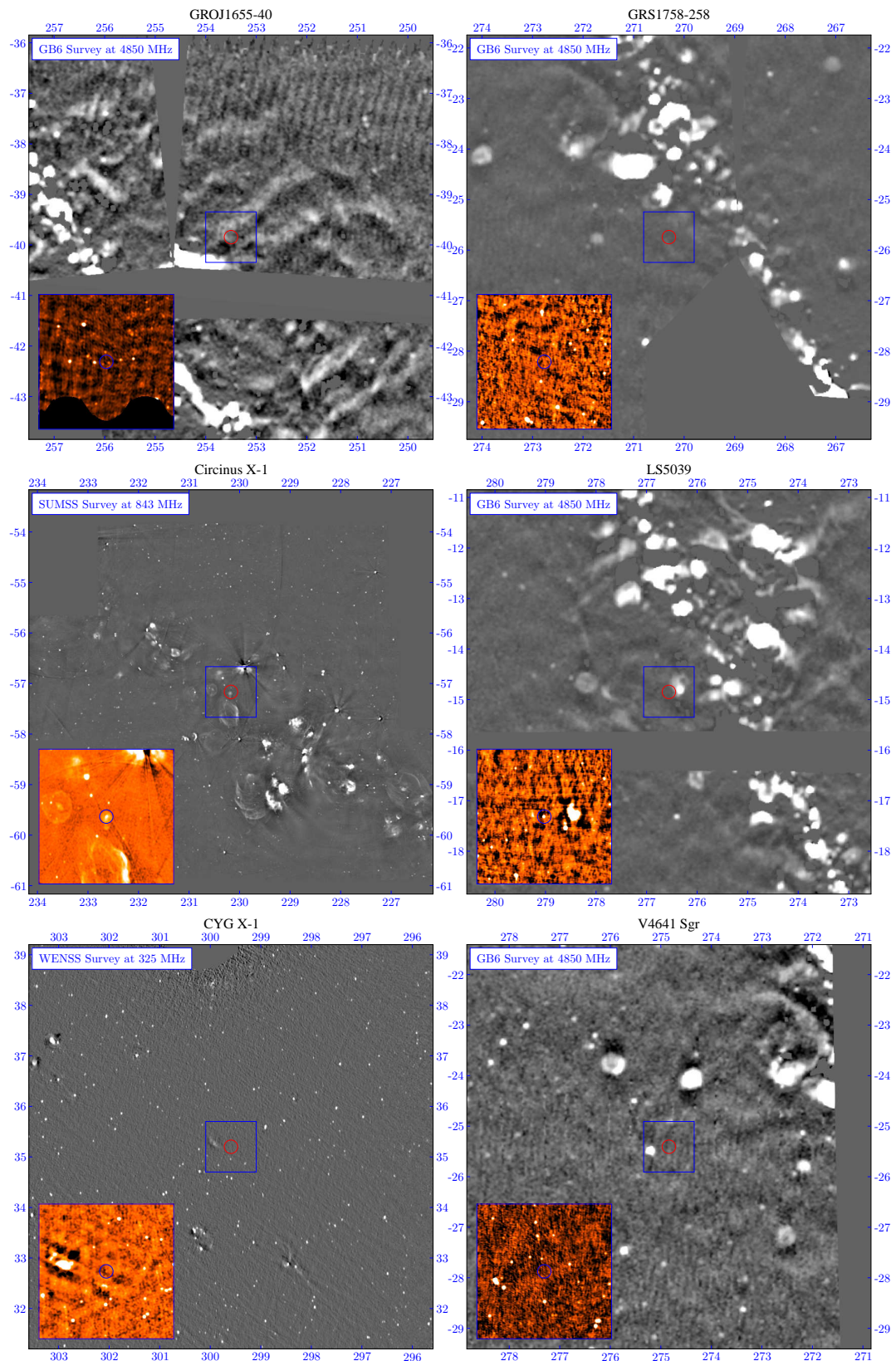
Figure 2.7: Using NVSS, WENSS, GB6 and SUMSS radio surveys to search for extended SNR structures around known microquasars (part2). The inlays are zoomed-in sections of the sky indicated by the blue boxes in each panel. The red and blue circles indicate the coordinates of a microquasar in the main panels and inlays respectively.
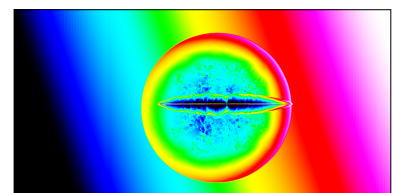
the edges of the survey ranges). The microquasar coordinates in each field are indicated by a red circle, and the inlay shows a zoomed-in section of $1° \times 1°$ from the NVSS (or SUMSS in the case of Circinus X-1), corresponding to the blue box around the microquasar. The greyscale images represent the log of the normalised flux of each image, and the colour scales are arbitrarily adjusted for each image to improve the visible contrast, in an attempt to reveal any hints of faint extended structure. Among the microquasars that are detected (the bright point sources within the red or blue circles) at the sensitivity of the surveys shown are SS 433, Cygnus X-3, LSI+61 303, GRS 1915+105, LS 5039 and Circinus X-1, however only SS 433 appears to be embedded within the well-defined structure of a large and evolved SNR. Circinus X-1 is centred on some small diffuse emission which could indicate the presence of a nebula or SNR.

A few of the microquasars listed here have been observed in the radio in more detail than shown in these surveys, with the aim of detecting large-scale structure around the jet sources, as evidence of the jet interaction with the surrounding ISM. Among the most convincing are Gallo et al. (2005) who show a semi-ring-like structure to the north-east of the jets of Cygnus X−1 with symmetry about the jet axis, and Tudose et al. (2006) who observe a nebula surrounding the microquasar Circinus X−1. Interestingly, the latter has jets very close to our line-of-sight, and it has been suggested that the surrounding nebula could be quite similar to W 50 if its jet axis had been closer to the plane of the sky.

The remarkable connection between SS 433 and W 50 is central to the research carried out in this thesis. The apparent lack of SNRs around most other microquasars is still an open question.

2.7   Simulating the SS 433-W 50 system

The range in physical sizes involved in the SS 433-W 50 system[5] makes it an extremely difficult object to model numerically, however several authors have confronted the challenge of simulating

---

[5]From VLBI observations with resolution of just a few milliarcseconds, to the ~ 2 degree extent of W 50 (see Figure 2.2), gives 6 orders of magnitude difference in size scales.

the jet-SNR interaction (notably Kochanek & Hawley (1990); Velázquez & Raga (2000); Zavala et al. (2008)). Although a more detailed discussion of previous works will be given in §9.1, we briefly introduce some of the early approaches in §2.7.1, and then describe the need for more accurate numerical models as presented in this thesis.

2.7.1 Previous simulation work

An early hydrodynamical study of SS 433's jets was carried out by Kochanek & Hawley (1990), who consider various forms of hollow cylindrical and conical jets, as well as filled conical jet models. The effect of "self interaction" of the jets with previous ejecta and with the jet cocoon itself is mentioned in their paper, and in several of the references therein. They use an axisymmetric model, and report that their hollow conical jets are neither recollimated, nor refocused. They discuss how their results are in disagreement with a model for jet refocusing proposed by Eichler (1983), in which precessing jets were suggested to experience a focusing effect caused by the pressure from the ambient ISM through which they propagate.

Velázquez & Raga (2000) recognised the physical attractiveness of the jet-SNR interaction scenario. They modelled the W 50 nebula by instantaneously imposing an analytical Sedov profile upon the ISM to mimic the supernova explosion, upon which the relativistic jets of SS 433 are later incident. Due to the computational constraints at the time, they modelled only one quadrant of the SNR in two dimensions, with the simplification of a scaled-down version of W 50 of radius 10 pc and a uniform density background ISM. The system evolution was closely followed until 2700 years after the jets were switched on, such that the simulated jet-SNR lobe extends to approximately 33 pc from the SNR origin. They follow the example of Clarke et al. (1989) who describe a neat model for computing the synchrotron emission from 2-D simulations, by assuming a toroidal magnetic field configuration about the jet axis, and revolving the resulting emission about 2π radians to create the projected 3-D emission. The hydrodynamics of the jet-SNR was further studied in the 3-D simulations of Zavala et al. (2008), who invoke both hollow and filled
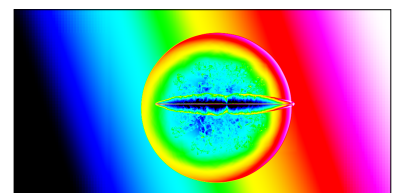
conical jets to simulate the precession in SS 433. They also conduct a small number of tests to investigate the physical parameters such as jet mass-loss rate and the radius of the SNR at the time when the jets switch on. The possibility of a time-variable jet precession angle is also tested in their investigations, and their results show a qualitatively similar morphology to that observed in W 50, in the sense that a spherical SNR shell is present with lateral extensions in the form of jet lobes, of arbitrary size.

2.7.2   My Simulations

Despite the successes of the previous pioneering numerical works, there are several invalid assumptions made in the models which have significant effects upon the results, and can be improved upon. The physical significance of the morphology present in W 50 has (so far) not been adequately addressed with relevance to the pressing questions of §2.5. The inconsistencies in these previous works will be discussed more fully in section chapter 9, and I endeavour to show that it is possible to produce a model of the SS 433-W 50 interaction that is consistent with observational data, if reasonable assumptions are made.

I emphasise the importance of including relevant observational data in simulation models, such as the appropriate sizes of the SNR and jet lobes, if we are to provide useful constraints on the system. I incorporate all of these observational constraints (with the exception of orbital motion) into our hydrodynamical model, to give an accurate representation of the dynamics of SS 433's jets. Using the observed parameters as a basis for our models of the SS 433-W 50 complex, I consider three possible evolutionary scenarios in detail in order to see if any of these consistently explain the origins of this extremely large and rare nebula. The results of these three scenarios are discussed in detail in chapter 9, but their mechanisms can be summarised as follows: (i) a supernova blast wave expanding in the presence of the Galactic baryon density background (ii) the interaction of SS 433's jets with the ISM only (no supernova), and finally (iii) the interaction of SS 433's jets with an evolved SNR shell from (i).

However, my intention is not solely to replicate the morphology of SS 433-W 50 complex, but to explore the effects of important astrophysical parameters such as the jet mass loss rate, supernova blast energy, and the ambient ISM density, which are among input parameters to the supernova and jet models. The distinctiveness of the W 50 nebula produced through these interactions, allows useful constraints to be placed upon the system parameters.

2.8 Summary

In this chapter I have described the key components of SS 433 and W 50, along with details of the latest observational parameters. The hypotheses regarding the SS 433-W 50 interaction are introduced, and the geometry of the system is illustrated as a framework for the numerical simulations which follow in the next few chapters. The striking correspondence between the X-ray emission and radio emission from W 50 are discussed, and will be referred to in later chapters. The motivation for improved numerical simulations is also given here. I have attempted to describe some of the puzzles that have so far prevailed concerning the formation of W 50 and concerning microquasars in general.
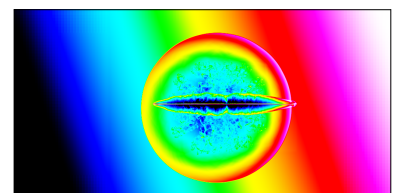
Chapter 3

Radio Interferometry with the Very Large Array

Astrophysical systems that exhibit relativistic jets from compact objects present astronomers with a rare opportunity to probe interesting physics across scales that differ by many orders of magnitude. This can include regions as small as a neutron star radius or $3R_S$ for a black hole, to enormous astrophysical length scales produced by their associated relativistic jets upon the interstellar medium (ISM) or intergalactic medium (IGM). In order to achieve what is arguably the *"holy grail"* of astronomy, and observe the inner regions of an accretion disc close to a compact object, then very powerful telescopes are needed. For the example of SS 433, whose jet interactions with the ISM have produced the lobes of W 50 spanning of order 10^2 pc, the black hole of $\sim 16\,M_\odot$ that is responsible for causing the surrounding mayhem has a Schwarzschild radius of just $\approx\ 50$ km. In other words, the inner regions where the activity occurs is an astonishing $\sim 10^{14}$ times smaller than the large scale effects we observe in W 50. The Schwarzschild radius (50 km) appropriate to SS 433 therefore subtends an angle on the sky of about ~ 10 nanoarcseconds based upon the distance of 5.5 kpc from us. Observationally we still have a long way before we have the ability to resolve such fine structure in astrophysical terms, but radio interferometers
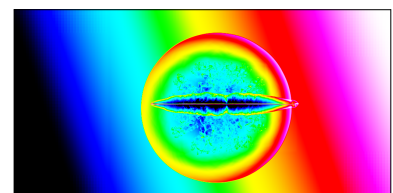
are leading the way in terms of resolving power, where the *Aperture Synthesis Technique* allows us to emulate the behaviour of a single telescope dish many kilometres in size (or as large as you care to extend the baseline between your antennae!), without actually having to build something so impractically large and expensive. Interferometers provide both high angular resolution (as determined by the longest baselines) across large fields of view (as determined by the smallest telescope dish size), and so radio interferometers are ideal instruments for probing the activity of compact systems on both the large and the small scales.

Very Long Baseline Interferometers (VLBI's) can achieve sub-milliarcsecond resolution. With the construction of a new generation of radio telescope, the Atacama Large Millimetre Array (ALMA), shorter wavelengths will be used to increase the resolution further, probing down to microarcsecond scales. This new technology will allow us to expand greatly upon our current understanding of the goings-on in the inner regions of black hole systems, near the point of jet-launch.

3.1   Merits of using interferometers

A super-sized single circular dish of radius R is sensitive to the continuum of spatial scales equal to and larger than its maximum resolution of $1.22\,\lambda/(2R)$. An interferometer of smaller dishes distributed across the same area covered by the super-size single dish, discretely samples the spatial scales that correspond to the discrete baselines of the interferometer, which vary in length in the range 0 to $2R$. Hence an interferometer with more baselines produces an image which more closely represents the true image of the sky. The advantage of the single dish in this case is that its larger collecting area of a completely filled dish, provides better sensitivity and collects all flux emitted from the spatial scales that it is sensitive to. The downside is that a single dish radio telescope only measures the flux from a single spot on the sky with each pointing. In other words, the field of view for a single radio dish is equal to its resolution, and even if practicality

did afford us the construction of an arbitrarily large single dish, the telescope would have to scan across the source of emission in order to produce a 2D image. The interferometer loses some flux from a given radio source on the scales to which it is not sensitive, due to not having a continuum of baseline coverage in the way that the single dish has. However, the power of the *Aperture Synthesis Technique* (Burns & Yao, 1970; Thompson et al., 1986) as described in §3.4 is such that an interferometer can (after some data reduction) produce a 2D image of the sky that is representative of all the spatial frequencies to which is sensitive, in a single pointing! However, by far the biggest selling point for an interferometer is that the resolution of the telescope at a given frequency can be improved simply by the inclusion of more telescope dishes at large distances from each other.

The increasing need for better spatial resolution in astrophysics is the primary motivation for building bigger and better interferometers, and the *Aperture Synthesis Technique* allows progress to continue on this front where a single dish telescope of the required size would be impossible to manufacture, and unfeasibly expensive.

3.2   Two dishes are better than one...

An interferometer measures the sky brightness distribution by correlating the signals (voltages) from pairs of antennae or "baselines" for the entire telescope array. Each telescope baseline (or pair of antennae) samples a point of the Fourier transform of the sky brightness distribution. A telescope array with N dishes has a total of $N_{BL} = N \times (N-1)/2$ independent baselines, and instantaneously has N_{BL} discrete samplings of the sky brightness distribution in the Fourier plane. This sampling of the sky brightness in the Fourier plane is referred to as the "uv-coverage" of a particular observation. For an interferometer, increasing the total time for which the telescope array is pointed at a particular source helps in two ways to improve the quality of the observation. Firstly, as is the case with single-dish telescopes commonly used in optical and X-ray astron-

omy, increasing the observation time improves the signal-to-noise of the image produced by the telescope. Images in radio astronomy that have a good signal-to-noise are said to have a *high dynamic range*. The second benefit in the case of ground-based interferometer observations, is that the total integration time on-target increases the uv-coverage of a dataset. This is because the projected baselines in the uv-plane change as the Earth rotates with respect to the source, during the observation. The total uv-coverage of an interferometer observation is then the combination of all the uv-plane snapshots for each integration time-step of the telescope. The "real" image produced (after a series of data reduction steps, described in §3.6) has resolution equivalent to a telescope of diameter equal to the largest baseline of the interferometer, across the field of view of the observation, as described in the next section.
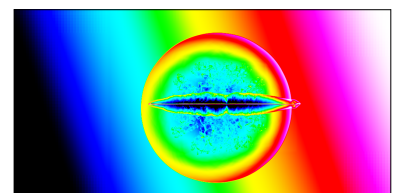
3.3 The Very Large Array

The Very Large Array (VLA) telescope began construction in the mid 1970's and has been continually improved and updated with the addition of new technology over the years. A comprehensive description of the original VLA is given by Thompson et al. (1980). The current VLA is sensitive to frequencies in the range 74MHz to 50GHz in designated observing bands, corresponding to radio waves of $\sim$4m to 6mm respectively. The array consists of 27 antennae in a Y-shape configuration, giving a total of $N_{BL} = 351$ baselines. The shortest baselines provide information about the large-scale emission from an extended source, and the longer baselines present the finer details of the small structures in the target source.

The maximum useful field-of-view (FOV) or "largest believable image set" for an interferometer is determined by the smallest dish in the array. This FOV is known as the *primary beam*, and is calculated in degrees as:

$$\theta_{\mathrm{PB}} = \frac{1.22\,\lambda}{D} \times \left(\frac{180}{\pi}\right) \qquad (3.1)$$

where D is the diameter of the smallest dish and λ is the wavelength of the observation. In reality, the usable field of view is affected by other things such as *bandwidth smearing*, *time smearing*, and *non-coplanar baselines*, but for simplicity we will assume that this is not the case here. For the data reduced in this chapter (details in §3.6) the VLA was used in D-configuration (explained below) in *L-band* $\approx 1.4\text{GHz} \approx 21\,\text{cm}$ radiation, and all of the VLA dishes have the same diameter of 25 metres, giving a primary beam of $\theta_{\text{PB21}} \approx 0.6°$ per telescope pointing. As mentioned in previous chapters, the W 50 nebula spans $\approx 2° \times 1°$ on the sky, so several telescope pointings are necessary to map the region completely.

The VLA dishes are mounted on plynths attached to railway tracks such that the dishes can be routinely moved, once at the beginning of each observing semester, to one of the four con-figurations named **A**, **B**, **C**, or **D**, where the maximum extent decreases by a factor of $\sim \pi$ with each configuration, as follows:

Configuration	Min. baseline	Max. baseline
A	25m	36km
B	25m	10km
C	25m	3.6km
D	25m	1km

Table 3.1: The baseline ranges for each VLA configuration.

A-config (being the most extended state) provides the highest resolution, whereas **D**-config has a lower resolution, but has other benefits. Although both configurations have the same small-est baseline equal to the telescope dish size (and hence the same primary beam) the structures within the primary beam are smeared to the size of the resolution element, as determined by the longest baseline. **A**-config has relatively more "resolution elements" across the field of view, and as a result the required exposure time to gain a good signal-to-noise per beam is relatively high compared to that of **D**-config. An appropriate analogy to this is the technique of binning data, where increasing the bin-size (i.e. **D**-config) improves the signal in a given bin, at the cost of
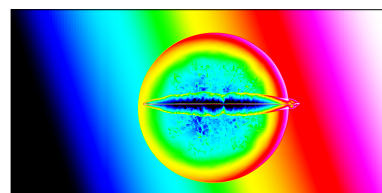
losing information on scales smaller than the bin-size. The use of **D**-config for the observations in this chapter is useful in showing any dim extended structures in the W 50 nebula, and with a longest baseline of 1km gives a resolution element of $\theta_{\mathrm{res}} = 53''$.

In the following section I will briefly introduce the *Aperture Synthesis Technique* in more detail.

3.4   Aperture Synthesis Technique: a whirlwind tour

An interferometer can be considered as an ensemble of baselines formed by the correlation of two antennae, and so the function of an interferometer can be understood by considering just one of the building blocks that constitute it. In this section I consider only one baseline formed by two dishes as in Figure 3.1, but the principle is the same when extended to N dishes of $N(N-1)/2$ baselines. The material from this section follows the approach given in "Synthesis Imaging in Radio Astronomy II" by Taylor et al. (1999), which is a useful reference text and gives a much more detailed account than that featured here.

3.4.1   The simplest case: A Single baseline interferometer

Consider for a moment, the special (and quite fictitious) monochromatic radio point source "*Astronomous-A*", which is located at an astronomical distance from Earth, such that its wave-front vectors arrive in parallel at the single-baseline interferometer shown in Figure 3.1. The vector **b** represents the baseline between the two antennae, and the projected baseline is thus $b\cos\theta$. The yellow lines indicate the parallel wavefronts, and the purple arrows are in-phase. The geometric time delay between the in-phase signals arriving at each antenna is given by $\tau_g = (b/c)\sin\theta$, where c is the speed of light. The electric field of the radio wave cause the free electrons of the metallic receiver to oscillate with an amplitude proportional to the field strength, and since this particular source is monochromatic, emitting only at the frequency ν the induced

A single-baseline interferometer
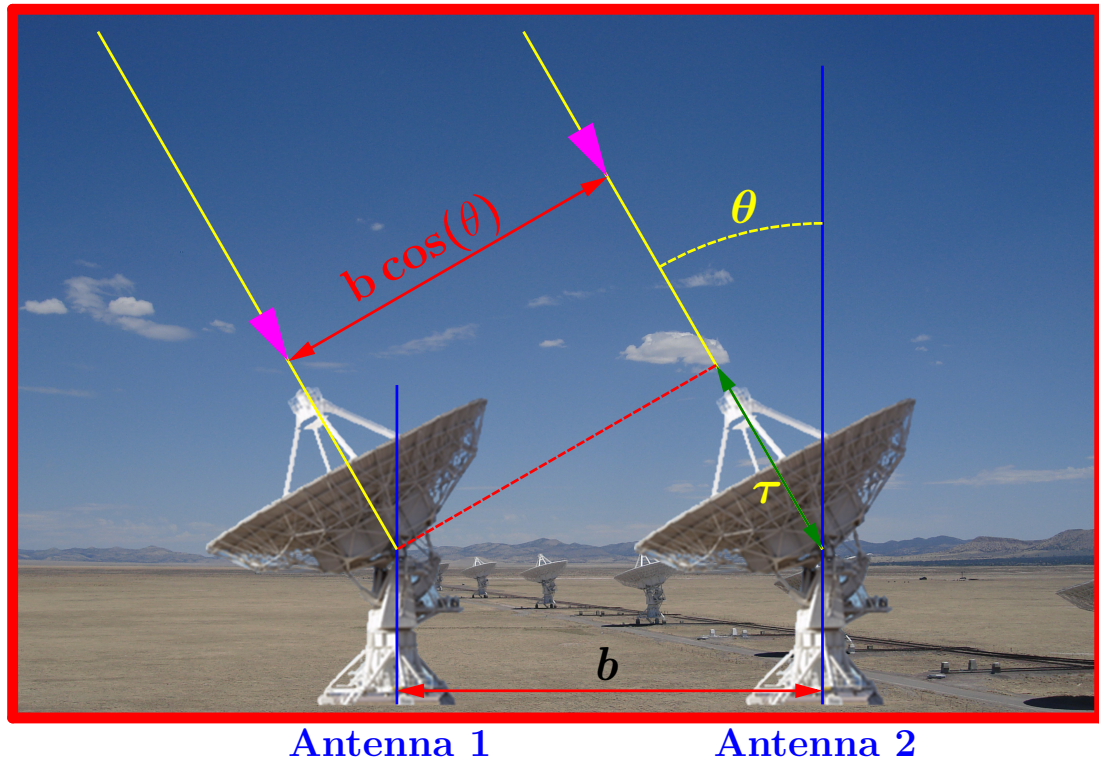
Figure 3.1: Illustration of an interferometer composed of two identical antennae from the VLA, connected to form a single-baseline interferometer of baseline length b pointed towards a target source at zenith angle θ, resulting in a delay of τ between antennae 1 and 2. (Image credit: ptg.)

voltages at antennae 1 and 2 can be written:

$$V_1(t) = v_1 \cos(2\pi\nu t) \tag{3.2}$$

$$V_2(t) = v_2 \cos(2\pi\nu(t - \tau_g)) \tag{3.3}$$

where v_1 and v_2 are the amplitudes of the induced voltages. These voltages are processed by the interferometer's *correlator*, which integrates the time-averaged product $\langle V_1(t)V_2(t) \rangle$. Since we only have monochromatic radiation in this case, output r from the correlator is:

$$r(\tau_g) = \langle V_1(t) \times V_2(t) \rangle = v_1 v_2 \cos\left(2\pi\nu\tau_g\right) \tag{3.4}$$
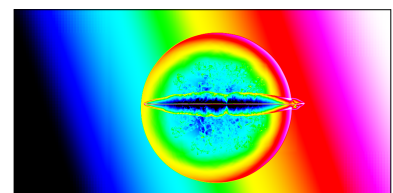
because the delay τ_g is a function of the zenith angle (θ in Figure 3.1) and thus varies relatively slowly as the Earth rotates, such that the averaging done by the correlator does not sufficiently change the result. On the other hand, the higher frequency component 2ν which occurs as a consequence of the multiplication, is effectively filtered out.

3.4.2 Extended radio sources

The fictional source "Astronomous-A" isn't very interesting as a perfect point source (although it would probably make a very good calibrator source!). In reality, we often wish to observe the structure of the radio emission in an astrophysical object of more interest, like W 50.

Consider a more realistic source with extended radio emission that is not monochromatic, but emitted within a small frequency interval $\Delta\nu$. The brightness[1] (at central frequency ν) of the source as a function of position is denoted by $I(\mathbf{s})$, where $\mathbf{s}$ is the unit vector pointing from Earth to a point on the surface of the emission region. Note that the source is still far enough away that the wavefronts come in parallel, and the source is a 2-D region with no depth perception. For simplicity, we assume that the antenna responses to a source of given brightness are identical, which is a fair assumption if the antennas are made in the same way such as the VLA antennas (and especially true for the antennas of Figure 3.1). Mathematically this means that the antenna response can be written as $A(\mathbf{s})$ which depends only on the vector $\mathbf{s}$ towards the source, rather than the more general case of $A_i(\mathbf{s})$, in which case the responses vary slightly from antenna to antenna as the subscript indicates. The signal from a small solid angle element $d\Omega$ of the sky, across the small bandwidth $\Delta\nu$ is then

$$dr = A(\mathbf{s})\, I(\mathbf{s}) \cos\left(2\pi\nu\tau_g\right) \Delta\nu\, d\Omega. \tag{3.5}$$

---

[1]"Brightness" and "Intensity" are used synonymously here, and have units of $\mathrm{W\,m^{-2}\,Hz^{-1}\,sr^{-1}}$, or more appropriately for radio sources, in Janskys per steradian ($\mathrm{Jy\ sr^{-1}}$), where $1\,\mathrm{Jy} = 10^{-26}\,\mathrm{W\,m^{-2}\,Hz^{-1}}$.

Integrating the above equation over the entire celestial sphere of 4π radians:

$$r = \Delta\nu \int_S A(\mathbf{s}) \, I(\mathbf{s}) \cos\left(\frac{2\pi\nu \, \mathbf{b} \cdot \mathbf{s}}{c}\right) d\Omega \tag{3.6}$$

where the substitution $\tau_g = \mathbf{b} \cdot \mathbf{s}/c$ has been made. Note however that the antenna response function $A(\mathbf{s})$ tails off to zero at distances greater than the primary beam from the pointing direction. This raises an important point about the distribution of the source about the pointing centre, which is technically referred to as the *phase tracking centre* or *phase reference position*. If we represent this central reference point by the position vector $\mathbf{s_0}$ then all positions within the extended source can be described in the plane of the sky in terms of the displacement vector $\boldsymbol{\sigma}$ from the reference position as $\mathbf{s} = \mathbf{s_0} + \boldsymbol{\sigma}$. Using this new definition with (3.6) we then obtain

$$\begin{aligned} r = \Delta\nu \, \cos\left(\frac{2\pi\nu \, \mathbf{b} \cdot \mathbf{s_0}}{c}\right) \int_S A(\boldsymbol{\sigma}) \, I(\boldsymbol{\sigma}) \, \cos\left(\frac{2\pi\nu \, \mathbf{b} \cdot \boldsymbol{\sigma}}{c}\right) d\Omega \\ -\Delta\nu \, \sin\left(\frac{2\pi\nu \, \mathbf{b} \cdot \mathbf{s_0}}{c}\right) \int_S A(\boldsymbol{\sigma}) \, I(\boldsymbol{\sigma}) \, \sin\left(\frac{2\pi\nu \, \mathbf{b} \cdot \boldsymbol{\sigma}}{c}\right) d\Omega \end{aligned} \tag{3.7}$$

It is useful to now define the *visibility*, which is a complex quantity and is a measure of the coherence of the electric field as seen by the interferometer:

$$V \equiv |V| e^{i\phi_V} = \int_S \mathbb{A}(\boldsymbol{\sigma}) \, I(\boldsymbol{\sigma}) \, e^{-2\pi i\nu \, \mathbf{b} \cdot \sigma/c} \, d\Omega \tag{3.8}$$

where the antenna response pattern has been normalised to the value at the beam centre: $\mathbb{A}(\sigma) = A(\sigma)/A_0$. As the telescope tracks the source across the sky, the brightness distribution is modified as $\mathbb{A}(\sigma)I(\sigma)$. The real and imaginary parts of the visibility will allow us to write (3.7) more concisely, where

$$A_0 |V| \cos\phi_V = \int_S \mathbb{A}(\boldsymbol{\sigma}) \, I(\boldsymbol{\sigma}) \cos\left(\frac{2\pi\nu \, \mathbf{b} \cdot \boldsymbol{\sigma}}{c}\right) d\Omega \tag{3.9}$$
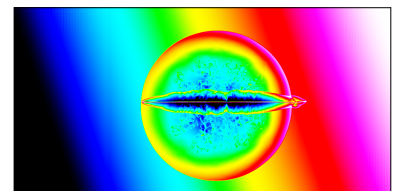
$$A_0|V|\sin\phi_V = \int_S \mathbb{A}(\boldsymbol{\sigma})\, I(\boldsymbol{\sigma}) \sin\left(\frac{2\pi\nu\, \mathbf{b}\cdot\boldsymbol{\sigma}}{c}\right) d\Omega \tag{3.10}$$

are the real and imaginary parts respectively, and the correlator output is then

$$r = A_0\Delta\nu|V|\cos\left(\frac{2\pi\nu\, \mathbf{b}\cdot\mathbf{s_0}}{c} - \phi_V\right) \tag{3.11}$$
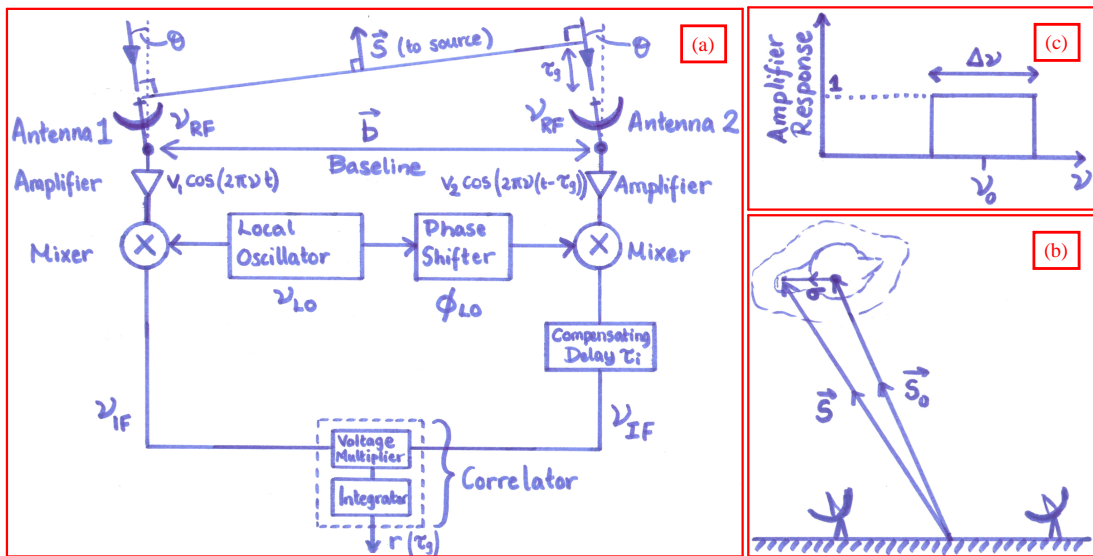
Figure 3.2: (a) A simplified schematic showing the principal components of an interferometer. (b) Representation of the position vector $\mathbf{s} = \mathbf{s_0} + \boldsymbol{\sigma}$ to an element of the extended source on the sky. (c) The (normalised) ideal rectangular response of the amplifier.

3.4.3 The effect of bandwidth

In the ideal case, the bandwidth is truncated to $\pm\Delta\nu/2$ about the central frequency ν_0 by the rectangular response of the amplifier as shown in Figure 3.2c. The correlator output for an infinitesimal bandwidth $d\nu$ (3.11) can then be expressed as

$$dr(\tau_g) = A_0|V|\cos\left(2\pi\nu\,\tau_g - \phi_V\right) d\nu \tag{3.12}$$

which can then be integrated in the range $\pm\Delta\nu/2$ about the central frequency:

$$r(\tau_g) = A_0|V| \int_{\nu_0-\Delta\nu/2}^{\nu_0+\Delta\nu/2} \cos\left(2\pi\nu\,\tau_g - \phi_V\right)d\nu \qquad (3.13)$$

$$r(\tau_g) = A_0|V|\Delta\nu \frac{\sin\left(\pi\Delta\nu\,\tau_g\right)}{\left(\pi\Delta\nu\,\tau_g\right)} \cos\left(2\pi\nu\,\tau_g - \phi_V\right)$$

$$r(\tau_g) = A_0|V|\Delta\nu\, sinc(\pi\Delta\nu\,\tau_g) \cos\left(2\pi\nu\,\tau_g - \phi_V\right) \qquad (3.14)$$

The interferometric procedure is to measure the fringe pattern of the cosine term in (3.14), and then (after some appropriate calibration) to determine the amplitude and phase of the *visibility*. As (3.8) provides a relationship between the measured *visibility* data and the actual sky brightness, and since $A(\mathbf{s})$ is known from the calibration process, the visibility equation can be inverted to produce the actual brightness distribution of the source $I(\mathbf{s})$. In order for this to work well, the visibility V must be measured over a sufficiently wide range of $\nu\mathbf{b} \cdot \boldsymbol{\sigma}/c$ (i.e. good uv-coverage), which are the distribution of baselines as viewed from the direction $\mathbf{s}$ of the source.

3.4.4   Technical Challenges of Interferometry

As mentioned previously, the primary beam, or field-of-view that an interferometer sees at a given frequency, depends primarily upon the smallest dish size, however there are a few extra effects that can limit the *useful* size of the field as seen by an interferometer. These effects for a particular interferometer are all well-studied such that problems with imaging can be minimised, but briefly these consist of:

- *Bandwidth smearing* - The principles of synthesis imaging discussed so far are really only intended for monochromatic radiation, since the fringe pattern produced by the interferometer is frequency dependant. This never happens in practice, since receivers are usually
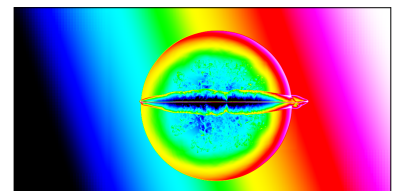
effective in a given frequency range, and furthermore, as the width of the frequency interval tends to zero, so too does the flux received. It is often desirable to observe an object using as wide a bandwidth as possible to maximise the integrated flux received during an observing run. This is particularly important for faint objects. However, if the frequency interval is sufficiently large that $\nu_0 - \Delta\nu/2$ and $\nu_0 + \Delta\nu/2$ are quite different, then chromatic aberration causes the resulting image to be increasingly "out-of-focus" with radial distance from the phase tracking (or pointing) centre. Modern instruments (for example, the GMRT and E-VLA antennas) are responsive across a wide bandwidth, and as such the data must be split into (often hundreds!) of individual frequency channels, which must be calibrated individually during the data reduction to prevent this "bandwidth smearing" effect.

- *Integration time losses* - the techniques described in §3.4.1 and thereafter are dependant upon the integration time over which the correlator multiplies the antenna voltages being small such that changes in the array shape (i.e. the projected baselines as seen by the source) due to the rotation of the Earth, does not change significantly during the integration period. If this condition is not met, the signal is attenuated, or suffers a loss of amplitude due to time-averaging of quantities that are varying in a non-random way. For the VLA, integration times of order a few seconds are often used to minimised in this attenuation.

3.5   Motivation for use of VLA archival data

The accurate measurement of the proper motions of the bright structures within the W 50 nebula (described in chapter 4), requires data (images) of W 50 spread as far apart in time as possible from each other. Observations separated in time by some period Δt then provide a velocity resolution of $\Delta x/\Delta t$ where Δx is the resolution of the images, provided the images have similar resolution.

The detailed image of W 50 shown in previous chapters (for example, Figure 2.3b) as created by Dubner et al. (1998), is the result of 57 individual pointings of the VLA in D-configuration, in $L - band$ (1.4GHz), and this provides an excellent description of the positions of the bright filaments in W 50 in 1996.

The fully reduced data from these 57 pointings, were (thankfully!) provided by Gloria Dubner[2] for the purposes if this investigation. The National Radio Astronomy Observatory (NRAO) provide an online database of the observational data covering several decades, and observation data are freely available to be downloaded (via http://archive.cv.nrao.edu/) after the proprietary period has expired. After some digging through the VLA archives database, I discovered a suitable observation of W 50 from 1984 as detailed by Elston & Baum (1987), which was ideal for the kinematics study because the observation was performed using the same VLA configuration and frequency band as Dubner's observation. These two observations provide a time-baseline of ~12 years, over which to examine the W 50 nebula for movement.

Elston's data consisted of 9 VLA pointings, which I downloaded from the VLA archive and reduced using the well-tested Astronomical Image Processing System ($\mathcal{AIPS}$). $\mathcal{AIPS}$ has improved a lot since 1984, so too have our computing capabilities. The combined effect of new tasks such as $\mathbb{IMAGR}$ within $\mathcal{AIPS}$ that have been designed to give superior signal-to-noise, and enough computer memory that very large images can be processed simultaneously and then "mosaiced" together, means that the final image produced here is of better quality than the data originally published in (Elston & Baum, 1987). The data reduction steps I used are briefly outlined in the remainder of this chapter, along with the final image produced.

3.6 Data reduction techniques

This section is intended as a brief summary of the data reduction steps I performed, however it is possible to include many more careful steps (and spend a proportionally longer amount

---

[2]To whom I am very grateful.
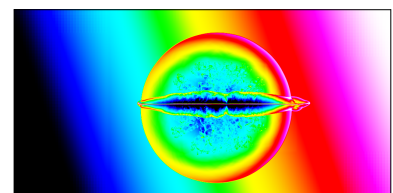
of time) in "massaging" of radio data. However, the filaments in W 50 are quite bright, and so producing a reasonably well-calibrated image was not too difficult in this case. The data reduction steps roughly consist of: *Editing, Calibration, Imaging, Self-calibration*, where the last stage is optional but was performed here because it can considerably improve the dynamic range of the resulting image. Throughout this section, a $\mathbb{THIS\ FONT}$ is used in reference to $\mathcal{AIPS}$ tasks and `parameter=value` denotes a value being assigned to an $\mathcal{AIPS}$ adverb. The data reduction was performed using an 8-core (2.2GHz,4Gb RAM) Mac Pro with $\mathcal{AIPS}$ version 2008 installed.

3.6.1   Preliminaries

The data as downloaded from the VLA archives were loaded into $\mathcal{AIPS}$ using the $\mathbb{FITLD}$ task, without data compression (`douvcomp=-1`) and without digital correction (`digicor=-1`), into catalogue slot 1. Before proceeding with the data reduction, I first ran the task $\mathbb{INDXR}$, which ensure that the index ("NX") table is accurate for the uv data of input file. This step is sometimes redundant (but is harmless) and can provide faster access to the uv data. Modern $\mathcal{AIPS}$ also prefers that the data entries are sorted chronologically, which sometimes isn't the case for older VLA data. Information about the observation was then obtained by inspecting the header, and using the tasks $\mathbb{LISTR}$ with `optype='scan'`, and the output from each is summarised in Figure 3.3.

The 9 pointings across the W 50 source are labelled *F1C, F2, F3, F4A, F4B, F5, F6, F7, F8*, where *3C286* is the amplitude calibrator and *1905+190* is the phase calibrator. The bandwidth here is $\Delta\nu = 50$MHz centred upon $\nu_0 = 1.4649$GHz, and over 300,000 visibility datapoints are stored in this dataset.

```
Image=MULTI     (UV)        Filename=19840812   .L BAND.  1
Telescope=VLA               Receiver=VLA
Observer=AB274              User #=  480
Observ. date=12-AUG-1984    Map date=13-APR-2010
# visibilities   303344     Sort order  TB
Rand axes: UU-L-SIN  VV-L-SIN  WW-L-SIN  BASELINE  TIME1
          SOURCE  FREQSEL
-------------------------------------------------------
Type   Pixels   Coord value    at Pixel    Coord incr  Rotat
COMPLEX    3   1.0000000E+00     1.00  1.0000000E+00   0.00
STOKES     4  -1.0000000E+00     1.00 -1.0000000E+00   0.00
FREQ       1   1.4649000E+09     1.00  5.0000000E+07   0.00
IF         2   1.0000000E+00     1.00  1.0000000E+00   0.00
RA         1    00 00 00.000     1.00      3600.000    0.00
DEC        1    00 00 00.000     1.00      3600.000    0.00
-------------------------------------------------------
Coordinate equinox 1950.00
```

```
ID Source         Qual  Calcode RA(1950.0)     Dec(1950.0)  No. vis
 1 3C286        : 0000    B    13:28:49.6570  30:45:58.640    6476
 2 1905+190     : 0000    T    19:05:11.1600  19:51:36.400   22107
 3 F1C          : 0000         19:06:18.0000  05:00:20.000   35646
 4 F2           : 0000         19:09:19.0000  05:22:20.600   33083
 5 F3           : 0000         19:08:27.0000  04:39:13.000   33750
 6 F4A          : 0000         19:11:46.0000  04:56:47.000   32815
 7 F4B          : 0000         19:10:58.0000  04:36:47.000   30369
 8 F5           : 0000         19:13:30.0000  04:45:46.000   33911
 9 F6           : 0000         19:08:15.0000  04:59:60.000   32337
10 F7           : 0000         19:10:20.0000  04:59:60.000   34424
11 F8           : 0000         19:14:60.0000  04:36:60.000    6805
12 1803+784     : 0000    C    18:03:39.1790  78:27:54.300    1621

ID Source         Freq(GHz) Velocity(Km/s) Rest freq (GHz)
 1 All Sources     1.4649       0.0000         0.0000
   IF(  2)         1.5149       0.0000         0.0000
```

Figure 3.3: The specifics of Elston's 1984 VLA observation. The left panel shows the header information produced by the task $\mathbb{IMHE}$, including useful at-a-glance information such as the observation date, frequency, and observer name. The right panel shows the output produced by the task $\mathbb{LISTR}$, including useful information about the names of the calibration and target sources observed, the *phase reference position* for each target, and the integration time for each source.

3.6.2 Editing

Editing, or flagging of bad data, is done throughout according to the mantra "Bad data is worse than no data", which refers to adverse affects that a malfunctioning antenna, bad weather conditions, or Radio Frequency Interference (RFI) can have. This process is usually the most time-consuming aspect of radio data reduction, but the aforementioned effects must be identified and flagged (wighted as "zero") or they could hinder the calibration process that follows.

The first task is to apply $\mathbb{QUACK}$ to flag the first 5 or 10 seconds of each observing scan, when the antenna amplitudes can be inaccurate due to remnant vibrations in the antennae which occurs due to slewing.

The flagging steps that follow after $\mathbb{QUACK}$ depend in the data and indeed the preferences of the astronomer. Usually I use a combination of $\mathbb{UVPLT}$, $\mathbb{UVFND}$ and $\mathbb{UVFLG}$ to plot, track down, and eliminate spurious blips in the antennae amplitudes versus baseline-length and time, for each of the sources listed above. Sometimes however, a more brutal approach is required, and $\mathbb{TVFLG}$ provides a clickable user-interface to select and flag bad data. I will proceed through the remainder of this section using the example of field *F4A* (source='F4A'') as the information in Figure 3.3 indicates that this is part of the eastern lobe of W 50. The use of $\mathbb{UVPLT}$ for
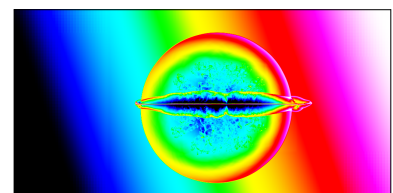
displaying bad data is demonstrated in Figure 3.4. The first panel (a) shows the uv-coverage for the *F4A* source, while (b) and (c) show the un-flagged amplitude and phase distributions respectively, as a function of baseline length. After some inspection of the data, I determined that antenna 21 was bad, and the effects of flagging antenna 21 is evident by comparing the amplitude versus baseline distrubution before (Figure 3.4(b)) and after (Figure 3.4(d)) flagging the antenna. The remaining panels (e)-(j) in Figure 3.4 are described further in sections §3.6.3 and §3.6.4.

3.6.3 Calibration

The calibration procedure begins with $\mathbb{SETJY}$ which calculates the flux appropriate for the flux calibrator *3C286* using `optype='calc'`, and finds a flux of 14.5 Jy which is in agreement with the VLA calibrator manual for *3C286* at 1.4GHz. Next, $\mathbb{CALIB}$ is used on this source and the phase calibrator *1905+190* to determine the gain solutions for this source, and in this case the task ends with 200/200 and 1284/1284 good solutions respectively. The flux of the phase calibrator is then set using $\mathbb{GETJY}$ with `source='1905+190''` and `calsource='3C286''`, and in doing so *1905+190* inherits $\sim$0.9 Jy. Antenna 8 has been used throughout as the reference antenna, because it is at the centre of the array (according to $\mathbb{PRTAN}$) and showed no signs of misbehaviour in $\mathbb{UVPLT}$s. At this stage the amplitude and phase solutions are stored separately in $\mathcal{AIPS}$ "SN" (solution) tables, and must be combined together into a "CL" table, using the task $\mathbb{CLCAL}$. The appropriate calibration solution tables are then applied to the *F4A* field, and it is "split-off" from the rest of the data using $\mathbb{SPLIT}$, and I can now work on *F4A* independently because I know it contains several strong radio sources as seen by the VLA in this configuration (by consulting the NRAO VLA Sky Survey), and so these point sources can be used for *self-calibration*. Figure 3.4e shows a plot of amplitude .vs. baseline length now for the split *F4A* field, and the axes now display the appropriate flux.
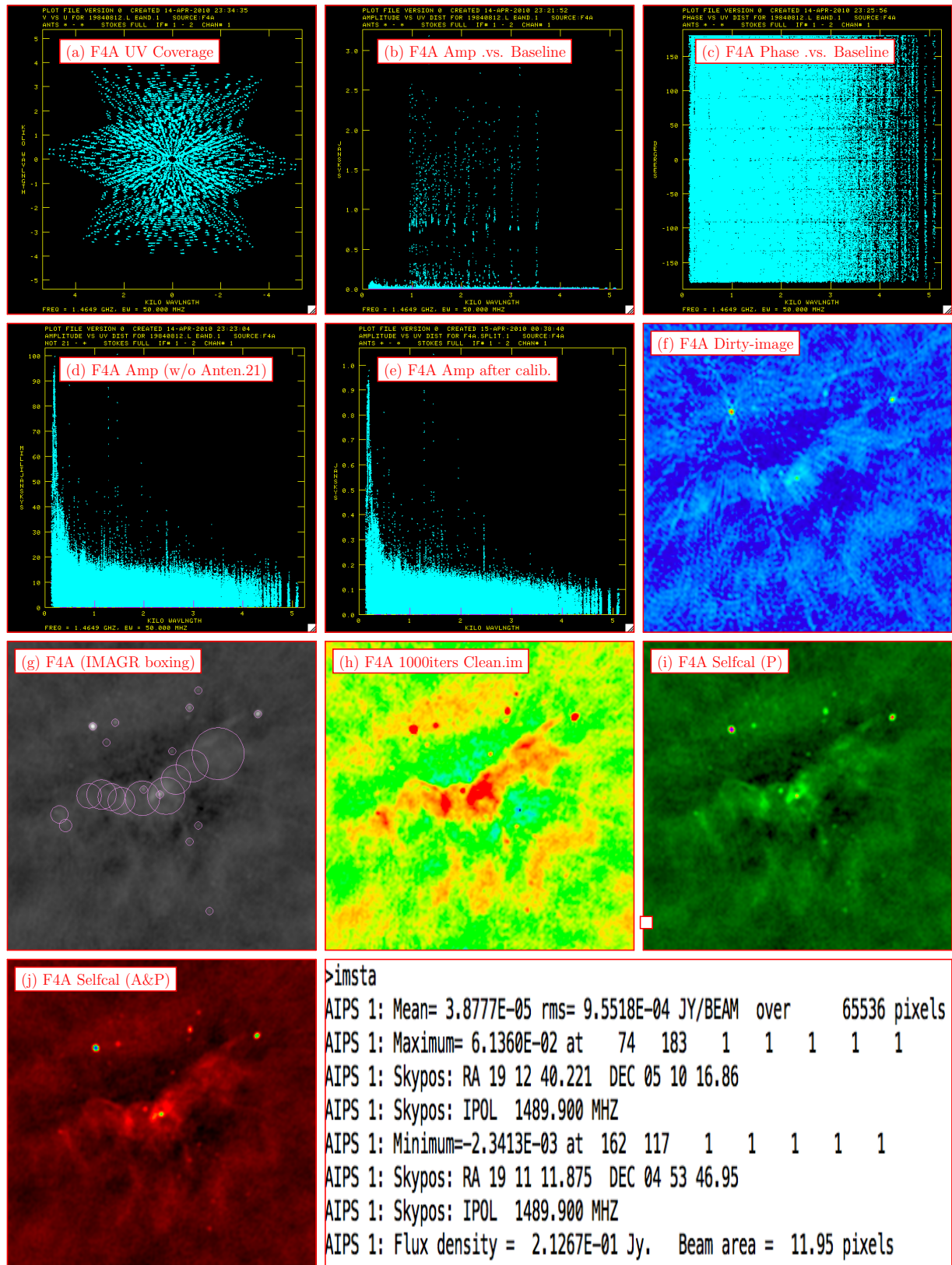
Figure 3.4: This section shows various snapshots of the data reduction steps performed using $\mathcal{AIPS}$. Refer to sections §3.6.2, §3.6.3, and §3.6.4 for a description of each panel.
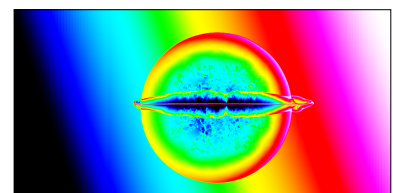
3.6.4 Imaging & Self Calibration

I now begin the process of *clean*-ing the data using the task $\mathbb{IMAGR}$. *Clean*-ing is a whole topic in itself, and I refer the reader to (Högbom, 1974; Clark, 1980) for further details on the subject. Briefly, the *clean* process uses the beam pattern of the telescope to subtract some gain factor (usually 10%) from the brightest pixel in the image, and this is an iterative process. According to the UVPLT's the maximum baseline range in units of the observing wavelength (21cm) is $\sim$5000, which implies an image resolution of $\sim 50''$. Setting the pixelsize to $15''$ in $\mathbb{IMAGR}$ then ensures full (i.e. better than *Nyquist*) sampling of the data, so `cellsize=15`.

Figure 3.4f shows the result of a non-interactive $\mathbb{IMAGR}$ run with no iterations of clean (`NITER=0`) and the result is known as the "Dirty Image", which means it shows the sky brightness distribution that is still convolved with the telescope beam pattern. To produce a *clean* image, I will run $\mathbb{IMAGR}$ with 1000 interations in the first instance, so `NITER=1000`. The process is made interactive by setting the parameter `DOTV=1` and this allows the user to *box* the image. The act of *boxing* with $\mathcal{AIPS}$ is more of an art than an exact science, but it allows the user to assist the cleaning process by selecting features which are believed to be real[3]. The boxes I applied to this cleaning run are shown in Figure 3.4g. It helps in this case, that I have an idea of what the region looks like, but regardless of this the "rule of thumb" is that symmetrical features about the centre (i.e cosine symmetry) is indicative of amplitude errors and antisymmetric features (sine) are indicative of phase errors. The real features are usually point sources, and extended emission that has no symmetry (unless the source is known to exhibit symmetry!). The clean map produced as a result of and $\mathbb{IMAGR}$ run with 1000 iterations is shown in Figure 3.4h, and this clean image can be used as a model for the self-calibration process.

Self-calibration is a kind of boot-strapping technique, whereby the clean image (as produced from the previous run of $\mathbb{IMAGR}$) is used as an input model for the calibration. The first few rounds of self-calibration is aimed at improving the phase solutions, by setting `solmode='p'`.

---

[3]As in a true representation of the sky, not the antonym of "complex".

The process is iterative, whereby a clean image (with conservative cleaning boxes applied) is produced from the latest round of $\mathbb{CALIB}$, and then the latest clean image is then used as an input model for the next round, and so on. After a few iterations of self-calibration in phase mode, one may decide to include amplitude self-calibration via `solmode='a&p'`, and it is a good idea to start with a relatively long solution interval of say `solint=400` and then decrease this by a factor of two or so with each iteration of $\mathbb{CALIB}$. Figure 3.4i is the image result after 3 iterations of phase self-calibration, and Figure 3.4j shows the final image created for the reduction example, after an additional 3 iterations of self-calibration in amplitude and phase mode. Further massaging of the data could continue beyond this point, but is unnecessary for the purposes of this observation, where 8 further fields of W 50 are in need of reduction. The image statistics for field *F4A* are appended to Figure 3.4.

3.7   Results of modern re-reduction of Elston's data

Upon repeating the basic data reduction steps described in §3.6 for all 9 fields of Elston's 1984 VLA observation of W 50, a mosaic image was created using code written in PDL. The code calculates the size of the template image (an array of zeroes) in pixels that will be required to contain all fields in the mosaic, using the positional information from headers of the respective FITS files. Each field is normalised to the same exposure time on target, such that variations in brightness across the fields are representative of the relative variations in the true sky brightness. The code then determines all cases where the fields will overlap with each other in the template image, and such pixels are then weighted with a contribution of $w = 1/N$, where N is the number of overlapping fields that will contribute to a given pixel (i.e. w=1 if there is no overlapping). Each of the 9 fields is then weighted according to w and "pasted" into the appropriate location in the template image, and this ensures that pixels in overlap regions assume the average value of the contributing fields. Figure 3.5 shows the mosaic image produced by this method.
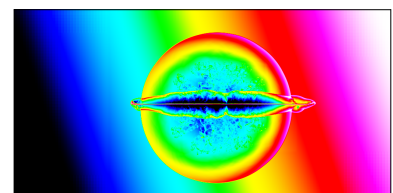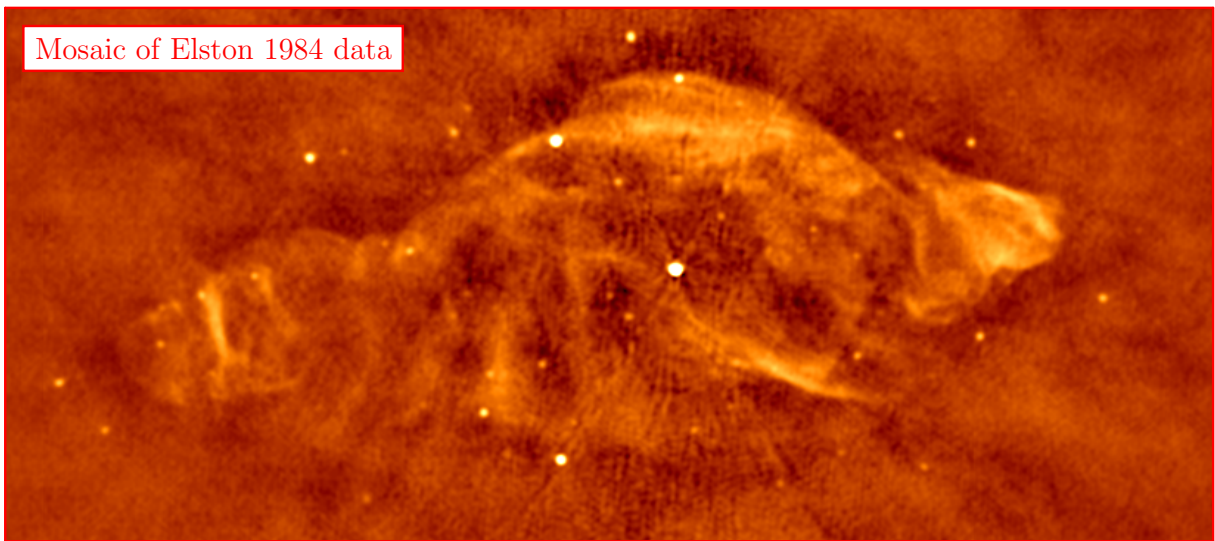
Figure 3.5: The final article.

Although this image is not as well sampled as the Dubner observation from 1996 that consisted of 57 pointings, it still contains all of the brightest filaments necessary to conduct the kinematics study of W 50 (see the next chapter), which was the goal of the project. It is left as an exercise for the reader to recognise the field *F4A* in the final mosaic[4], and it is noted that it is probably the dimmest part of the nebula (i.e. the overall dynamic range is better than the image statistics in Figure 3.4 indicate). The beam area is 11.9 pixels, where the pixel size was set to $15'$, hence the synthesised beam size is $\sim 58''$.

---

[4]Clue: it's in the north-east quadrant

Chapter 4

The kinematics of the W 50 nebula

4.1   Kinematics: Proper motions in the plane of the sky

The spectacular interaction between the relativistic jets of the microquasar SS433 and the supernova remnant (SNR) W 50, has been captured at several epochs by radio telescopes that are sensitive to both its angular extent (over two degrees across the sky) as well as to its fine structure on arcsecond scales. The distances to both objects in this structure are now very well known via two distinct methods, and as such the connection between microquasar and SNR has been confirmed. In the first instance, a distance to SS 433 of 5.5 ± 0.2 kpc was determined by examination of light-travel time induced aberrations of the arcsec-scale jets of SS 433 (Blundell & Bowler, 2004). The second method is based upon the detection of neutral hydrogen, in both absorption and in emission, at a high Galactic rotation speed corresponding to the same distance of 5.5 kpc to W 50 (Lockman et al., 2007). Accurate distances to objects within our Galaxy are still rare, but when such objects are identified their angular sizes translate directly into physical sizes, proper motions convert nicely to velocities, and this information enables a quantitative assessment of the system energetics.

The compact object in SS 433 is known to eject jet material with a mean speed of $\sim$0.26c as
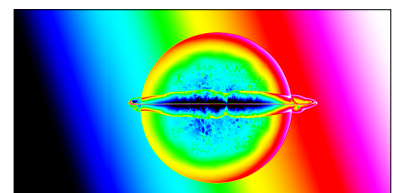
determined from optical spectroscopy (Eikenberry et al., 2001) and this is found to be consistent with proper motions of the central engine using long-baseline radio interferometry (Vermeulen et al., 1987; Paragi et al., 1999b) with a standard deviation in the jet speed of $0.01c$ (Blundell & Bowler, 2005). Although the kinematics of SS 433's jets have been generally well-studied in optical and radio regimes, the relativistic propagation of jet material at the outermost periphery has not yet been observed. Indeed, any deceleration of the jet material, or the point at which deceleration happens, has yet to be established. The SS 433-W 50 system is amenable to numerical simulations, and the results of comprehensive hydrodynamic models will be presented in a series of companion papers (Goodall et al. (2010)).

In this chapter, I present a detailed examination of the multi-epoch radio images of this nebula observed over a decade apart. I aim to ascertain whether meaningful constraints can be placed on the proper motion of the persistent radio features (the filamentary structure in W 50) where the jets have impinged and penetrated through the supernova remnant (SNR) shell. In particular, I aim to identify any evidence for the deceleration of the jets at the furthest point they are observed from the microquasar nucleus.

4.2 Data Analysis

4.2.1 VLA Data Reduction

The three datasets used in this analysis are each observations of W 50 performed using the VLA in its most compact configuration D-array. The image from the most recent observation (1996) was kindly made available to me by Gloria Dubner, consisting a mosaic of 57 telescope pointings at 1.4 GHz (Dubner et al., 1998). A further dataset was downloaded from the NVSS "postage stamp server", observed in 1993 at 1.4 GHz. The final dataset was observed in 1984 by Elston & Baum (1987) and these data were retrieved from the NRAO VLA data archive. These archival data comprised of nine pointings observed at 1.4 GHz, and were reduced individually using stan-

dard procedures in AIPS (as discussed in chapter 3). The individual pointings were sequenced together using bespoke code written in PerlDL. For clarity, these images will be referred to by source and observation year according to their respective FITS headers, as *Elston-84* (*date-obs*: 12/08/1984), *NVSS-93* (*date-obs*: 15/11/1993), and *Dubner-96* (*date-obs*: 19/08/1996) respectively.

4.2.2　Image Preparation

The three epochs of W 50 observations from VLA in L-band and D-array configuration, provide maps of very similar resolution (the VLA synthesised beamwidth[1] in this configuration is $44''$) and size, with differences being due to the restoring beam used for each observation and the fact that each image is comprised of a series of mosaicked pointings. An interactive kinematics pipeline was written using the Perl Data Language[2] (Glazebrook & Economou, 1997) to extract the accurate fitted coordinates of the SNR filaments from the radio observations. The pipeline performs a series of image preparation steps to ensure accurate image matching before kinematics can be measured, and the basic stages are outlined below.

The images were scaled-up from their original sizes (by a factor of at least 5) such that the image sizes and pixel scales approximately matched, using a Jacobian interpolation method to ensure accurate resampling. Each image was then normalised such that the brightest pixel (always centred upon the unresolved source SS 433) has a value of unity. An accurate astrometric correspondence between the three observations was created using a select group of 15 bright point sources common to all three images (see Figures 4.4, 4.5 and 4.6). This was done by fitting Gaussians to the point source centroids. Due to the inhomogeneity of the background emission across the region, both 1D and 2D Gaussian fits were performed, and the best-fit of these two methods determined by inspection as to ensure positional reliability. The inspection of each

---

[1] http://www.vla.nrao.edu/astro/guides/vlas/current/node10.html

[2] The Perl Data Language (PDL) has been developed by K. Glazebrook, J. Brinchmann, J. Cerney, C. DeForest, D. Hunt, T. Jenness, T. Luka, R. Schwebel, and C. Soeller and can be obtained from http://pdl.perl.org.
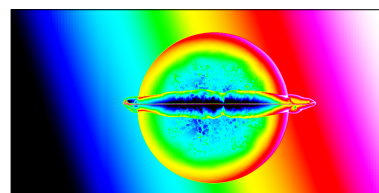
Gaussian fit to the centroid position is especially important for the *Elston-84* image, where (due to the small number of telescope pointings covering a large field of view) the sources near the edges of the primary beam for each telescope pointing, are less well-defined. In this case the 2D Gaussian routine fails to find a reasonable fit, and the 1D Gaussian fit is used as shown in the examples of Figures 4.1 and 4.2.

The averaged coordinates $C=(\bar{x}_c, \bar{y}_c)$ of all 15 point sources (the centre of mass if all point sources are assigned an equal mass) was chosen as the principal reference point for each image:

$$\text{CRPIX1} = \bar{x}_c = \frac{1}{n} \sum_{i=1}^{n} x_i \,, \tag{4.1}$$

and

$$\text{CRPIX2} = \bar{y}_c = \frac{1}{n} \sum_{i=1}^{n} y_i \,, \tag{4.2}$$

where n is the number of point sources used, and the error associated with any one measured centroid position is therefore minimised. We define the east centre $E=(\bar{x}_E, \bar{y}_E)$ as the average coordinates of all the point sources to the east of SS 433 (point sources 2-9), and west centre $W=(\bar{x}_W, \bar{y}_W)$ as the average coordinates of the remaining point sources including SS 433 (point sources 10-15 and 1) such that:

$$\bar{x}_e = \frac{1}{a} \sum_{i=2}^{9} x_i \,, \tag{4.3}$$

$$\bar{y}_e = \frac{1}{a} \sum_{i=2}^{9} y_i \,, \tag{4.4}$$

$$\bar{x}_w = \frac{x_1}{b} + \frac{1}{b} \sum_{i=10}^{15} x_i \,, \tag{4.5}$$

$$\bar{y}_w = \frac{y_1}{b} + \frac{1}{b} \sum_{i=10}^{15} y_i \,, \tag{4.6}$$

Round 3 : 1D Gaussian fitting to Elston Star centroids.
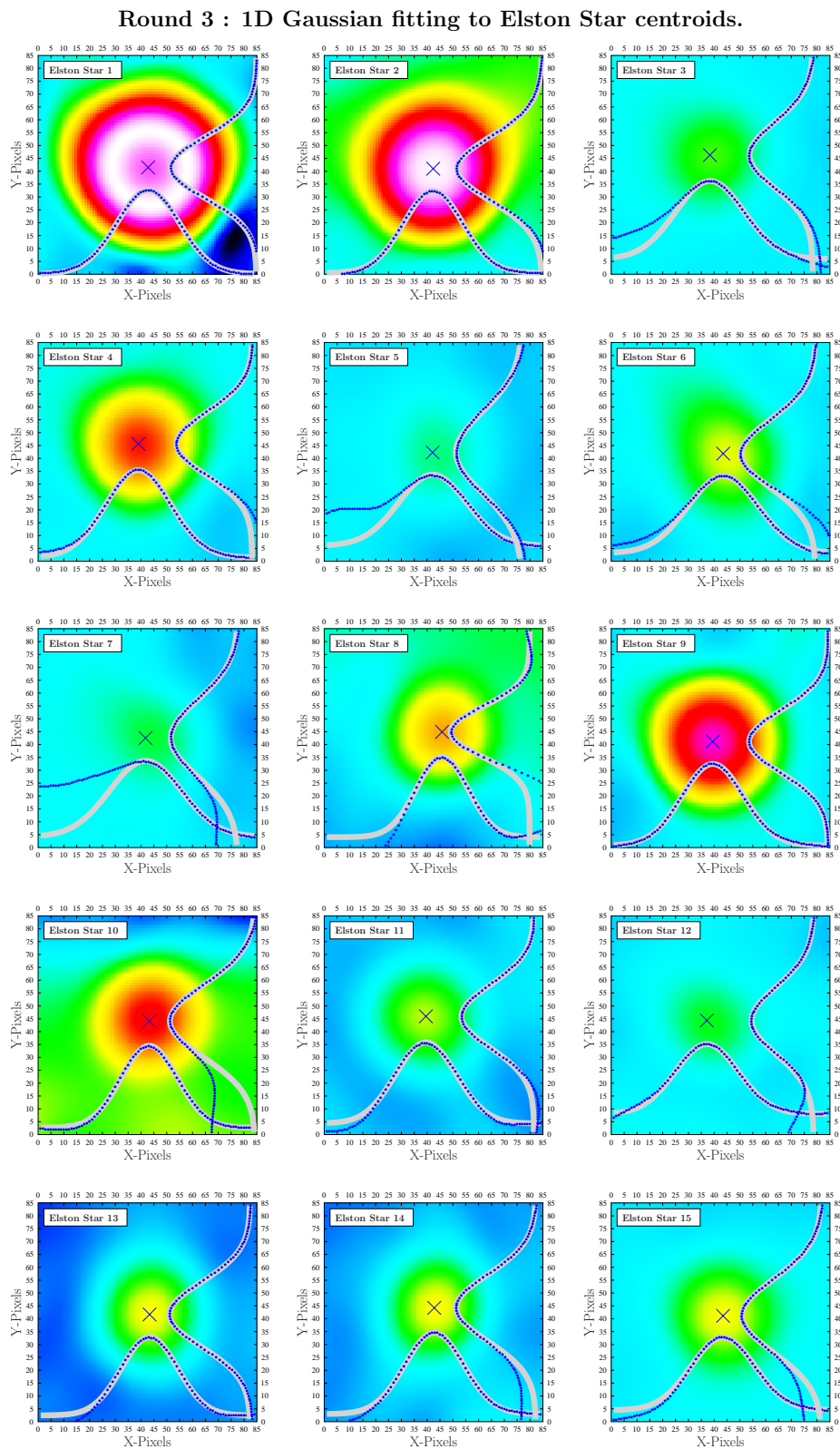
Figure 4.1: Fitting 1D Gaussians to the *Elston-84* point source positions. Each colourmap is a zoomed-in section of a point source from Figure 4.4. The blue dots indicate the summed intensity profiles along the x and y axes for each point source, and the purple lines indicate the 1D Gaussian fits to the points.
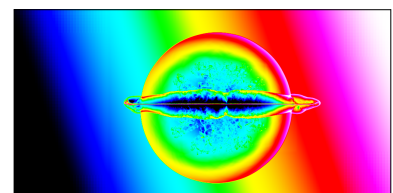
Round 3 : 2D Gaussian fitting to Elston Star centroids.
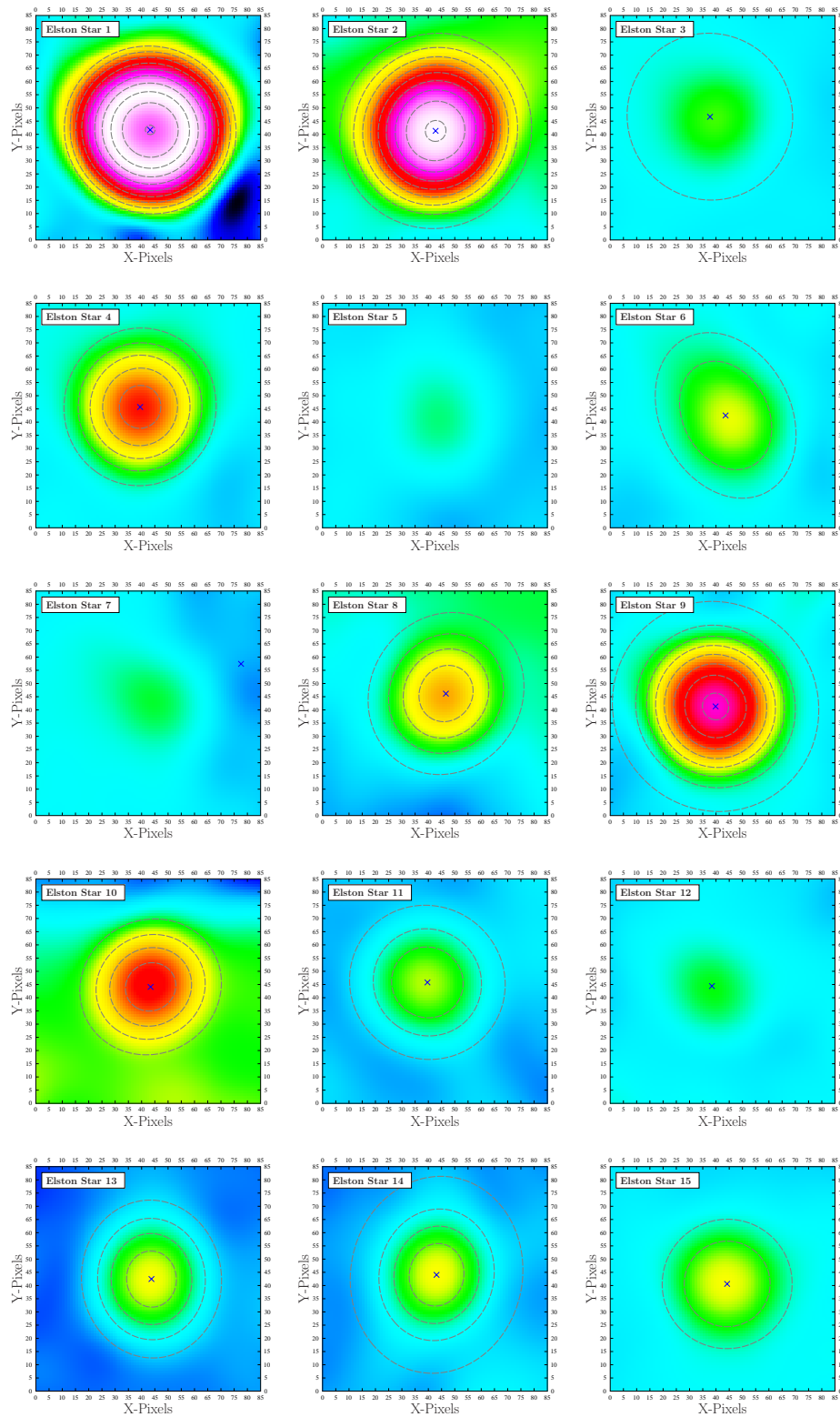
Figure 4.2: Fitting 2D Gaussians to the *Elston-84* point source positions. Each colourmap is a zoomed-in section of a point source from Figure 4.4. The grey dashed ellipses indicate the contours of the 2D Gaussian fits to the intensity maps for each point source. The crosses indicate the centroid for each 2D fit.

where $a = 8$ and $b = 7$ are the number of sources used for the east and west sides respectively. The separation between the east centre (E) and west centre (W) then defines an accurate image pixel scale for each image:

$$\delta x = \bar{x}_{\rm w} - \bar{x}_{\rm e} \, , \tag{4.7}$$

$$\delta y = \bar{y}_{\rm w} - \bar{y}_{\rm e} \, , \tag{4.8}$$

$$CDELT1 = CDELT2 = \frac{1}{\sqrt{\delta x^2 + \delta y^2}}. \tag{4.9}$$

The angle θ made by the vector $\overrightarrow{EW}$ (joining the east and west centres) with the horizontal axis is indicative of any residual rotation that must be performed to match the images:

$$\theta = \arctan \frac{\delta y}{\delta x}. \tag{4.10}$$

The *Elston-84* and *NVSS-93* images were scaled and rotated to match the new header values of the *Dubner-96* image, and the Gaussian fitting to the 15 point source centroids was repeated to establish the correct header information for the newly transformed images, followed by a convolution to match both of *Elston-84* and *NVSS-93* to the slightly coarser resolution of $\theta_{\rm res} = 56''$ of the *Dubner-96* image. Finally, the images were matched to within 0.01 pixels by performing an image covariance maximisation based upon the 15 point sources. A final transformation was applied using a Jacobian interpolation, and the image FITS headers were updated one last time by fitting Gaussian centroids to the point sources in the matched images[3].

Throughout the analysis, non-linear corrections in astrometry were not accounted for, because the linear approximation is satisfactory over the scales (approximately 1°) involved.

---

[3]An animation sequencing the final images is available here:
$http://www\text{-}astro.physics.ox.ac.uk/{\sim}ptg/RESEARCH/research.html$
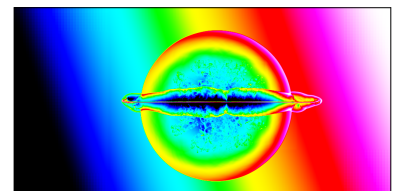
4.2.3   Velocity resolution

The bright filaments in the images generally have a relatively high signal-to-noise and the Gaussian curves we fit to the cross sections of the filaments are well sampled across a given reliable range (determined by inspection, detailed in §4.2.4). Under these conditions, the accuracy with which one can determine the centroid position from a Gaussian fit is typically much finer than the Gaussian FWHM, often by a factor of 10 or more depending on the signal-to-noise. Hence, the Gaussian centroid-fitting accuracy x_{res} can be written as

$$x_{\mathrm{res}} = \mu_{\mathrm{fit}} \, \frac{\theta_{\mathrm{res}}}{3600} \frac{\pi}{180} \, d_{\mathrm{SS433}} = 0.149 \, \mathrm{pc} = 0.487 \, \mathrm{ly} \tag{4.11}$$

where $d_{\mathrm{SS433}} = 5500 \, \mathrm{pc}$ is the distance from us to SS 433 and W 50, and $\mu_{\mathrm{fit}} = 0.1$ represents the modest factor of 10 times better accuracy in determining the centroid position, as compared with the image resolution. The time baseline t_{base} between the *Elston-84* and *Dubner-96* images is 12 years and 4 days (with three of those years being leap years) giving a total of 4387 days, or of $t_{\mathrm{base}} = 12.01$ years based upon the 365.25-day year. The velocity resolution in units of the speed of light is then:

$$v_{\mathrm{res}} = \frac{x_{\mathrm{res}}}{t_{\mathrm{base}}} = 0.0405 \, c. \tag{4.12}$$

This velocity resolution is a factor of 6.5 times smaller than the measured speed of SS 433's jets of $v_{\mathrm{jet}} = 0.2647c$ (Eikenberry et al., 2001) close to their launch point, and so the kinematics of the movement of filaments associated with the jets (or turbulence caused by the jets) should be measurable, unless significant deceleration has occurred.

4.2.4   Measuring Filament Kinematics in W 50

The ten brightest filament-like structures common to all three images were selected and labelled A-H as shown in Figures 4.4, 4.5, and 4.6. Using the interactive kinematics pipeline (as described

in 4.2.2), the longest axis of each filament was determined and rotated to the vertical, such that the Gaussian curve fitting could be applied to the horizontal direction, to each pixel-row of the filament region. The fitting process could not be automated[4] due to extended structural variations in the background emission around each filament, and each Gaussian curve fit was inspected by-eye to ensure the best-fit was measured for the peak position of the filament and not to background structure which contributed to the Gaussian wings. An example of the Gaussian fit curves to Filament-A is given in Figure 4.3, and the complete set of filaments are overlaid upon their respective images in Figure 4.4, Figure 4.5, and Figure 4.6.

4.3 Results

The filament positions for each of the three epochs are overlaid together upon a contour image of the *Dubner-96* observation in Figure 4.7. A pseudo-dataset was generated using the data from the *Elston-84* observation, by projecting those filament positions 12 years into the future (based upon SS 433's current jet speed at the point of launch) in order to compare the expected pseudo-filament positions with the *Dubner-96* data. This projection was only applied to filaments that fall within SS 433's precessional jet cone, as material far from the mean jet axis will not have interacted directly with the jets and cannot be expected to propagate at similar speeds. Inspection of Figure 4.7 reveals that the filament positions from each of the three observations are remarkably coincident, with little indication of any conclusive movement, whereas the projected filaments are noticeably displaced from the rest. This raises two possibilities:

1. either considerable deceleration has occurred prior to the jet reaching the filaments, or

2. the filaments in W 50 have not interacted with the current jet (of speed $\sim 0.26c$) observed to be active near the central engine SS 433.

---

[4]This involved over 2000 Gaussian fit curves per image.
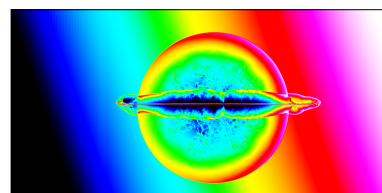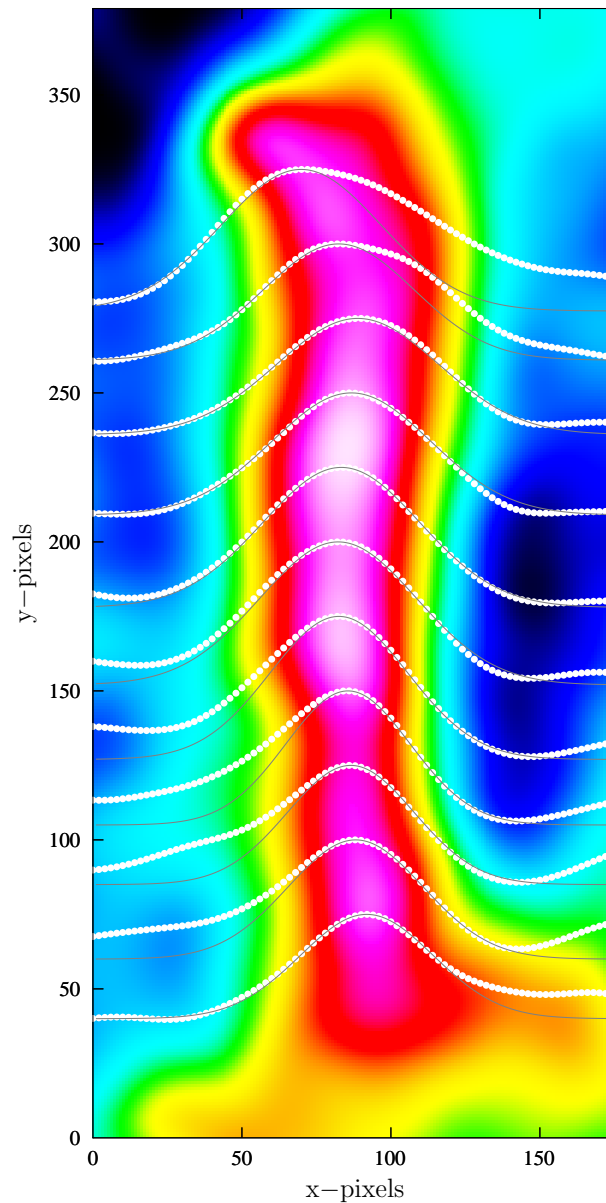
Figure 4.3: An example of the Gaussian centroid fitting to determine the filament mean positions along its length. The filament has been rotated such that its longest axis is along the vertical, and the Gaussian curves are then fit horizontally line by line, before rotating the coordinates back to the image frame. Note that only every 25th sampling is shown, and only every second datapoint per intensity profile. Difficulties arise when the structure of the filament is more extended, causing the horizontal intensity profile to diverge from a Gaussian shape. To compensate for this, each Gaussian curve is fit individually to determine a reliable range for the fit, and each fit is inspected by-eye to ensure a good match to the peak-position (the wings of the Gaussian are not important here). The white points represent the data, and the grey lines indicate the best fit to each line of data shown. Each Gaussian curve here has been overlaid upon the image, so that its peak aligns with the y−position from which it was taken.
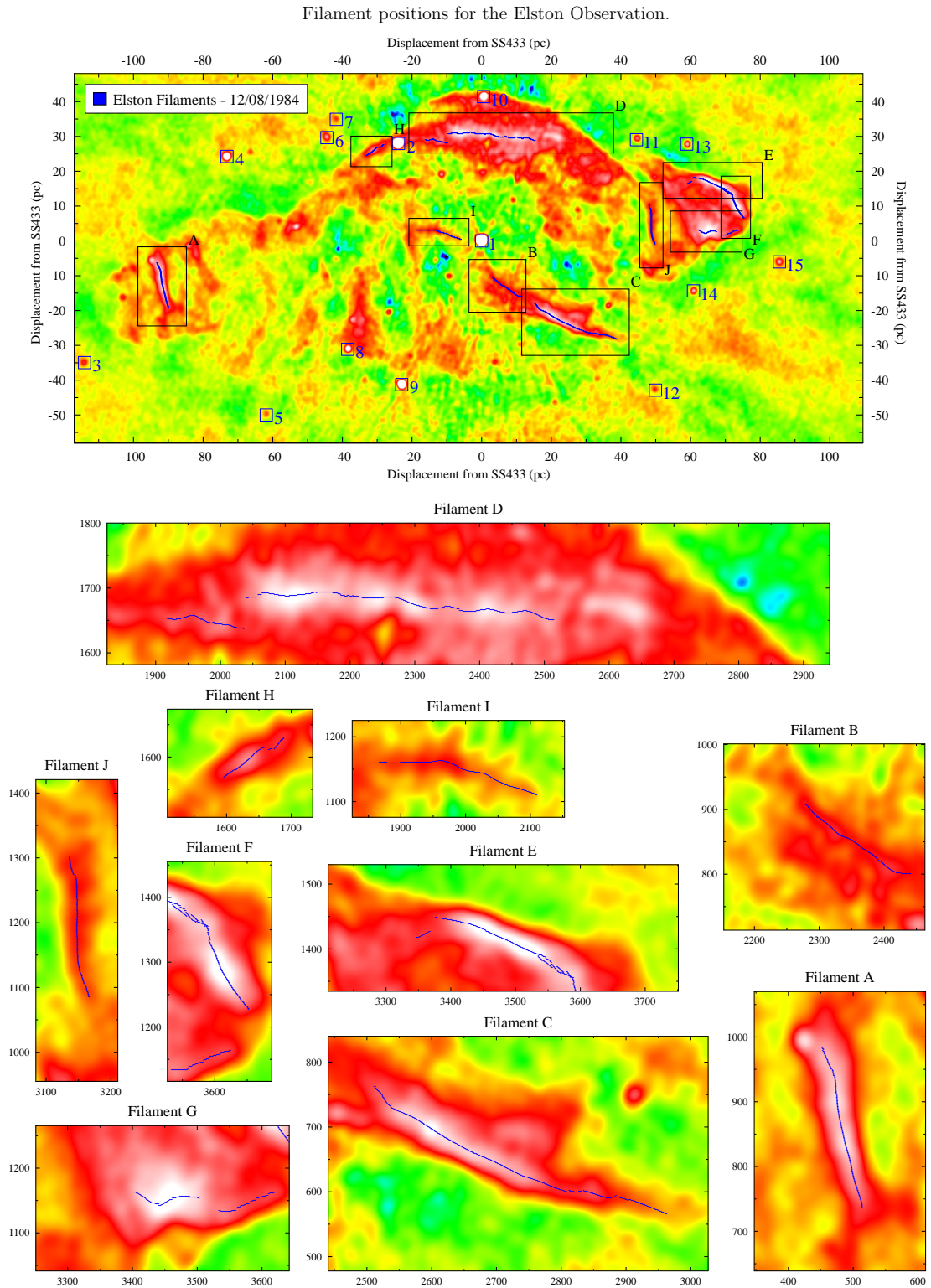
Figure 4.4: The centroid positions are shown for the filaments of the *Elston-84* observation.

Filament positions for the NVSS Observation.
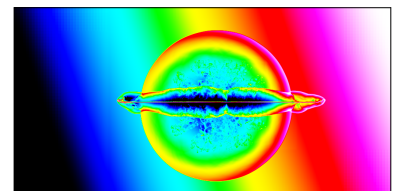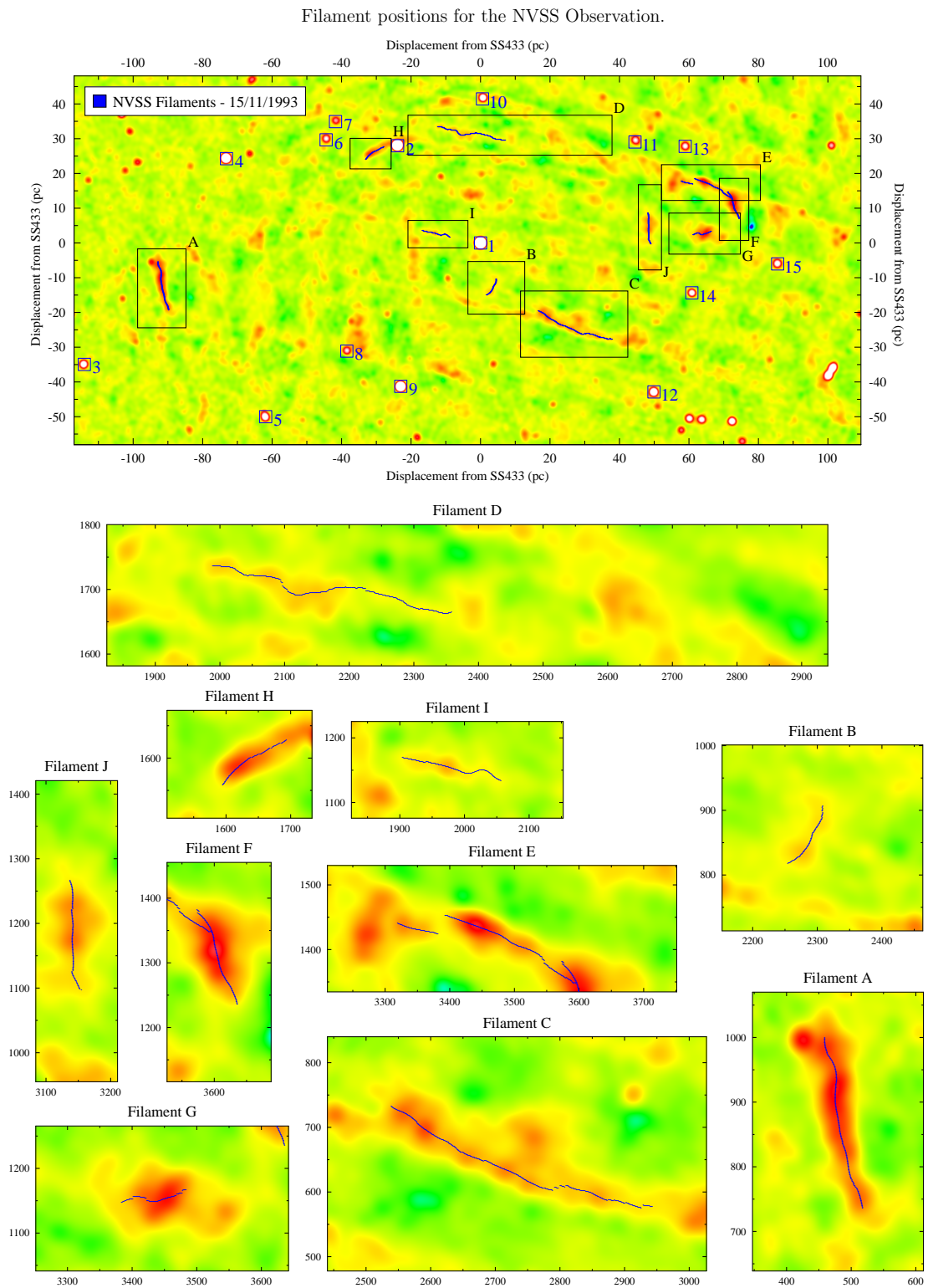
Figure 4.5: The centroid positions are shown for the filaments of the *NVSS-93* observation.

Filament positions for the Dubner Observation.
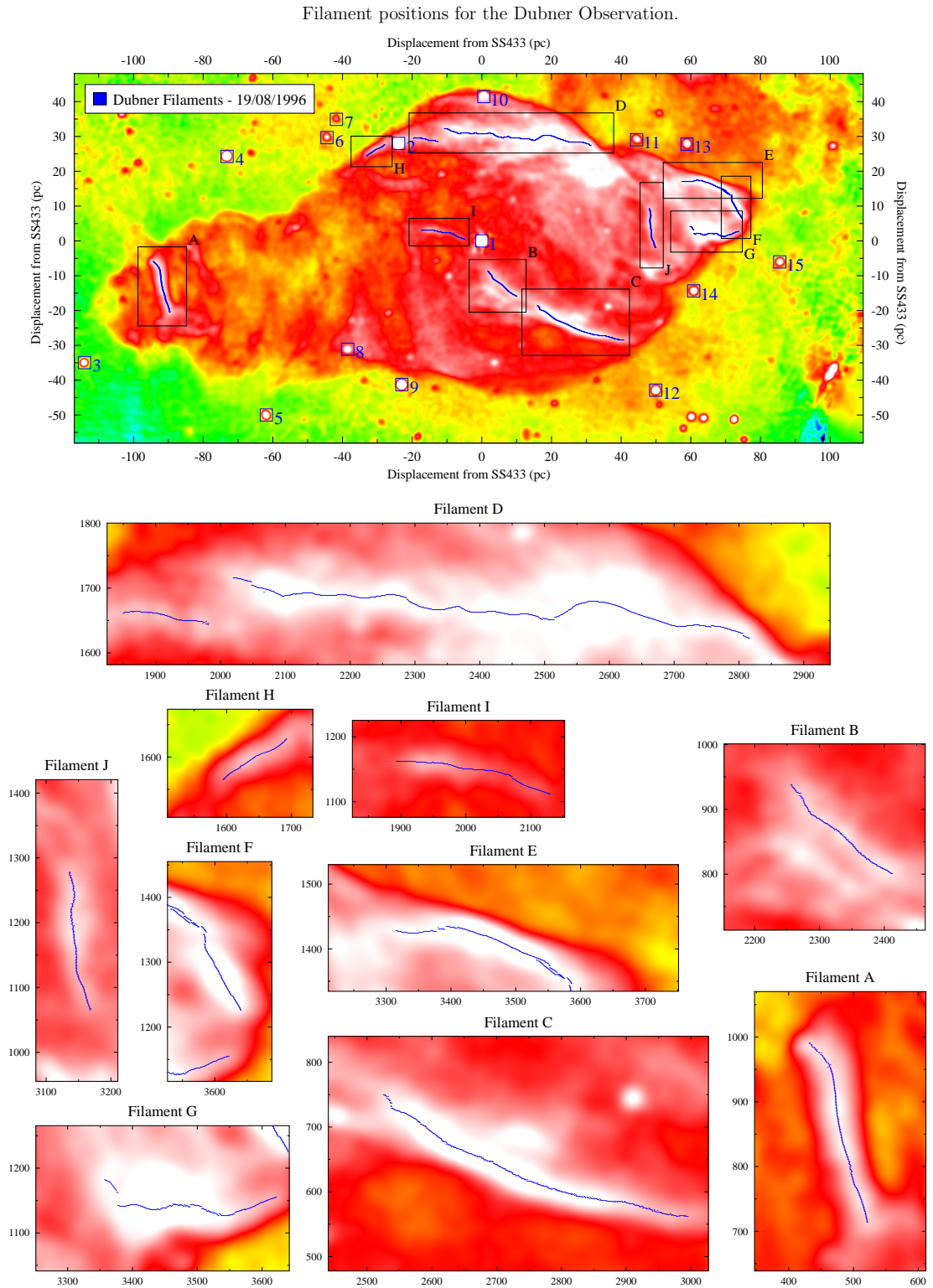
Figure 4.6: The centroid positions are shown for the filaments of the *Dubner-96* observation.
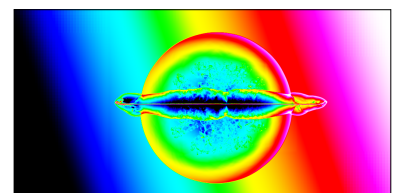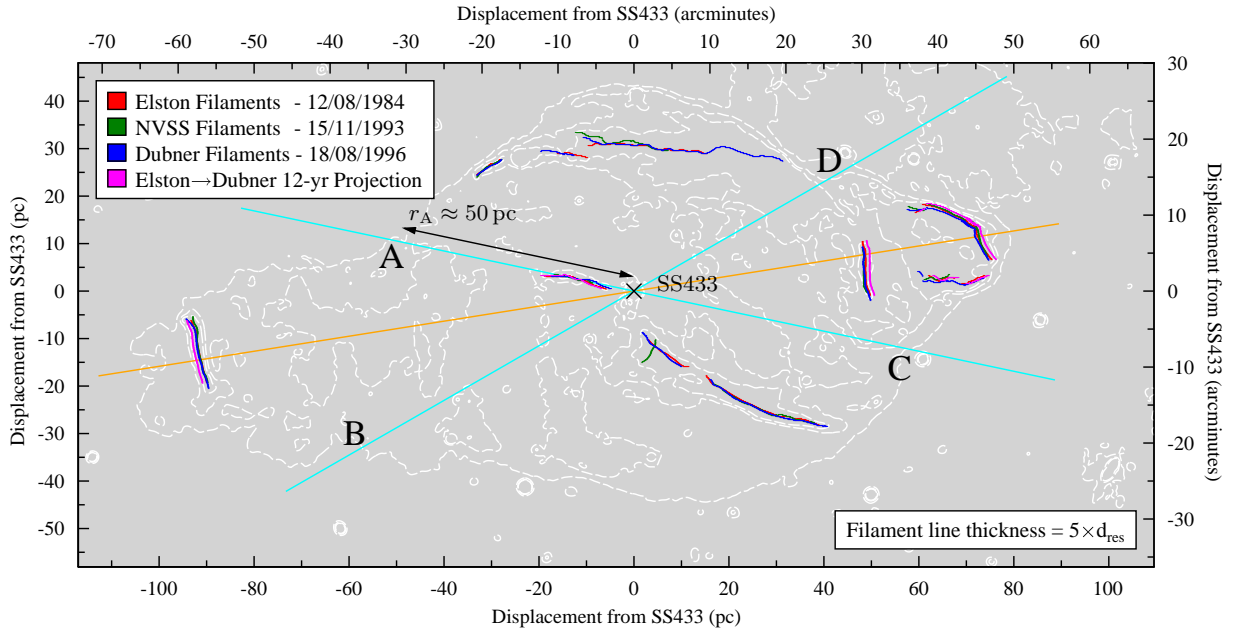
Figure 4.7: The filament positions of each of the three observations are overlaid upon a contour map of the *Dubner-96* observation. The magenta lines represent the pseudo-dataset generated by projecting the *Elston-84* filament positions 12 years into the future, assuming a speed of 0.26c in the direction radially away from SS 433. The orange line indicates SS 433's mean jet axis and the light-blue lines correspond to the precession cone, based upon the cone semi-angle at the current epoch of $\theta_{\mathrm{jet}} = 20.92°$ (Eikenberry et al., 2001). The points **A**,**B**,**C** and **D** indicate the locations where SS 433's current jet configuration would penetrate the W 50 nebula. Note the remarkable alignment between the bright filament nearest to SS 433 and the north-east jet cone line at image coordinates $\sim$(-10,+3) parsecs. The radial distance d_{A} from SS 433 to point **A** is approximately 50 parsecs. The errors in the fitted positions of the filaments are of the order of (or smaller than) the thickness of the filament lines plotted on the figure.

A velocity map (Figure 4.8) taken from high resolution hydrodynamic simulations of the SS 433-W 50 interaction (detailed in Goodall et al. (2010), and chapter 8) shows no signs of the required deceleration along the jet axis, and therefore supports the second possibility.

4.4   Discussion

The analysis reveals no discernible changes in the filament positions during the 12-year baseline covered by these observations. One conclusion to draw from this (as from (i) above) is that

considerable deceleration of the jet ejecta has occurred through interactions with the interstellar medium (ISM) present along the path of the jet lobes of W50, causing a reduction in the speed of the material in the lobes of W50 to below the detectable velocity resolution ($v_{\mathrm{res}} = 0.0405c$) of this investigation. These data would imply a lower limit of $\sim 85\%$ kinetic energy loss in the jets, and this energy would have been transferred to the ISM of the lobes. However, high resolution hydrodynamic simulations of the jets in SS 433 (Goodall et al. (2010) and chapter 8 of this thesis) reveal that, for any reasonable combination of jet mass-loss rate in the range $10^{-5} - 10^{-4}\,\mathrm{M_\odot\,yr^{-1}}$ and ISM density in the range $0.1 - 1$ particles cm^{-3}, a *persistently active* jet of speed $v_{\mathrm{jet}} = 0.26c$ does not suffer such extreme deceleration (see Figure 4.8). We stress however, that this model is based upon a *persistent* jet, whereby kinetic energy is continually injected from the central engine in SS 433 to replenish the kinetic energy (and momentum) lost to the jet, and transferred to the surroundings via interactions with the ISM.

In order to create a possible scenario in agreement with both the kinematics data presented here and the hydrodynamical simulations (henceforth "hydrodynamic simulations" refers to Goodall et al. (2010)), we must invoke the idea of intermittent, rather than persistent, jet behaviour in SS 433. The case for discontinuous jet activity in SS 433's history can be summarised with reference to the data presented here and the results of high resolution hydrodynamic simulations (Goodall et al., 2010), by the following kinematical arguments:

1. Referring to Figure 4.7, the light-blue lines indicate an extrapolation of SS 433's precession cone about the mean jet axis, based on the cone angle currently observed. It has been suggested (Eichler, 1983) that the jets may undergo a process of refocusing back towards the mean jet axis in order to avoid penetration of the nebula at the points indicated A,B,C, and D, and create the surprisingly well-collimated lobes of W 50. However, a series of comprehensive hydrodynamical simulations (Goodall et al., 2010) were carried out to investigate this possibility, and it has been proven not to be the case. Although refocusing of the jets does occur in our simulations, the mechanism is different to that suggested by
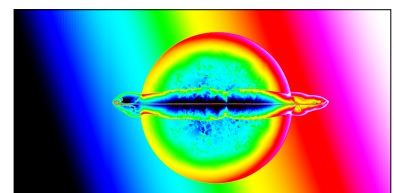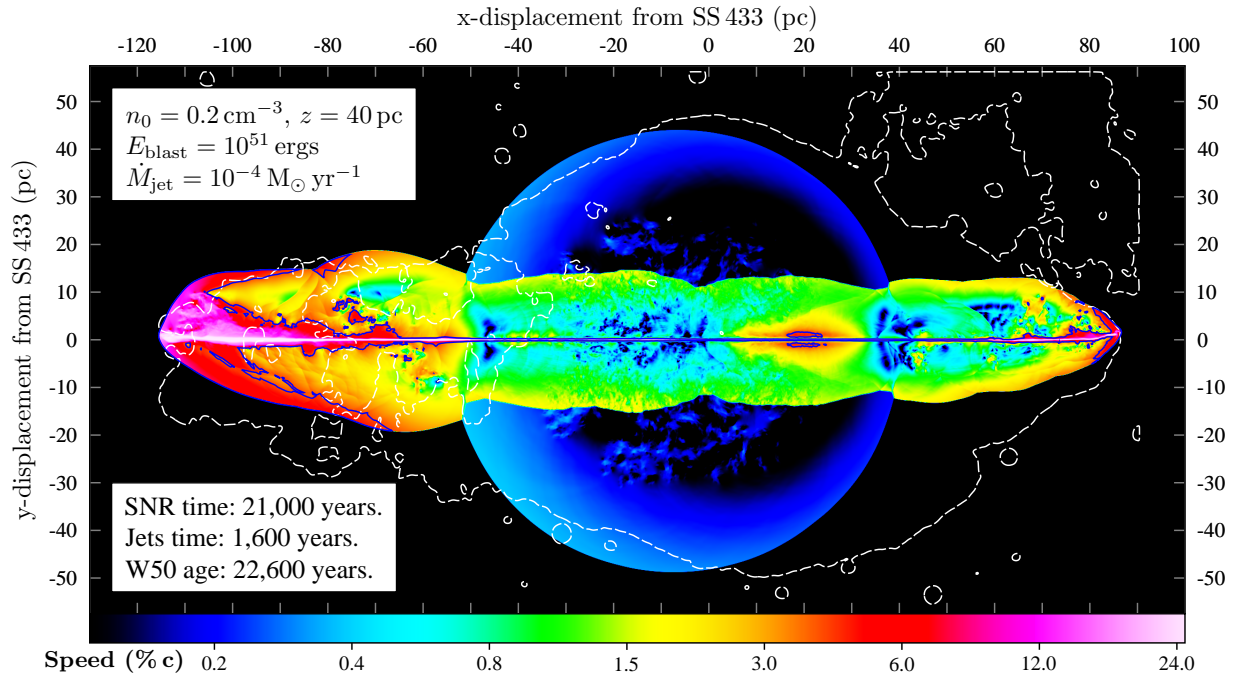
Figure 4.8: We present a velocity map from high-resolution hydrodynamic simulations of the SNR-Jet interaction in SS 433 (see Goodall et al. (2010) for a detailed account of these simulations). A contour map of the *Dubner-96* observation (white dashed line) has been overlaid upon the image to trace out the outline of the W 50 nebula. The above model can be summarised as a persistent cylindrical (zero precession cone angle) jet with speed 0.26c. The jet is incident upon an evolved SNR (blue circular region) of radius $\gtrsim$40pc and age 21,000 years. The background density profile ($n_0 = 0.2$ particles cm^{-3}, $z = 40$pc) has been optimised to match the observations of the east-west asymmetry in W 50, and it takes 1,600 years for the jets to reach the extent of W 50's lobes. The colour bar indicated the speed of the moving gas as a percentage of the speed of light, and the blue contour (solid line) indicates jet material which is travelling faster than the velocity resolution calculated in §4.2.3. The harpoon-like light-pink/white regions (particularly evident in the western lobe) shows material which is travelling very close to the speed of the jet (0.26c) at the launch-point, which is a consequence of continuous ejection of kinetic energy from the persistent jet.

Eichler (1983), and the level of collimation is not sufficient to form the lobes of W 50, nor does it prevent the jets from affecting the morphology of W 50 at the points A,B,C and D in Figure 4.7. Furthermore, Goodall et al. (2010) and chapter 8 of this thesis, show that the interaction of a cylindrical jet (zero precession cone angle) along the mean jet axis can produce lobes wider than we observe in W 50, and so any jet with a larger precession cone

angle is highly unlikely to do the trick. This is the first piece of evidence that SS 433's jets were quite different in the past.

2. By extrapolating the trajectory followed by the jet when in the plane of the sky (again, light-blue lines, Fig. 4.7), one would expect the jets to penetrate the W 50 nebula at the positions A,B,C, and D, and impose an observable change in the nebular morphology. Judging by the smooth morphology and lack of extrusions at the locations indicated by A,B,C, and D, it is clear that this has not yet happened. Based upon this evidence, dynamical arguments can be used to estimate the age/duration of the current jet precession state. Our hydrodynamic simulations (Goodall et al., 2010) imply that the age of the circular (45 pc radius) SNR region of W 50 lies in the range $\sim$20-40 kyrs, depending on the value background ISM density at SS 433 in the range 0.1-1 particles cm^{-3}. For comparison, the "in vacuo" jet travel time from SS 433 to the closest point (A) on the figure, is $\sim$ 600 years based upon 0.26c for the jet speed. In contrast, our hydrodynamic simulations show that jets with the same precession angle as SS 433 propagating through the ISM (density 0.2) at speed 0.26c, produce noticeable changes in the SNR morphology at points A,B,C,D after $\sim$3500 years after the jets are switched on. Comparing these SNR and jet timescales, we conclude that SS 433's current jet activity is relatively recent in the history of the SS 433-W 50 system.

3. Intermittent jet activity is thought to be a common property of both microquasars and quasars Nipoti et al. (2005), and jet flares are routinely observed in other microquasars such as Cygnus X-3 (Mioduszewski et al., 2001; Miller-Jones et al., 2004), also GRS1915-105 (Mirabel & Rodríguez, 1994) and V4641 (Hjellming, 2000). For these microquasars however, the intermittency timescales are sub-year, whereas we find hints of sub-millenium intermittency timescales for the SS 433 system.

4. The kinematic data suggests that SS 433's jet activity which gave rise to the lobes we
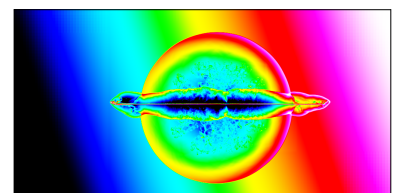
observe today in W 50, discontinued some time in the past. Upon cessation of the past jet activity, the transfer of kinetic energy from the jets to the surrounding ISM would then (and only then, without further input of energy from the power source SS 433) become sufficient to cause significant deceleration of the jet lobes, in agreement with the data presented here and from hydrodynamic simulations (Goodall et al., 2010).

4.5   Kinematics: Line-of-sight Proper motions

In 2008 I submitted a proposal to Gemini-South observatory, to conduct long-slit observations using GMOS of the bright filaments seen in the radio images of W 50. The science goals of this project were to try to measure the line-of-sight proper motions of the fast-moving gas in W 50 through doppler shifting of optical emission lines from hydrogen which is known to be in abundance in both the gas of W 50 and jet ejecta from SS 433.
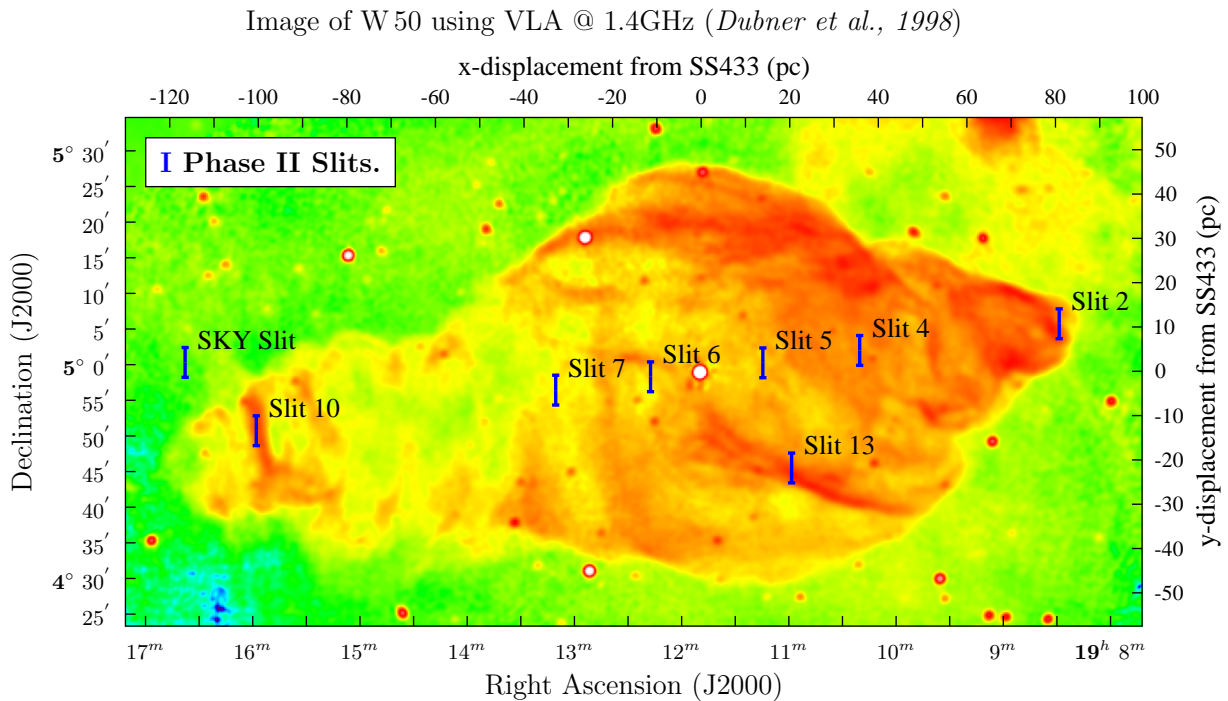
Figure 4.9: The slit positions observed using GMOS on Gemini South in 2009.

The project was awarded ∼10 hours of observation in "any" weather conditions of the first observing semester of 2009. The awarded time was divided between several pointings, resulting in a total of 1 hour integration on-target for each of the slits (2,4,5,6,7,10 and sky) shown in Figure 4.9, where the slit positions were chosen so as to sample the kinematics as a function of the distance from the jet launch point in SS 433. After a long and careful data reduction process, the data proved of insufficient quality to determine any useful constraints upon the line-of-sight kinematics.

4.6   Chapter Summary

In this chapter I presented the results of a kinematical study of the W 50 nebula using high resolution radio observations from the Very Large Array (VLA) spanning a 12-year period, sampled in 1984,1993 and 1996. With a careful analysis of the proper motions of the radio filaments across the W 50 nebula at each epoch, I detected no significant evidence for movement of the radio filaments during this period, based upon a spatial resolution of 0.149 pc from the observations, over a time baseline of 12.01 years. This places an upper limit on the speed of the large-scale motion of the nebular gas along the axis of the jets to < 0.0405 c. The apparent lack of movement in the radio filaments mandates either a high degree of deceleration of SS 433's jet ejecta in the W 50 nebula, or that the lobes of W 50 formed a long time ago in SS 433's history during a jet outburst with appreciably different characteristics to the currently well-known precessing jet state. The possible scenarios which could explain these result are discussed here (and in chapter 9), with relevance to the nature of SS 433's jet activity.
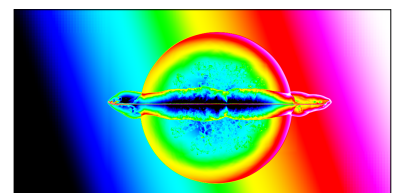
Chapter 5

Computational Hydrodynamics with

FLASH

This chapter briefly introduces some of the fundaments of Computational Fluid Dynamics (CFD), which are relevant to the numerical simulations in the chapters that follow. Among the topics covered are the Euler conservation equations in §5.3, discretisation of a plasma in §5.5, the constraints upon the computational time-step in §5.6, and a brief description of the Riemann solver §5.7. I aim to set the scene for the simulations by providing some discussion of the Adaptive Mesh Refinement (AMR) in §5.8.

5.1   About FLASH...

"FLASH" (Fryxell et al., 2000) is a well-known (and well tested) fully parallel hydrodynamic code, designed for simulating supernova explosions and thermonuclear reactions occurring on the surface of compact stars, and is developed by the University of Chicago Center for Astrophysical Thermonuclear Flashes[1]. The code utilises the Adaptive Mesh Refinement (AMR, see

---

[1]$http://flash.uchicago.edu/website/home/$
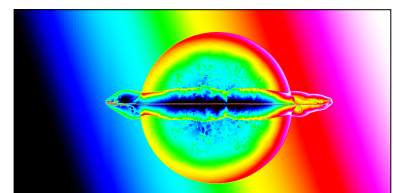
§5.8) technique, and implements the Piecewise Parabolic Method (PPM, a higher order Godunov method, see §5.7.3, Colella & Woodward (1984)). FLASH is noted for its flexibility, and I adapted it to include additional models that describe SS 433's jets (see chapter 7 for details) and a case-specific model for describing the supernova explosion involving SS 433's progenitor (see chapter 6). The details of my use of FLASH for the simulation work in this thesis will follow after a short summary of some relevant computational physics.

5.2   Fluids in nature

Fluids are omnipresent in the universe we live in, from the air that we breath to the water that flows from mountain to ocean, or indeed the ionised plasma of the sun's corona. Any fluid can be described as a continuous field in space and time $\eta(x, y, x, t)$, using a collection of primitive variables (such as total energy E, velocity $\mathbf{v}$, density ρ) specified at any point in the fluid.

In order to describe a fluid computationally, we impose an artificial grid upon it in some appropriate coordinate system (in this case, cartesian), such that the properties of the fluid are sampled discretely at each grid-point, at a given snapshot in time. Through the principles of conservation of mass, momentum and energy, we are then able to predict the subsequent behaviour of the fluid (in terms of ρ,$\mathbf{v}$,E) at some later time Δt. These conservation equations are a set of Partial Differential Equations (PDEs) know as the *Euler* equations, as per §5.3.

5.3   The Euler conservation equations

For a fluid flow in three spatial dimensions plus time (x,y,z,t), the principal variables are density $\rho \equiv \rho(x, y, z, t)$, pressure $P \equiv P(x, y, z, t)$, the velocity

$$\mathbf{v} \equiv \mathbf{v}(x, y, z, t) = v_x(x, y, z, t)\hat{x} + v_y(x, y, z, t)\hat{y} + v_z(x, y, z, t)\hat{z} \tag{5.1}$$

and the total (internal, kinetic and gravitational potential) energy density

$$\epsilon \equiv \epsilon(x, y, z, t) = \frac{P}{(\gamma - 1)} + \frac{1}{2}\rho\mathbf{v}^2 + \rho\Psi \qquad (5.2)$$

where γ is the ratio of specific heats, and Ψ is the gravitational potential. Then the Euler equations are:

$$\frac{\partial \rho}{\partial t} + \nabla \cdot (\rho\,\mathbf{v}) = 0 \qquad (5.3)$$

$$\frac{\partial \rho\mathbf{v}}{\partial t} + \nabla \cdot (\mathbf{v} \otimes \rho\mathbf{v}) + \nabla P + \rho\nabla\Psi = 0 \qquad (5.4)$$

$$\frac{\partial \epsilon}{\partial t} + \nabla \cdot \left[(\epsilon + P)\mathbf{v} \right] - \rho\frac{\partial \Psi}{\partial t} + \rho\dot{Q}_{\text{cool}} = 0. \qquad (5.5)$$

Although the above equations are quite general, for most cases the gravitational potential is a function of position only (no time-variable gravitational fields) and therefore the $-\rho\frac{\partial \Psi}{\partial t}$ term in equation (5.5) becomes zero. The term $\rho\dot{Q}_{\text{cool}}$ in equation (5.5) signifies energy lost through radiative cooling, where $\dot{Q}_{\text{cool}}$ is the radiative luminosity per unit mass.

5.4   Simplified Euler equations

For illustrative purposes, consider the simplistic case whereby gravity[2] and radiative cooling are both negligible, such that all terms involving Ψ or $\dot{Q}_{\text{cool}}$ in equations (5.4) and (5.5) can be dropped. The total energy per unit volume then only has kinetic and thermal components:

$$\epsilon_{\text{tot}} = \epsilon_{\text{int}} + \epsilon_{\text{kin}} = \frac{P}{(\gamma - 1)} + \frac{1}{2}\rho\mathbf{v}^2. \qquad (5.6)$$

---

[2]Note that gravity is not included in the numerical work for this thesis, see §5.11 for details.
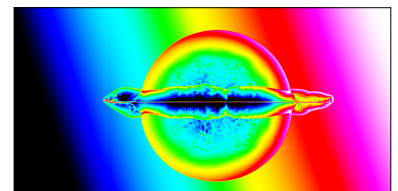
Equations (5.3) to (5.5) can then neatly be represented by:

$$\frac{\partial \mathbf{U}}{\partial t} + \frac{\partial \mathbf{I}}{\partial x} + \frac{\partial \mathbf{J}}{\partial y} + \frac{\partial \mathbf{K}}{\partial z} = 0 \tag{5.7}$$

where I, J, K and U represent the terms associated with the partials of (x,y,z,t) according to

$$\mathbf{U} = \begin{pmatrix} \rho \\ \rho v_x \\ \rho v_y \\ \rho v_z \\ \epsilon \end{pmatrix} \quad \mathbf{I} = \begin{pmatrix} \rho v_x \\ \rho v_x^2 + P \\ \rho v_x v_y \\ \rho v_x v_z \\ v_x(\epsilon + P) \end{pmatrix} \quad \mathbf{J} = \begin{pmatrix} \rho v_y \\ \rho v_x v_y \\ \rho v_y^2 + P \\ \rho v_y v_z \\ v_y(\epsilon + P) \end{pmatrix} \quad \mathbf{K} = \begin{pmatrix} \rho v_z \\ \rho v_x v_z \\ \rho v_y v_z \\ \rho v_z^2 + P \\ v_z(\epsilon + P) \end{pmatrix}. \tag{5.8}$$

Thus, there are 6 variables (v_x,v_y,v_z,ρ,P,ϵ) and only 5 equations, and the equations of state provides the 6th equation by relating P and ϵ, making the system solvable. In this case the ideal gas equation of state $P = \rho k_B T / \mu m_p$ is used along with $\epsilon_{\text{int}} = c_v T$ so to eliminate the extra variable T (temperature), where c_v is the specific heat of the gas at a constant volume equal to $c_v = R/(\gamma - 1)$ where R is the gas constant and γ is the ratio of specific heats (which is taken to be $\gamma = 5/3$ for the simulation work described in chapter 6 onwards). The usual symbols have been used for Boltzmann's constant (k_B), the mean particle mass (μ) and the proton mass (m_p).

5.5   Discretisation

The success of computational fluid dynamics comes from the ability to describe the macroscopic or bulk physical properties of a fluid, by splitting the fluid into small regions called *cells*, such that the average cell properties are representative of the fluid at each cell-centre. This process of splitting the fluid into small *discrete* regions or *cells* is called *Discretisation* of the fluid. Dis-

cretisation is a very common and computer-friendly way of storing information about continuous objects, whether that be a grid of fluid elements, or (analogously) a CCD (Charge Coupled Device) image of the smoothly varying emission from a nebula.

Naturally we require a description of the fluid in time and space, and many increasingly clever and complicated ways of evolving the discretised fluid in time and space have been devised. One simplistic but intuitive scheme that can be used to demonstrate this is the *finite difference* method.

The computational domain is *discretised* into *cells* of $\Delta x \Delta y \Delta z$ volume (for a 3D case) and is described in small time intervals Δt equal to the computational time-step (see §5.6).
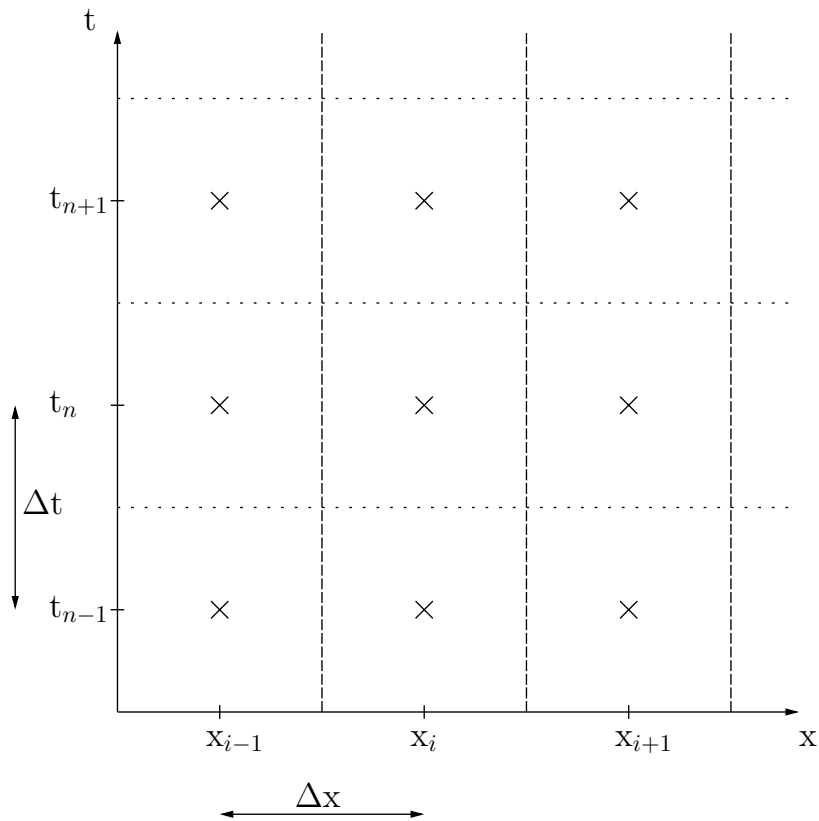
Figure 5.1: A 1D example of the discretisation of the simulation domain. The plasma is sampled discretely by cells of size Δx centred on all points x_i on the grid, in snapshots of time of duration Δt. Although it is not shown in this example, the cell-size and time-step could easily be made variable i.e. Δx_i and Δt_n.

I will demonstrate discretisation using the simple case of a 1D simulation domain in $\hat{x}$, where
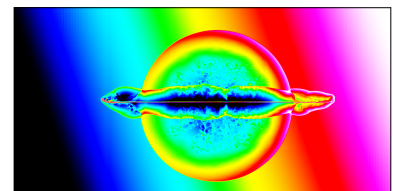
all cells and time-steps are equal across the grid (see Figure 5.1 for a graphical representation of this). Discretisation via the *finite difference* method for the 1D example means that the partials of (5.7) become finite differences, mathematically represented by substituting ∂ by Δ such that:

$$\frac{\Delta \mathbf{U}}{\Delta t} + \frac{\Delta \mathbf{I}}{\Delta x} = 0. \tag{5.9}$$

To express this more generally, I introduce the notation whereby $\mathbf{U}_i^n \equiv \mathbf{U}(x_i, t_n)$ which represents the quantity $\mathbf{U}$ at a given position on the grid at a given snapshot in time:

$$\frac{\mathbf{U}_i^{n+1} - \mathbf{U}_i^n}{\Delta t} + \mathcal{O}(\Delta t) + \frac{\mathbf{I}_{i+\frac{1}{2}}^n - \mathbf{I}_{i-\frac{1}{2}}^n}{\Delta x} + \mathcal{O}(\Delta x) = 0 \tag{5.10}$$

where $\mathcal{O}(\Delta x)$ and $\mathcal{O}(\Delta x)$ correspond to the numerical truncation errors of order Δx and Δt. These errors could be reduced by expanding the above equation to higher orders of the Taylor expansion, but to first order the quantity $\mathbf{U}$ at the next time-step $(n + 1)$ can be found from its value at the current time-step n and the spatial change of the quantity $\mathbf{I}$ at the current time-step as:

$$\mathbf{U}_i^{n+1} \approx \mathbf{U}_i^n - \frac{\mathbf{I}_{i+\frac{1}{2}}^n - \mathbf{I}_{i-\frac{1}{2}}^n}{\Delta x} \Delta t \tag{5.11}$$

5.6   Constraints upon the time-step

The resolution in the time domain (time-step Δt) with which we sample the fluid dynamics, must be chosen carefully such that *information* cannot cross an entire grid-cell during Δt. This is known as the *Courant-Friederich-Levy* condition, and by *information* I mean sound waves, or the physical advection of the plasma. This condition is satisfied in the code by computing the minimum value of the quantity $\Delta x_i / cmax_i$ across the simulation grid, where Δx_i is the cell size and $cmax_i$ is the greatest speed of cell i (the maximum of the physical and sound speeds of the

fluid in that cell). The computational time-step is then set according to:

$$\Delta t_{\text{step}} = t_{\text{fac}} \, \Delta x_i \, cmax_i \qquad (5.12)$$

where t_{fac} is some value less than unity, and typically in my simulations it is set to 1/6. FLASH does have the capability of using different time-steps for different cells, but I do not use this facility, and the time-step is a constant for all cells in the simulation domain.

5.7 The all-important Riemann solver

The topic of Riemann solvers is quite detailed in itself, and is the means by which a code numerically solves the Euler equations to advance to the next time-step. Various schemes have been investigated in the literature, with advantages and disadvantages in terms of accuracy with which the fluid is represented (minimising the truncation errors described above which can lead to problems of numerical diffusion), at the compromise of computation time per iteration. I will introduce the subject by talking about Godunov's method, before discussing the more sophisticated Piecewise Parabolic Method (PPM), which is the scheme adopted by FLASH and is described in §5.7.3.

5.7.1 1D Sod Shock tube

One such example of the Riemann problem is the Sod shock tube problem (see Sod (1978)). This involves two separate regions of fluid at different pressures P_1 and P_2 which are at rest, until the intervening barrier between them is instantaneously removed. Here I consider the 1D case whereby, upon removal of the barrier, a shock forms as gas from the high pressure side seeks to equilibrate with the low pressure gas. The is depicted in Figure 5.2.

Obviously both adjacent regions at rest with respect to each other is a special case. Other
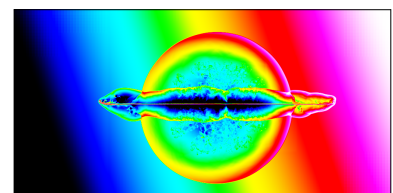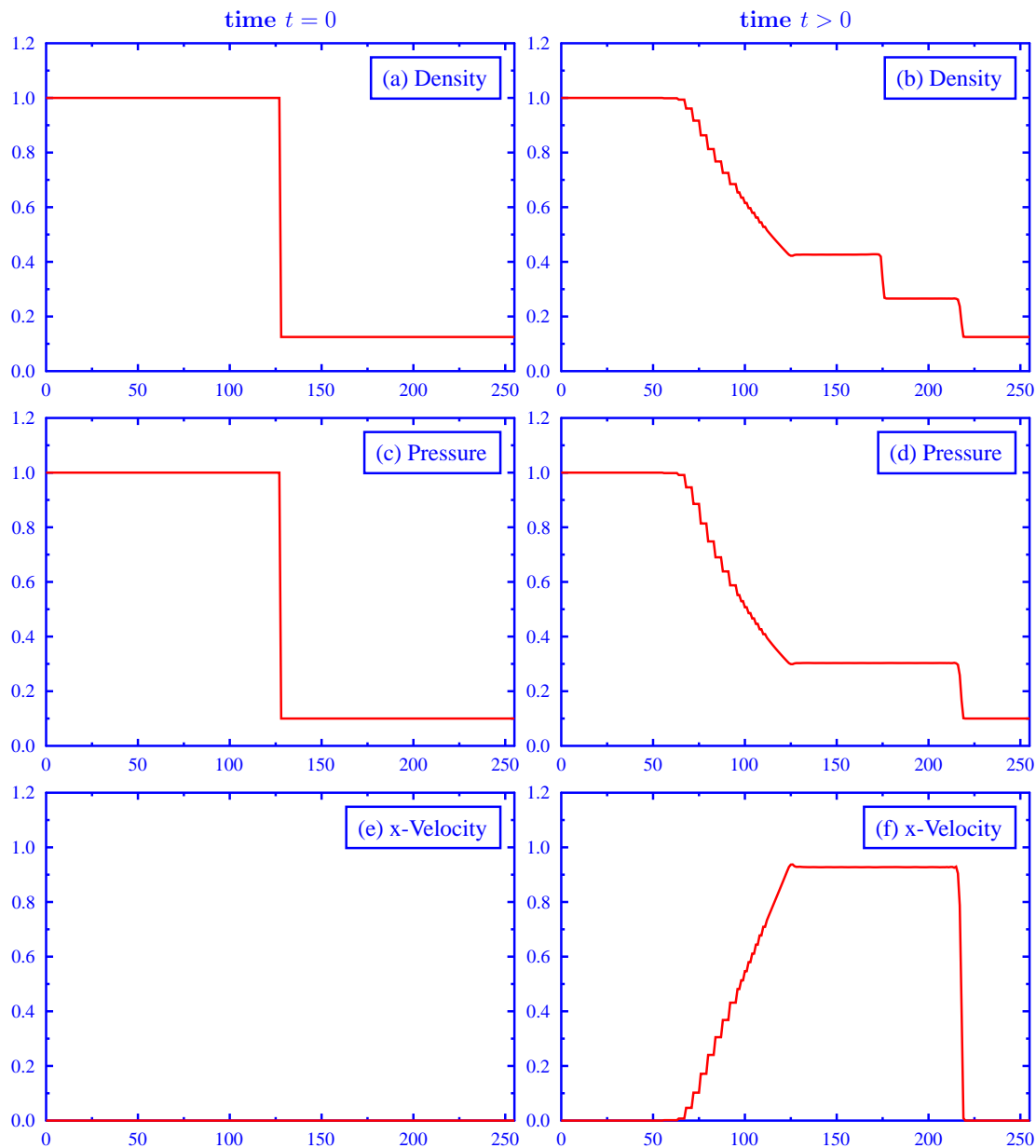
Figure 5.2: The figure shows profiles for the density (top), pressure (middle) and velocity in the $\hat{x}$ direction, for the 1D Sod tube shock problem. These are real data from a test run I conducted using FLASH, and the x and y axes for all three variables have arbitrary units. The left panels show the fluid properties at $t = 0$ before the barrier is removed. Note the abrupt difference in pressure and density between the left and right sides, and that the velocity is initial zero for the gas in each side. The right panels show the how the fluid has evolved. some time after the barrier has been removed. Note the appearance of the rarefaction wave from $x = 70$ to $x = 125$ on panels (b) and (d), and also the shock which has formed near $x = 220$ in the same panels.

special cases of the Riemann problem differ only in their initial conditions, such as: (i) the gas in the two adjacent zones are not at rest, but moving towards the intervening barrier, (ii) both zones have the gas moving away from the common barrier. Each of these cases have well-known analytical solutions, which allow for exact calculation of the fluxes of conserved variables between the boundaries of adjacent cells. The exact solutions can then be used to evolve the system to the next time-step.

5.7.2   Godunov's Method

Godunov's original *piecewise constant* scheme (Godunov, 1959) is accurate only to first order, and as such it can introduce numerical diffusion errors to the simulation grid. However, it formed the basis for the more sophisticated schemes used today (such as PPM, §5.7.3), and so is worth briefly mentioning. The Godunov scheme uses the exact analytical solution to the relevant Riemann problem to evolve the system to the next time-step. The basic stages are as follows:

1. **Reconstruction:** The discrete values $\mathbf{U_i}$ from several adjacent cells on the grid, are used to generate a function $\bar{u}(x)$ that smoothly represents the distribution of values across the adjacent cells. Enforcing the criterium

$$\mathbf{U_i} = \frac{1}{\Delta x} \int_{x-\Delta x/2}^{x+\Delta x/2} \bar{u}(x) \tag{5.13}$$

   ensures that mass. momentum and energy are conserved.

2. **Constructing a Riemann Problem:** An *Equivalent Riemann Problem* must be selected according to the *reconstruction* of $\bar{u}(x)$, with appropriate initial conditions.

3. **Computing the cell boundary fluxes:** This is where the analytical solution to the *Equivalent Riemann Problem* becomes relevant. The flux across the cell wall F_w is computed by integrating the analytical solution over the interval of the time-step Δt_step.
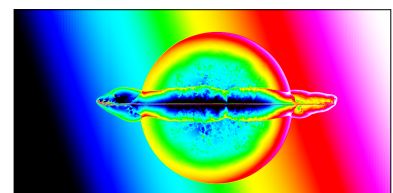
4. **Computing new cell values:** The cell values on the grid are recalculated according to the cell flux and cell value at the previous time-step: $\mathbf{U}_i^{n+1} = \mathbf{U}_i^n + \sum F_w$.

All methods that follow the above guidelines are known as *Godunov-type* schemes, and more modern revisions of this scheme adopt higher order polynomials to recreate the representative function $\bar{u}$ more accurately. One such method is the *Piecewise Parabolic Method*.

5.7.3   Piecewise Parabolic Method

The PPM method Colella & Woodward (1984) is based upon Godunov's original method, but it achieves a higher order accuracy by using a quadratic polynomial (parabolic segments) for the reconstruction of $\bar{u}(x)$ (rather than the *piecewise linear approach* used by Godunov) according to:

$$\bar{u}(x) = A(x - x_i)^2 + B(x - x_i) + C \tag{5.14}$$

in the range $x_{i-\frac{1}{2}} < x < x_{i+\frac{1}{2}}$ where A, B, and C are constants.

The equation (5.14) used in conjunction with (5.13), the coefficients can be solved for:

$$A = \frac{6}{(\Delta x)^2}\left(\frac{\bar{u}_R + \bar{u}_L}{2} - \mathbf{U_i}\right) \tag{5.15}$$

$$B = \left(\frac{\bar{u}_R - \bar{u}_L}{\Delta x}\right) \tag{5.16}$$

$$C = \frac{3\,\mathbf{U_i}}{2} - \left(\frac{\bar{u}_R + \bar{u}_L}{4}\right) \tag{5.17}$$

where I have used the notation $\bar{u}_L = \bar{u}(x_{i-\frac{1}{2}})$ for the value at the left wall of cell i and $\bar{u}_R = \bar{u}(x_{i+\frac{1}{2}})$ for the value at the right wall.

The above is meant to serve as very short introduction to PPM as an improvement to the

original Godunov method. In reality the values of A, B, and C are further refined in the PPM scheme, and I refer the reader to the original paper Colella & Woodward (1984) for more details.

5.8 Adaptive Mesh Refinement

Adaptive Mesh Refinement (AMR) is a technique used to maximise the practicable simulation resolution, increase iteration speed per time-step, and reducing the system memory requirements as compared to a uniform grid of the same resolution and dimensions. The AMR method works by providing a high spatial resolution description in the regions where it is needed most (i.e. where the interesting physics happens, in this case the activity of SS 433's jets) and lower resolution elsewhere. This has the effect that the cell-size obviously varies across the simulation domain. FLASH uses the package PARAMESH (Olson et al., 1999), which decides whether a region requires a higher resolution description (in which case it is refined), or can be adequately described using lower resolution (in which case it is derefined). The decision-making algorithms are described in Olson et al. (1999), but essentially a region is refined to a higher resolution if the specified *refinement variables*[3] begin to appear discontinuous between adjacent cells, in other words the refinement is increased in order to maintain a smooth or continuous representation of physical variables (such as density) across the grid. This becomes difficult for example in the case of shocks that develop in the fluid, and regions of strong shocks on the AMR grid are always described by the maximum possible resolution. The spatial resolution Δx of a particular region on the AMR grid is determined from its refinement level η according to:

$$\Delta x \; = \; \frac{L_{\mathrm{x}}}{\left[\, n_{\mathrm{xb}} \; \times \; 2^{\eta-1} \,\right]} \tag{5.18}$$

---

[3]For the case of the simulations here, both pressure and density were used as refinement variables.
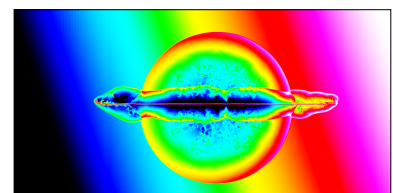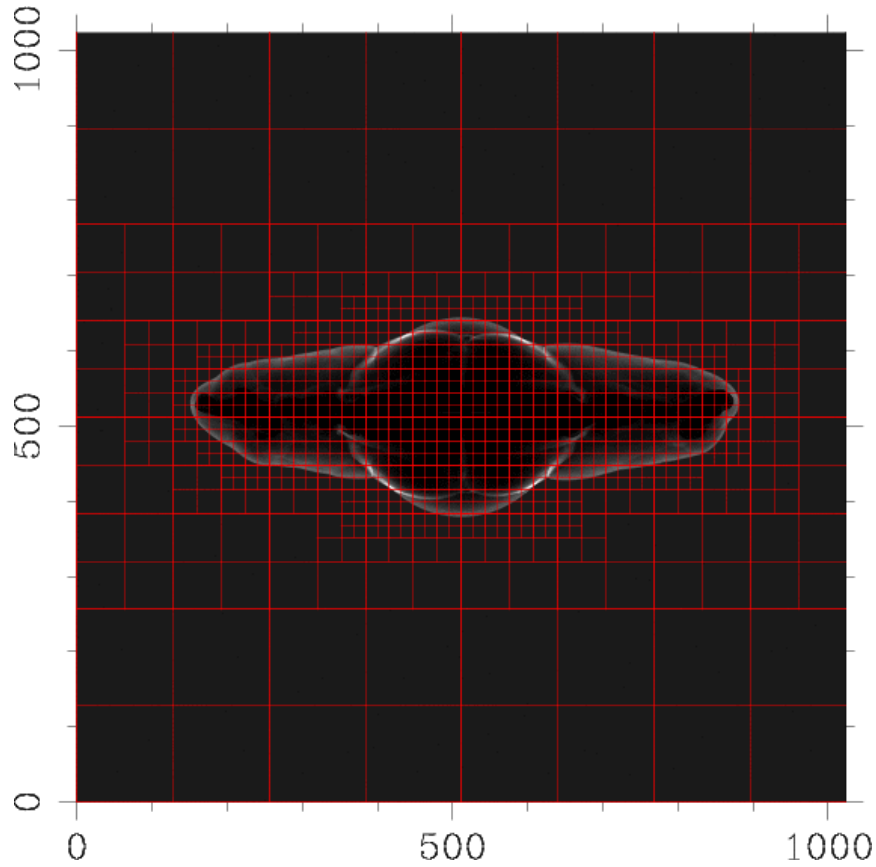
Figure 5.3: The refinement of the adaptive grid (red) is shown here as determined using PARAMESH, which provides higher resolution in the regions of interest close to the jets and around the shocked gas. The greyscale background image is a density map from a preliminary test simulation.

where n_{xb} is the initial number of blocks in the x-direction. The refinement level is permitted to vary between 1 and the maximum allowed[4] refinement level η_{max}, for which the corresponding maximum resolution is:

$$\delta x = \frac{L_x}{\left[n_{xb} \times 2^{\eta_{max}-1} \right]} \tag{5.19}$$

Aside from providing a more efficient use of memory, AMR also reduced the computation time by only using the minimum required number of cells, and hence minimising the number of calculations needed to advance the entire simulation to the next time-step. Figure 5.3 shows an example of the use of PARAMESH, where the AMR grid is overlaid upon a snapshot of the

---

[4]See details in §5.10.

density distribution created by primitive jets moving through a uniform medium.

5.9   Parallel Computation

All of the parallel computational work pertaining to this thesis was performed using the Oxford Astrophysics *Glamdring* cluster. *Glamdring* consists of 9 computing nodes, each of which is a dual-CPU 2.33GHz quad-core, with 8Gb of shared RAM per node. The MPI (Message Passing Interface) communication between nodes utilises a Gigabit Ethernet link. The combined storage capacity is 3.6Tb, from two RAID 5 arrays each of 1.8Tb. The available MPI compilers are as follows: mpicc uses gcc, mpif90 uses gfortran, mpiccintel uses Intel's icc, and mpif90intel uses ifort. FLASH on *Glamdring* is configured to use mpicc and mpif90.

The simulation domain in FLASH is composed of cells, which sample the properties of the plasma at each point on the grid (which can be 1,2 or 3D depending on the settings at compilation). Cells come in groups of blocks, where one simulation block consists of $nxb \times nyb \times nzb$ cells, as defined by the user when compiling the code. The initial level of refinement across the simulation domain is set using the subroutine `mark_grid_refinement.F90`, where the user can specify that the grid initially has the same refinement everywhere, or can specify different refinement criteria for certain regions of the simulation domain. For example (as described in chapter 6), I specify that the region of the simulation domain that surrounds the initial supernova explosion, remains at the maximum refinement (resolution) level at all time-steps. However, this constraint only affects a small fraction of the simulation domain (the innermost region, very close to the supernova epicentre), and the rest of the simulation domain may be refined/de-refined as the AMR routine sees fit. Thus, the number of blocks increases as the simulation progresses in this case, because the supernova expands into a larger domain, or the jets propagate through a larger extent of the ISM, and require a higher resolution description than the background (unperturbed) medium.
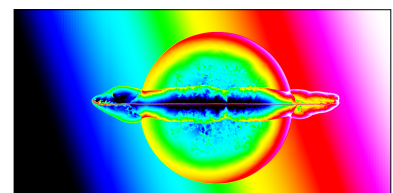
For a single processor, the computation time required per iteration (or time-step) increases (roughly) linearly with the number of blocks in the simulation grid. When multiple processors are used in parallel, one of the processors is designated the "*Master*" processor, and the blocks in the simulation are shared roughly equally between the processors. Each processor then performs the calculations necessary to advance to the next time-step, for the blocks that are allocated to it, and the process repeats. If it is time to write data to an output file[5], each processor returns its results to the master processor to be recorded in the output file. On *Glamdring*, submitting to N_{procs} processors, roughly decreases the computation time by a factor of N_{procs} if $N_{\mathrm{procs}} \leq 8$. The speedup factor is slightly less than N_{procs} if $N_{\mathrm{procs}} > 8$, because 8 or fewer processors communicate through the RAM of the compute node to which they belong, whereas more than 8 procs (processors) requires that MPI communication occurs via the gigabit ethernet connecting the nodes, which is significantly slower than RAM access. The required computation time per simulation time-step is roughly $\Delta t_{calc} + \Delta t_{\mathrm{comm}}$ corresponding to the calculation time and the MPI communication time, respectively. Hence, submitting a simulation job to more than 1 node (i.e. more than 8 procs) is only practical if $\Delta t_{calc} > 2\Delta t_{comm}$ if the resources are to be used efficiently. For this reason, I would often begin a simulation on 1 (nodes $\times$ 8 procs) until Δt_{calc} became large, at which point I would stop the simulation and then resubmit the simulation job to 2 nodes, and so on.

5.9.1   Motivation for using computer simulations

High resolution VLBI imaging of the central engine in SS 433 reveals jet structure on scales of a few tens of AU, a factor of 10^6 or so smaller than the extent of W 50[6]. The need for a high resolution representation of the core region of SS 433, and the large-scale field of view (FOV)

---

[5]The user specifies that output files should be written ever Δt_{w} years of simulated time, where Δt_{w} is set to 100 years for the SNR-only simulations and every 10 years for simulations involving SS 433's jets.

[6]The site of jet-launch in SS 433 is thought to be very much closer to the black hole than the resolution of modern telescopes. Based on the Schwarzschild radius for a $M_{\odot}$ black hole, the base of the jets in SS 433 are likely to be of order 10^{14} times closer to the singularity than the lobes of W 50.

necessary to enclose W 50, makes for a challenging computational problem.

However it is possible (with modern supercomputers) to construct numerical models with sufficient resolution to probe the regions of W 50 on scales comparable to high-resolution radio interferometry. In my simulations the best resolution is comparable (within a factor of three) to that of the high-resolution VLA image revealing the corkscrew in SS 433 (Figure 2.2c) and a field of view large enough to contain the entire W 50 nebula (Figure 2.2b) of more than 200 pc across. This is very useful, because one can create a numerical model that accurately describes of SS 433's jets very near to the central engine where the precession is resolved in observations, and then allow the system to evolve to discern the effects of the jets with the larger surroundings. Comparing simulations and observations then allows conclusions to be made about the history of the jet activity, and (as I hope to show in the chapters that follow) some very interesting hydrodynamical effects are revealed which must be factored into current models for precessing jet activity.

5.9.2   Foreword on Simulation Data Analysis

A total of 40 full simulations were conducted to produce the results for this thesis, along with at least an equal number of test runs and countless other experimental trials. Each of the full/test simulations required approximately 4-days of supercomputer time on a total of 32 processors (4 *Glamdring* nodes), and typically output of order 200 HDF5-PLT (plot) files and 20 HDF5 CHK (checkpoint) files weighing in at 100Mb and 1Gb each respectively. These are average file sizes, as the size of a given HDF5 datafile increases linearly with the number of simulation blocks being used by the *Adaptive Mesh* (see §5.8) at the time when the file is created. In turn, the number of simulation blocks increases with the duration of the simulations in this case, as the supernova and/or jets propagate through the simulation domain and necessitate further refinement (a higher resolution description) of the coarser grid which was previously used to describe the unperturbed ISM. However, the HDF5 format is still a compressed file format, where the adaptive mesh means
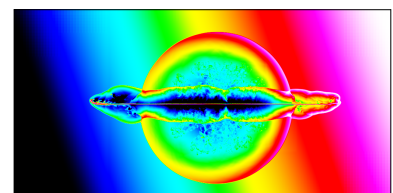
that the pixel size varies across the simulation grid. In order to analyse the simulation results, each physical variable (density, vx, vy, vz, temperature, pressure) for each PLT files was mapped onto a uniform grid[7], and I chose to use the Flexible Image Transport System (FITS) format for this purpose. In the final stage, each physical variable from each of the PLT files is represented in (floating-point) FITS format on a uniform grid of 8192×4096 pixels, for which the file size is 128Mb (independent of the input PLT file size).

To summarise, the computational work featured in this thesis used approximately 250,000 CPU-hours (the number of CPU's used multiplied by the duration for which the CPU's were used), with roughly 3.3Tb of disk space used for the simulations. A total of 13Tb of disk space would be required to store each of the physical variables from each of the PLT files, from each of the simulations, as uniform-grid FITS files.

Obviously the above disk space requirements become impractical even at the relatively low cost of hard disk storage space in the present day. However, there were several tips and tricks I used to eliminate the problems of disk space and computer analysis time:

- The *gzip* compression tool was extremely valuable, often decreasing the file size by a factor of 100.

- Where possible, physical variables were read into memory and manipulated "on-the-fly" without saving the FITS files to disk.

- I used the Perl Data Language to write a useful pipeline of data reduction scripts, which allows for extremely fast manipulation of very large arrays of numbers.

---

[7]With a uniform grid size of 8192×4096 pixels and a domain size of $230\,\mathrm{pc}\times115\,\mathrm{pc}$, each pixel corresponds to $\approx 0.028\,\mathrm{pc}$.

5.10   Implementing the model of SS433 using FLASH

To maximise the simulation resolution in the regions of interest, I limit the simulation domain to a thin slice through the centre of the SS 433-W 50 complex, with dimensions $(L_x \times L_y) = (230 \times 115)$ parsecs in $\hat{x}$ and $\hat{y}$ respectively, with $(n_{xb} = 16)$ blocks in $\hat{x}$ and $(n_{yb} = 8)$ blocks in $\hat{y}$, such that all pixels are squares. The chosen domain size ensures that neither jets nor the SNR reach the domain boundaries, such that outflow boundary conditions can be suitably applied. The limiting resolution depends on the maximum level of refinement $(\eta_{\max})$ allowed, such that:

$$\delta x = \frac{L_{\mathrm{x}}}{\left[\, n_{\mathrm{xb}} \times 2^{\eta_{\max}-1} \,\right]} = \delta y = \frac{L_{\mathrm{y}}}{\left[\, n_{\mathrm{yb}} \times 2^{\eta_{\max}-1} \,\right]}. \tag{5.20}$$

I set the maximum refinement level to $\eta_{\max} = 10$, resulting in a maximum resolution of $\delta x = \delta y = 0.028\,\mathrm{pc} = 8.66 \times 10^{14}$ metres, or $\simeq 1$ arcsecond on the sky for objects at a distance of $d_{\mathrm{W}\,50} = 5.5\mathrm{kpc}$. This is about three times the synthesised beam-width in the famous VLA corkscrew observation of SS 433's jets (Blundell & Bowler (2004), and also shown in Figure 2.2c). For simplicity we refer to the maximally refined cells as pixels (cells for which $\eta_{\mathrm{cell}} = \eta_{\max}$), such that (due to the nature of AMR, refer to §5.8) every cell in the simulation domain has sides equal to an integer power of 2 times the pixel size. The width L_{z} of the simulation domain slice (i.e. the thickness in $\hat{z}$) is variable across the simulation domain, because the z-dimension of each cell is assumed equal to the cell-size in the x-direction. Thus, although each cell has a volume of $dx\,dy\,dz = dx^2\,dy$, the simulations are effectively just 2D.

5.11   Creating SS433's environment

I make the simple but effective assumption of approximately cosmological abundances of Hydrogen (90%) and Helium (10%) by number[8], such that $\mu = 1.3$ is the mean mass per particle in

---

[8]I realise that this corresponds to approximately 70% Hydrogen and 30% Helium by mass, which is overabundant in Helium by a few percent with respect to cosmologically accepted values.
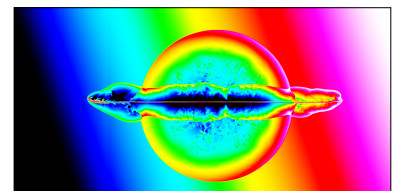
atomic mass units. I adopt an exponential ISM Galactic density profile as adapted from Dehnen & Binney (1998) of the form:

$$\rho_{\mathrm{ISM}}(R, z) = \rho_0 \, \exp\left(-\frac{R_{\mathrm{m}}}{R_{\mathrm{d}}} - \frac{R}{R_{\mathrm{d}}} - \frac{z}{Z_{\mathrm{d}}} \right) \tag{5.21}$$

where the values of the constants are also from Dehnen & Binney (1998) such that $R_{\mathrm{m}} = 4\,\mathrm{kpc}$, $R_{\mathrm{d}} = 5.4\,\mathrm{kpc}$ is the scale length of the stellar disc, and $Z_{\mathrm{d}} = 40\,\mathrm{pc}$ is the scale height of the disc in the direction perpendicular to the Galaxy plane. The prefactor ρ_0 is determined from a normalisation condition that the density at the location of SS 433 is:

$$\rho_0 = \rho_{\mathrm{ISM}}\left(R_{\mathrm{SS433}}, z_{\mathrm{SS433}}\right) = n_0 \, \mu \, m_{\mathrm{p}} \tag{5.22}$$

where m_{p} is the proton mass, and n_0 is a parameter (for m_{p} in CGS units this defaults to 1 particle per cc, as shown in Figure 2.2b). The cylindrical coordinates[9] of SS 433 are $R_{\mathrm{SS433}} = 5.1\,\mathrm{kpc}$ and $z_{\mathrm{SS433}} = 204\,\mathrm{pc}$ as shown in Figure 2.2.

A gravitational term would usually be invoked to maintain static equilibrium of the background gas. In this scenario, the gravitational centre of the Milky Way galaxy resides far outside of the simulated field of view. As a simple remedy, I allow the background temperature profile to have an inverse behaviour to that of the background density in order to keep the thermal pressure constant, which artificially creates hydrostatic equilibrium in the background medium. Preliminary tests were carried out on an unperturbed background to verify the stability of this, and the system remained static over a period of 10^6 years of simulated time. Therefore, over the timescales involved in these simulations (typically $< 4 \times 104$ years), I can reliably conclude that subsequent hydrodynamic motion is solely driven by the supernova and/or jet interaction.

---

[9]This is calculated using $d_{\odot-\mathrm{GC}} = 8\,\mathrm{kpc}$ as the Sun-Galaxy centre distance, $d_{\odot-\mathrm{SS433}} = 5.5\,\mathrm{kpc}$ as the distance from the Sun to SS 433, which has Galactic coordinates $(l_{\mathrm{SS433}}, b_{\mathrm{SS433}}) = (39.7°, -2.24°)$.

5.12   Radiative Cooling

Radiative cooling in this case refers to a slightly modified version of the standard cooling functions provided with FLASH, as follows.

Smoothed representation of the cooling function $\Lambda(T)$.

$$\Lambda(T) = \begin{cases} (10^{-5.97}T)^{11.7} & 10^{3.65}\text{ K} < T < 10^{3.9}\text{ K} \\ (10^{-7.85}T)^{6.15} & 10^{3.9}\text{ K} < T < 10^{4.3}\text{ K} \\ 10^{-21.85} & 10^{4.3}\text{ K} < T < 10^{4.6}\text{ K} \\ 10^{-31}T^2 & 10^{4.6}\text{ K} < T < 10^{4.9}\text{ K} \\ 10^{-21.2} & 10^{4.9}\text{ K} < T < 10^{5.4}\text{ K} \\ 10^{-10.4}T^{-2} & 10^{5.4}\text{ K} < T < 10^{5.75}\text{ K} \\ 10^{-21.94} & 10^{5.75}\text{ K} < T < 10^{6.3}\text{ K} \\ 10^{-17.73}T^{-2/3} & 10^{6.3}\text{ K} < T < 10^{7}\text{ K} \\ 10^{-18.21}T^{-0.6} & 10^{7}\text{ K} < T < 10^{7.6}\text{ K} \\ 10^{-26.57}T^{1/2} & 10^{7.6}\text{ K} < T < 10^{8}\text{ K} \end{cases}$$
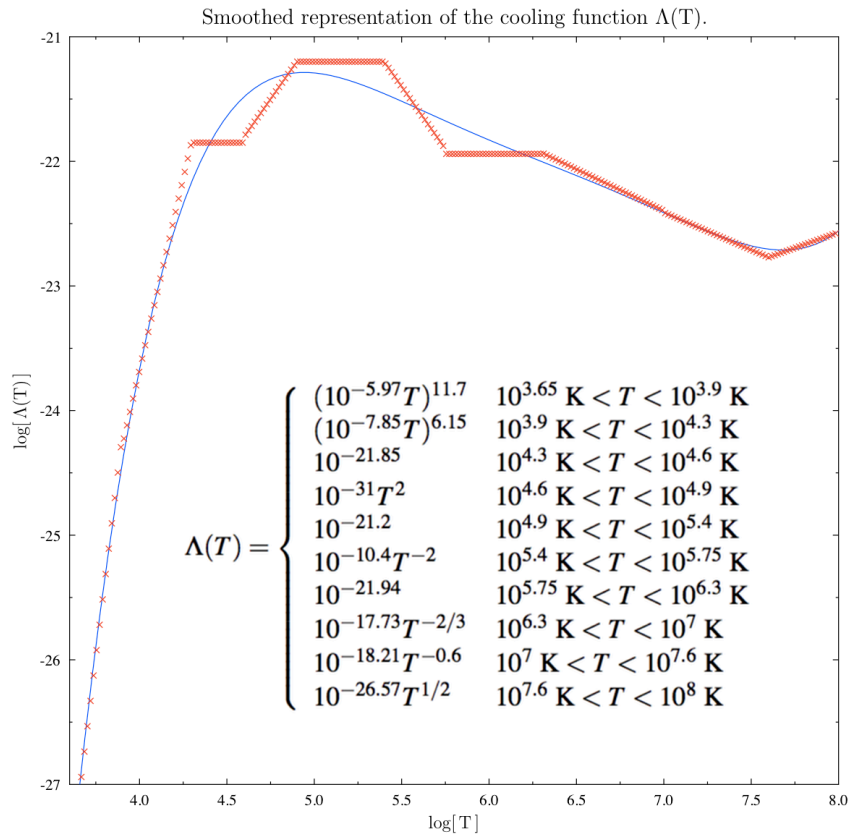
Figure 5.4: The radiative cooling function used by default in FLASH is shown by the red points and set according to the data (inlay), and the blue line shows a 7th order polynomial fit to the data points.

The standard radiative cooling in FLASH2.5 assumes an optically thin plasma, where the cooling function $\Lambda(T)$ is based upon models of the energy losses from the transition region of the solar corona (Rosner et al., 1978) and the chromosphere (Peres et al., 1982), and the resulting cooling function is given as a piecewise-power law approximation according to the inlay information in Figure 5.4. This function is plotted in Figure 5.4 as the red datapoints. However, this is not a continuous function, and can result in two adjacent cells in the simulation domain with
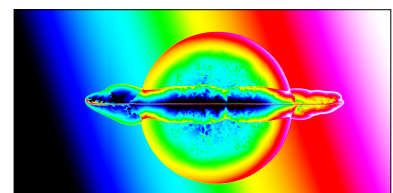
unreasonably different cooling rates, when their cell temperatures differ only slightly. I applied a simple 7th order polynomial fit to the data to provide a more smoothly varying, continuous function that is representative of the same cooling data. The smoother cooling function is used throughout my simulations.

The radiative luminosity per unit volume is simply calculates as follows:

$$\lambda_{\text{cool}} = n_{\text{e}} \, n_{\text{p}} \, \Lambda(T) \tag{5.23}$$

where $\Lambda(\text{T})$ has units of $\text{ergs}\,\text{cm}^3\text{s}^{-1}$, and the radiated energy loss per cell is computed per timestep by multiplying λ_{cool} by the timestep and subtracting this from the internal energy budget ϵ_{int}. As detailed in §5.11, the simulations use only hydrogen (90% abundance by number) and helium (10%), thus $n_H = 0.9\,n$ is the number density of hydrogen in terms of the number density n of ionised nuclei. For the completely ionised plasma, the electron number density becomes $n_{\text{e}} = n_{\text{H}} + 2\,n_{\text{He}} = 1.1\,n$. Hence, (5.23) can be rewritten according to the cell density:

$$\lambda_{\text{cool}} = 0.99\,n^2\,\Lambda(T) = 0.99 \left(\frac{\rho}{\mu\,m_{\text{p}}} \right)^2 \Lambda(T) \tag{5.24}$$

where μ, ρ and m_{p} have the usual meanings.

This concludes the description of the the simulation preliminaries. The subsequent sections chapter 6 and chapter 7, are concerned with the specifics of the supernova and jet models respectively, while chapter 8 details the combination interacting jets from SS 433 with the supernova

remnant created by SS 433's progenitor.
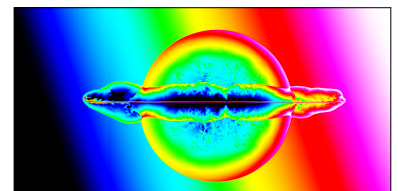
Chapter 6

Simulating a Supernova Explosion

Typically in supernova simulations, a Sedov-Taylor analytic solution for a strong blast wave is adopted and used to initialise the density, temperature, pressure and velocities of the supernova explosion. This has the advantage that, for a given background density and explosion energy, the radius of the advancing shockwave behaves predictably with time, according to the Sedov-Taylor (Sedov, 1959; Taylor, 1950) blastwave relation:

$$r_{\text{blast}}(t) \;\; = \;\; \alpha \left(\frac{E_{\text{blast}}}{\rho_0} \right)^{\frac{1}{5}} t^{\frac{2}{5}}. \tag{6.1}$$

However, this description is appropriate only during the Sedov phase of a SNR blast wave, when the mass swept-up by the supernova shock front is comparable to, or greater than the ejected mass from the progenitor. For a sensible progenitor mass ejection and an ISM particle ($\mu = 1.3$) density in the range $n_0 = 0.1$-1 cm^{-3}, the Sedov phase occurs when the SNR radius falls in the approximate range $10^0 - 10^1$ pc, which is quite large compared to our resolution capability. Thus, we model the supernova in the pre-Sedov *free-expansion* phase, and there are two main advantages to this.

Firstly, it is difficult to guess the initial blast energy of the supernova explosion which may have produced W 50. To compensate for this unknown we test two values for the initial kinetic
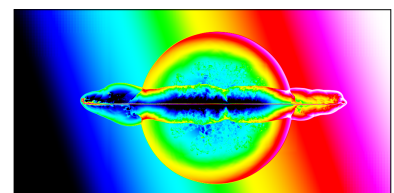
energy of the gas ejected through the supernova blast. We adopt the notation whereby supernova model SNR_{50} has an initial blast kinetic energy of $E_{50} = 10^{50}$ ergs and model SNR_{51} has $E_{51} = 10^{51}$ ergs, and together these encompass a reasonable range of supernova cases. A purely Sedov-like expansion with these parameters requires 10^5 years (for the E_{51} case) to 10^6 years (for the E_{50} case) to expand to a radius $R_{W\,50} = R_{45} = 45$pc (the current size of W 50's circular shell region, as per Figure 2.3b). The free-expansion phase expansion is much more rapid initially, but eventually the system hydrodynamically establishes a Sedov-like behaviour (i.e. the expansion follows $R(t) \propto t^{2/5}$ as demonstrated in Figure 6.3a). This method reduces the required time for the SNR radius to reach R_{45} (Figure 6.3a) to something much more reasonable, in agreement with observational predictions of other old SNRs. The free-expansion SNR reaches a maximum radial expansion speed of [1-2]% c (Figure 6.3d) and as such a relativistic treatment is not critical at this stage.

Secondly, the scene of our supernova explosion is set within an exponential density background from the Milky Way. As such it is beneficial to initialise the supernova explosion as early as possible in order to fully investigate the effects of the non-uniform ISM upon the SNR as it evolves and sweeps up ambient material. This is particularly relevant in order to study the East-West asymmetry present in W 50.

6.1   Implementing the Pre-Sedov Supernova Explosion

We define the radius R_{Sedov} to be the radius at which a sphere of ISM density[1] ρ_0 contains the mass M_{ej} equal to that ejected from the progenitor. Therefore, the pre-Sedov phase is valid for $R(t) < R_{\text{Sedov}}$. A compromise must be made in the initial radius of the supernova blast, such that the earliest possible evolution is incorporated, whilst adequately describing a circularly symmet-

---

[1]The background density can be considered constant across the small scales relevant here.

ric SNR and thus avoiding early propagation of the unwanted artifacts[2] commonly encountered when modelling using cartesian grids. We parameterise the initial radius as a function of the Sedov radius by

$$R_\mathrm{i} = f_\mathrm{r}\, R_\mathrm{Sedov} = f_\mathrm{r} \left(\frac{3M_\mathrm{ej}}{4\pi\rho_0} \right)^{\frac{1}{3}} \tag{6.2}$$

and we find that $f_\mathrm{r} = 0.25$ defines such a compromise radius, for a mass ejection of $M_\mathrm{ej} = 5\mathrm{M}_\odot$ and an ambient density of $n_0 = 1$ particle cm^{-3}. This typically results in an initial radius R_i of 50-100 pixels. Thus, the pre-Sedov SNR is initialised as an over-dense disc[3] of density

$$\rho_\mathrm{i} = f_\mathrm{r}^{-3}\, \rho_0 \tag{6.3}$$

and initial radius R_i about the explosion epicentre $(x_\mathrm{c}, y_\mathrm{c})$. Our grid setup is such that all blocks within $R_\mathrm{maxref} = \alpha_\mathrm{maxref}\, R_\mathrm{i}$ of $(x_\mathrm{c}, y_\mathrm{c})$ are maximally refined so that the region in which the SNR is initialised is always described by our maximum resolution, and preliminary tests show that $\alpha_\mathrm{maxref} = 1.2$ is sufficient. Using the reasonable approximation that the supernova blast energy is initially entirely kinetic, we explore two velocity profiles; the first velocity profile assigns a constant speed v_1 to all cells across the supernova initialisation zone, with radial unit vector direction:

$$v_1 \hat{r} = \sqrt{\frac{2\,E_\mathrm{blast}}{M_\mathrm{ej}}}\; \hat{r}. \tag{6.4}$$

More realistically, very young SNR can be modelled as uniformly expanding spheres (*homologous expansion*), whereby the radial velocity of the expanding gas is proportional to the radial distance from the sphere centre. Thus, the second velocity profile allows the gas speed to increase linearly (a trick also used by Jun & Norman (1996)) from zero at the explosion epicentre,

---

[2]An example of such an artifact would be a non-circular or jagged/pixellated features in the evolving SNR, as a result of making the initial supernova blast radius too small.

[3]Note that the total kinetic energy injected into the simulation domain by this method is a factor $\chi = \frac{4}{3}\frac{R_\mathrm{i}}{\delta x}$ less than E_blast, due to the ratio of the volume of a sphere of radius r_i with the volume of the disc of thickness δx used in the simulation domain.

Shortname	Description	Parameter Details
SNR1	Supernova only	SNR defaults and: ρ-profile = 0, v-prof = 0, Cooling=off
SNR2	Supernova only	SNR defaults and: ρ-profile = 0, v-prof = 1, Cooling=off
SNR3	Supernova only	SNR defaults and: ρ-profile = 1, v-prof = 0, Cooling=off
SNR4	Supernova only	SNR defaults and: ρ-profile = 1, v-prof = 1, Cooling=off
SNR5	Supernova only	SNR defaults and: ρ-profile = 0, v-prof = 1, Cooling=on
SNR6	Supernova only	SNR defaults and: ρ-profile = 1, v-prof = 1, Cooling=on
SNR6b	Supernova only	As SNR6 but: $E_{\mathrm{blast}} = 10^{50}$ ergs
SNR6c	Supernova only	As SNR6 but: $n_0 = 0.1\,\mathrm{cm}^{-3}$
SNR6d	Supernova only	As SNR6 but: $M_{\mathrm{ej}} = 10\,\mathrm{M}_\odot$
SNR6e	Supernova only	As SNR6 but: $T_{\mathrm{bg}} = 10^2$ Kelvin

SNR default parameters: $M_{\mathrm{ej}} = 5\,\mathrm{M}_\odot$, $n_0 = 1\,\mathrm{cm}^{-3}$, $E_{\mathrm{blast}} = 10^{51}$ ergs, $T_{\mathrm{bg}} = 10^4$ Kelvin, $Z_{\mathrm{d}} = 40\,\mathrm{pc}$

Table 6.1: Summary of our preliminary simulations testing the SNR parameters. The first six runs test the background profiles and radiative cooling. The last four simulation runs are variations of SNR6, where meaningful astrophysical parameters are tested.

to a maximum value $k_{\mathrm{v}} v_1$ at R_{i}:

$$v_2(r)\,\hat{r} = k_{\mathrm{v}}\,\frac{v_1}{R_{\mathrm{i}}}\,\hat{r} \tag{6.5}$$

where $k_{\mathrm{v}} = \sqrt{10/3}$ is the necessary constant to maintain the total kinetic energy as E_{blast}. Although preliminary tests indicate that these profiles are indistinguishable from one another at large scales (see Figure 6.3a for example), the second velocity profile minimises the asymmetry in the internal shocks and instabilities to which the supernova explosion is susceptible at very early times (see §6.2.2 for more details on this).

We follow each supernova simulation until the radius reaches approximately 44 pc, allowing for some further expansion of the SNR towards R_{45} once the jets are switched on.

6.2 SNR evolution in the Galactic density profile

A series of 10 preliminary supernova tests were performed to investigate the effects of the key physical parameters governing the evolution of the SNR (see Table 6.1). The supernova blast
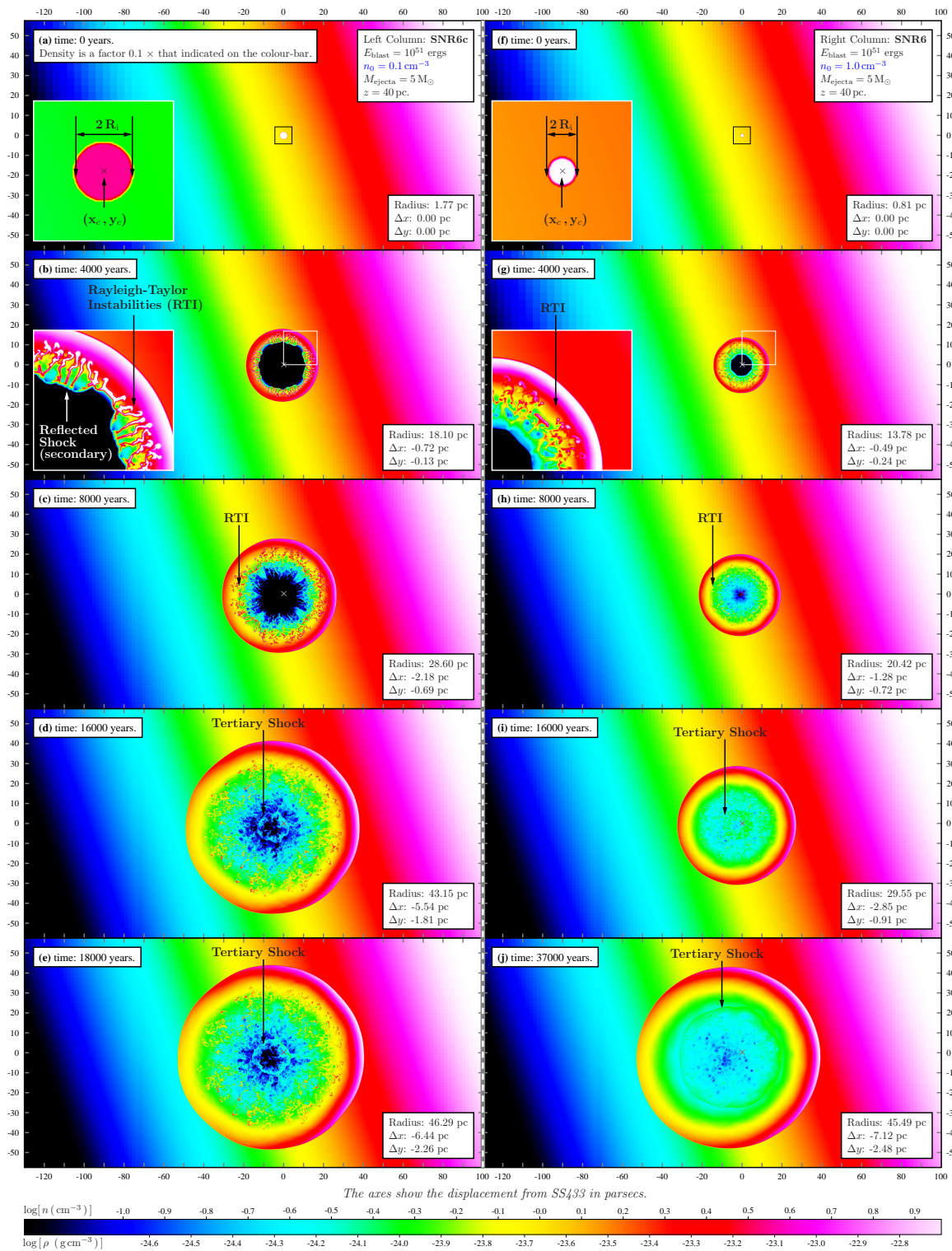
Figure 6.1: The evolution of 10^{51} erg supernova explosions in the presence of the Galaxy density gradient. Supernova simulations *SNR 6* and *SNR 6c* are shown at 4000 year intervals, and the final snapshot when the SNR exceeds 45pc in radius. The × symbols indicate the explosion epicentre, and the displacements Δx and Δy of the SNR from the epicentre (x_c, y_c) are indicated at each snapshot in time. The animations associated with these simulations are available at: *http : //www-astro.physics.ox.ac.uk/~ptg/RESEARCH/research.html*
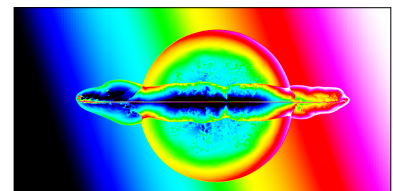
energy E_{blast}, the background density n_0 at SS 433, and the mass ejected by the progenitor M_{ej} were among the parameters tested, as well as the effects of radiative cooling and changing the background density profile from uniform to exponential.

6.2.1   The effects of the background density distribution

Figure 6.1 gives a sample of snapshot images from two of the SNR simulations detailed in Table 6.1, where *SNR 6c* (left column) and *SNR 6* (right column) are shown at 4000 year intervals. The figure illustrates the difference in the SNR evolution when the background density at SS 433 is varied from $n_0 = 0.1\text{cm}^{-3}$ (left column) to $n_0 = 1\text{cm}^{-3}$ (right column). The difference in the initial radii of the supernova blasts from the first image in each column is a consequence of the first density difference by a factor of 10 in equation (6.2). The most obvious difference is in the time taken for the SNR to expand to R_{45}, whereby increasing the density by an order of magnitude causes the duration of expansion to increase by more than a factor of 2. As the supernova shockwave expands into the ISM, the effects of the exponential density gradient become apparent in a number of ways. Firstly, the density of the west side of the SNR (nearest the Galaxy plane) is noticeably higher than the density at the east side in the evolved shell. The ratio of the densities $R_\rho = \rho_{\text{W}}/\rho_{\text{E}}$ on opposite sides of the SNR shell reaches a maximum of $R_\rho \simeq 10$ along the direction normal to the Galactic plane (vector **GD** in Figure 2.2) in the final snapshots in Figure 6.1. As expected, the east-west density ratio has approximately the same value for both *SNR 6* and *SNR 6c*. Secondly, the position of the centre (x_0, y_0) of the SNR quite noticeably shifts as a function of time, with respect to the initial blast epicentre $(x_{\text{c}}, y_{\text{c}})$, moving away from the Galaxy plane, downstream in the density gradient.

6.2.2 Concerning reflective shocks and the velocity profile

Figure 6.1 clearly shows two such examples whereby the expanding supernova ejecta drives a fast shock into the ambient medium, accelerating the ambient medium, compressing it and heating it. When the primary (expanding) blast-wave/shock-front begins to sweep up a mass comparable to the supernova ejecta mass, the shock begins to decelerate noticeably. Material internal to the shock begins to catch up to the shock front and a reverse shockwave then propagate inwards, creating the Rayleigh-Taylor instabilities seen in Figure 6.1(b) and Figure 6.1(g) for example. Minimising these early asymmetries is particularly important because it can have a noticeable effect on the jet propagation. For example, asymmetric shocks can create density variations that are not the same on the east and west sides of the SNR, voiding any meaningful comparison between the east and west jet evolution. The second velocity profile as per equation (6.5) provides a neat trick to ensure that the ensuing SNR is more closely radially symmetric. This happens due to the nature of homologous expansion, whereby it takes longer for the post-shock gas to catch up with the decelerating shock, and so the reflective (secondary) shock occurs later in the SNR evolution, when the SNR is larger (hence more circular). This velocity profile is used for both the example SNR simulation runs shown in Figure 6.1, where the Rayleigh-Taylor instabilities occur symmetrically on diametrically opposing sides of the SNR. These instabilities and shocks are present independent of whether radiative cooling is switched on or off.

To quantify the morphological differences discussed in §6.2.1 and §6.2.2 of the respective SNR produced by the simulations detailed in Table 6.1, a shock-front detection algorithm (see §6.3.2) was applied to each data set.

6.3 Analysing the SNR simulation data

This section briefly describes the code I wrote to detect the shocks and quantify the morphology of the shock, for each of the SNR simulations. The code works iteratively in finding the
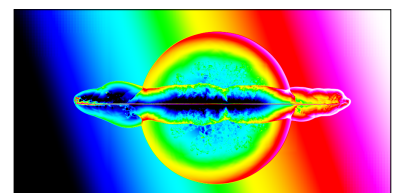
coordinates of the shock-front, and assumes that the ellipticity is small (i.e. $e \lesssim 0.5$, where e is defined in equation (6.11)). The code also requires an approximate guess for the coordinates of the centre of the shell.

6.3.1   Outlining the basic stages

The code begins by working on the pressure maps from the simulation data files, because (unlike the density maps shown in Figure 6.1) the pressure is uniform across the background ISM, even though the background density follows an exponential profile (refer back to §5.11 for an explanation). The pressure map consists of an expanding bubble centered on the reference point (x_0, y_0) which is coincident with the explosion epicentre (x_c, y_c) at $t = 0$, but shifts away from the explosion epicentre at later times as shown in the density maps of Figure 6.1. For clarity here I will use the notation (x_0, y_0, t_n) to represent the centre coordinates of the bubble at time t_n. At $t = 0$ the code sets the reference position to the explosion epicentre: $(x_0, y_0) = (x_c, y_c)$, and the coordinates of the shock front are calculated according to the shock detection algorithm in §6.3.2. A general ellipse is then fit to the shock front coordinates data, such that the origin (x_0, y_0) (shock centre) and ellipticity of the shell are determined as detailed in §6.3.3. The coordinates of the origin determined by the ellipse fitting routine are then used as an input for the next data file in the sequence: $(x_0, y_0, t_n) = (x_0, y_0, t_{n-1})$. This allows for the shifts in the position of the shell-centre to be calculated, provided the shift occurs smoothly with time, which it does.

6.3.2   Detecting the Shock-front

Firstly, the shock front edges on the left, right, top and bottom sides of the SNR are detected as per Figure 6.2, where the outermost maxima in pressure are interpreted as being due to the shock shell. The centre (x_0, y_0) of the SNR (the reference position) is roughly determined from the mid-point of the shock extrema in the $\hat{x}$ and $\hat{y}$ directions, as illustrated by the solid white line in
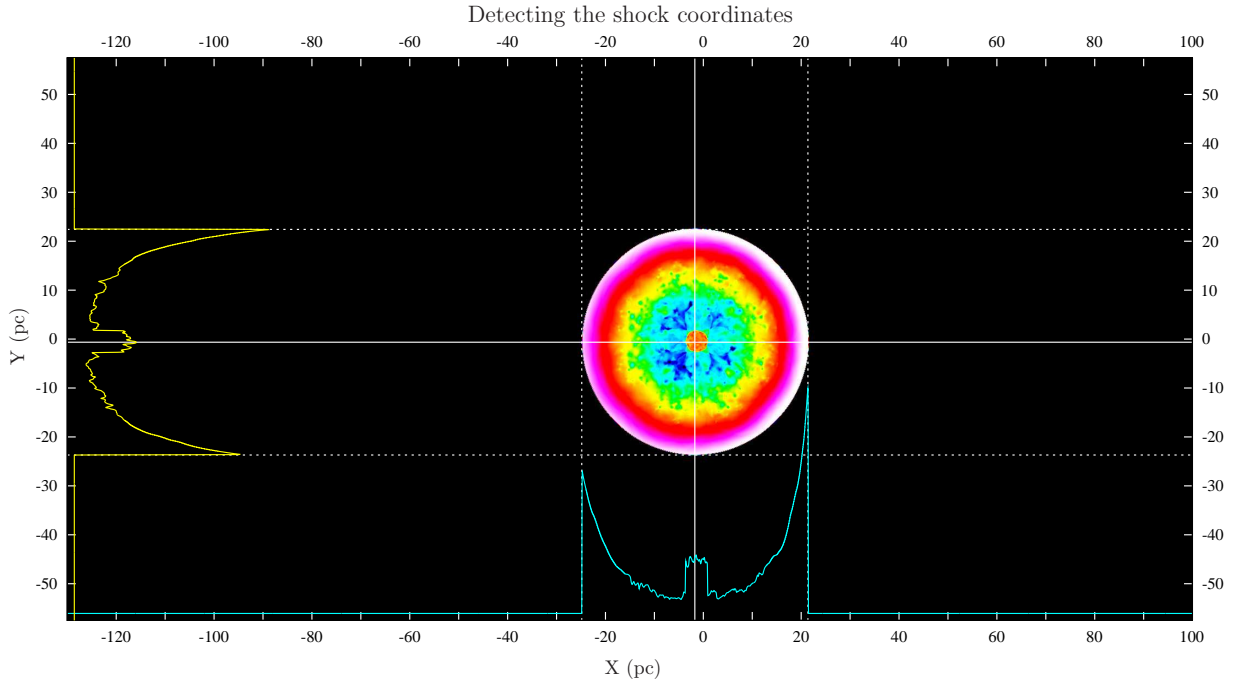
Figure 6.2: The pressure map is shown for simulation *SNR 6* at time 10,000 years. The blue line near the x-axis shows the horizontal line profile of the pressure taken from a row of pixels through y_0. The yellow line near the y-axis shows the vertical line profile of the pressure taken from a column of pixels through x_0. The dotted white lines indicate the location of the maxima in pressure approximately corresponding to the location of the shock-front. The solid white lines indicate the reference position (x_0, y_0) determined by finding the mid-point between the dotted lines. The tertiary shockwave labelled in Figure 6.1d for example, shows up well here in the pressure map.

Figure 6.2. An estimate of the SNR radius $r_s(t)$ is also calculated, by halving the average of the diameters in the $\hat{x}$ and $\hat{y}$ directions. A circular mask $M(r_0)$, where r_0 is the radial distance from the reference point (x_0, y_0), is created to select an annulus of thickness $\pm 10\%$ of $r_s(t)$ about the SNR shell, according to:

$$
M(r_0) =
\begin{cases}
1 & for \quad 0.9\, r_s < r_0 < 1.1\, r_s \\
0 & otherwise.
\end{cases}
\tag{6.6}
$$
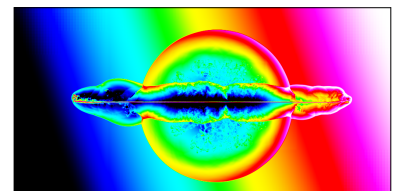
This mask is then applied to the density map for the same simulation time-output, to remove any confusion from the exponential background when it comes to detecting maxima in the density profile. Once the mask has been applied, the code searches for the maxima in density in a similar way to that in Figure 6.2, except by taking radial line profiles from the reference point to the edge of the mask. This allows the coordinates of the shock front to be sampled around the entire circular shell. These coordinates are then served as an input to the ellipse fitting routine of §6.3.3, which uses all points on the surface of the shell to refine the initial guess for the SNR centre reference point (x_0, y_0). After a successful ellipse-fit, the refined centre coordinates and ellipticity coefficients from (6.7) and (6.8) are used as initial guesses for the next round of data (i.e at time t_{n+1}), until all time snapshots of the simulation have been analysed.

6.3.3 Ellipse fitting to the Shock-front data

The coordinates (x_i, y_i) of the points lying on the shock-front were fit to a general ellipse of the parametric form:

$$x_i(\theta_i) = x_0 + a \cos(\phi) \cos(\theta_i) - b \sin(\phi) \sin(\theta_i) \tag{6.7}$$

$$y_i(\theta_i) = y_0 + a \sin(\phi) \cos(\theta_i) + b \cos(\phi) \sin(\theta_i) \tag{6.8}$$

where (x_0, y_0) is the centre, θ_i is the angle each point (x_i, y_i) subtends between the $\hat{x}$ axis and the centre in the anti-clockwise sense, ϕ is the angle between the $\hat{x}$ axis and the semi-major axis, and a and b the semi-major and semi-minor axes respectively. The eccentricity (or ellipticity) as well as the displacements of the SNR shell centre (x_0, y_0) from the explosion epicentre (x_c, y_c) are then easily calculated as:

$$\Delta x = x_c - x_0 \tag{6.9}$$

$$\Delta y = y_{\mathrm{c}} - y_0 \tag{6.10}$$

$$e = \sqrt{1 - \left(\frac{b}{a}\right)^2}. \tag{6.11}$$

6.3.4 Analysis of the Shock-front data

The physical variables (density, pressure, velocities etc) are sampled[4] at the detected shock-front coordinates, and various quantities are plotted as a function of time or SNR radius in Figure 6.3. The figure key included in Figure 6.3 gives an at-a-glance summary simulation parameters for each coloured line plotted, where "E" precedes the log of the blast energy in ergs, "v" precedes the the velocity profile used (see §6.1), "rho" precedes the background density profile used (0=uniform, 1=exponential), and "cool" indicates whether cooling is on (=1) or off (=0). For simulations *SNR 6b−SNR 6e*, parameters are only specified where they differ from those used in simulation *SNR 6*. The unbinned data are shown to allow easier distinction between the coloured lines.

The shift in centre position of the SNR are plotted in Figure 6.3(g) and (h), and it is clear from Figure 6.3(i) that although the SNR becomes slightly elliptical in the presence of an exponential density background, the effect is a minor one ($e \lesssim 0.2$) compared to the shift of the SNR centres. In Figure 6.3(a) the average radius $R = \sqrt{a^2 + b^2}$ of the SNR is plotted as a function of its age, and the dotted lines show the best-fit to a $t^{2/5}$ Sedov-like function of the form $k + \alpha \left(\frac{E}{\rho}\right)^{1/5} t^{2/5}$ where k is some offset in parsec (the fit values are given as an inlay to the plot panel). The shock generated through the supernova explosion is extremely strong as evident from the compression[5]

---

[4]The data maps are sampled at all points around the circular shock front, and the sampled values are averaged to give a single value that is representative of the shock front as a whole. Note that the actual values change as a function of position on the shock front due to the east-west density asymmetry, but the average values are used for the plots for simplicity.

[5]Note that the shock-front densities plotted in Figure 6.3 are actually averaged values from an annulus 1 pixel
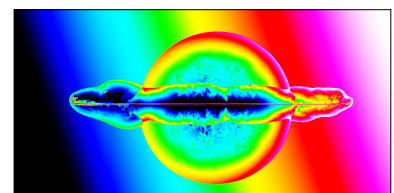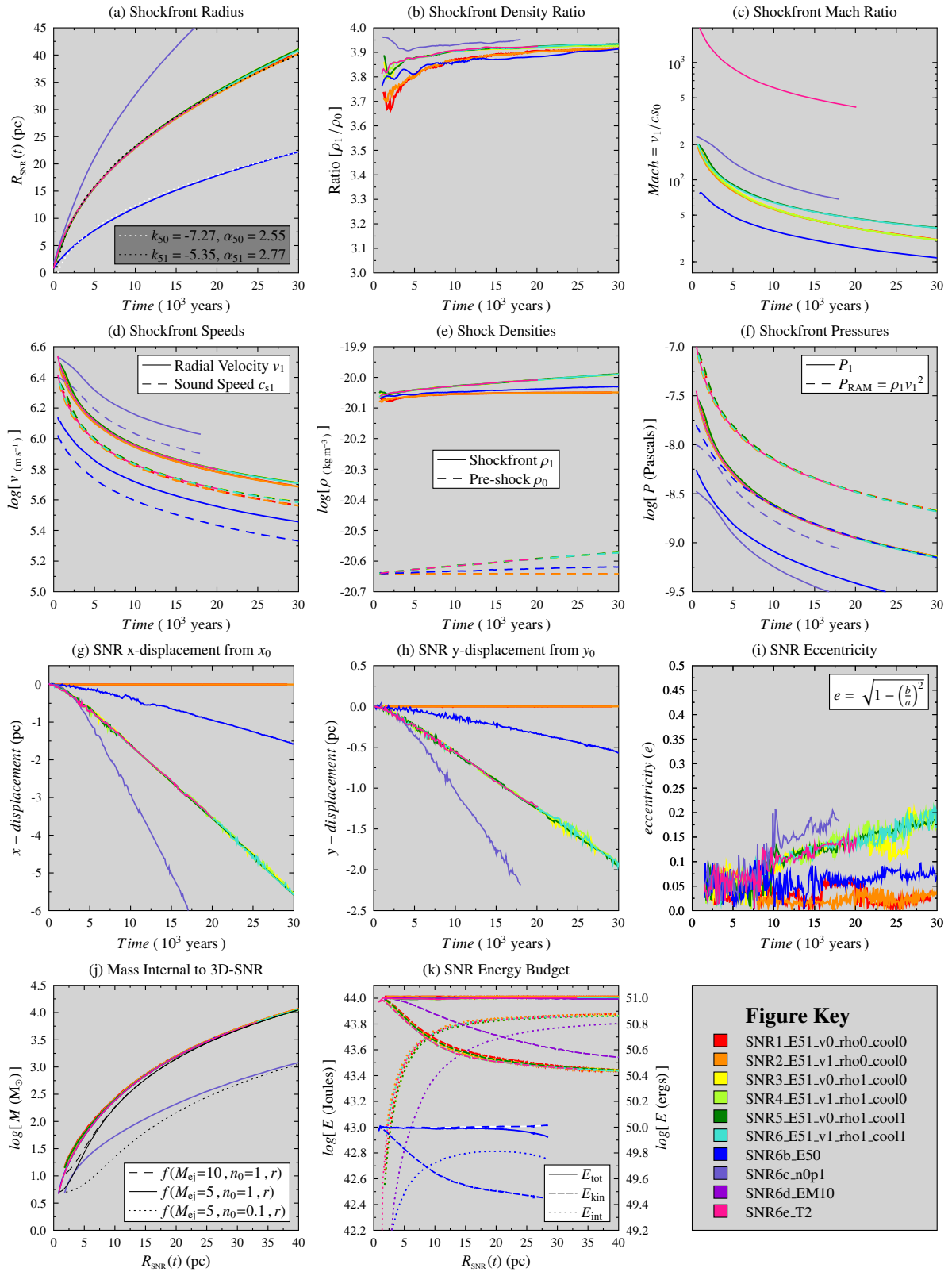
Figure 6.3: A shock-front detection algorithm is used to monitor the size and shape of the SNR, and to sample the density, pressure and velocities of the SNR shell as a function of time. The information given in the figure key is intended as a reminder of the SNR simulation details given Table 6.1.

ratio of $\rho_1/\rho_0 \simeq 4$ across the shock (Fig. 6.3b) as well as the ram pressure being higher than the thermal pressure (Fig. 6.3f), and the shock speed remains hypersonic (Mach$\gg$5) for the duration of the simulations as per Fig. 6.3c and 6.3d. The density ratio of $\rho_1/\rho_0 \simeq 4$ is close to the analytical solution for a strong shock, according to:

$$\frac{\rho_1}{\rho_0} = \frac{\gamma+1}{\gamma-1} = \frac{5/3+1}{5/3-1} = 4.0 \tag{6.12}$$

where $\gamma = 5/3$ is used as the ratio of specific heats for an ideal monatomic gas appropriate to these simulations. The reason for the plotted values in Figure 6.3b being slightly less than 4.0 is a consequence of the way in which the data at the shock-front was sampled, whereby a representative average value for the entire shock introduces an error in the density ratio due to the east-west density gradient. This error is biased towards decreasing the value of the density ratio, because the density on the west side of the SNR increases faster than the density on the east side decreases, thereby the average values of ρ_0 taken by evaluating the background at $r_s + dr$ is slightly higher than would expect. If the slope of the density background was linear, the east-west effect would cancel out, but this is not true for the exponential case.

In Figure 6.3j, the mass contained within a spherical SNR sphere roughly estimated by averaging the density of the SNR disc of radius R in the simulation domain, and scaling up by the volume of a sphere of the same radius. An estimate of the mass expected to be swept up by a spherical SNR in a uniform background of density n_0 is also plotted for comparison, with the functional form

$$f(M_{\text{ej}}, n_0, r) = M_{\text{ej}} + \frac{4\pi\,\mu\,m_{\text{p}}\,n_0}{3}(r^3 - R_{\text{i}}^3), \quad \text{for } r \geq R_{\text{i}} \tag{6.13}$$

such that the initial mass contained within the young SNR of radius R_{i} is equal to the mass

---

thick about the detected location of the shock-front, and that densities on the east and west side of the SNR differ by an order of magnitude when the background follows the exponential density profile.
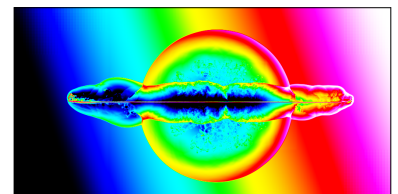
ejected M_{ej} by the progenitor. This is a crude model, as it makes no attempt to account for the exponential background density or the ISM material contained within R_{i}, but it proves to be consistent with the scaled-up mass from the SNR to within a factor of a few or so. The final plot (Figure 6.3k) tracks the total energy of the system, which is again scaled up by a factor $\chi = \frac{4}{3}\frac{R_{\mathrm{i}}}{\delta x}$, representing the ratio of the volume of a sphere of radius R_{i} to the volume of the initial disc of radius the same radius, used to initialise the supernova explosion in the simulation domain (see §6.1 for details about this). The projected energy in a sphere of radius $R_{\mathrm{SNR}}(t)$ as shown in Figure 6.3k is then:

$$E_{tot} = \chi \sum_{i}^{n} \left(\frac{P_{\mathrm{i}}}{(\gamma - 1)} + \frac{\rho_{\mathrm{i}} v_{\mathrm{i}}^2}{2} \right) dV_{\mathrm{i}} \tag{6.14}$$

representing the discrete summation of the internal and kinetic energies per unit volume, for concentric annuli of volume elements dV_{i} from the origin of the SNR to $R_{\mathrm{SNR}}(t)$. The energy radiated via cooling is tracked as a function of time for each dataset, and radiative loss of energy from the system via cooling is negligible[6] for all but one of the SNR simulations. *SNR 6b*, with an order of magnitude lower blast energy than the others, was found to slow down much faster than the other SNRs. This is expected of a remnant passing through the Sedov phase into the radiative phase in which cooling does become important, and the addition of cumulative radiative losses is included in the total energy budget of the system, as indicated by the dashed blue-white line in Figure 6.3k. *SNR 6b* eventually began to disperse and lose its circular SNR identity, at which point the shock-front detection algorithm failed to detect a well-defined shock and for this reason the blue lines in Figure 6.3 are truncated at 28 pc. The other 9 SNR simulations can be thought of as adiabatic to a good approximation, evident through the constancy of the total energy E_{tot} shown by the solid lines in Figure 6.3k. As one might expect, the shock deceleration is less noticeable in the lower density background of *SNR 6c*, and the transfer of kinetic energy into thermal energy is more gradual, as Figure 6.3k shows.

---

[6]Note that the microphysics of emission-line cooling is not yet fully implemented in this version of the code.

6.4   On the displacement of SS 433 from the SNR centre

The shockfront detection algorithm I applied to each of the SNR simulations, allowed me to fit an ellipse to the shockfront and track the movement of its centre away from the blast epicentre, as a function of time (Figure 6.3g and h). The cause of the shifting is not buoyancy, but rather due to the relative ease with which the eastern side of the SNR can propagate in the lower density ISM, compared to the much higher inertial resistance met by the western side of the SNR in the higher density towards the Galactic plane.

Movement of a SNR's centre in the presence of a density gradient is something which was mentioned over three decades ago by Chevalier & Gardner (1974), a paper far ahead of its time. This is an *apparent* effect due to the independent propagation of the east and west shockfronts into different media, and the system does not physically move as a rigid body. However, this does have consequences for any calculations concerning the displacement of SS 433 from the fitted centre of the circular SNR region in W 50. According to *SNR 6* of Figure 6.1b, by the time the SNR expands to 40-45 pc in radius we can expect the centre position to have shifted by $(x_{\mathrm{sh}}, y_{\mathrm{sh}}) \simeq$ (-7.1,-2.5) pc or (-4.4,-1.6) arcmin from explosion epicentre in the $\hat{x}$ and $\hat{y}$ directions of the simulation domain (and the values from *SNR 6c* differ only slightly from those of *SNR 6*). This has implications for calculations that estimate the age of the SNR based upon SS 433's systemic proper motion and its off-centre displacement from the SNR origin. I refer the reader to the detailed account given by Lockman et al. (2007), where the offset of 4 pc is used in conjunction with the proper motion measurements of SS 433 (A. Mioduszewski & M. Rupen, private communication), thus estimating the age of W 50 of order 10^5 years.

I apply a rotation matrix through the clockwise angle θ_α from Figure 2.2 to determine the
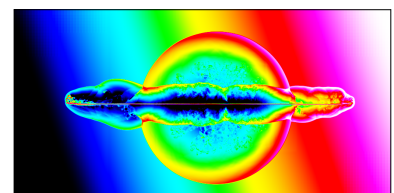
equivalent SNR shifts along the ordinates of right ascension and declination:

$$
\begin{pmatrix} d\alpha \\ d\delta \end{pmatrix} = \begin{pmatrix} \cos\theta_\alpha & \sin\theta_\alpha \\ -\sin\theta_\alpha & \cos\theta_\alpha \end{pmatrix} \begin{pmatrix} x_{\rm sh} \\ y_{\rm sh} \end{pmatrix} = \begin{pmatrix} -4.6 \\ -1.0 \end{pmatrix} \text{arcmin} \qquad (6.15)
$$

Note that these shifts are taken from Figure 6.1b and are appropriate for a galactic scale height of $Z_{\rm d} = 40$ pc. These displacements from SS 433 are likely to be larger in a steeper background density gradient (e.g. $Z_{\rm d} = 30$ pc). Without understanding that the SNR shell hydrodynamically shifts position in the density gradient of the Galaxy, one might mistakenly calculate that SS 433 is moving away from the SNR centre.

Chapter 7

Simulating SS 433's Jets

Care must be taken when modelling the observed (but unresolved) jets emanating from an un-
observed and unresolvable compact object. Furthermore, the mechanism(s) by which the jets
are launched and collimated remain unclear. Despite the persistence of these questions, in this
section we describe the construction of our models that best represent the wealth of observational
data on SS433's jets to-date.

Primarily we consider the geometry of the jet which, during the current epoch, consists of
a conical jet precession picture for SS433. We stress however, that this need not have always
been the case[1], and we must allow for the possible evolution with time of SS433's jets since
the formation of the compact object. We discuss various interesting jet geometries in turn, in
the subsections that follow. The parameters which govern jet behaviour in our models are sum-
marised below (Table 7.1), along with their default values in convenient units, however SI units
are assumed wherever these parameters appear in equation form.

Note that the constraints on $\dot{M}_{\mathrm{jet}}$ and T_{jet} are very rough. As the mass loss in the jets is not
well known, we investigate three orders of magnitude in $\dot{M}_{\mathrm{jet}}$ ranging from a relatively weak jet

---

[1]In fact, it is much more likely that SS433's jets behaved somewhat differently in the past, see chapter 9.
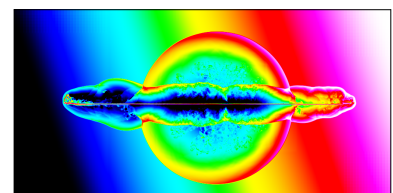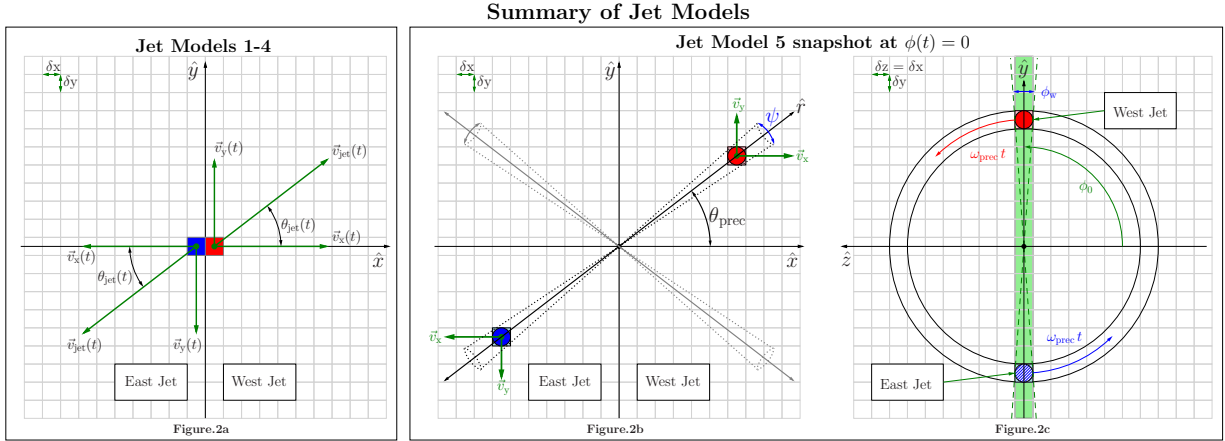
Figure 7.1: A graphical summary of our jet models. For ease of recognition, we use blue and red colours to denote SS 433's east (mostly-blushifted) and west (mostly redshifted) jets respectively, from the point of view of an observer at Earth. However, this is purely to differentiate between the east and west jets in the figure, and we note that our simulated jets spend an equal amount of time in approach and recession in the simulation frame, due to the axis of symmetry. The green section in (c) indicates the simulation slice, in which the precessing jets contribute plasma. The z-axis approximately points towards Earth (note the inclination of the mean jet axis to our line-of-sight θ_{inc}).

Symbol	Description	Constraint
$\dot{M}_{\text{jet}}$	Jet mass loss rate	$\gtrsim 10^{-6} \, \text{M}_\odot \, \text{yr}^{-1}$
v_{jet}	Average jet speed	0.2647 $\mathbf{c}$
θ_{prec}	Jet cone half-angle	20.92°
t_{prec}	Jet precession period	162.375 days
ω_{prec}	Jet angular speed	$3.8695 \times 10^{-2} \, \text{rads s}^{-1}$
T_{jet}	Jet temperature	10^4 Kelvin

Table 7.1: Summarising the jet parameters described in the text.

$10^{-6} \, \text{M}_\odot \, \text{yr.}^{-1}$, an intermediate jet of $10^{-5} \, \text{M}_\odot \, \text{yr}^{-1}$, and a strong jet of $10^{-4} \, \text{M}_\odot \, \text{yr.}^{-1}$. The jet temperature T_{jet} is also not very well known, but the prominent Hydrogen-α emission in the jets suggest the temperature is at least 10^4 Kelvin. An estimate of the jet temperature was given in the comprehensive review (Fabrika, 2004) of SS 433 as 2×10^4 K.

Numerically, we introduce SS 433's jets by including relevant source terms in the Euler hydrodynamic conservation equations. The conservation equations governing SS 433's jets can be

written as:

$$\frac{\partial \rho}{\partial t} + \boldsymbol{\nabla} \cdot (\rho \mathbf{v}) = \dot{\rho}_{jet} \tag{7.1}$$

$$\frac{\partial \rho \mathbf{v}}{\partial t} + \boldsymbol{\nabla} \cdot (\rho \mathbf{v} \otimes \mathbf{v}) = -\boldsymbol{\nabla} P + \dot{\rho}_{\mathrm{jet}}\, \mathbf{v}_{\mathrm{jet}} \tag{7.2}$$

$$\frac{\partial \rho \epsilon}{\partial t} + \boldsymbol{\nabla} \cdot (\rho \epsilon\, \mathbf{v}) = -\boldsymbol{\nabla} \cdot (P \mathbf{v}) - \dot{\epsilon}_{\mathrm{rad}} + \dot{\epsilon}_{\mathrm{jet}} \tag{7.3}$$

where ρ, v, p, and ϵ are the mass density, velocity, thermal pressure and total energy density respectively, and $\dot{\epsilon}_{\mathrm{rad}}$ is the radiated power (per unit volume) due to cooling. A non-relativistic treatment for the jet gas is adopted, i.e. the ISM and jet plasmas are assumed to have the same adiabatic index $\gamma = 5/3$. The density, temperature, and velocities of the jet injection region are reset to $[\,\rho_{\mathrm{jet}}\,,\ T_{\mathrm{jet}}\,,\ v_{\mathrm{x}}\,,\ v_{\mathrm{y}}\,]$ for each time-step ($v_{\mathrm{z}} = 0$ everywhere), and the density ρ_{jet} is model-dependant.

The structure created by each jet in its surrounding environment is primarily determined by the jet velocity components v_{x}, v_{y} and v_{z} which are also model dependant, but their most generalised forms follow the kinematic model[2] of SS 433 such that:

$$\mathbf{v}_x\big(\theta_{\mathrm{jet}}(t), \phi(t)\big) = v_{\mathrm{jet}}\, \cos\big(\theta_{\mathrm{jet}}(t) + C_\theta\big)\, \hat{\mathbf{x}} \tag{7.4}$$

$$\mathbf{v}_y\big(\theta_{\mathrm{jet}}(t), \phi(t)\big) = v_{\mathrm{jet}}\, \sin\big(\theta_{\mathrm{jet}}(t) + C_\theta\big) \sin\phi(t)\, \hat{\mathbf{y}} \tag{7.5}$$

$$\mathbf{v}_z\big(\theta_{\mathrm{jet}}(t), \phi(t)\big) = v_{\mathrm{jet}}\, \sin\big(\theta_{\mathrm{jet}}(t) + C_\theta\big) \sin\phi(t)\, \hat{\mathbf{z}} \tag{7.6}$$

---

[2]Note that here the kinematic model is adapted slightly because SS 433's mean-jet-axis is the x-axis of the simulation domain. This explains the absence of the inclination angle dependence $\cos\theta_{\mathrm{i}}$ and $\sin\theta_{\mathrm{i}}$ in this representation.
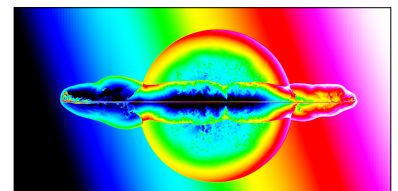
$$\phi(t) = \omega_{\text{prec}} (t - t_0) + \phi_0 \tag{7.7}$$

$$C_\theta = \begin{cases} 0 & for\ the\ Western\ jet \\ \\ \pi & for\ the\ Eastern\ jet \end{cases} \tag{7.8}$$

where $\phi(t)$ is the precession phase angle at time t, and t_0 is the time when the jets began. Throughout this paper we use the definition whereby precessional phase zero occurs when the red-most (western) jet is maximally[3] red-shifted (or equally the blue-most jet is maximally blue-shifted). SS 433 precesses[4] in a clockwise fashion when looking along the direction of the western jet from the viewpoint of SS 433. Consequently, if the phase angle starts from zero at $t = t_0$ then the offset $\phi_0 = \frac{-\pi}{2}$ ensures that $\phi(t) = \frac{n\pi}{2}$ when the jets are in the xz-plane (maximum Doppler shifts), and $\phi(t) = n\pi$ when the jets are in the xy-plane (the plane of the simulation-sky), where $\{n \in \mathbb{Z}^*\}$ is the revolution number.

To allow for the possibility that the precessional motion in SS 433 has changed during its lifetime as an X-ray binary, either smoothly or as a discontinuous process (c.f. episodic jet outbursts in Cyg X-3 mentioned in §2.5.3), we introduce into our models some simple time-dependence in the precession cone angle:

$$\theta_{\text{jet}}(t) = \theta_0 + (t - t_0)\,\dot{\theta} \tag{7.9}$$

which can be made constant by setting $\dot{\theta}=0$.

The jet density depends on the jet mass loss rate $\dot{M}_{\text{jet}}$ and some model-dependant geometry,

---

[3] Due to the axis of symmetry used in the simulations, the maximum redshifts are equal for the east and west jets.
[4] The right hand grip rule is useful here: gripping the x-axis with the right hand, with the thumb in the $+\hat{x}$ direction, the curled fingers indicate the precession direction.

and the internal pressure is calculated from the density:

$$\rho_{\rm jet} = \alpha_{\rm geom} \, \dot{M}_{\rm jet} \tag{7.10}$$

$$P_{\rm jet} = \frac{\rho_{\rm jet} \, k_{\rm B} \, T_{\rm jet}}{\mu \, m_p} \tag{7.11}$$

where $\alpha_{\rm geom}$ has units of $time/volume$. The total power per unit volume for the jets has kinetic and thermal components:

$$\dot{\epsilon}_{\rm jet} = \frac{\dot{P}_{\rm jet}}{(\gamma - 1)} + \frac{1}{2} \, \dot{\rho}_{\rm jet} \, v_{\rm jet}^2 \;=\; \dot{\rho}_{\rm jet} \, \Big(\frac{k_{\rm B} \, T_{\rm jet}}{\mu \, m_p \, (\gamma - 1)} + \frac{v_{\rm jet}^2}{2} \Big). \tag{7.12}$$

For reasons relating to numerical limitations in resolution, we explore 5 different jet initialisation models, and later discuss the relative successes of each. Models 1 to 4 are based upon the jet motion described in equations (7.4) through (7.9) and depicted in Figure 9.1a, whereas model 5 attempts to mimic SS 433's discrete ballistic jet ejecta, as depicted in Figure 9.1b.

7.1   Jet Model 1 - Static Cylindrical Jet

Our most basic jet model consists of a static (non-precessing) cylindrical jet along the x-axis. This is a special case of the general equations (8) through (12), created by setting $[\theta_0 = 0]$, $[\dot{\theta} = 0]$, and $[\phi(t) = 0]$, such that the velocity components are reduced to $\mathbf{v_x} = v_{\rm jet} \cos C_\theta \, \hat{x}$ and $\mathbf{v_y} = \mathbf{v_z} = 0$.

The density of the jet is simply a product of three factors: the mass loss rate $\dot{M}_{\rm jet}$ in the jets, the (resolution-dependant) pixel crossing time $t_\times = \frac{\delta x}{v_{\rm jet}}$, and the model-dependant jet volume $(\Delta x_{\rm jet} \, \Delta y_{\rm jet} \, \Delta z_{\rm jet} \, \delta x^3)$. This issue can be simplified by choosing the initial jet size (as in Figure 9.1a) to be 1 cubic pixel $(\Delta x_{\rm jet} = \Delta y_{\rm jet} = \Delta z_{\rm jet} = 1)$, which makes the most physical sense,
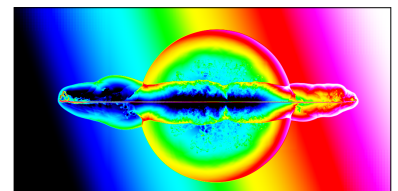
since the jet structure revealed by VLBI imaging (and indeed, the $3R_{\text{Schwarzschild}}$) is very much smaller than the pixel size. Thus, the density in this model is given according to equation (7.10) with:

$$\alpha_{\text{geom}} = \frac{1}{2\, v_{\text{jet}}\, \delta x^2} \tag{7.13}$$

where the above summed over both jets will give the required mass loss rate per unit length (one pixel) in $\hat{x}$.

This model was run for each of the three M_{jet} values, both with and without the presence of an evolved SNR. The simulation runs for this model are also used to quantify the east-west jet asymmetry in W 50 (as discussed in §7.7), by constraining the Galaxy scale-height Z_{d} in equation (5.21) appropriate at the location of SS 433 in our Galaxy.

7.2   Jet Model 2 - Conical Phase-shifting Jet: $(\dot{\theta}_{\text{jet}} = 0)$

This model invokes a time-averaged representation of SS 433's precessing conical jet, termed *phase-shifting*. As with model 1, the east and west jets are each just 1 cubic pixel in size. This model uses present-day observed parameters describing SS 433's precession at the current epoch, and assumes the jets have not changed throughout their history.

The computational time-step is adjusted so that precession phase-space is sampled n_{s} times per precession period:

$$\Delta t_{\text{step}} = \frac{t_{\text{prec}}}{n_{\text{s}}} \tag{7.14}$$

$$\Delta\phi_{\text{step}} = \frac{2\pi}{n_{\text{s}}} \tag{7.15}$$

If we define a phase-tolerance as $\phi_{\text{tol}} = \frac{\Delta\phi_{\text{step}}}{2}$, then the precessing jet contributes[5] to the simulation domain when the phase $\phi(t)$ falls within $\pm\phi_{\text{tol}}$ of 0 (for the upper-half-plane) or π (for the

---

[5]The jet pixels are set according to the jet values $(\rho_{\text{jet}}, T_{\text{jet}}, \mathbf{v_{jet}})$ rather than the background ISM values.

lower-half-plane). When this happens, the phase $\phi(t)$ is rounded to the nearest of either of $(0, \pi)$, and this is equivalent to introducing an error of $\pm(50/n_{\mathrm{s}})$ percent to the precession period (hence the term *phase-shifting*).

The velocities are initialised by setting $[\theta_0 = \theta_{\mathrm{prec}}]$, $[\dot{\theta} = 0]$ and $[\phi(t) = \omega_{\mathrm{prec}}t]$ in equations (8) through (12), where $[\omega_{\mathrm{prec}} = \frac{2\pi}{t_{\mathrm{prec}}}]$. Assuming that the amount of mass outflowing in the jets in one precession period can be written as $\dot{M}_{\mathrm{jet}}\,t_{\mathrm{prec}}$, the density is set according to equation (7.10) with:

$$\alpha_{\mathrm{geom}} = \frac{t_{\mathrm{prec}}}{2\,n_{\mathrm{s}}\,\delta x^3} \tag{7.16}$$

We choose $n_{\mathrm{s}} = 20$ as a compromise value to prevent impractical inflation of the computational time, whilst limiting the error in precessional period to just $\pm 2.5\%$.

7.3   Jet Model 3 - Conical Phase-shifting Jet: $(\dot{\theta}_{\mathrm{jet}} > 0)$

This model is similar to Jet Model 2 in that it follows the same precession *phase-shifting* model, but with the exception that the precession cone angle is allowed to increase linearly with time. The basis for this model comes from the discrepancy between the opening angle of the jet precession cone θ_{prec} currently observed in SS 433, and the angle subtended by the lobes of W 50 with the central source SS 433. The green lines in Figure 2.3b and Figure 4.7 represent the current jet precession angle projected out to the extent of W 50. Had SS 433's jets penetrated the lobes of W 50 at this angle, we would expect quite a different morphology to result. To investigate the effects of a smoothly evolving jet using equation (7.9), the initial half-cone angle is set to $\theta_0 = 0$ and the derivative becomes

$$\dot{\theta} = \frac{\theta_{\mathrm{prec}} - \theta_0}{t_{\mathrm{jets}}} \tag{7.17}$$

such that the cone half-angle increases linearly to the currently observed value, where t_{jets} is the time taken for the jets to reach the extent of the lobes in W 50. The jet density is as described in
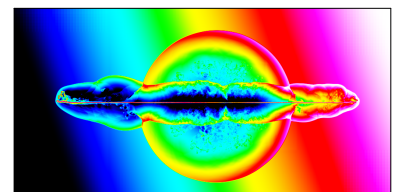
model 2.

7.4   Jet Model 4 - Conical Phase-shifting Episodic Jet

In this model we investigate the possibility that SS 433's jet activity is discontinuous. This is inspired by the microquasar Cyg X-3, which exhibits episodic jet outbursts, each with quite different jet speeds and precession cone angles. To emulate this behaviour, we use the same *phase-shifting* model and jet density as described in jet model 2. The outbursts are created by using $\dot{\theta} = 0$ in equation (12) and setting θ_0 according to:

$$\theta_0 = \begin{cases} \theta_1 & for \quad t_1 < t < t_2 \\ \\ \theta_2 & for \quad t_3 < t < t_4 \\ \\ \theta_3 & for \quad t_5 < t < t_6. \end{cases} \tag{7.18}$$

7.5   Jet Model 5 - Fireball Jet Model

The fireball model was inspired by the spectacular animation[6] showing the discrete "blob" nature of SS 433's jets from the work of Mioduszewski et al. (2003). The optical spectroscopy observations of Blundell et al. (2007) estimate the expansion speed u_e of the jet fireballs in the innermost regions of SS 433 as approximately $u_e \simeq 1\%$ of the jet speed. Using this estimate of the fireball expansion rate and assuming the initial fireball size upon ejection is negligible compared to our resolution, we approximate the initial jet collimation angle as $\psi \simeq \frac{u_e}{v_{jet}} \simeq 0.01$ radians, and calculate the distance from the origin at which we can reasonably resolve the discrete ejecta. For approximately spherical fireballs of radius R_{fb} then $[\, 2\, R_{fb} = r_{fb}\, \psi = \delta x\,]$ gives the appropriate fireball displacement r_{fb} along its trajectory $\hat{r}$. Hence we can write the coordinates of the fireball

---

[6]See for example: $http://www.nrao.edu/pr/2004/ss433/ss433.movie.gif$

pixel in each quadrant as:

$$x_{\text{fb}} = x_0 \pm \frac{\delta x \, \cos \theta_{\text{prec}}}{\psi} = x_0 \pm 93.4 \, \delta x \tag{7.19}$$

$$y_{\text{fb}} = y_0 \pm \frac{\delta x \, \sin \theta_{\text{prec}}}{\psi} = y_0 \pm 35.7 \, \delta x \tag{7.20}$$

and there are 4 such fireball pixels; one in each quadrant of the xy-plane as indicated in Figure 9.1b.

In three dimensions the jet sweeps out part of a corkscrew structure in space over one precession period, however our domain is effectively a slice one pixel (δx) thick in the $\hat{z}$ direction. It is useful to define the quantity f_{fb} which is the angle subtended by one fireball pixel about the x-axis, as a fraction of one whole precessional period (2π radians):

$$f_{\text{fb}} = \frac{\delta x}{2\pi r_{\text{fb}}} = \frac{\psi}{2\pi \sin \theta_{\text{prec}}} \tag{7.21}$$

where δx is the pixel size and effective width of the simulation slice in $\hat{z}$. We now introduce a user-defined constant κ_{fb} (equal to 1 by default), which allows the user to establish a compromise between computation time and resolution of the fireballs. The precessing jet only contributes plasma when it sweeps through the simulation domain slice. In phase-space this spans half of the phase-width $\phi_{\text{w}} = 2\pi \, \kappa_{\text{fb}} \, f_{\text{fb}}$ each side of the xy-plane, or $[0 \pm \pi \kappa_{\text{fb}} f_{\text{fb}}]$ for the fireballs in the northern (upper-half) plane, and $[\pi \pm \pi \kappa_{\text{fb}} f_{\text{fb}}]$ for the southern (lower-half) plane. This phase range is specified by the criterion:

$$\cos^2 \phi(t) > \cos^2 \phi_{\text{w}} \tag{7.22}$$

The computational time-step Δt_{step} must be reduced for this model, to ensure that the jet
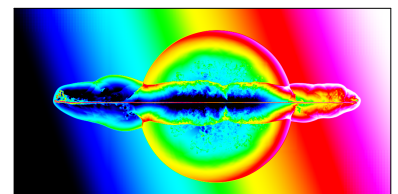
phase $\phi(t)$ evaluated at t_n and $t_\mathrm{n} + \Delta t_\mathrm{step}$ does not cause the jet to skip the xy-plane altogether. The precession crossing time Δt_cross as the jet sweeps through the simulation slice is equal to $\kappa_\mathrm{fb}\, f_\mathrm{fb}\, t_\mathrm{prec}$. To ensure adequate sampling of the precession period, the computational time-step in this model needs to be equal to or smaller than the precession crossing time:

$$\Delta t_\mathrm{step} \lesssim \Delta t_\mathrm{cross} = \frac{\kappa_\mathrm{fb}\, \psi\, t_\mathrm{prec}}{2\pi \sin\theta_\mathrm{prec}} \approx 0.72 \text{ days} \qquad (7.23)$$

which (with $\kappa_\mathrm{fb} = 1$) is typically a few orders of magnitude smaller than other dynamical timescales on the simulation grid. The jet plasma density is given according to equation (7.10) with:

$$\alpha_\mathrm{geom} = \frac{\kappa_\mathrm{fb}\, f_\mathrm{fb}\, t_\mathrm{prec}}{2\, \delta x^3}. \qquad (7.24)$$

The jet plasma is initialised for the fireball pixels according to:

$$\left(\rho\,, T\,, \mathbf{v}\right) = \begin{cases} \left(\rho_\mathrm{jet}\,, T_\mathrm{jet}\,, \mathbf{v}_\mathrm{jet}\right) & \text{for} \quad \cos^2\phi(t) > \cos^2\phi_\mathrm{w} \\[3mm] \left(\rho_\mathrm{ISM}\,, T_\mathrm{ISM}\,, 0\right) & \text{otherwise.} \end{cases} \qquad (7.25)$$

If the criterion of equation (20) is met (thus signifying a jet intersection with the xy-plane), the precessional phase must be very close to either of $[0, \pi]$ and we round $\phi(t)$ to the nearest of these. This ensures that tiny residual v_z values are set to zero when the fireball velocities are initialised:

$$\begin{pmatrix} v_\mathrm{x} \\[3mm] v_\mathrm{y}\big(\phi(t)\big) \\[3mm] v_\mathrm{z} \end{pmatrix} = \begin{pmatrix} \cos(\theta_\mathrm{prec} + C_\theta) \\[3mm] \sin(\theta_\mathrm{prec} + C_\theta) \cos\phi(t) \\[3mm] \sin(\theta_\mathrm{prec} + C_\theta) \sin\phi(t) \end{pmatrix} v_\mathrm{jet} \qquad (7.26)$$

where C_θ has the usual meaning of zero for the west jet ($x > 0$) and π for the east jet ($x < 0$).

Shortname	Description	Parameter Details		
Jet1	Jets only (Model 1)	Jet defaults and: $\theta_0 = 0°$, $\dot{\theta} = 0°\,\mathrm{yr}^{-1}$		
Jet2	Jets only (Model 1)	As Jet1 but: $\dot{M}_{\mathrm{jet}} = 10^{-5}\,\mathrm{M_\odot\,yr^{-1}}$		
Jet3	Jets only (Model 1)	As Jet1 but: $\dot{M}_{\mathrm{jet}} = 10^{-6}\,\mathrm{M_\odot\,yr^{-1}}$		
Jet4	Jets only (Model 1)	As Jet1 but: $n_0 = 0.1\,\mathrm{cm}^{-3}$		
Jet5	Jets only (Model 2)	As Jet1 but: $\theta_0 = 10°$		
Jet6	Jets only (Model 2)	As Jet1 but: $\theta_0 = 20°$		
Jet7	Jets only (Model 2)	As Jet1 but: $\theta_0 = 40°$		
Jet8	Jets only (Model 3)	As Jet1 but: $\dot{\theta} = \frac{20°}{1000\,yr}$		
Jet9	Jets only (Model 4)	Jet defaults but $n_0 = 0.1\,\mathrm{cm}^{-3}$ and:	$\theta_1 = 40°$ for $0 < t < 1000$ yrs $\theta_2 = 0°$ for $1000 < t < 2600$ yrs $\theta_3 = \theta_{\mathrm{prec}}$ for $2600 < t < 2700$ yrs	
Jet10	Jets only (Model 5)	Jet defaults but $n_0 = 0.1\,\mathrm{cm}^{-3}$ and $\kappa_{\mathrm{fb}} = 10$		
	Jet default parameters: $\dot{M}_{\mathrm{jet}} = 10^{-4}\,\mathrm{M_\odot\,yr^{-1}}$, $n_0 = 1\,\mathrm{cm}^{-3}$, $Z_{\mathrm{d}} = 40\,\mathrm{pc}$			

Table 7.2: Summary of our preliminary simulations testing the jet parameters. Simulation Jet1 is used as the control group to which Jet2-Jet8 are compared. Jet9 investigates the effects of an episodic (rather than continuous) jet, and Jet10 demonstrates the fireball model described in the text. The Galaxy scale height parameter Z_{d} is tested in another series of simulations, as detailed in §7.7.

7.6   Jet evolution in the Galactic density profile

A series of 10 simulations were performed to investigate the effects of the jet kinematics, such as the jet precession cone angle and jet power (influenced through M_{jet}), and the details of the simulations are given in Table 7.2. Each jet simulation was allowed to continue running until it became obvious that a particular jet model was unlikely to produce the required morphology observed in W 50. An image showing the density map for each simulation in its final stage is shown in Figure 7.2, and a contour map of the Dubner et al. (1998) observation of W 50 has been overlaid upon each density map for comparison. The magnitude of the jet velocity is kept constant at $v_{\mathrm{jet}} = 0.2647c$ for each jet simulation. The inlay image for each panel in Figure 7.2 shows a zoomed-in section of the central region where the jet is initiated, and aims to give the reader an idea of the collimation and opening angle of the jet near to the site of jet-launch before significant interaction with the surroundings have occurred.
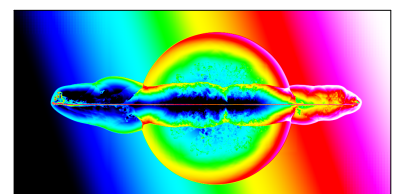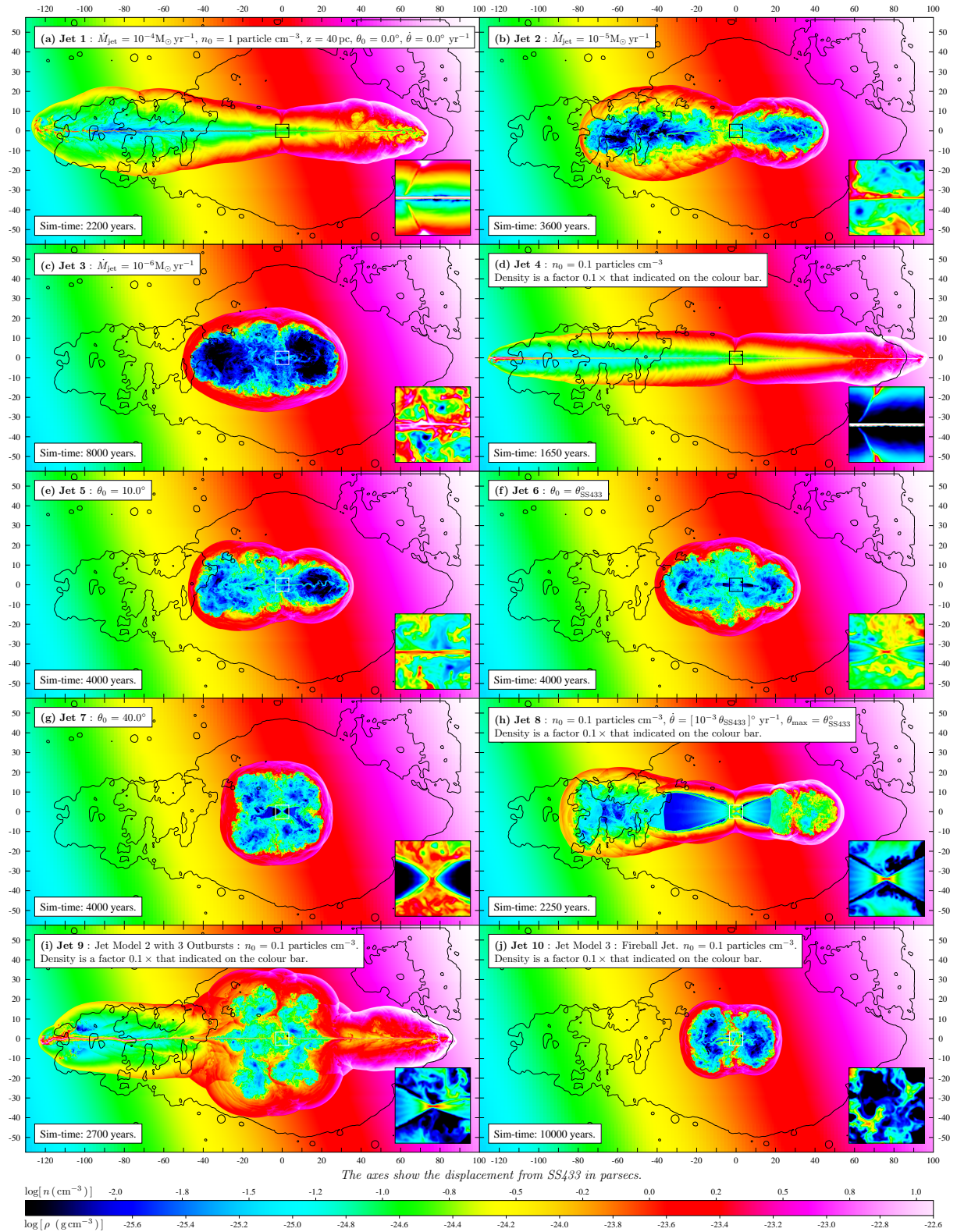
Figure 7.2: Final density snapshots are shown of a series of jet simulations demonstrating the effects of relevant jet parameters upon the morphology of the jet cocoon. Refer to Table 7.2 for a summary of the differences between these simulations, and §7.6 for a detailed commentary on the interpretation of each one. The animations associated with these simulations are available at: $http://www-astro.physics.ox.ac.uk/\sim ptg/RESEARCH/research.html$.
Note: full-size images of the above panels are available in the appendices.

Figure 7.2a shows *Jet 1* which invokes Jet Model 1, consists of a simple static cylindrical jet along the $\hat{x}$ axis, with a mass loss rate of $\dot{M}_{\mathrm{jet}} = 10^{-4}\,\mathrm{M}_\odot\,\mathrm{yr}^{-1}$ in an exponential Galactic density gradient of scale-height $Z_{\mathrm{d}} = 40\,\mathrm{pc}$ and normalised to $n_0 = 0.1\,\mathrm{cm}^{-3}$ at SS 433's location on the grid. Although the east-west extent of the lobes from *Jet 1* approximately matches that of W 50, the eastern jet lobe has reached a displacement of $\sim$125 pc from SS 433 which is in excess of W 50's eastern lobe extent, whilst the simulated western jet lobe is short of W 50's western lobe, as clearly indicated by the contour line. This could indicate that the galaxy scale-height used was too small, and this is investigated in §7.7. As the jets plough through the ISM, they carve out a cavity of lower density which enables the easier propagation of the proceeding jet material. Referring to the colour scale used in Figure 7.2a, a contrast of two orders of magnitude in density is achieved in some places, between the lower density ISM directly surrounding the eastern jet (blue) and the denser gas of the cavity walls (red) indicating the jet shock front. We can define an average lobe speed as the ratio of the average extent of the lobes to the time taken for the jet shock front to reach such an extent:

$$v_{\mathrm{lobes}} = \frac{d_{\mathrm{lobes}}}{2\,\Delta t} \tag{7.27}$$

where $v_{\mathrm{lobes}} = 0.148c$ for *Jet 1*, based on 200 pc as the east-west lobe extent and 2200 yrs of simulation time. Note however, that since the jet is "on" for the duration for this simulation, that the kinetic energy of the jets is continually replenished, and the preceding jet activity has already evacuated a cavity in the ISM. This results in the speed of the jet itself remaining very close to v_{jet} until very near to the bow shock at the ends of the jet lobes (see velocity maps of Figure 8.1). Upon reaching the ends of the lobes, the jet ejecta decelerates rapidly as momentum and kinetic energy are dissipated into the denser ambient ISM, to drive the shock forward. As the jet shock-front propagates, it imparts momentum into the transverse ($\hat{y}$) direction, such that the wake of the jet has a well-defined width at a given distance from the jet launch point. The result is that
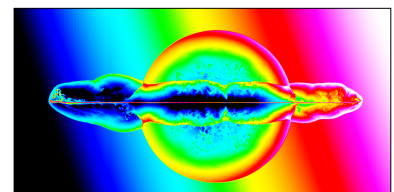
even a cylindrical jet (zero cone angle) has a substantial width as evident in Figure 7.2a, where clearly the western jet lobe is as wide as (and in some parts, wider than) W 50's western lobe. The width of the jet lobe at a given distance from SS 433 could prove to be a useful diagnostic in constraining the nature of the jet which sculpted W 50's lobes (see Figure 8.3 in chapter 8).

Jet 2 of Figure 7.2b is identical to *Jet 1* but for the mass-loss rate which is an order of magnitude lower at $\dot{M}_{\mathrm{jet}} = 10^{-5}\,\mathrm{M}_\odot\,\mathrm{yr}^{-1}$. The level of jet collimation shown in figure *Jet 1* is not true for *Jet 2*, and although the jet mass loss rate is still relatively high it is clear that, if allowed to expand to double the size shown in Figure 7.2b, the peanut-like lobes created by *Jet 2* would be much too wide to produce the lobes of W 50. In this case the jets have significantly decelerated before moving far from the jet launch point, and the jet loses its well defined shape, bending and buckling and thereby transferring relatively more momentum in the transverse direction than does *Jet 1*. The averaged lobe speed for *Jet 2* is $v_{\mathrm{lobes}} = 0.058c$. As one might expect, the deceleration and lack of collimation are both even more obvious in *Jet 3* of Figure 7.2c, where the jet mass-loss rate has been reduced by a further order of magnitude to $\dot{M}_{\mathrm{jet}} = 10^{-6}\,\mathrm{M}_\odot\,\mathrm{yr}^{-1}$, resulting in an elliptical bubble with average speed $v_{\mathrm{lobes}} = 0.017c$.

Jet 4 of Figure 7.2d has the same jet mass loss rate as *Jet 1*, but in this case the density normalisation is lower by an order of magnitude: $n_0 = 0.1\,\mathrm{cm}^{-3}$. The relative ease with which this jet propagates through the ISM is apparent both through the level of collimation of the jets and also the jet lobe extents exceed those of W 50 on each side. As one might expect, the jets require only a relatively short time (less than 1650 years) to propagate to the full extent of W 50's lobes ($v_{\mathrm{lobes}} = 0.219c$), as the background density is lowered and we tend towards the *in vacuo* limit described in §2.5.2. The transverse momentum component is reduced relative to the axial component, and jet travel time is short enough that the wake of the jet is thinner than the lobes of W 50. There is a satisfying relationship between the thickness of the jet wake (the level of collimation of the jet lobes) and the ratio $\dot{M}_{\mathrm{jet}}/n_0$. The effect upon the jet lobes morphology of *reducing* n_0 by a factor of 10 is equivalent to *increasing* $\dot{M}_{\mathrm{jet}}$ by the same factor. For example,

repeating *Jet 4* with $\dot{M}_{\mathrm{jet}}$ reduced by a factor of 10, reproduces the same jet morphology as *Jet 1*, and running *Jet 1* with an order of magnitude decrease in the background density, reproduces the same jet morphology of *Jet 4*. This relationship is investigated further in §7.7.

Jet 5 of Figure 7.2e utilises Jet Model 2, and has similar parameters to *Jet 1* with the addition of time-averaged precession of the jet with half-cone angle 10°, approximately half the jet cone angle θ_{prec} of SS 433 current precession state. Even with this relatively small half-cone angle it is easy to see that the evolved lobes would be much wider than W 50's lobes, but despite the peanut shaped morphology this jet still produces two distinguishable lobes. Interestingly *Jet 6* of Figure 7.2f features a rounded central region between two stubby lobes, when the jet half cone angle is set to θ_{prec}. When the precession half-cone angle is increased to 40° with *Jet 7* of Figure 7.2g, the lobe structure is lost and the jet cavity more closely resembles a circular blown bubble. Each of the simulations with non-zero precession cone angles display evidence of hydrodynamic refocusing of the jets towards the mean jet axis (for more details see §7.8).

To investigate the possibility that SS 433's precession developed gradually over time, *Jet 8* of Figure 7.2h features a linearly growing jet with half-cone angle starting from zero, and reaching θ_{prec} after 1000 years. It was thought that this jet in early stages (with a small precession cone angle) could produce the desired elongated lobes of W 50, and then at later times when the precession cone angle is larger, the jet would assist in inflating the circular SNR-like region. Interestingly, the result is quite different because the jet interacts with itself. As before, the jet ploughs through the ISM and carves out a cavity of low density, providing much lower resistance for the jet that follows at later times. However, the dense shock-front of ISM gas swept-up by the early jet, also acts to confine the later jet. Rather than penetrating the cavity walls, the jets interact with the shell at a grazing angle, and are "guided" back towards a path of lower resistance. More details of this effect follow in §7.8.

Jet 9 of Figure 7.2i is an attempt to reproduce W 50 by assuming episodic outbursts for SS 433's jet activity, with varying parameters for each outburst. This simulation begins with
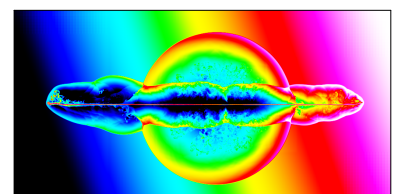
an 1000-year long jet outburst with a large precession cone angle of 40°, before a further 1600-year long outburst of a cylindrical jet similar to that of *Jet 4*. The third and final jet outburst lasts 100 years and is a conical jet model with the precession cone angle θ_{prec} appropriate to that of SS 433's current precession state. Although these outburst parameters are somewhat contrived in the sense that they are not based on any observations, the purpose of this simulation was really to show that it may be possible to produce a W 50 like nebula with jets alone. The simulated nebula in *Jet 9* does fairly well at mimicking W 50, but further evidence would be required in order to constrain the possible jet parameters in each outburst, in order for this simulation to move from mere speculation towards a feasible mechanism for the formation of W 50. Note that the background density normalisation for this jet simulation is $n_0 = 0.1$ particle cm^{-3} rather than the default $n_0 = 1$.

Jet 10 of Figure 7.2k adopts the fireball model described in §7.5, whereby the jet precession cone angle is θ_{prec}. The fireball model achieves a similar end result to that of a hollow conical jet of the same precession cone angle, however the jet is much weaker due to the comparatively small time for which the jet contributes to the simulation domain. This is a consequence of the way the model is coded (see §7.5), and I predict that this model might be more successful with a complete 3D description. The conclusion to draw from simulation *Jet 10* however, is that it seems clear that the fireball jet model is not capable of independently producing the W 50 nebula, nor even simply the lobes of W 50. This gives further strength to the argument that SS 433's current jet state is a relatively recent one in terms of SS 433's active age/history, a lower limit for which comes from the jet propagation time of 1650-2200 yrs for *Jet 4* and *Jet 1* to produce W 50's lobes of the required size.

7.7   Jet lobe propagation: Constraining SS 433's environment.

The unique east-west asymmetry in W 50's jet lobes, if due to the Galaxy density gradient, provides us with a unique opportunity to do two things: (i) to investigate hydrodynamically the large-scale effects of jet propagation in a non-uniform background density environment, for comparison with observations, and (ii) to constrain the parameters of the Galactic density profile appropriate to the location of SS 433. The purpose of this section is to constrain the parameters n_0 and Z_d by comparing the jet lobe extents from the simulations to those observed in W 50. These two parameters have the following effects:

1. **Density normalisation** n_0 - this defines the relative ease/difficulty with which the jets propagate through the ISM. Increasing n_0 causes greater deceleration of the jets, because both the east and west jets experience greater resistance from the ISM through which they propagate. The momentum lost from the jets during deceleration is transferred to the ISM, a large portion of the momentum transfer being in the direction perpendicular to the mean jet axis. As a result, the jets become lesser collimated, and in extreme cases the jets create a peanut-like cocoon shape, rather than well defined lobes.

2. **Galaxy disc density scale-height** Z_d - this scale height determines how fast the density decreases with distance from the Galaxy plane, such that moving further away from the Galaxy plane by Z_d parsec causes the density to change by a factor e^{-1}, as described in (5.21). Decreasing Z_d therefore increases the density gradient, and the density ratio between the east and west sides of SS 433. Increasing the density gradient means that SS 433's west jet decelerates rapidly due to the sharp increase in density on the west side of SS 433, in contrast to the east jet, which decelerates much less due to a rapid decrease in the ISM density over short distances to the east of SS 433.

Various combinations of n_0 and Z_d were tested in a series of simulations to reproduce the correct east-west jet lobe ratio as seen in W 50, and the results are presented in Figure 7.3.
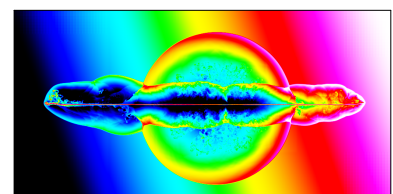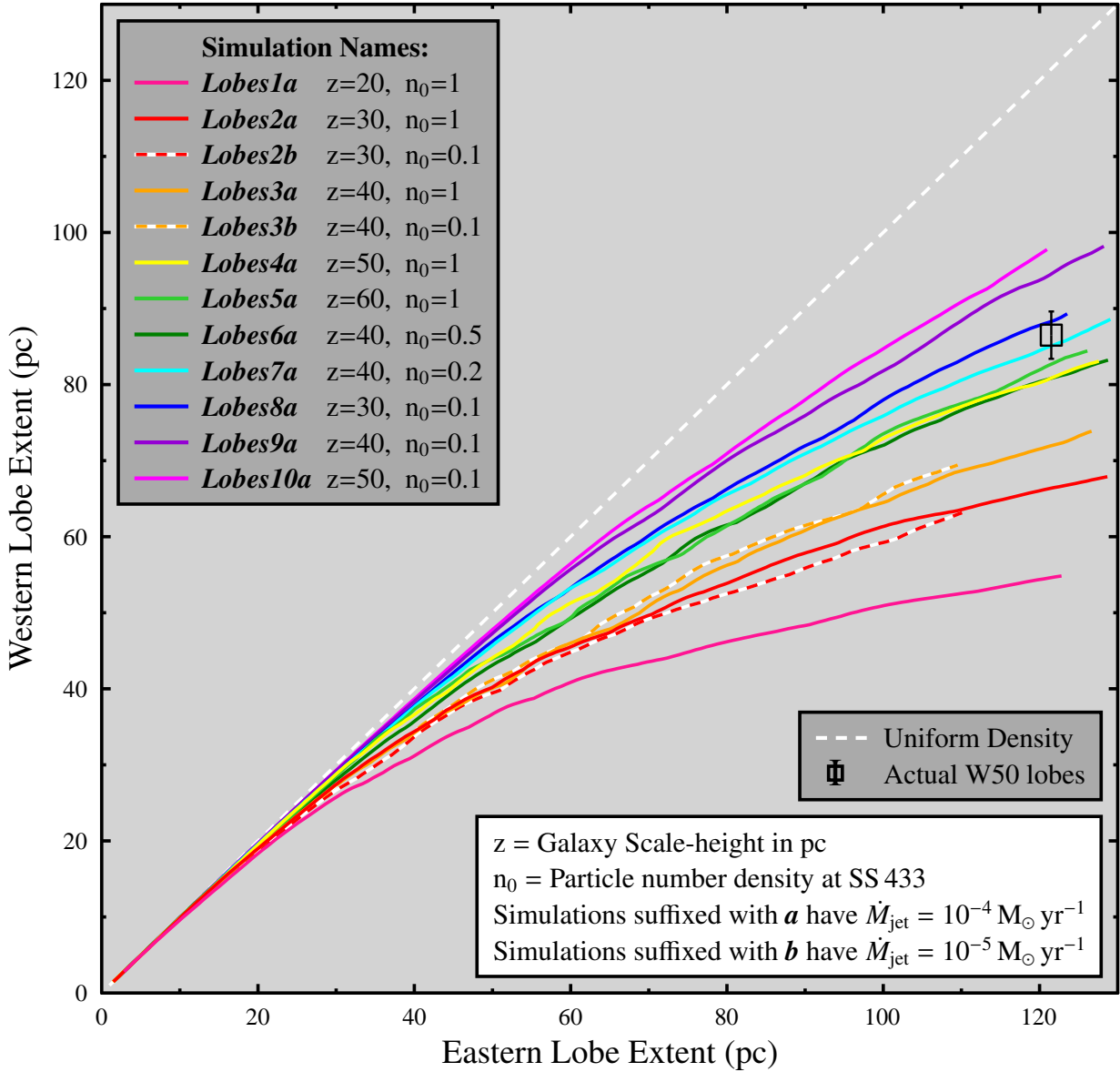
Figure 7.3: We monitor the east and west lobe lengths as a function of time for each simulation. Each coloured line represents a different combination of the Galaxy scale-height Z_d and ambient density n_0, as indicated in the key. The white dashed line shows the case of a uniform density background, where the east and west jet lobe extents grow symmetrically with time. The black data point indicates the location of W 50's east and west jet lobe extents, according to Figure 2.3. The distinctive morphology of W 50 can thus be used to constrain the physical parameters most appropriate to the SS 433-W 50 system. The jet shock-front detection technique used to determine the east and west jet extents can be seen in action at: $http://www\text{-}astro.physics.ox.ac.uk/{\sim}ptg/RESEARCH/research.html$

Interestingly, the simulation results presented in Figure 7.3 show that the two parameter combinations $(n_0 = 0.2\,\mathrm{cm}^{-3}, Z_\mathrm{d} = 40\,\mathrm{pc})$ and $(n_0 = 0.1\,\mathrm{cm}^{-3}, Z_\mathrm{d} = 30\,\mathrm{pc})$ reproduce W50's east-west lobe extents very well. It is important to realise however, that these two combinations are only relevant for a jet mass-loss rate of $\dot{M}_\mathrm{jet} = 10^{-4}\mathrm{M}_\odot\,\mathrm{yr}^{-1}$. This realisation comes from a particularly important result demonstrated by the dashed red-white and orange-white lines in Figure 7.3 corresponding to simulations **Lobes2b** and **Lobes3b** respectively. These simulations prove that changes in the background density normalisation n_0 and the jet mass loss rate $\dot{M}_\mathrm{jet}$ can become indistinguishable, as previously hypothesised in §7.6. For example, increasing the jet power by a factor of 10 (equivalent to increasing $\dot{M}_\mathrm{jet}$ if the jet speed is a constant) whilst keeping all other parameters constant, is equivalent to reducing the background density normalisation (equivalent to the resistance felt by the jets) by a factor of 10. Thus, I define the quantity χ_p to indicate the penetrative ability of a given jet:

$$\chi_\mathrm{p} = n_0\,\dot{M}_\mathrm{jet} \tag{7.28}$$

such that any two jets with the same value of χ_p in will follow the same curve in Figure 7.3, provided that $\dot{M}_\mathrm{jet}$ and n_0 are the only parameters that differ (i.e they have the same Z_d value).

7.8 Hydrodynamic refocusing of SS 433's jets.

It has been suggested that astrophysical jets of the hollow conical type, may undergo refocusing towards the centre of the cone (Eichler, 1983) due to the ambient pressure from the ISM through which the jet propagates. However, we find evidence of refocusing of our hollow conical jets through a different mechanism which is purely dependent upon the kinematics of the ISM within the cocoon of the jet. Two subtly different refocusing mechanisms are suggested here, but both are based upon momentum exchange between the jet and its environment, as follows:
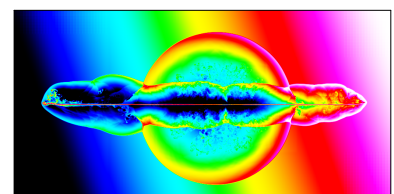
1. **Kinetic refocusing** - the jets are hydrodynamically refocused via collisions with the low-density but fast-moving and turbulent ISM within the jet cocoon, which has been energised through past interactions with earlier jet ejecta. Due to the low density of the gas within the jet cavity, it is quite easy for this material to be accelerated to high speeds through interactions with the jets. After gaining momentum from the jets, the fast-moving gas interacts with the wall of the cocoon and develops a vortex-like rotation, as indicated by the arrows of the velocity field of the gas superimposed onto Figure 7.4a. In this case, momentum transfer from the jets to the cocoon ISM has the dual effect of altering the jet trajectory and further stirring the turbulent ISM motion. This effect is self-sustaining once it begins. This effect is seen in all of our simulations that have a constant jet cone angle greater than zero, such as *Jet 5*, *Jet 6* and *Jet 7* of Figures 7.2e, 7.2f and 7.2g. The process of momentum exchange with the turbulent ISM is depicted in Figure 7.4b.

2. **Static refocusing** - a more gradual focusing mechanism occurs when the jets interact at a grazing angle with the dense, but comparatively slow-moving, cavity walls of the jet cocoon. The interaction occurs at a grazing angle when the jet cocoon is sufficiently elongated, such as that created by a cylindrical jet (or a jet with a near-zero cone angle). Due to the high density of the cavity wall, it experiences a much smaller acceleration per unit momentum-exchange than does the low-density gas of the kinematic refocusing method. As a result, the jet is redirected back towards the mean jet axis upon collision with the cavity walls. This mechanism is seen to occur in *Jet 8* of Figure 7.2h.
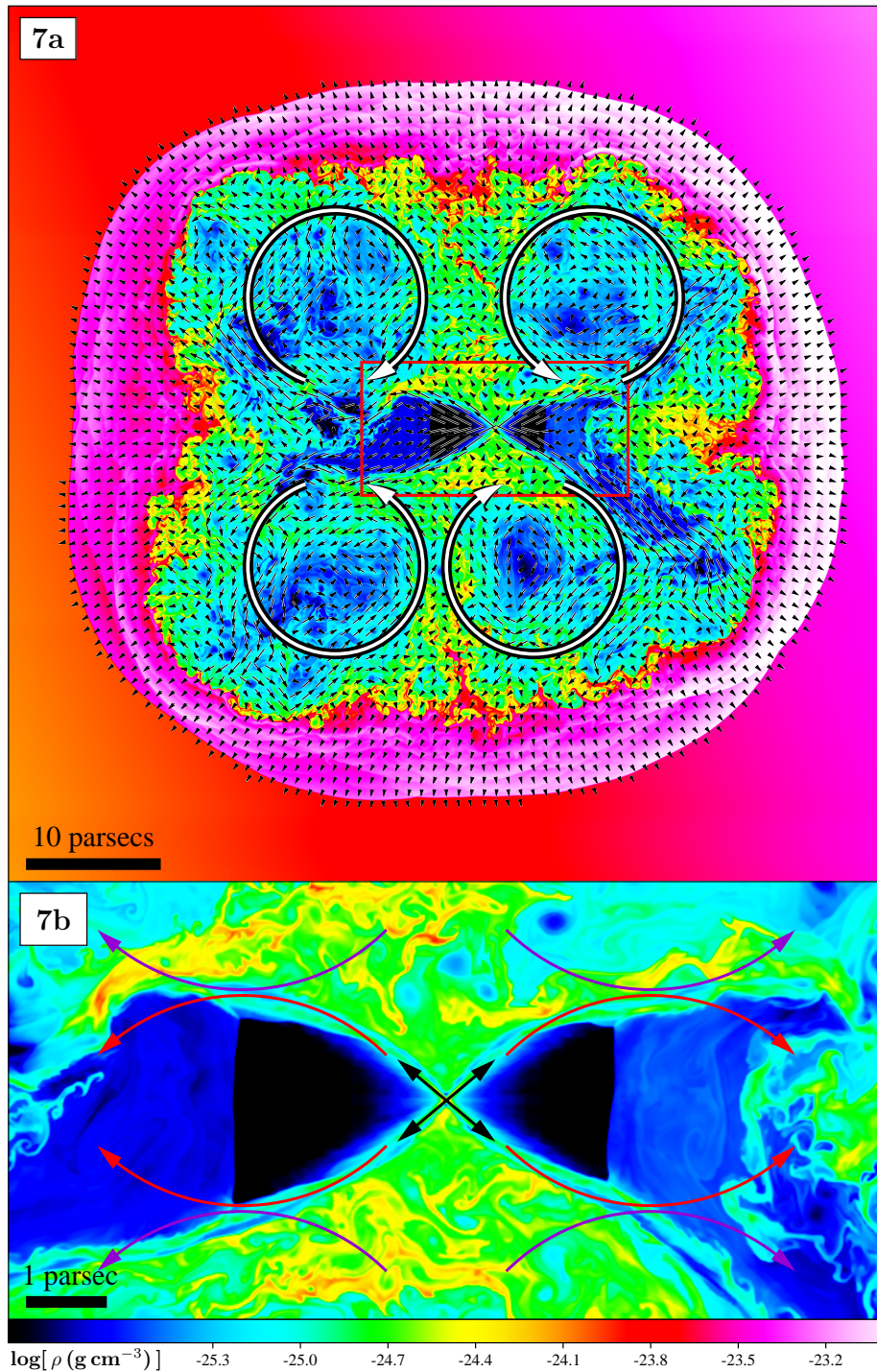
Figure 7.4: Demonstration of the *kinetic* hydrodynamical refocusing of hollow conical jets. The small black velocity vectors in (a) have magnitude proportional to the square-root of the average speed at each point, and are overlaid upon a zoomed-in density map of *Jet 7*. The large white arrows in (a) show the net vortex-like movement of the turbulent gas in each quadrant. These vortices tend to move around appreciably within each quadrant, which is the reason for the asymmetry in their locations in this snapshot. The black arrows in (b) indicate the initial trajectory of the jets. The purple arrows indicate the turbulent motion of the agitated gas within the jet cocoon, and the red arrows indicate the subsequent interaction and refocusing of the jets back towards the jet-axis. A short animation showing this effect is avilable at: *http : //www-astro.physics.ox.ac.uk/∼ptg/RESEARCH/research.html*
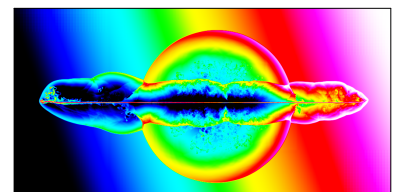
Chapter 8

Simulating the Jet-SNR interaction

Following from §7.7, the combination of parameters $(n_0 = 0.2 \,\mathrm{cm}^{-3}, Z_\mathrm{d} = 40 \,\mathrm{pc})$ and $(n_0 = 0.1 \,\mathrm{cm}^{-3}, Z_\mathrm{d} = 30 \,\mathrm{pc})$ were determined to be most representative of the observations of W 50, for a jet mass loss rate of $\dot{M}_\mathrm{jet} = 10^{-4} \mathrm{M}_\odot \,\mathrm{yr}^{-1}$. Although both of these combinations of parameters are feasible, they are also almost equivalent in terms of the jet morphology produced, and so I will investigate only one of these combinations here.

In this chapter I adopt the combination $(n_0 = 0.2 \,\mathrm{cm}^{-3}, Z_\mathrm{d} = 40 \,\mathrm{pc})$ as the control group for this section, and I investigate the effects of the interaction between the jets and SNR for an environment that is determined by these parameters.

All jet models featured in this chapter use the same jet speed of 0.26c corresponding to the observed speed for SS 433's current jet state. We acknowledge that the jet speed is one of the variable parameters that can change between outbursts of jet activity, and the choice to keep the jet speed constant here has no physical basis other than to limit the number of free parameters in the models. This chapter focuses on the effects of changing the jet precession cone angle with each different jet outburst. The effects of varying jet speed and indeed jet mass loss rate will be investigated in further publications beyond this thesis.
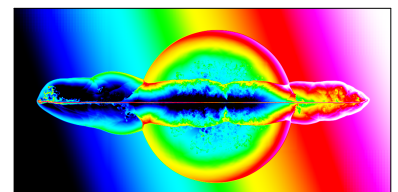
Shortname	Description	Parameter Details
SNR A	SNR only	SNR defaults and: ρ-profile = 1, v-prof = 1, $n_0 = 0.1\,\mathrm{cm}^{-3}$, $Z_\mathrm{d} = 40\,\mathrm{pc}$
SNR B	SNR only	SNR defaults and: ρ-profile = 1, v-prof = 1, $n_0 = 0.2\,\mathrm{cm}^{-3}$, $Z_\mathrm{d} = 30\,\mathrm{pc}$
SNRJet1	*SNR A* with a modified *Jet 1*	Modified parameters: $n_0 = 0.1\mathrm{cm}^{-3}$
SNRJet2	*SNR B* with a modified *Jet 1*	Modified parameters: $Z_\mathrm{d} = 30\,\mathrm{pc}$
SNRJet3	*SNR A* with a modified *Jet 6*	Modified parameters: $\theta_0 = 20°$
SNRJet4	*SNR A* with a modified *Jet 8*	Modified parameters: $\dot{\theta} = \frac{20°}{1500\,yr}$
SNRJet5	*SNR A* with a modified *Jet 9*	Modified parameters: $\theta_1 = 0°$, $\theta_2 = 20°$
	Jet default parameters: $\dot{M}_\mathrm{jet} = 10^{-4}\,\mathrm{M}_\odot\,\mathrm{yr}^{-1}$	

Table 8.1: A description of the key parameters relevant to each of the SNRJet simulations.

8.1 Simulating the Jet-SNR interaction

The new parameters (as determined in §7.7) were used to create two new supernova simulations in an attempt to recreate the most appropriate background environment for the SNR evolution. *SNR A* and *SNR B* are very similar to *SNR 6* of Figure 6.1, with the following modifications: *SNR A*= $(n_0 = 0.2\,\mathrm{cm}^{-3}, Z_\mathrm{d} = 40\,\mathrm{pc})$ and *SNR B*= $(n_0 = 0.1\,\mathrm{cm}^{-3}, Z_\mathrm{d} = 30\,\mathrm{pc})$. As per §6.1, the SNR evolution is followed until the radius approaches 45 parsec, which happens at $\approx 21{,}000$ yrs for *SNR A*, and $\approx 17{,}000$ yrs for *SNR B*, due to the slightly lower density of *SNR B*. Various jet models were then invoked to investigate the SNR-jet interaction, and the simulation parameters are described in Table 8.1.

8.2 Results of the SNR-Jet interaction

Each of the simulations detailed in Table 8.1 are shown in Figure 8.1, where the left column shows the density maps for the final simulation snapshot, and the right column shows the gas speed $\sqrt{v_\mathrm{x}^2 + v_y^2}$ for the same simulation snapshot. The purple contours on the left column of Figure 8.1 show the outline of W 50 from the *Dubner-96* observation (Dubner et al., 1998). The green contours on the right column of Figure 8.1 show the structure of SS 433's jet lobes from the X-ray observations of Brinkmann et al. (1996). The inlay on each panel shows an $4\times$ magnified

region about the coordinates of the jet launch.

8.2.1   Concerning *SNRJet 1*

SNRJet 1 of Figure 8.1(a & b) shows how *Jet 1* from Figure 7.2a would interact with *SNR A*. The extents of the east and west jet lobes are in good agreement with the radio observations of W 50 as shown by the purple contours in (a). This confirms that the parameters were determined correctly $(n_0 = 0.2\,\mathrm{cm}^{-3}, Z_\mathrm{d} = 40\,\mathrm{pc})$, and that the presence of the SNR has little effect upon the east-west lobe asymmetry along the jet-axis direction. The SNR does however widen the jet at the point where the jet penetrates the SNR shell, in a similar manner to waves diffracting through an aperture. This is because the jet breaks through the relatively high density of the compressed SNR shell into the surrounding lower-density ISM, and the impact of the jets with the shell increases the momentum of the SNRJet material in the direction perpendicular to the jet axis. Note that the jet lobes produced in *SNRJet 1* have a higher degree of collimation than those of *Jet 1* from Figure 7.2a, due to the background density normalisation being a factor of 5 lower. Judging by the purple contours, the east lobe of *SNRJet 1* seems to be approximately equal in width to the eastern radio lobe, whereas the transition between the SNR shell and the western lobe seems to be more gradual in the purple radio contours than the simulation would indicate. This could be due to a previous jet episode impacting on the younger SNR at an earlier time, such that the SNR shell is inflated more rapidly at the location of the jet impact. The green contours in (b) indicate again that the eastern jet lobe has similar dimensions for both the simulation and X-ray observations, however the western lobe X-ray emission is abruptly truncated short of the full extent of the simulated jet lobe. The X-ray lobe is both wider and shorter than the west lobe of the simulation, as though the X-ray emitting jet material is hitting a dense wall of material, which is true if the increased radio brightness of the nebula at this position indicates an increase in density (see point D in Figure 2.4).
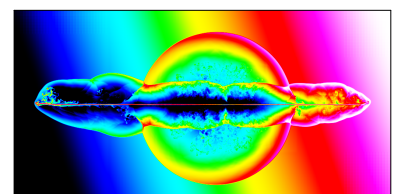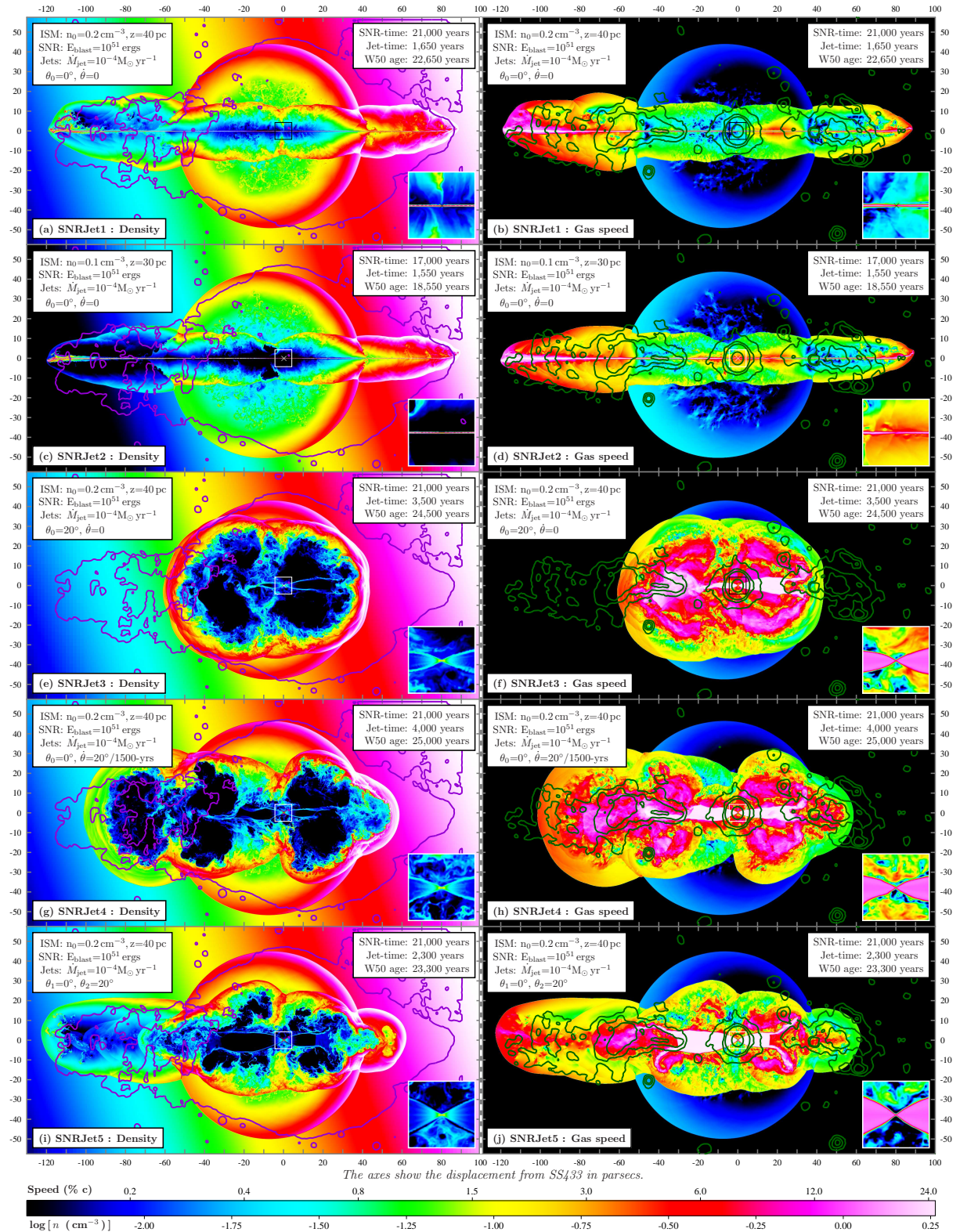
Figure 8.1: This figure illustrates the varying nebular morphologies produces through the interaction of 5 different jet models with an evolved SNR. Refer to Table 8.1 for a summary of the differences between these simulations, and §8.2 for a detailed commentary on the interpretation of each one. The animations associated with these simulations are available at: *http : //www-astro.physics.ox.ac.uk/∼ptg/RESEARCH/research.html*.
Note: full-size images of the above panels are available in the appendices.

8.2.2   Concerning *SNRJet 2*

SNRJet 2 of Figure 8.1(c & d) is similar to *SNRJet 1* in most respects, except for the fact that the jet lobes are more highly collimated than *SNRJet 1* due to a decrease in the density normalisation by a factor of 2. The jet lobes produced by *SNRJet 2* are thinner than the radio/X-ray lobes as indicated by the purple/green contours, and this probably means that the density of $n_0 = 0.1$ particles cm^{-3} is too low, and it's likely that *SNRJet 1* with $n_0 = 0.2$ particles cm^{-3} is more representative of the environment at the locality of SS 433.

8.2.3   Concerning *SNRJet 3*

*SNRJet 3* of Figure 8.1(e & f) features a precessing jet with half-cone angle of $20°$, very similar to that of the current jet in SS 433. Although this jet model doesn't reproduce the lobes of W 50, it does accelerate the expansion of the east and west hemispheres of the SNR bubble. This is further evidence that a previous jet episode with a large cone angle probably contributed to the shape of W 50. It is unlikely that this inflation of the east and west hemispheres were caused by the current jet episode in SS 433 due to time arguments, as explained in §8.2.5. This hollow conical jet model is also affected by the *Kinetic Refocusing* mechanism described in §7.8, and the effects are noticeable at around 500 years onwards in the simulation (refer to the simulation movies link at: *http : //www-astro.physics.ox.ac.uk/∼ptg/RESEARCH/research.html*).

8.2.4   Concerning *SNRJet 4*

SNRJet 4 of Figure 8.1(g & h) features a conical jet whereby the jet precession cone half-angle linearly increases from $0°$ to $20°$ over a period of 1500 years. The jet parameters are almost identical to that of *Jet 8* from §7.6, with the only difference being the time taken for the jet to reach the maximum cone angle of $\sim20°$, which was 1000 years rather than 1500 years. However, the difference in the nebular morphology produced by *Jet 8* and *SNRJet 4* is striking (compare Figure
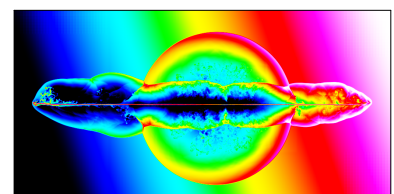
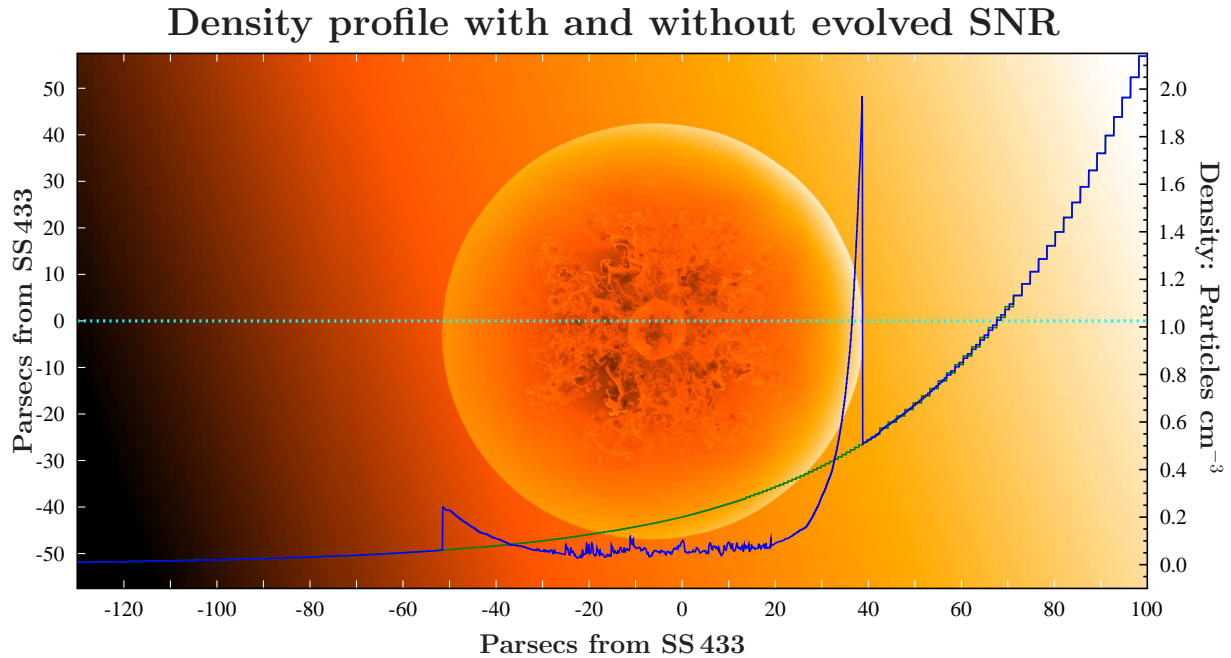7.2h with Figure 8.1g), and this difference is due entirely to the presence of the compressed SNR shell.

Figure 8.2: The image shows a density map (logarithmic colour scale, white = high density, black = low density) of *SNR A* in the final stages of evolution. The blue line shows a density line profile taken through the centre of the displayed image (indicated by the dotted line). The green line shows the same density line profile of the unperturbed ISM (before the supernova explosion occurred). This figure illustrates the difference in the local density distribution as seen by *Jet 8* (green line, without SNR), and *SNRJet 4* (blue line, after SNR has ploughed through the ISM). The lower density environment through which the jet from *SNRJet 4* propagates, is the reason for the morphological differences with *Jet 8*.

The key to this difference is the lower density environment internal to the SNR. The hypersonic shockwave created by the supernova explosion swept up most of the gas in the ISM, and the density distribution from the final snapshot of *SNR A* is shown in Figure 8.2, along with the original density profile of the background ISM before the supernova explosion.

The morphological difference between *Jet 8* and *SNRJet 4* demonstrates (yet again) the importance of the ISM density distribution in the vicinity of the jet launch site, and the profound influence this can have upon the resulting jet cocoon.
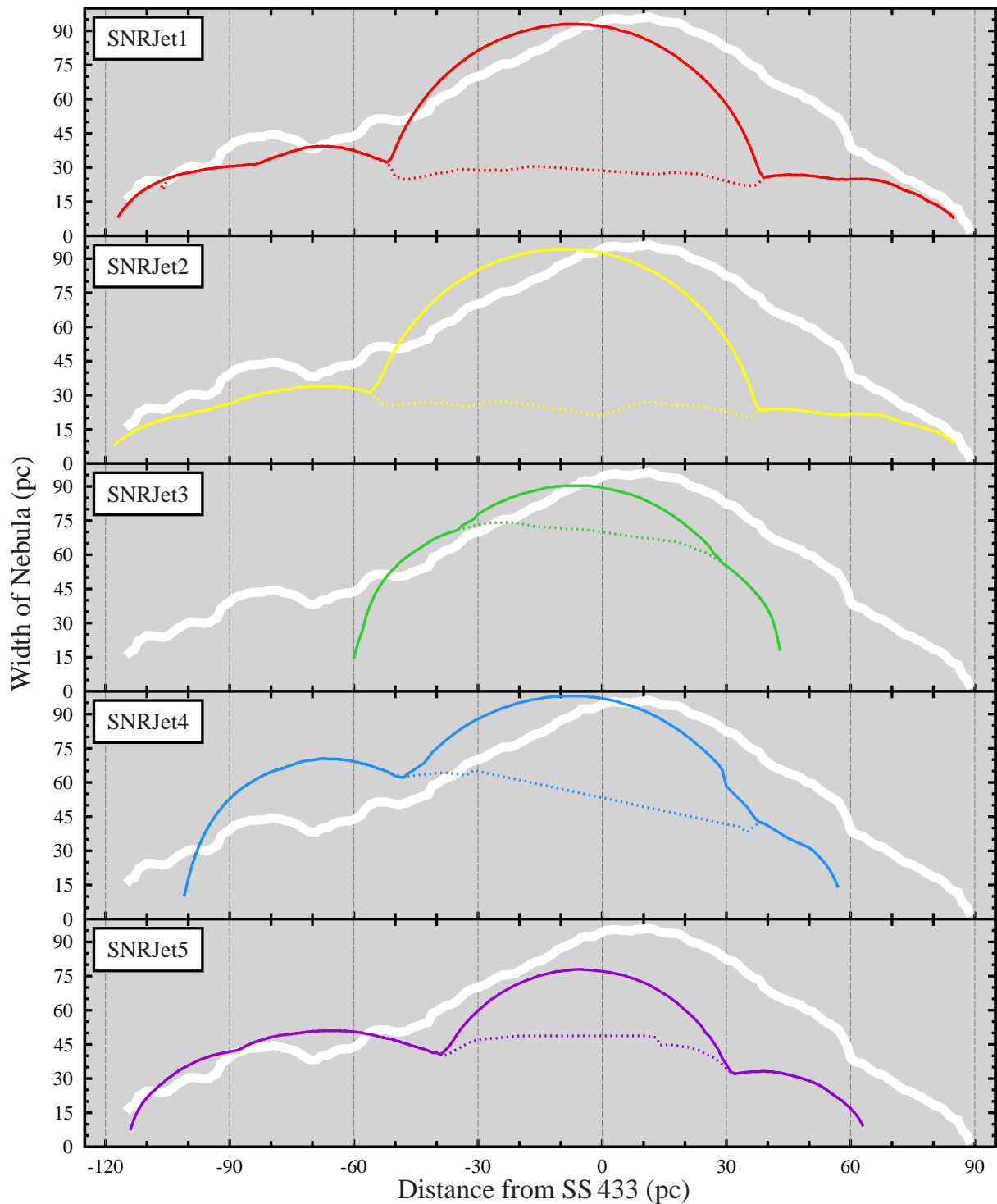
Figure 8.3: The vertical width of each nebula produced from the SNR-jet interaction simulations from Figure 8.1, is shown as a function of distance from SS 433 by the coloured lines in each panel. The width of W 50 as a function of distance form SS 433 is also shown by the thick white line in each panel, as measured from the *Dubner-96* image (Dubner et al., 1998). Note how the transition between SNR and jet lobes is very smooth in reality (white lines), and in fact it is difficult to say where the SNR shell ends and the jet lobes begin when viewed in this way. The dashed coloured lines show the width of the jet internal to the SNR. The bumps in the lobes indicate the locations of the annular features in W 50's lobes.
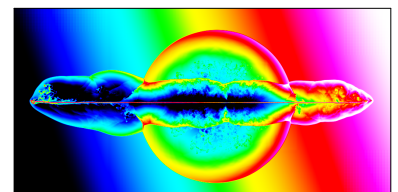
8.2.5 Concerning *SNR Jet 5*

SNR Jet 5 of Figure 8.1(i & j) uses an episodic jet model with two outbursts; the first jet outburst features a cylindrical jet which lasts for 200 years, and the second outburst is a precessing conical jet with half-angle 20° of 2300 years in duration. *SNR Jet 5* displays both *Kinetic* and *Static refocusing* (*http* : //*www-astro.physics.ox.ac.uk/∼ptg/RESEARCH/research.html* contains a link to the movie associated with this simulation). *Kinetic refocusing* becomes noticeable around ∼700 years after the jet is first switched on, and is readily recognisable as four regions the swirling gas within the SNR, which are (approximately) symmetrically located about the jet launch point (one in each quadrant). *Static refocusing* begins approximately 2000 years after the jets are switched on, whereby the jets are refocused towards the jet axis upon interaction of the denser jet co-coon gas located near the SNR shell, which was penetrated several hundred years earlier by the cylindrical jet.

This jet model was devised to combine the successes of both cylindrical jets *SNR Jet 1* in reproducing the correct jet lobe extents, and the conical jets *SNR Jet 3* in producing the required inflation of the east and west sides of the SNR such that a gradual transition from SNR shell to lobes is created. However this attempt was unsuccessful, because the cylindrical jets (despite the short episode duration of just 200 years) exceed the extent of W 50's lobes in the time it takes for the conical jets to catch up with the SNR shell and contribute to its expansion, as shown in Figure 8.1i.

8.3 Jet symmetry and collimation

The level of collimation is actually higher for pulsed jets rather than continuous. For a continuous jet, although the jets receive constant replenishment of the kinetic energy and therefore don't show signs of deceleration, a side-effect is that the jet bunches-up and crashes into the jet in front. Any tiny asymmetric displacement of the bunched-up jet about the jet axis will cause

the upstream jet to transfer an increased amount of momentum in the transverse direction. An appropriate analogy for this effect is drawn with that of a cue-ball struck off-centre by the cue. This effect is much less noticeable when the jet is pulsed, presumably due to a lower occurrence of jet blockages.

8.4   Energetics of the SS 433-W 50 system

Due to the size of this SNR, to consider higher SNR blast energies of 10^{52} ergs or so, would not be unreasonable. This would usefully lessen the latency period before the jets become active, and the increased kinetic energy per unit mass of the expanding gas could make W 50 an ideal contributor of high energy cosmic rays. We note that with the large radius of 45 pc for W50 and the galactic field strength of 5 μGauss makes confinement of particles with energies up to 2×10^{17}eV possible.

8.5   Conclusions for SNR-Jet Interaction

The cylindrical jet models reproduce the lobes of W 50 very well in terms of their absolute and relative extents in the east and west directions. As Figure 8.1 and Figure 8.3 show, the cylindrical jets create jet lobes with well-defined boundaries at the site of the impact between jets and the SNR shell. This is not in agreement with the radio observations of Dubner et al. (1998) in which there is a more gradual transition between the circularity of the SNR shell and the elongated lobes (see Figure 8.3).

The conical jet models do produce lobes with a lower degree of collimation appropriate to W 50's lobes very near to the SNR shell, however these jets continue to diverge away from the jet axis and prove too wide at larger distances from SS 433 to be considered an accurate representation of W 50's lobes.
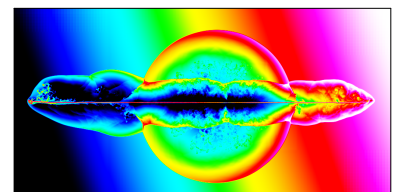
It was hypothesised that the smooth transition between SNR shell and lobes might be created if a conical jet model is used in conjunction with a cylindrical jet model. This was tested in *SNRJet 5* where a cylindrical jet (an earlier jet episode) was invoked before a conical jet with the precession cone half-angle approximately equal to that currently observed in SS 433. However, this leads to problems due to the large time interval (at least 2000 years) required for the conical jets to reach the surface of the SNR shell, during which time the cylindrical jet travels beyond the boundaries of the simulation domain, indicating that a real jet would have far exceeded the extent of W 50's lobes in the time required by the conical jets. This problem is eradicated if the conical jets begin first and are allowed to evolve for as long as is necessary before the cylindrical jets begin, because the latter only require of order $\sim$1600 years to reach the required lobe extent. However the situation gets more complex in that the final jet episode must be in agreement with current observations, and so a third jet episode representing SS 433's current jet precession state must be invoked in order to satisfy this requirement. This investigation is ongoing, and will be tacked in further publications in the years that follow from this thesis.

In summary, it seems clear that neither cylindrical nor conical jets can independently reproduce the interesting morphology displayed by W 50, and it seems several jet episodes from SS 433 with varying jet characteristics are needed in order to sculpt W 50 in the ISM.

Chapter 9

Concluding remarks

In this, the final chapter, I will summarise the most important discoveries made during the re-
search that I conducted throughout my D.Phil, with reference to the preceding chapters. Firstly,
it is worth briefly mentioning the problems with previous simulation work regarding SS 433 and
W 50, which prompted the computational research conducted herein. This is necessary in order
to explain the differences between my findings here, and the results of other computational works
which are based upon different (and sometimes inappropriate) assumptions.

9.1   Simulations: Comparison with previous work

Despite the appeal of some of the previous hydrodynamic models attempting to reproduce W 50,
there are some inconsistencies which must be discussed in order to begin to fully understand the
nature of the SNR-jet interaction in SS 433 and W 50. Firstly, we note that concrete graphical
evidence in the literature supporting claims of having reproduced the annular structure in the
lobes of W 50 through hydrodynamic simulations, is (so far) scant. In Fig. 3 of Velázquez &
Raga (2000), the pressure contour at 1150 years shows the emergence of two annuli through the
jet-SNR interaction, however it is not clear if these are artefacts of the reflective boundary con-

ditions imposed. The computed synchrotron emission (Fig. 5 of Velázquez & Raga (2000)) does resemble the annular structure in the eastern lobe of W 50 at approximately 3000 years after the jets are initiated. However, it is easy to create annular structures through azimuthal revolutions with axial symmetry. The follow-up paper Zavala et al. (2008) with improved jet models and in three dimensions, reports no evidence of any annular structure. They acknowledge that the annular structures created in the previous paper are a possible consequence of the reflective boundary conditions imposed therein, and the undesirable effects produced via axisymmetric codes with reflective boundary conditions are well known to those authors (Raga et al., 2007).
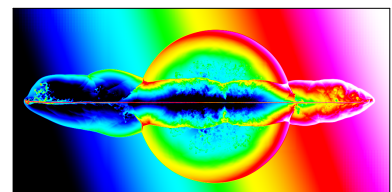
Each of the simulations shown so far in the literature have featured scaled-down versions of the W 50 system. The primary assumption for any work involving the SS 433-W 50 system, is that both objects are at the same location, and independent methods have determined a distance of 5.5 kpc is appropriate to each of SS 433 (Blundell & Bowler, 2004) and W 50 (Lockman et al., 2007). At this distance, the radius of the SNR is 45 parsecs and the jet extents are 86.5 and 121.5 parsecs for the west and east jet lobes respectively, as indicated in Figure 2.2. These physical sizes (and their ratios) are of paramount importance in forming a consistent model of the SS 433-W 50 interaction, that is in agreement with observations. We stress that (in contrast to the claims of Zavala et al. (2008)), it is *not* sufficient to simply scale-up simulated models of the system for comparison with observations. The reasons for this are as follows:

1. The absolute extents of the jet lobes at a given time are characteristic of the integrated column density along the path of the jets (a measure of the resistance faced by the jets) as they travel through the ISM. Similarly, the radius of the SNR at a given time is characteristic of the mass it has swept up, which depends roughly on the cube of the radius. Aside from the density normalisation, the evolution of each of these is also dependent upon the energy input, as governed by E_{blast} for the supernova, and $\dot{M}_{\mathrm{jet}}$ over some time period for the jets. The jets propagate much faster than the SNR at all times, and so a morphological match to W 50 at some scaled-down radius of the SNR will be lost at later times. In essence, the

jets would extend far beyond the domain of W 50 by the time the SNR has expanded to a radius that is in agreement with observations.

2. The relative extents of the east and west jet lobes are characteristic of the exponential density background, and the ratio of the lobe extents is not linearly scalable with either total jet travel time or total lobe extent, as shown in Figure 7.3.

3. Simulating the absolute extents of both SNR and jet lobes is important as this allows us to place constraints on the formation time and energetics for each component, and has relevance to the aforementioned latency period.

4. Jets could possibly inflate (accelerate the shell expansion of) a small SNR corresponding to some scaled-down version of W 50, such as those produced in the previous publications. However, we find that this is not the case for a SNR as large as 45 pc, and the jets have absolutely no effect upon the SNR expansion in the direction perpendicular to jet launch.

9.2   Kinematics: Proper motions in the plane of the sky

An investigation of the kinematics of W 50 through the proper motions of its filamentary structure over a 12-year period, revealed no detectable motions of the nebular gas. This means either that (i) the jet ejecta has lost ∼80% of its original kinetic energy, or (ii) that the current, constant jet source model of SS 433 (whereby it is continually injecting kinetic energy into the nebula via the active jets) is incorrect.

In contrast to SS 433's reputation as a persistent jet source, we propose that the wealth of observational data on SS 433 and W 50 are consistent with SS 433 having experienced (at least) two distinctly different states of jet activity.

The latest jet episode has been well-studied for more than three decades via doppler shifting of spectral emission lines in the optical and high-resolution radio interferometry, and as such
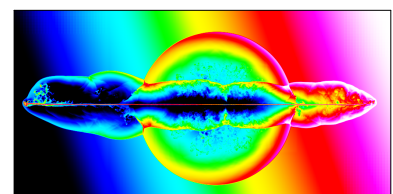
the current jet state is characterised by a $t_{\text{jet}} = 163$ day precession cycle with cone half-angle $\theta_{\text{jet}} = 20.92°$ and jet speed $v_{\text{jet}} = 0.2647c$ (Eikenberry et al., 2001). This jet episode cannot produce the lobes of W 50, as the hydrodynamic simulations of §8.1 show.

An additional jet episode is thought to have occurred some time in the past, with the same axis of symmetry as the current jet system. This jet state is required to have either a zero (or very small) jet precession cone angle, or a precession period significantly longer than the duration of the jet activity. This jet episode is observable indirectly through the formation of the lobes of W 50 (which cannot be produced via SS 433's current jet state).

We note that the observations of Cyg X-3's jet outburst in 1997 were reported to have $v_{1997} \geq 0.81c$ and precession cone angle $\psi_{1997} \lesssim 12°$ (Mioduszewski et al., 2001). Only four years later a speed $v_{2001} = 0.63c$ and precession cone angle $\psi_{2001} = 2.4°$ were observed by Miller-Jones et al. (2004). Hence, it is not extroadinary for microquasars to undergo outbursts of jet activity with significantly different characteristics.

The kinematic results presented herein, underline the need for further investigation via hydrodynamic simulations, of the possible intermittent jet activity in SS 433's past. This will follow in further publications subsequent to this thesis.

9.3   Energetics of the SS 433-W 50 system

Due to the large size of the W 50 nebula, it would be reasonable to test higher kinetic energies for the supernova explosion, of maybe a few times 10^{51} ergs or even as high as 10^{52} ergs. These explosion energies are entering into the realm of *Hypernova* explosions. It is interesting to note that *Hypernovae*, as progenitors for Gamma Ray Bursts (GRBs) usually feature short-lived (in astrophysical terms) jets that form early during the SNR history, often with very high Lorentz factors. The short life of the GRB jets with a higher speed, may be the required ingredients to explain the high level of collimation in W 50's lobes and yet have decelerated sufficiently after

a long period of time to be consistent with the kinematics data. Furthermore, given that the progenitor of SS 433 underwent the supernovae phase a long time ago, it was presumably more massive than the companion star in SS 433 (which has a mass of $24M_\odot$), and so it would be reasonable to assume that the progenitor star was very massive, as appropriate to Wolf-Rayet stars (*Hypernovae* progenitors). Although speculative at this stage, it will be interesting to test the possibility of a *Hypernova* progenitor in SS 433, and this will require the adaptation of the code to provide a relativistic treatment.

9.4 Addressing the key questions concerning SS 433-W 50

In chapter 2 I mentioned some interesting open questions concerning SS 433 and W 50, and will now attempt to briefly address each question in the light of the research I have conducted.

9.4.1 East-west Jet lobe asymmetry

It was previously postulated that the difference in the east and west lobe extents in W 50 could be due to the increased ISM density towards the Galaxy plane, and to tackle this question I conducted a series of jet simulations to investigate the effects of the background density profile upon the jet propagation.

I conclude that an exponential density profile can accurately reproduce the lobes of W 50 if the ISM density scale height in the direction perpendicular to the Galactic plane is $Z_d = 40\,$pc, with the normalisation condition that the density at SS 433 is $n_0 = 0.2$ particles cm^{-3}. Although a range of values for both density normalisation and scale-height were tested in the simulations, these best-fit values are in good agreement with other published work, where Dehnen & Binney (1998) quote $Z_d = 40\,$pc for the scale-height. The density at SS 433 here is slightly lower than the values quoted in Lockman et al. (2007) of $0.4 < n < 1.2$ hydrogen atoms cm^{-3}, corresponding to $0.3 < n_0 < 0.92$ for our case where the particle mass is $\mu = 1.3$, however the values given
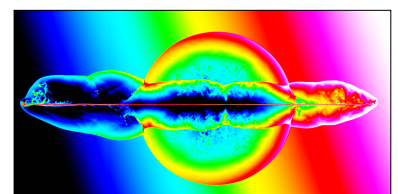
in Lockman et al. (2007) are rough values based on the estimated mass with the SNR shell, which has a reasonably large error associated with it. Hence, I think these parameter values can generally be considered to be in excellent agreement.

9.4.2   Annular structure in the lobes of W 50

The surface of the jet lobes produces in all simulations are relatively smooth, and I can report no evidence of any annular structure produced through simulations so far.

The annular structure seen in the lobes of W 50 could be a consequence of a particular combination of jet episodes interaction within the lobes themselves. Alternatively, there may be a way to produce the annular structure with a specific magnetic field configuration, and in future work §9.5.2 I will use the idea of a *Magnetic Bottle* to attempt to reproduce the W 50 nebula.

9.4.3   SS 433's latency period and Jet Activity

The jet simulations of Figure 7.3 determined that the density at the location of SS 433 is actually $n_0 = 0.2$ particles cm^{-3} rather than the initially assumed value of 1 particle cm^{-3}. This lower density ISM provides less resistance for the supernova blast as it propagates, and so the SNR reaches a radius of ~45 parsec in ~21,000 years (see Figure 8.1a for example) rather than the original expansion duration of ~37,000 years when $n_0 = 1$ was used. For the cylindrical jet case *SNRJet 1* of Figure 8.1a, the jets require just 1,650 years to reach the full extent of W 50's lobes, and this implies a latency period of 19,350 years.

The SNR expansion phase could be shortened further if a greater blast energy of ~10^{52} ergs is used, as suggested in §9.3. This is a factor of 10 increase in the initial kinetic energy $\frac{1}{2}mv_i^2$ of the supernova blast, and as such I would expect the expansion time to decrease by a factor $\sqrt{10}$. Thus 21,000 years becomes $\approx 6,640$ years, implying a latency period of just ~5,000 years.

The idea that W 50 requires several different jet episodes from SS 433 in order to produce the

smooth transition between SNR shell and lobes, could increase the jet time significantly, and it may well be the case that SS 433's latency period no longer exists at all.

9.5   Future work

There are several areas for extension of the work conducted during my D.Phil, which could make for interesting follow-up investigations during post-doctoral research position.

9.5.1   Future1: Search for extended structure

As shown through the observations (for example Figure 1.2) and from the simulations conducted for this thesis, it is clear that the jets themselves can have an enormous influence on their surroundings. It would be an excellent thing indeed to discover more such systems exemplifying the jet-SNR interactions that should feasibly occur in other microquasars. This could be achieved via a more detailed investigation similar to that discussed in §2.6.2, where deeper telescope observations of the regions around microquasars in Figures 2.6 and 2.7 could reveal some interesting new insights into the role of supernova explosion and jet outflows upon their local environments.

9.5.2   Future2: 3D Simulations and Magnetic Bottle

With regards to further work, I intend to conduct further simulations in 3D, to test the more successful jet and SNR models featured in this thesis. Computational work is already in progress, to incorporate magnetic fields into the simulations for a Magnetohydrodynamic (MHD) treatment.

One dramatic but particularly interesting idea, would be to consider the possibility of W 50 as an astronomical *Magnetic Bottle*. This would require quite specific initial condition constraints to be placed on the magnetic field structure at the location of SS 433. However, this idea includes some very appealing features, as any charged relativistic particles injected into the W 50
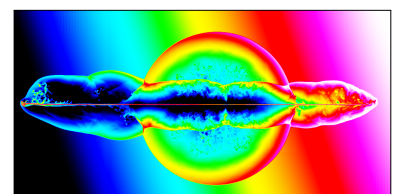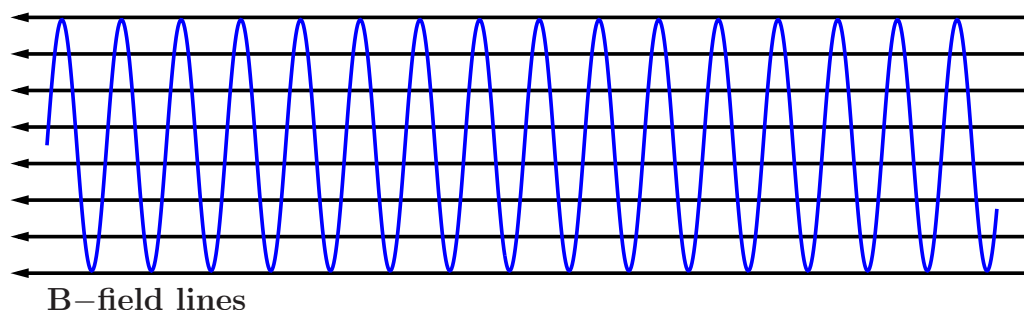
(a) Uniform Magnetic Field

(b) The effects of SNR Expansion
(Magnetic Bottle)
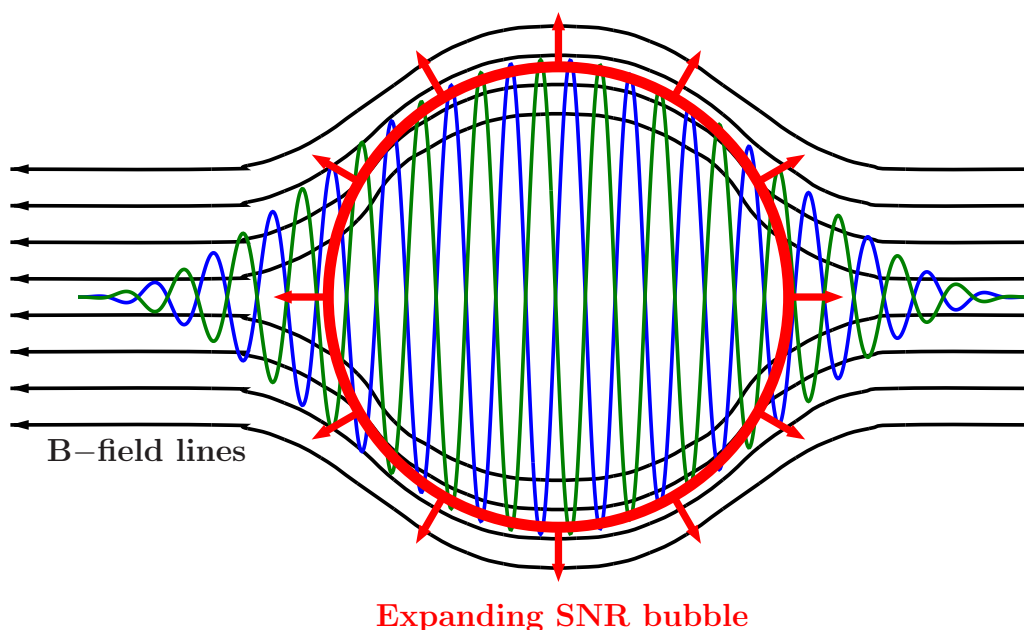
Figure 9.1: (a) A very simple case of a uniform magnetic field structure in the ISM. The blue sinusoid indicates a possible path of a particle spiralling around the magnetic field lines (of course, this is just a 2D representation). (b) If the magnetic field lines are frozen into the ISM, then an expanding SNR bubble might be able to distort the magnetic field structure in such a way that a magnetic bottle is produced. The blue sinusoid is a cartoon representation of a possible particle path through the magnetic field, and the idea is that the radius of curvature decreases in the regions of high magnetic flux density, such that the velocity component parallel to the magnetic field lines changes sign, and the particle moves back in the opposite direction, as indicated by the green sinusoid. As such, particles can become trapped inside this magnetic bottle nebula, and would continue to radiate via synchrotron emission, producing something like the observed W 50.

nebula by SS 433's jets would naturally follow a path that traces out the morphology of SS 433. Furthermore, this might also reproduce the annular structure in W 50's lobes.

9.5.3 Future3: Observations of jet refocusing

In §7.8 of this thesis, I describe two modes of hydrodynamic refocusing of hollow conical jets: *Kinetic refocusing* and *Static refocusing*. I intend to investigate whether such refocusing can be observed directly in SS 433's corkscrew jets, via deep radio interferometric observations with the VLA.
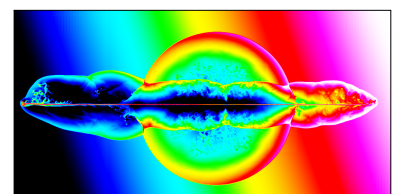
Bibliography

Begelman, M. C., Hatchett, S. P., McKee, C. F., Sarazin, C. L. & Arons, J., 1980. Beam models for SS 433. *ApJ*, **238**, 722–730.

Biretta, J. A., Zhou, F. & Owen, F. N., 1995. Detection of Proper Motions in the M87 Jet. *ApJ*, **447**, 582–+.

Blandford, R. D. & Znajek, R. L., 1977. Electromagnetic extraction of energy from Kerr black holes. *MNRAS*, **179**, 433–456.

Blundell, K. M. & Bowler, M. G., 2004. Symmetry in the Changing Jets of SS 433 and Its True Distance from Us. *ApJ*, **616**, L159–L162.

Blundell, K. M. & Bowler, M. G., 2005. Jet Velocity in SS 433: Its Anticorrelation with Precession-Cone Angle and Dependence on Orbital Phase. *ApJ*, **622**, L129–L132.

Blundell, K. M., Bowler, M. G. & Schmidtobreick, L., 2007. Fluctuations and symmetry in the speed and direction of the jets of SS 433 on different timescales. *A&A*, **474**, 903–910.

Blundell, K. M., Bowler, M. G. & Schmidtobreick, L., 2008. SS 433: Observation of the Circumbinary Disk and Extraction of the System Mass. *ApJ*, **678**, L47–L50.

Blundell, K. M., Mioduszewski, A. J., Muxlow, T. W. B., Podsiadlowski, P. & Rupen, M. P., 2001. Images of an Equatorial Outflow in SS 433. *ApJ*, **562**, L79–L82.

Bock, D., Large, M. I. & Sadler, E. M., 1999. SUMSS: A Wide-Field Radio Imaging Survey of the Southern Sky. I. Science Goals, Survey Design, and Instrumentation. *AJ*, **117**, 1578–1593.

Bondi, H., 1952. On spherically symmetrical accretion. *MNRAS*, **112**, 195–+.

Bondi, H. & Hoyle, F., 1944. On the mechanism of accretion by stars. *MNRAS*, **104**, 273–+.

Bridle, A. H. & Perley, R. A., 1984. Extragalactic Radio Jets. *ARA&A*, **22**, 319–358.

Brinkmann, W., Aschenbach, B. & Kawai, N., 1996. ROSAT observations of the W 50/SS 433 system. *A&A*, **312**, 306–316.

Brinkmann, W., Pratt, G. W., Rohr, S., Kawai, N. & Burwitz, V., 2007. XMM-Newton observations of the eastern jet of SS 433. *A&A*, **463**, 611–619.
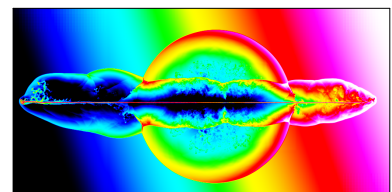
Burns, W. R. & Yao, S. S., 1970. A New Approach to Aperture Synthesis Processing. *A&A*, **6**, 481–+.

Capetti, A., Macchetto, F. D., Sparks, W. B. & Biretta, J. A., 1997. HST polarization observations of the jet of M87. *A&A*, **317**, 637–645.

Chevalier, R. A. & Gardner, J., 1974. The Evolution of Supernova Remnants. 11. Models of an Explosion in a Plane-Stratified Medium. *ApJ*, **192**, 457–464.

Clark, B. G., 1980. An efficient implementation of the algorithm 'CLEAN'. *A&A*, **89**, 377–+.

Clarke, D. A., Burns, J. O. & Norman, M. L., 1989. Numerical observations of a simulated jet with a passive helical magnetic field. *ApJ*, **342**, 700–717.

Colella, P. & Woodward, P. R., 1984. The Piecewise Parabolic Method (PPM) for Gas-Dynamical Simulations. *Journal of Computational Physics*, **54**, 174–201.

Collins, G. W. & Scher, R. W., 2002. A revised dynamical model for SS433 and the nature of the system. *MNRAS*, **336**, 1011–1020.

Condon, J. J., Cotton, W. D., Greisen, E. W., Yin, Q. F., Perley, R. A., Taylor, G. B. & Broderick, J. J., 1998. The NRAO VLA Sky Survey. *AJ*, **115**, 1693–1716.

Crampton, D. & Hutchings, J. B., 1981. The SS 433 binary system. *ApJ*, **251**, 604–610.

Curtis, H. D., 1918. Dark Nebulae. *PASP*, **30**, 65–+.

Dehnen, W. & Binney, J., 1998. Mass models of the Milky Way. *MNRAS*, **294**, 429–+.

D'Odorico, S., Oosterloo, T., Zwitter, T. & Calvani, M., 1991. Evidence that the compact object in SS433 is a neutron star and not a black hole. *Nature*, **353**, 329–331.

Dubner, G. M., Holdaway, M., Goss, W. M. & Mirabel, I. F., 1998. A High-Resolution Radio Study of the W50-SS 433 System and the Surrounding Medium. *AJ*, **116**, 1842–1855.

Eichler, D., 1983. Focusing of high-Mach number jets by an ambient medium. *ApJ*, **272**, 48–53.

Eikenberry, S. S., Cameron, P. B., Fierce, B. W., Kull, D. M., Dror, D. H., Houck, J. R. & Margon, B., 2001. Twenty Years of Timing SS 433. *ApJ*, **561**, 1027–1033.

Elston, R. & Baum, S., 1987. High-resolution radio observations of W50, the remnant associated with SS 433. *AJ*, **94**, 1633–1640.

Fabian, A. C. & Rees, M. J., 1979. SS 433 - A double jet in action. *MNRAS*, **187**, 13P–16P.

Fabrika, S., 2004. The jets and supercritical accretion disk in SS433. *Astrophysics and Space Physics Reviews*, **12**, 1–152.

Fryxell, B., Olson, K., Ricker, P., Timmes, F. X., Zingale, M., Lamb, D. Q., MacNeice, P., Rosner, R., Truran, J. W. & Tufo, H., 2000. FLASH: An Adaptive Mesh Hydrodynamics Code for Modeling Astrophysical Thermonuclear Flashes. *ApJS*, **131**, 273–334.

Fuchs, Y., Koch Miramond, L. & Ábrahám, P., 2006. SS 433: a phenomenon imitating a Wolf-Rayet star. *A&A*, **445**, 1041–1052.

Gallo, E., Fender, R. & Kaiser, C., 2005. Black hole X-ray binary jets. In L. Burderi, L. A. Antonelli, F. D'Antona, T. di Salvo, G. L. Israel, L. Piersanti, A. Tornambè, & O. Straniero, ed., *Interacting Binaries: Accretion, Evolution, and Outcomes*, vol. 797 of *American Institute of Physics Conference Series*, 189–196.

Gies, D. R., Huang, W. & McSwain, M. V., 2002. The Spectrum of the Mass Donor Star in SS 433. *ApJ*, **578**, L67–L70.

Gillessen, S., Eisenhauer, F., Fritz, T. K., Bartko, H., Dodds-Eden, K., Pfuhl, O., Ott, T. & Genzel, R., 2009. The Orbit of the Star S2 Around SGR A* from Very Large Telescope and Keck Data. *ApJ*, **707**, L114–L117.

Glazebrook, K. & Economou, F., 1997. PDL: The Perl Data Language. *Dr. Dobbs Journal*, "".

Godunov, S. K., 1959. A Difference Scheme for Numerical Solution of Discontinuos Solution of Hydrodynamic Equations. *Math. Sbornik*, **47**, 271–306.

Goodall, P. T., Alouni-Bibi, F. & Blundell, K. M., 2010. When Jets and Supernova Collide. *A&A*, **In preparation.**, "".

Goranskii, V. P., Esipov, V. F. & Cherepashchuk, A. M., 1998. Analysis of multi-color photometric observations of SS433 (V1343 Aql). *Astronomy Reports*, **42**, 336–345.

Gregory, P. C., Scott, W. K., Douglas, K. & Condon, J. J., 1996. The GB6 Catalogue of Radio Sources. *ApJS*, **103**, 427–+.

Hartigan, P., Heathcote, S., Morse, J. A., Reipurth, B. & Bally, J., 2005. Proper Motions of the HH 47 Jet Observed with the Hubble Space Telescope. *AJ*, **130**, 2197–2205.

Hillwig, T. C., Gies, D. R., Huang, W., McSwain, M. V., Stark, M. A., van der Meer, A. & Kaper, L., 2004. Identification of the Mass Donor Star's Spectrum in SS 433. *ApJ*, **615**, 422–431.

Hjellming, R. M., 2000. Light Curves and Radio Structure of the 1999 September Transient Event in V4641 Sagittarii (=XTE J1819-254=SAX J1819.3-2525). *ApJ*, **544**, 977–992.

Hjellming, R. M. & Johnston, K. J., 1981. An analysis of the proper motions of SS 433 radio jets. *ApJ*, **246**, L141–L145.

Högbom, J. A., 1974. Aperture Synthesis with a Non-Regular Distribution of Interferometer Baselines. *A&AS*, **15**, 417–+.
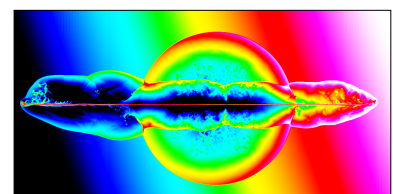
Hoyle, F. & Lyttleton, R. A., 1941. On the accretion theory of stellar evolution. *MNRAS*, **101**, 227–+.

Jun, B. & Norman, M. L., 1996. On the Origin of Radial Magnetic Fields in Young Supernova Remnants. *ApJ*, **472**, 245–+.

King, A. R., Taam, R. E. & Begelman, M. C., 2000. The Evolutionary Status of SS 433. *ApJ*, **530**, L25–L28.

Kochanek, C. S. & Hawley, J. F., 1990. Hollow conical jet models for SS 433 - A paradigm lost? *ApJ*, **350**, 561–577.

Liu, Q. Z., Paradijs, J. v. & Heuvel, E. P. J., 2006. Catalogue of high-mass X-ray binaries in the Galaxy (4th edition). *A&A*, **455**.

Liu, Q. Z., Paradijs, J. v. & Heuvel, E. P. J., 2007. A catalogue of low-mass X-ray binaries in the Galaxy, LMC, and SMC (Fourth edition). *A&A*, **455**.

Livio, M. & Soker, N., 2001. The "Twin Jet" Planetary Nebula M2-9. *ApJ*, **552**, 685–691.

Lockman, F. J., Blundell, K. M. & Goss, W. M., 2007. The distance to SS433/W50 and its interaction with the interstellar medium. *MNRAS*, **381**, 881–893.

Lopez, L. A., Marshall, H. L., Canizares, C. R., Schulz, N. S. & Kane, J. F., 2006. Determining the Nature of the SS 433 Binary from an X-Ray Spectrum during Eclipse. *ApJ*, **650**, 338–349.

Madrid, J. P., Sparks, W. B., Harris, D. E., Perlman, E. S., Macchetto, D. & Biretta, J., 2007. Deep Hubble space telescope ultraviolet imaging of the M87 jet. *Ap&SS*, **311**, 329–333.

Margon, B. & Anderson, S. F., 1989. Ten years of SS 433 kinematics. *ApJ*, **347**, 448–454.

Margon, B., Ford, H. C., Katz, J. I., Kwitter, K. B., Ulrich, R. K., Stone, R. P. S. & Klemola, A., 1979a. The bizarre spectrum of SS 433. *ApJ*, **230**, L41–L45.

Margon, B., Grandi, S. A., Stone, R. P. S. & Ford, H. C., 1979b. Enormous periodic Doppler shifts in SS 433. *ApJ*, **233**, L63–L68.

Marshall, H. L., Miller, B. P., Davis, D. S., Perlman, E. S., Wise, M., Canizares, C. R. & Harris, D. E., 2002. A High-Resolution X-Ray Image of the Jet in M87. *ApJ*, **564**, 683–687.

Milgrom, M., 1979. On the interpretation of the large variations in the line positions in SS433. *A&A*, **76**, L3–L6.

Miller-Jones, J. C. A., Blundell, K. M., Rupen, M. P., Mioduszewski, A. J., Duffy, P. & Beasley, A. J., 2004. Time-sequenced Multi-Radio Frequency Observations of Cygnus X-3 in Flare. *ApJ*, **600**, 368–389.

Mioduszewski, A. J., Rupen, M. P., Hjellming, R. M., Pooley, G. G. & Waltman, E. B., 2001. A One-sided Highly Relativistic Jet from Cygnus X-3. *ApJ*, **553**, 766–775.

Mioduszewski, A. J., Rupen, M. P., Walker, R. C. & Taylor, G. B., 2003. Unraveling a Precessing Jet: Forty Daily VLBA Observations of SS433. In *Bulletin of the American Astronomical Society*, vol. 35 of *Bulletin of the American Astronomical Society*, 1254–+.

Mirabel, I. F. & Rodríguez, L. F., 1994. A superluminal source in the Galaxy. *Nature*, **371**, 46–48.

Mirabel, I. F. & Rodríguez, L. F., 1998. Microquasars in our Galaxy. *Nature*, **392**, 673–676.

Mirabel, I. F., Rodriguez, L. F., Cordier, B., Paul, J. & Lebrun, F., 1992. A double-sided radio jet from the compact Galactic Centre annihilator 1E140.7 - 2942. *Nature*, **358**, 215–217.

Moldowan, A., Safi-Harb, S., Fuchs, Y. & Dubner, G., 2005. A multi-wavelength study of the western lobe of W50 powered by the galactic microquasar SS 433. *Advances in Space Research*, **35**, 1062–1065.

Nipoti, C., Blundell, K. M. & Binney, J., 2005. Radio-loud flares from microquasars and radio-loudness of quasars. *MNRAS*, **361**, 633–637.

Olson, K. M., MacNeice, P., Fryxell, B., Ricker, P., Timmes, F. X. & Zingale, M., 1999. PARAMESH: A Parallel, Adaptive Mesh Refinement Toolkit and Performance of the ASCI/FLASH code. In *Bulletin of the American Astronomical Society*, vol. 31 of *Bulletin of the American Astronomical Society*, 1430–+.

Paragi, Z., Vermeulen, R. C., Fejes, I., Schilizzi, R. T., Spencer, R. E. & Stirling, A. M., 1999a. The inner radio jet region and the complex environment of SS433. *A&A*, **348**, 910–916.

Paragi, Z., Vermeulen, R. C., Fejes, I., Schilizzi, R. T., Spencer, R. E. & Stirling, A. M., 1999b. VLBA multi-frequency monitoring of SS433. *New Astronomy Review*, **43**, 553–557.

Peres, G., Serio, S., Vaiana, G. S. & Rosner, R., 1982. Coronal closed structures. IV - Hydrodynamical stability and response to heating perturbations. *ApJ*, **252**, 791–799.

Perez M., S. & Blundell, K. M., 2009. Inflow and outflow from the accretion disc of the microquasar SS433: UKIRT spectroscopy. *MNRAS*, **397**, 849–856.

Perley, R. A., Dreher, J. W. & Cowan, J. J., 1984. The jet and filaments in Cygnus A. *ApJ*, **285**, L35–L38.

Raga, A. C., Esquivel, A., Riera, A. & Velázquez, P. F., 2007. The Three-dimensional Structure of a Radiative, Cosmic Bullet Flow. *ApJ*, **668**, 310–315.

Rees, M. J., 1984. Black Hole Models for Active Galactic Nuclei. *ARA&A*, **22**, 471–506.
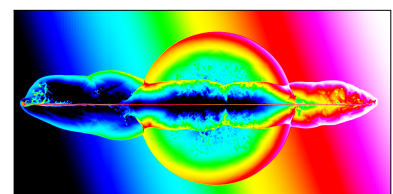
Rengelink, R. B., Tang, Y., de Bruyn, A. G., Miley, G. K., Bremer, M. N., Roettengering, H. J. A. & Bremer, M. A. R., 1997. The Westerbork Northern Sky Survey (WENSS), I. A 570 square degree Mini-Survey around the North Ecliptic Pole. *A&AS*, **124**, 259–280.

Rosner, R., Tucker, W. H. & Vaiana, G. S., 1978. Dynamics of the quiescent solar corona. *ApJ*, **220**, 643–645.

Safi-Harb, S. & Petre, R., 1999. Rossi X-Ray Timing Explorer Observations of the Eastern Lobe of W50 Associated with SS 433. *ApJ*, **512**, 784–792.

Sedov, L. I., 1959. Similarity and Dimensional Methods in Mechanics. *New York: Academic Press*.

Smith, N., Balick, B. & Gehrz, R. D., 2005. Kinematic Structure of H_2 and [Fe II] in the Bipolar Planetary Nebula M2-9. *AJ*, **130**, 853–861.

Sod, G. A., 1978. A survey of several finite difference methods for systems of nonlinear hyperbolic conservation laws. *Journal of Computational Physics*, **27**, 1–31.

Stephenson, C. B. & Sanduleak, N., 1977. New H-alpha emission stars in the Milky Way. *ApJS*, **33**, 459–469.

Tadhunter, C., Marconi, A., Axon, D., Wills, K., Robinson, T. G. & Jackson, N., 2003. Spectroscopy of the near-nuclear regions of Cygnus A: estimating the mass of the supermassive black hole. *MNRAS*, **342**, 861–875.

Taylor, G., 1950. The Formation of a Blast Wave by a Very Intense Explosion. II. The Atomic Explosion of 1945. *Royal Society of London Proceedings Series A*, **201**, 175–186.

Taylor, G. B., Carilli, C. L. & Perley, R. A., eds., 1999. *Synthesis Imaging in Radio Astronomy II*, vol. 180 of *Astronomical Society of the Pacific Conference Series*.

Thompson, A. R., Clark, B. G., Wade, C. M. & Napier, P. J., 1980. The Very Large Array. *ApJS*, **44**, 151–167.

Thompson, A. R., Moran, J. M. & Swenson, G. W., 1986. *Interferometry and synthesis in radio astronomy*.

Tudose, V., Fender, R. P., Kaiser, C. R., Tzioumis, A. K., van der Klis, M. & Spencer, R. E., 2006. The large-scale jet-powered radio nebula of Circinus X-1. *MNRAS*, **372**, 417–424.

van den Heuvel, E. P. J., 1977. Evolutionary Processes in X-Ray Binaries and Their Progenitor Systems. In M. D. Papagiannis, ed., *Eighth Texas Symposium on Relativistic Astrophysics*, vol. 302 of *New York Academy Sciences Annals*, 14–+.

Velázquez, P. F. & Raga, A. C., 2000. A numerical simulation of the W 50-SS 433 system. *A&A*, **362**, 780–785.

Vermeulen, R. C., Icke, V., Schilizzi, R. T., Fejes, I. & Spencer, R. E., 1987. Evolving radio structure of the binary star SS433 at a resolution of 15 MARC S. *Nature*, **328**, 309–313.

Yamauchi, S., Kawai, N. & Aoki, T., 1994. A non-thermal X-ray spectrum from the supernova remnant W 50. *PASJ*, **46**, L109–L113.

Zavala, J., Velázquez, P. F., Cerqueira, A. H. & Dubner, G. M., 2008. Three-dimensional hydrodynamical simulations of the large-scale structure of W50-SS433. *MNRAS*, **387**, 839–844.
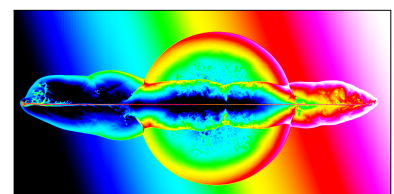
Appendix A

Jet Simulation Images

This appendix contains large, individual images of each panel from Figure 7.2.

(a) **Jet 1** : $\dot{M}_{jet} = 10^{-4} M_\odot \, \mathrm{yr}^{-1}$, $n_0 = 1$ particle cm^{-3}, $z = 40\,\mathrm{pc}$, $\theta_0 = 0.0°$, $\dot{\theta} = 0.0° \, \mathrm{yr}^{-1}$

Sim-time: 2200 years.

The axes show the displacement from SS433 in parsecs.
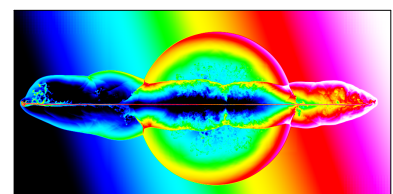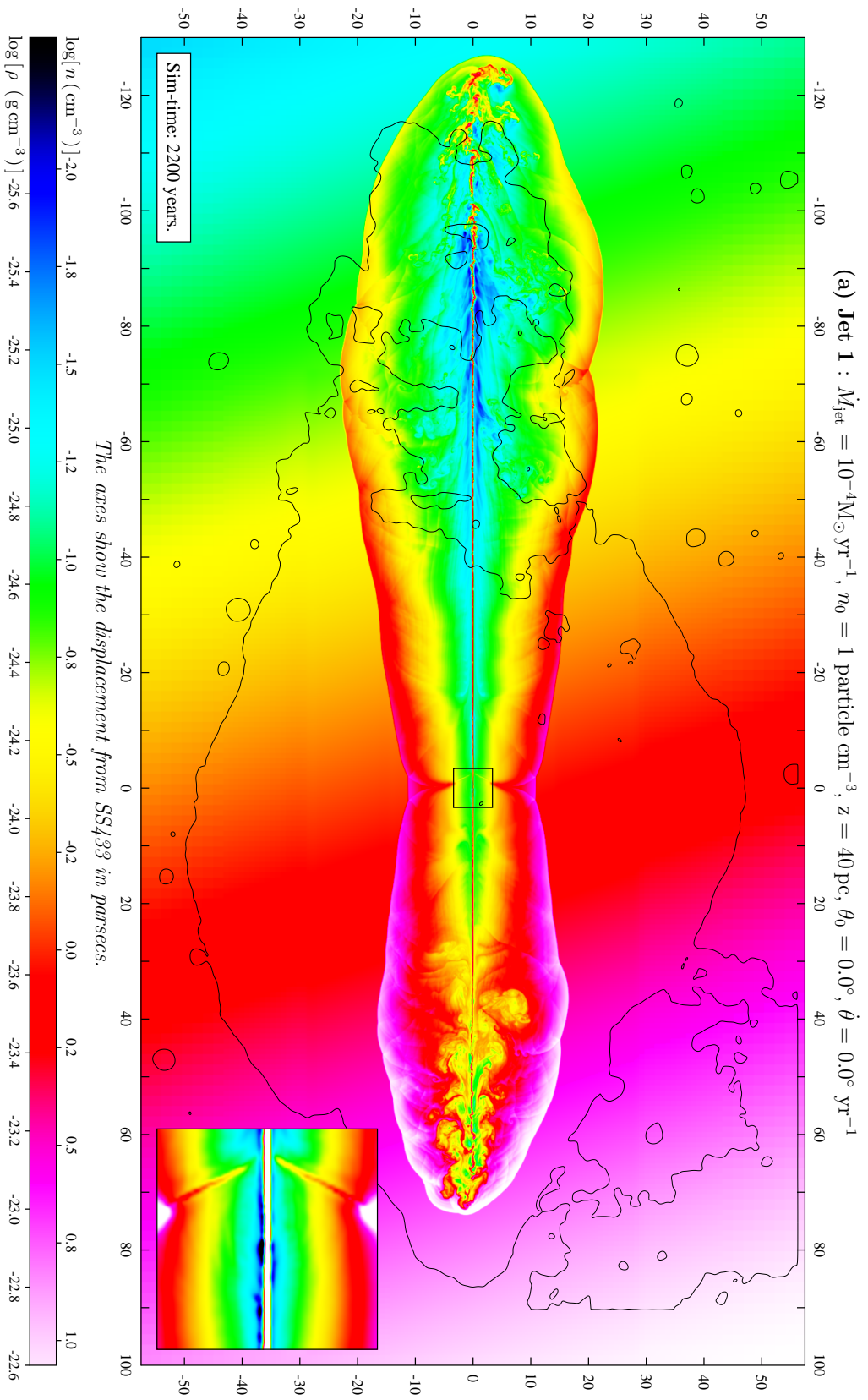
Figure A.1: This is the full size version of Figure 7.2a.

(b) **Jet 2** : $\dot{M}_{\text{jet}} = 10^{-5} \text{M}_\odot \, \text{yr}^{-1}$

Sim-time: 3600 years.

The axes show the displacement from SS433 in parsecs.

Figure A.2: This is the full size version of Figure 7.2b.

(c) Jet 3 : $\dot{M}_{\text{jet}} = 10^{-6} M_{\odot} \, \text{yr}^{-1}$

Sim-time: 8000 years.

The axes show the displacement from SS433 in parsecs.

$\log [\, n \, (\text{cm}^{-3})\,]$

$\log [\, \rho \, (\text{g cm}^{-3})\,]$

Figure A.3: This is the full size version of Figure 7.2c.

(d) **Jet 4** : $n_0 = 0.1$ particles cm^{-3}

The axes show the displacement from SS433 in parsecs.

Sim-time: 1650 years.

$\log[n\,(cm^{-3})]$

$\log[\rho\,(g\,cm^{-3})]$
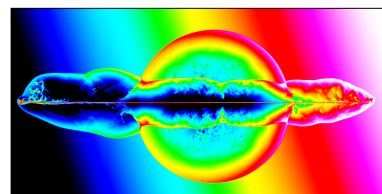
Figure A.4: This is the full size version of Figure 7.2d.

(e) Jet 5 : $\theta_0 = 10.0°$

Sim-time: 4000 years.

The axes show the displacement from SS433 in parsecs.

$\log[\rho\,(\mathrm{g\,cm^{-3}})]$

$\log[n\,(\mathrm{cm^{-3}})]$
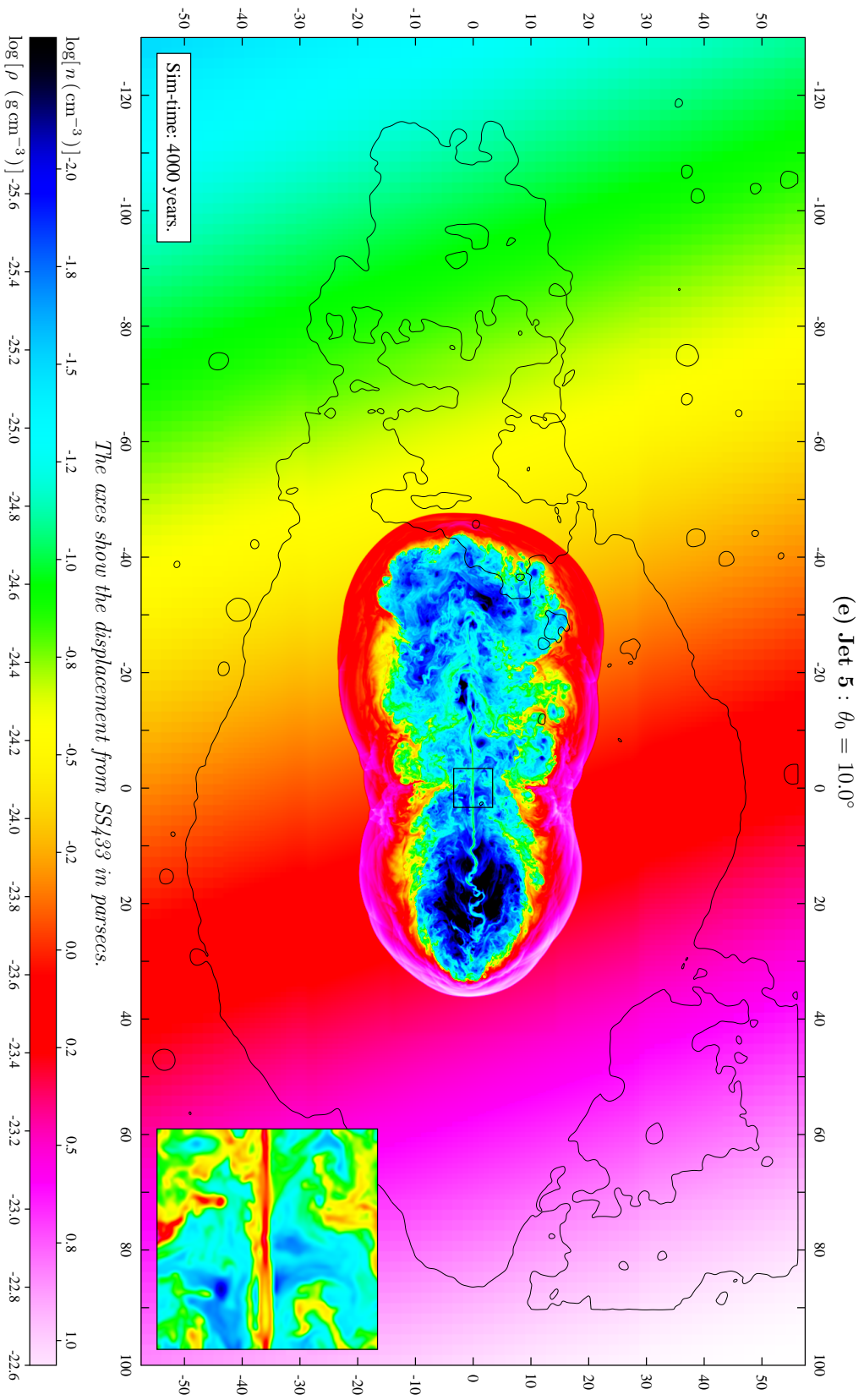
Figure A.5: This is the full size version of Figure 7.2e.

(f) **Jet 6** : $\theta_0 = \theta_{SS433}^{\circ}$

Sim-time: 4000 years.

The axes show the displacement from SS433 in parsecs.

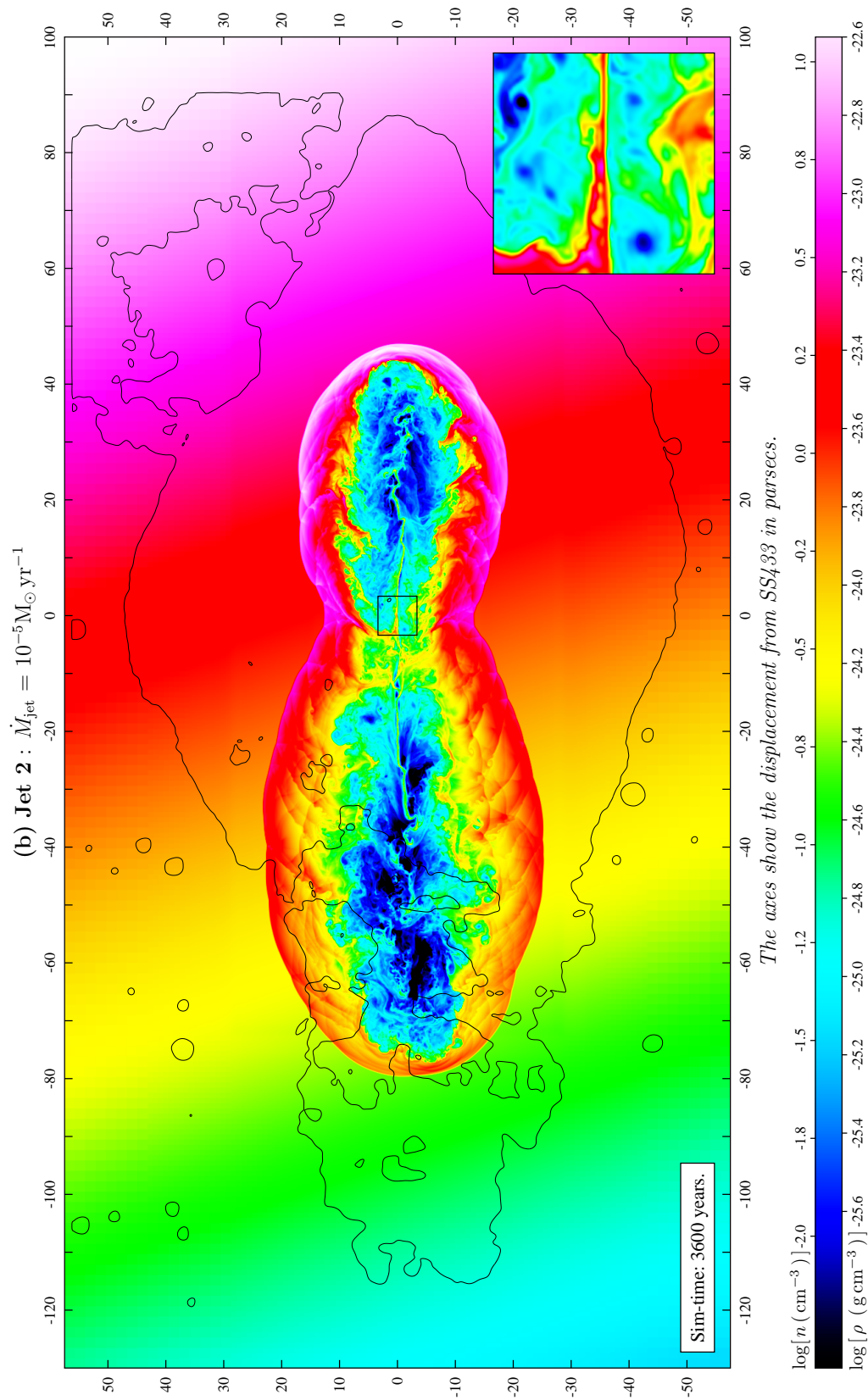$\log[n\,(\mathrm{cm}^{-3})]$
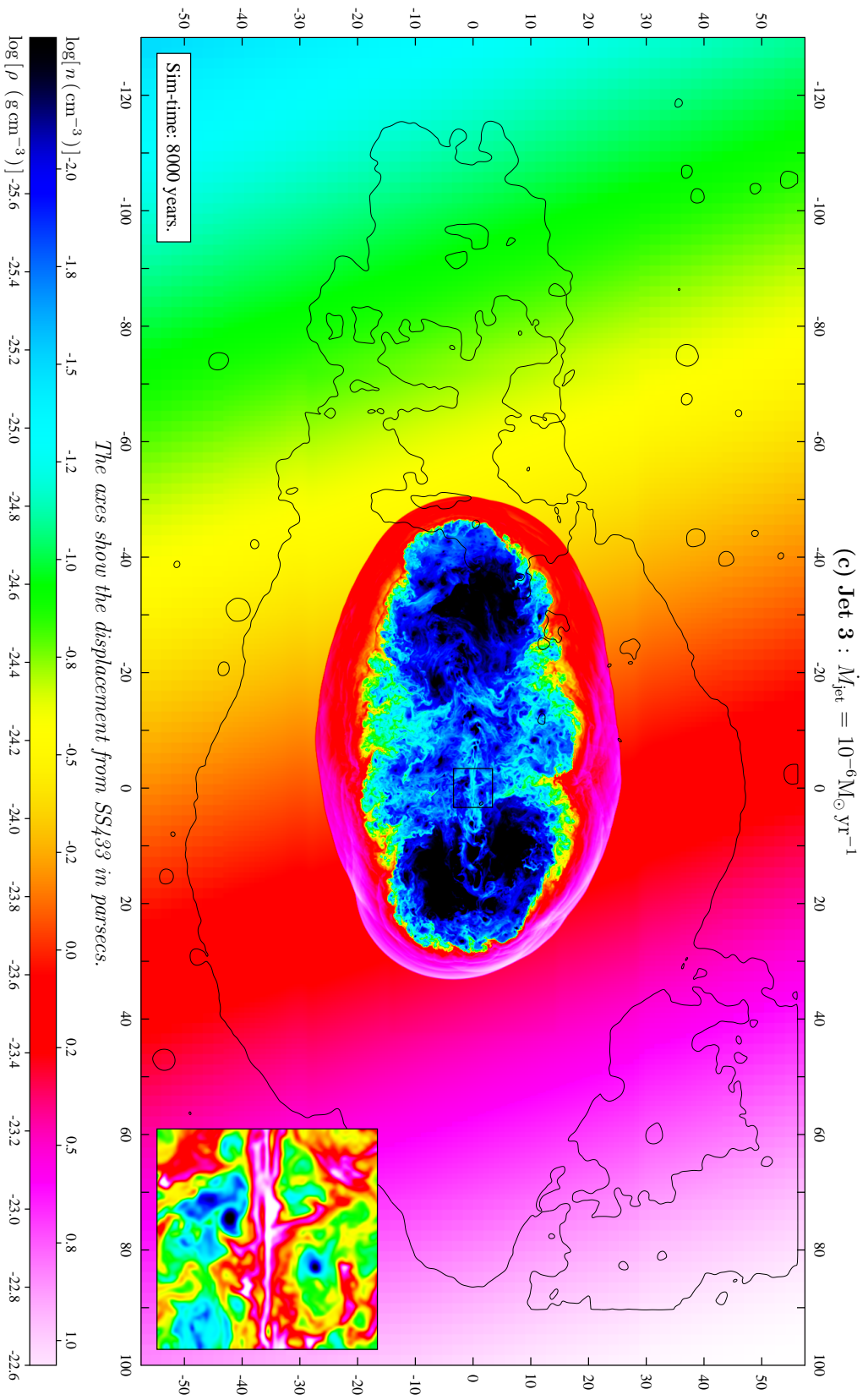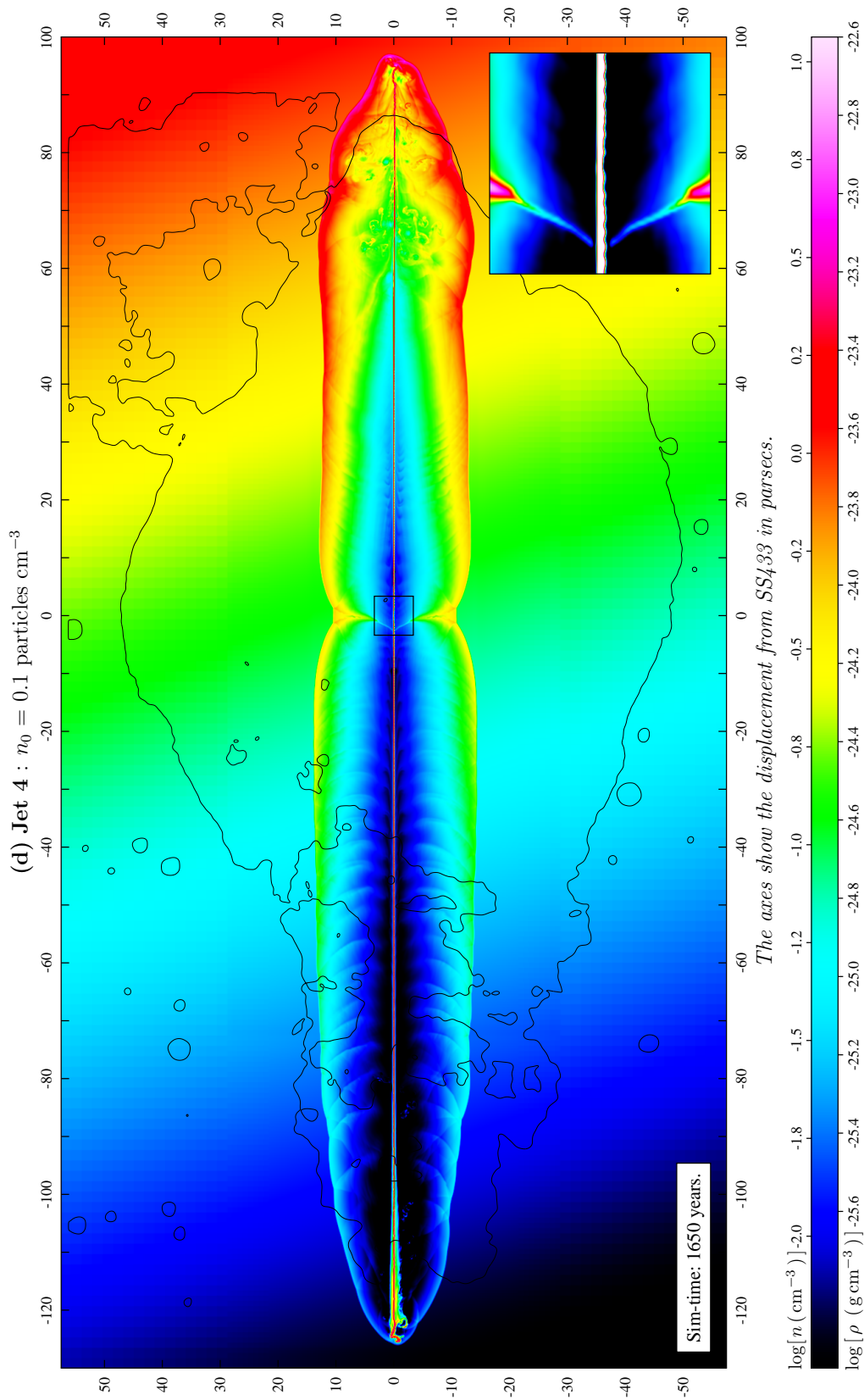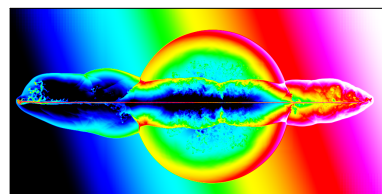$\log[\rho\,(\mathrm{g\,cm}^{-3})]$
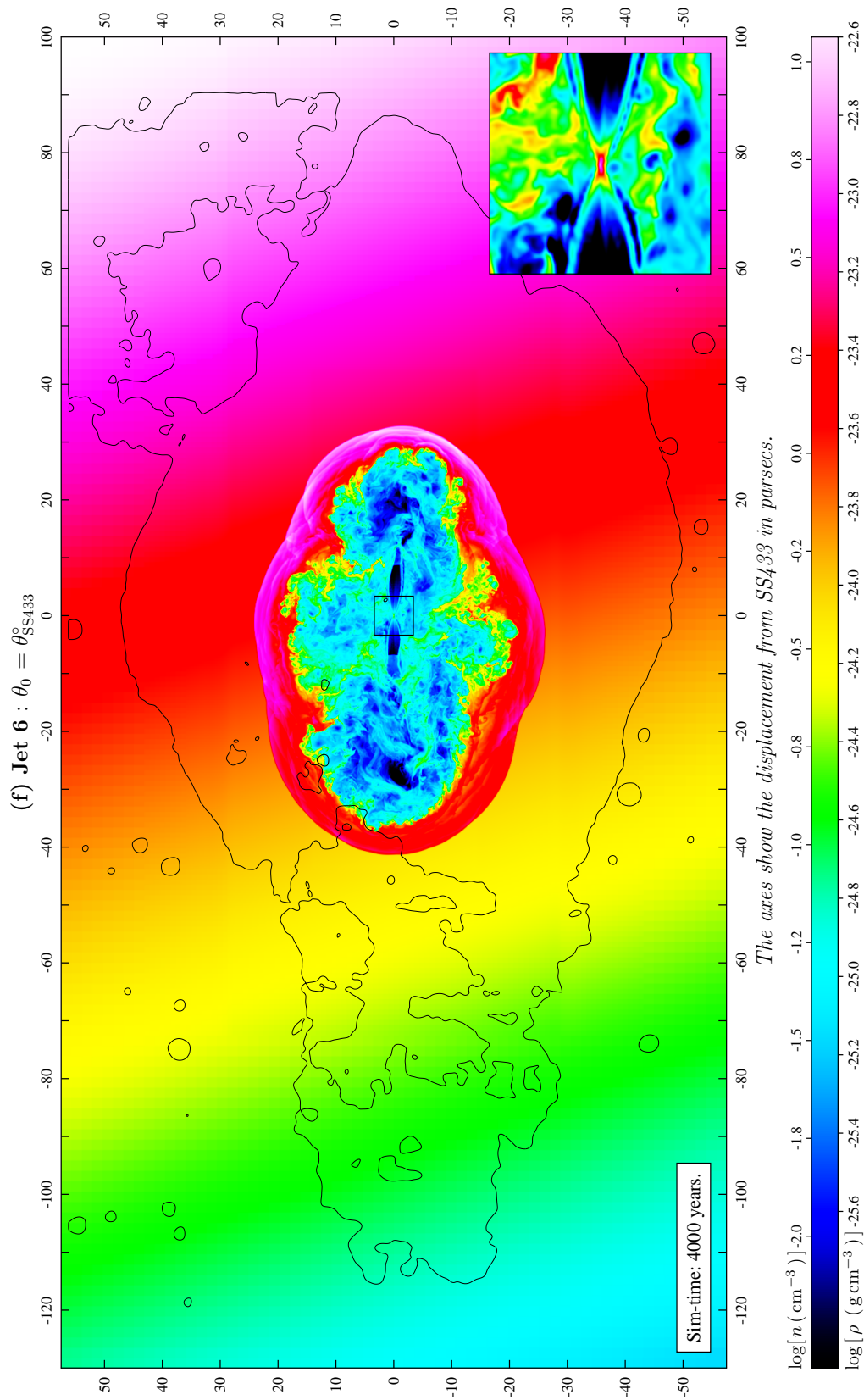
Figure A.6: This is the full size version of Figure 7.2f.
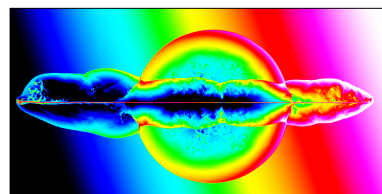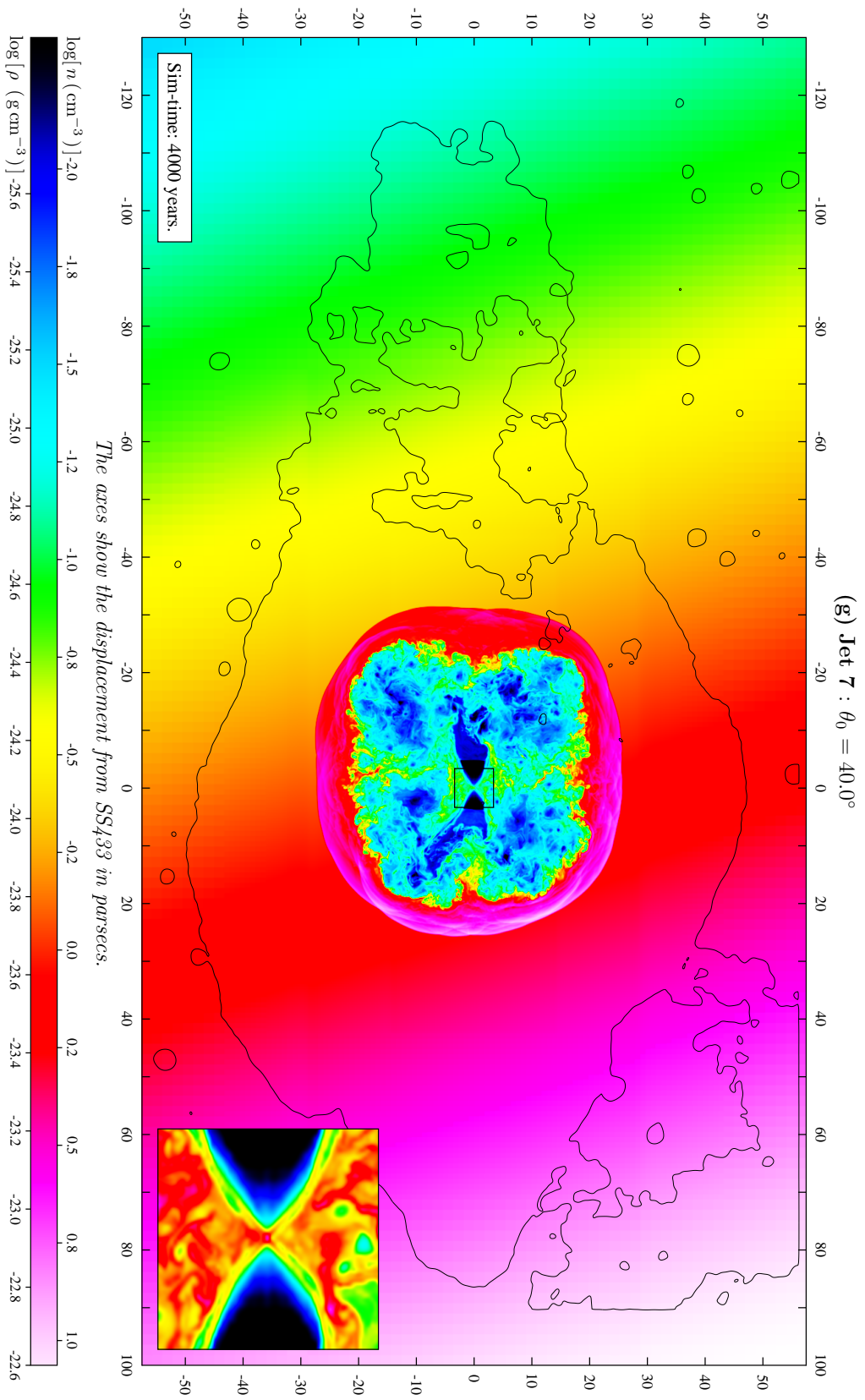
Figure A.7: This is the full size version of Figure 7.2g.

(h) Jet 8 : $n_0 = 0.1$ particles cm^{-3}, $\dot{\theta} = [10^{-3}\,\theta_{SS433}]°$ yr^{-1}, $\theta_{max} = \theta^°_{SS433}$

Sim-time: 2250 years.

The axes show the displacement from SS433 in parsecs.

$\log[n\,(\mathrm{cm}^{-3})]$

$\log[\rho\,(\mathrm{g\,cm}^{-3})]$
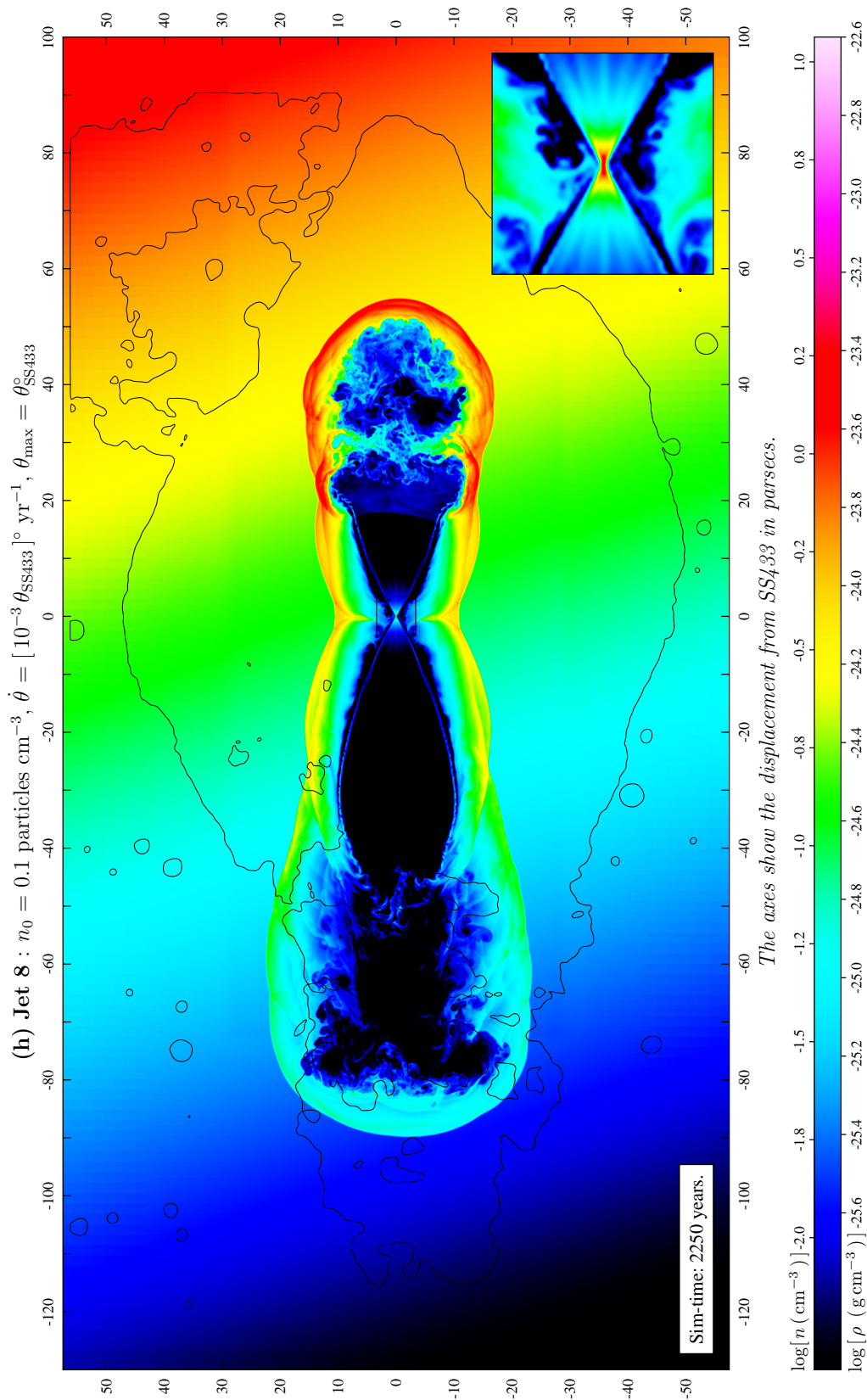
Figure A.8: This is the full size version of Figure 7.2h.

(i) **Jet 9** : Jet Model 2 with 3 Outbursts : $n_0 = 0.1$ particles cm^{-3}.

Sim-time: 2700 years.

The axes show the displacement from SS433 in parsecs.

$\log \left[n \left(\text{cm}^{-3} \right) \right]$

$\log \left[\rho \left(\text{g cm}^{-3} \right) \right]$
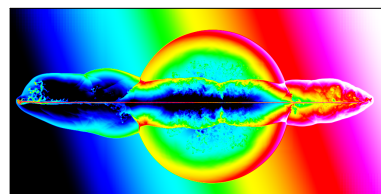
Figure A.9: This is the full size version of Figure 7.2i.

(j) **Jet 10** : Jet Model 3 : Fireball Jet. $n_0 = 0.1$ particles cm^{-3}.

The axes show the displacement from SS433 in parsecs.
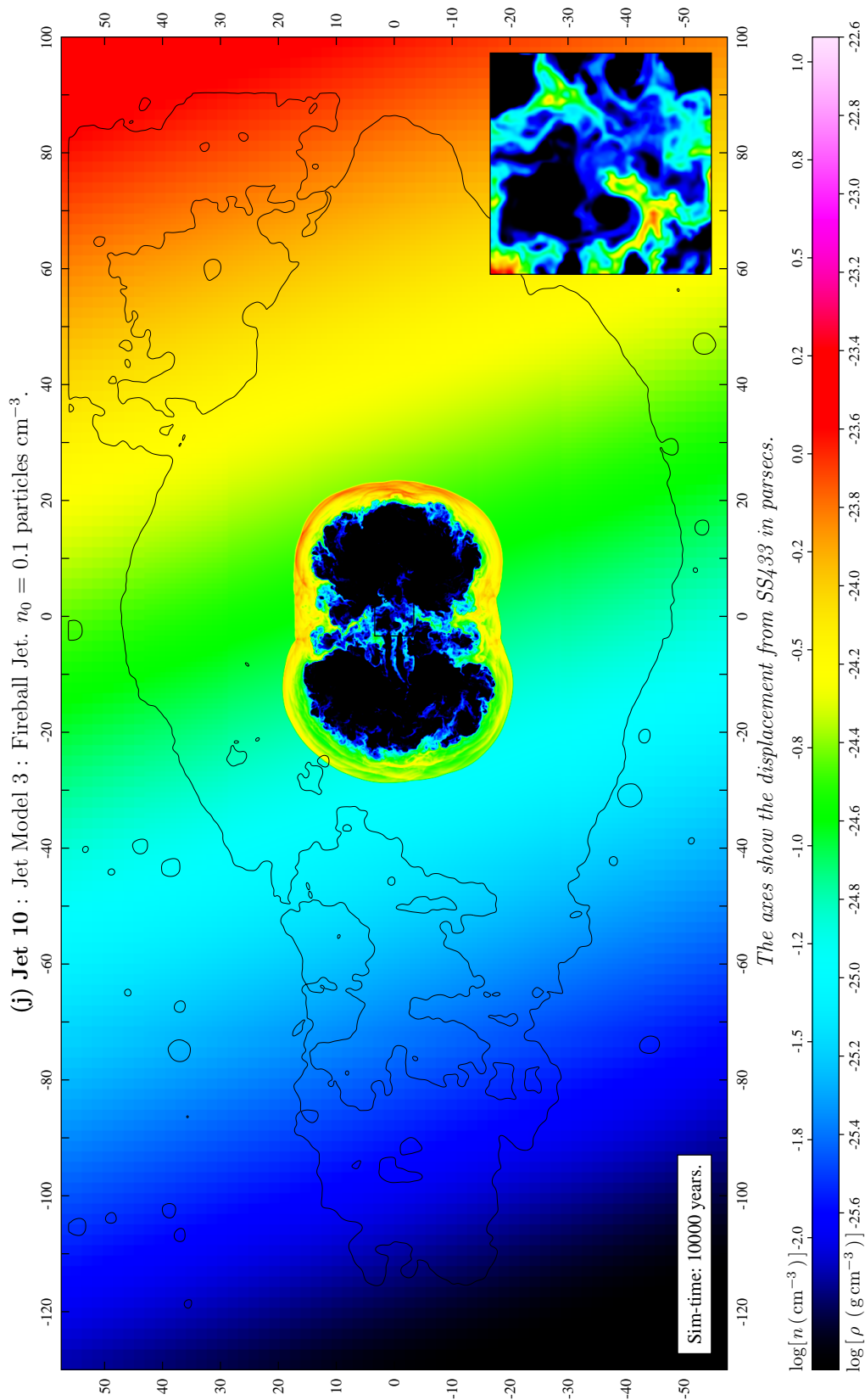
Figure A.10: This is the full size version of Figure 7.2j.

Appendix B

SNRJet Simulation Images

This appendix contains large, individual images of each panel from Figure 8.1.

(a) **SNR.Jet1 : Density**

ISM: $n_0 = 0.2\,\mathrm{cm^{-3}}$, $z = 40\,\mathrm{pc}$
SNR: $E_{\mathrm{blast}} = 10^{51}$ ergs
Jets: $M_{\mathrm{jet}} = 10^{-4}\,\mathrm{M_\odot\,yr^{-1}}$
$\theta_0 = 0^\circ$, $\dot{\theta} = 0$

SNR-time: 21,000 years
Jet-time: 1,650 years
W50 age: 22,650 years

Speed (% c)

log [n (cm^{-3})]

The axes show the displacement from SS433 in parsecs.
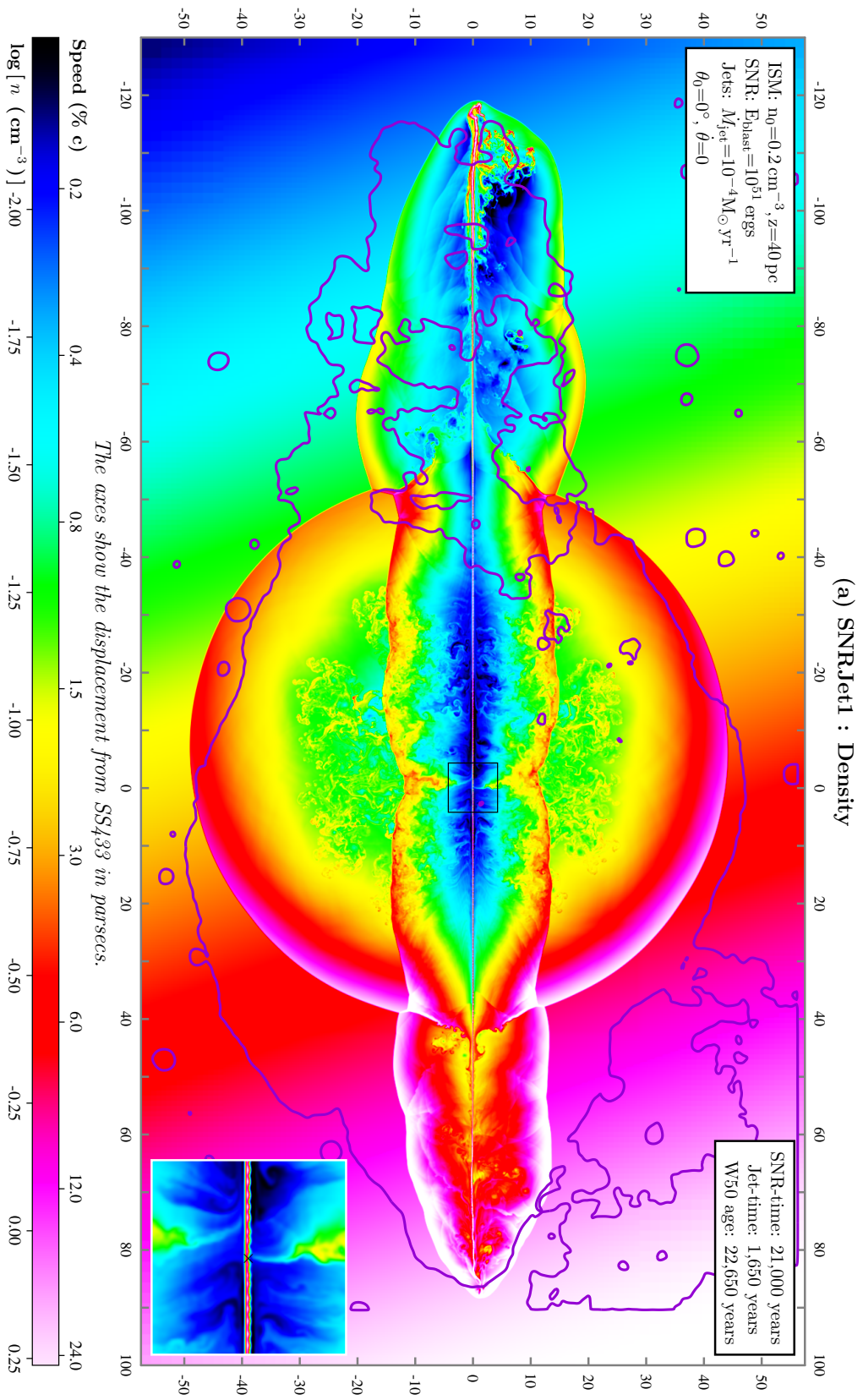
Figure B.1: This is the full size version of Figure 8.1a.

(b) **SNRJet1** : Gas speed

SNR-time: 21,000 years
Jet-time: 1,650 years
W50 age: 22,650 years

ISM: $n_0 = 0.2\,\mathrm{cm}^{-3}$, $z = 40\,\mathrm{pc}$
SNR: $E_{blast} = 10^{51}\,\mathrm{ergs}$
Jets: $\dot{M}_{jet} = 10^{-4}\,\mathrm{M_\odot\,yr^{-1}}$
$\theta_0 = 0°$, $\dot{\theta} = 0$

The axes show the displacement from SS433 in parsecs.

Speed (% c)   0.2   0.4   0.8   1.5   3.0   6.0   12.0   24.0

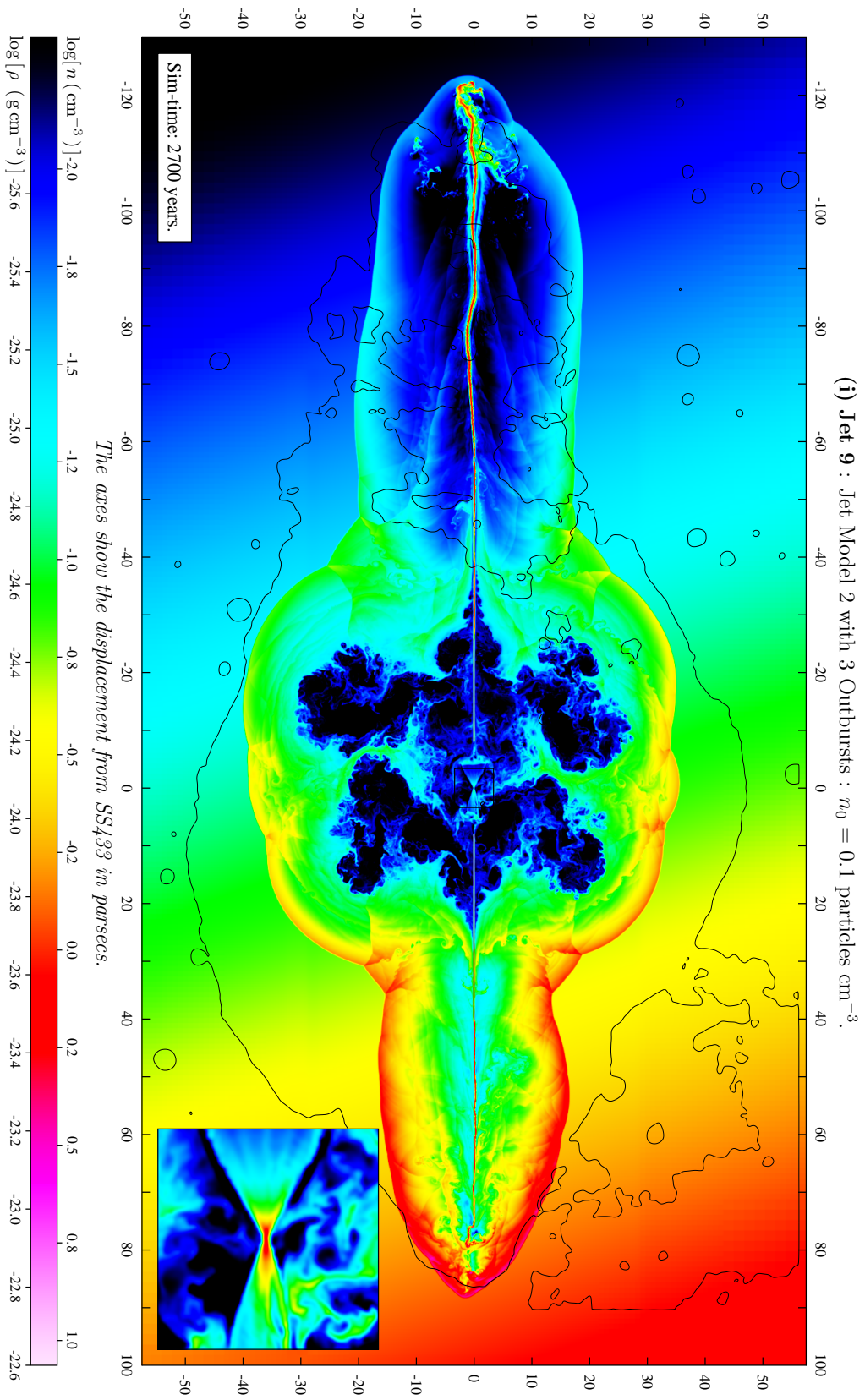$\log\,[\,n\,\,(\mathrm{cm}^{-3})\,]$ -2.00   -1.75   -1.50   -1.25   -1.00   -0.75   -0.50   -0.25   0.00   0.25
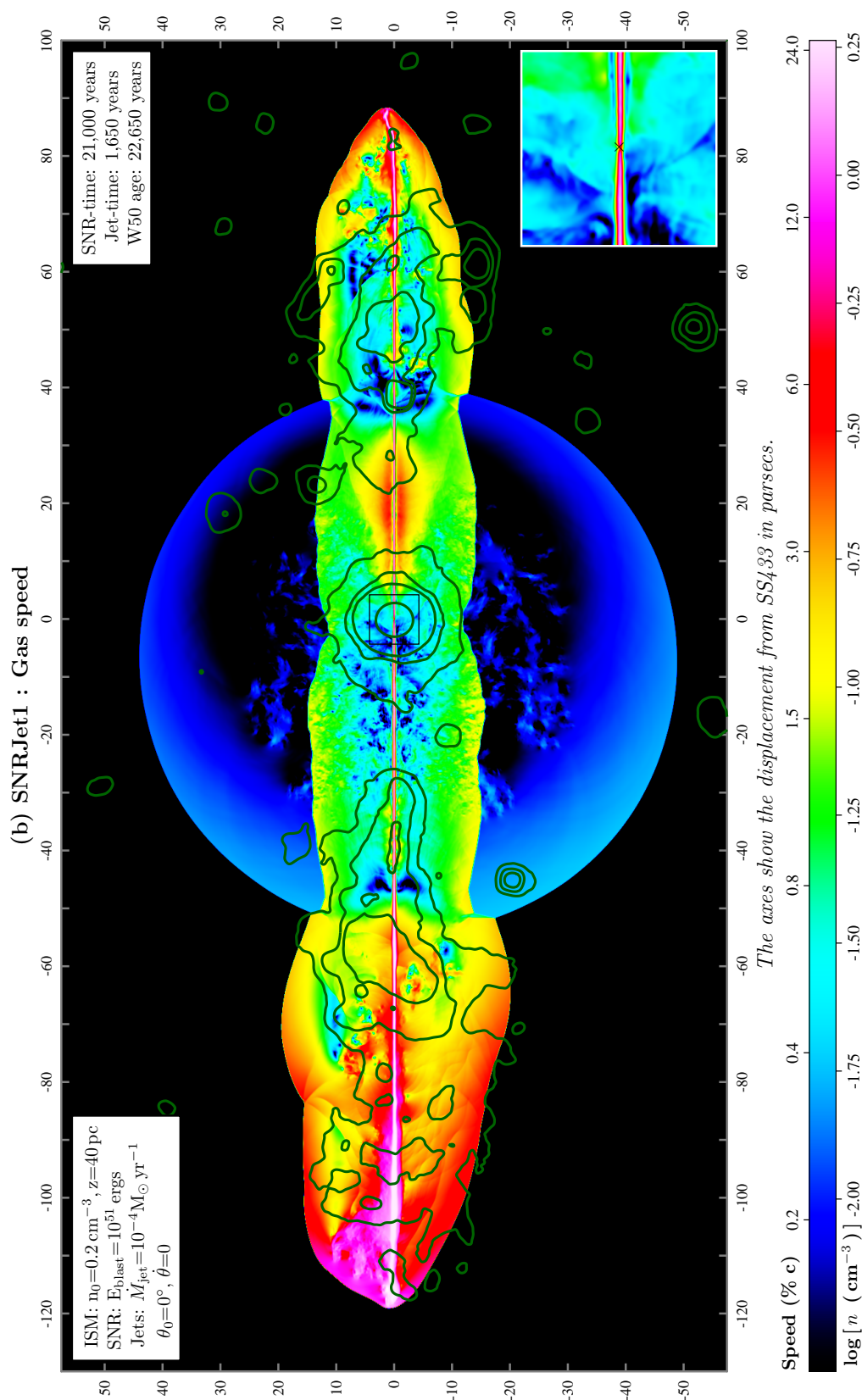
Figure B.2: This is the full size version of Figure 8.1b.

(c) SNRJet2 : Density

ISM: n_0=0.1 cm^{-3}, z=30 pc
SNR: E_{blast}=10^{51} ergs
Jets: $\dot{M}_{jet}$=10^{-4}M$_\odot$.yr^{-1}
θ_0=0°, $\dot{\theta}$=0

SNR-time: 17,000 years
Jet-time: 1,550 years
W50 age: 18,550 years

Speed (% c)

log [n (cm^{-3})]

The axes show the displacement from SS433 in parsecs.
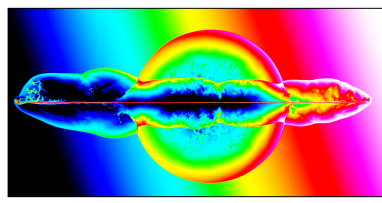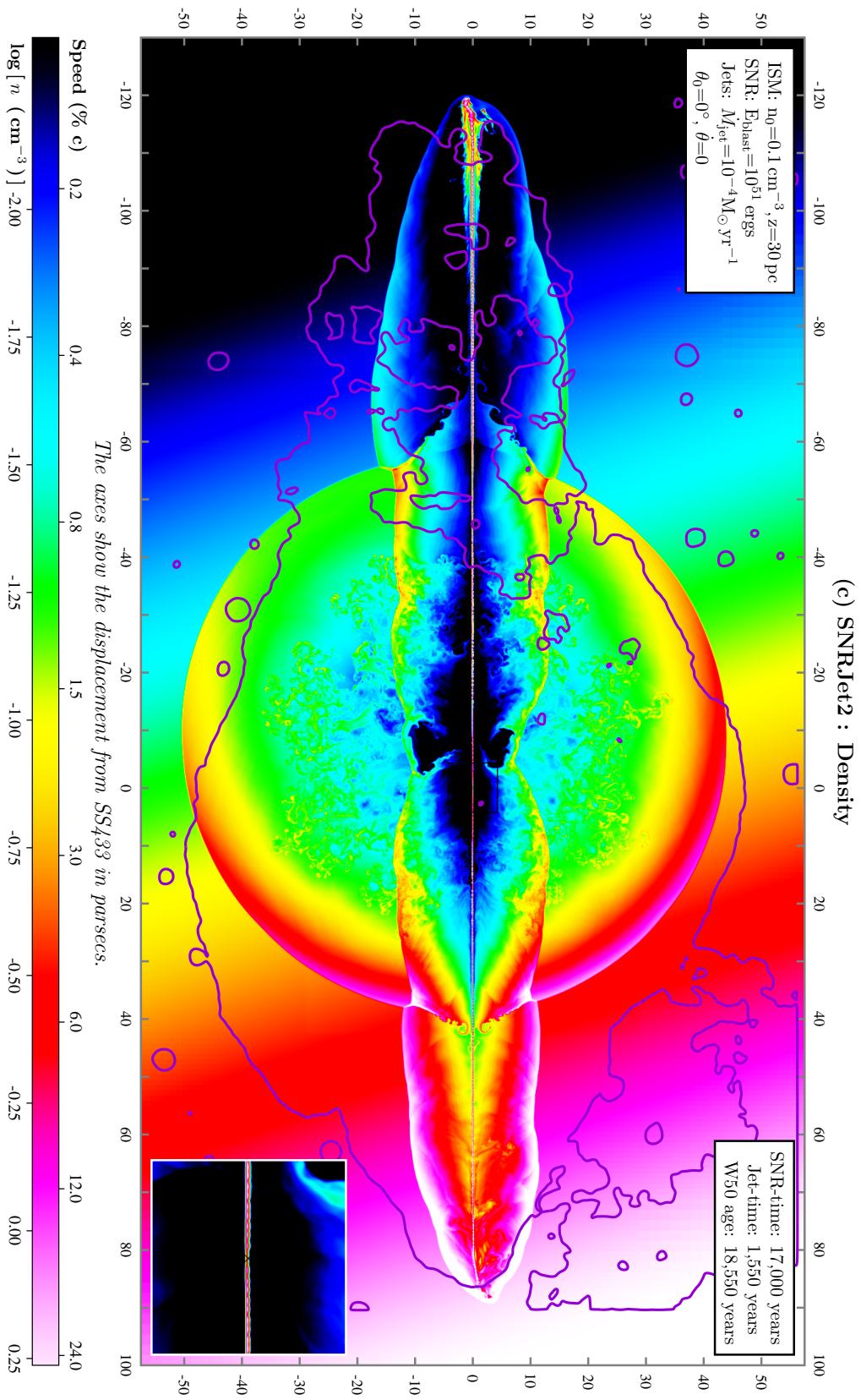
Figure B.3: This is the full size version of Figure 8.1c.

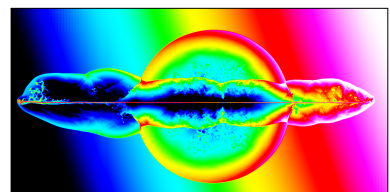**(d) SNRJet2 : Gas speed**

ISM: $n_0 = 0.1\,\mathrm{cm}^{-3}$, $z = 30\,\mathrm{pc}$
SNR: $E_{\mathrm{blast}} = 10^{51}\,\mathrm{ergs}$
Jets: $\dot{M}_{\mathrm{jet}} = 10^{-4}\,\mathrm{M_\odot\,yr^{-1}}$
$\theta_0 = 0°$, $\dot{\theta} = 0$

SNR-time: 17,000 years
Jet-time: 1,550 years
W50 age: 18,550 years

The axes show the displacement from SS433 in parsecs.

Speed (% c)

$\log\left[\,n\ (\mathrm{cm}^{-3})\,\right]$
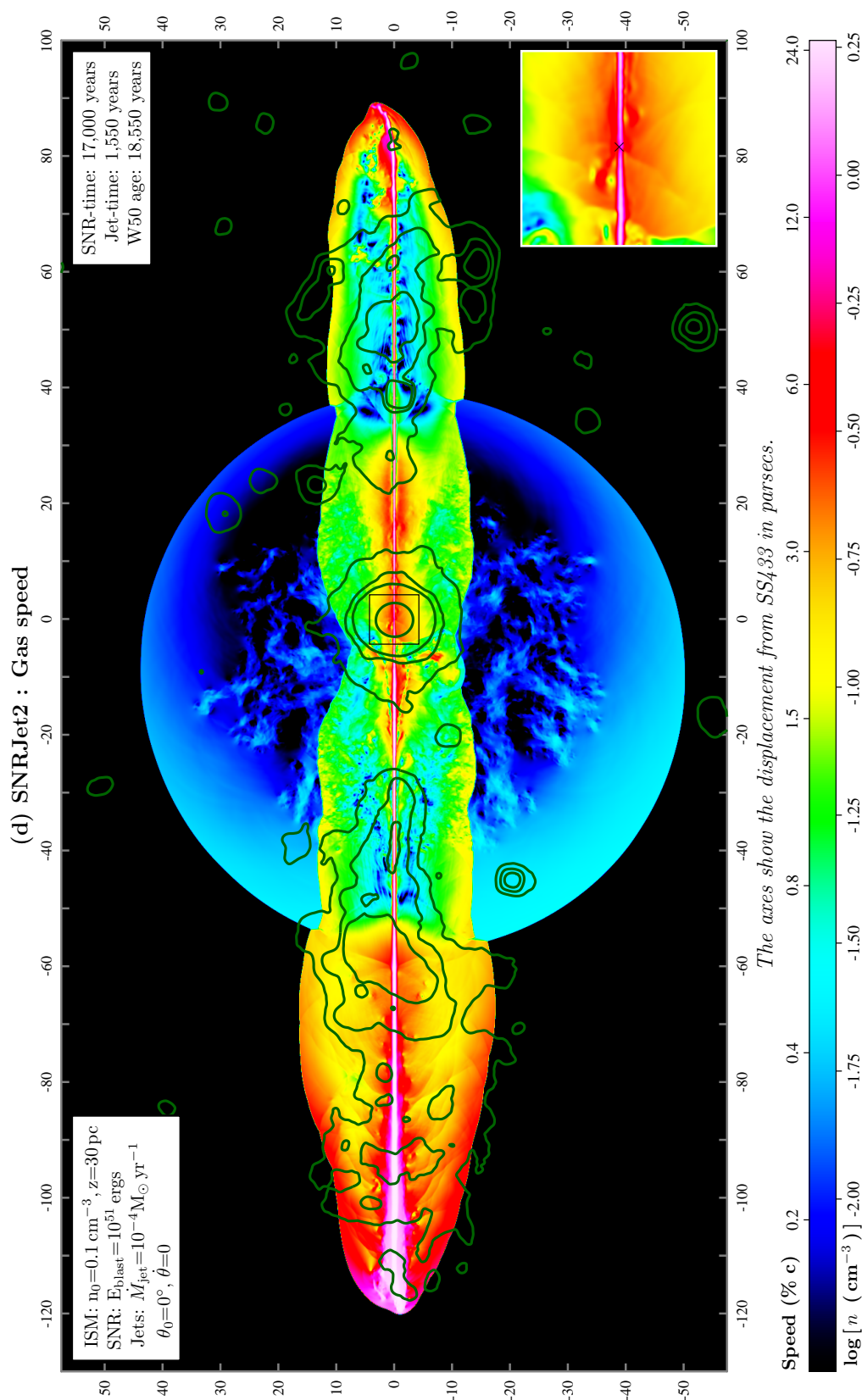
Figure B.4: This is the full size version of Figure 8.1d.

(e) SNRJet3 : Density

ISM: $n_0=0.2\,cm^{-3}$, $z=40\,pc$
SNR: $E_{blast}=10^{51}$ ergs
Jets: $M_{jet}=10^{-4}M_\odot.yr^{-1}$
$\theta_0=20°$, $\dot{\theta}=0$

SNR-time: 21,000 years
Jet-time: 3,500 years
W50 age: 24,500 years

log[n (cm^{-3})]

Speed (% c)

The axes show the displacement from SS433 in parsecs.
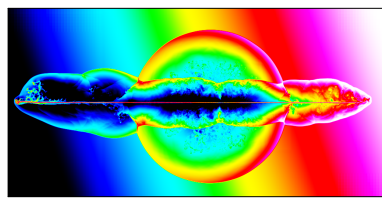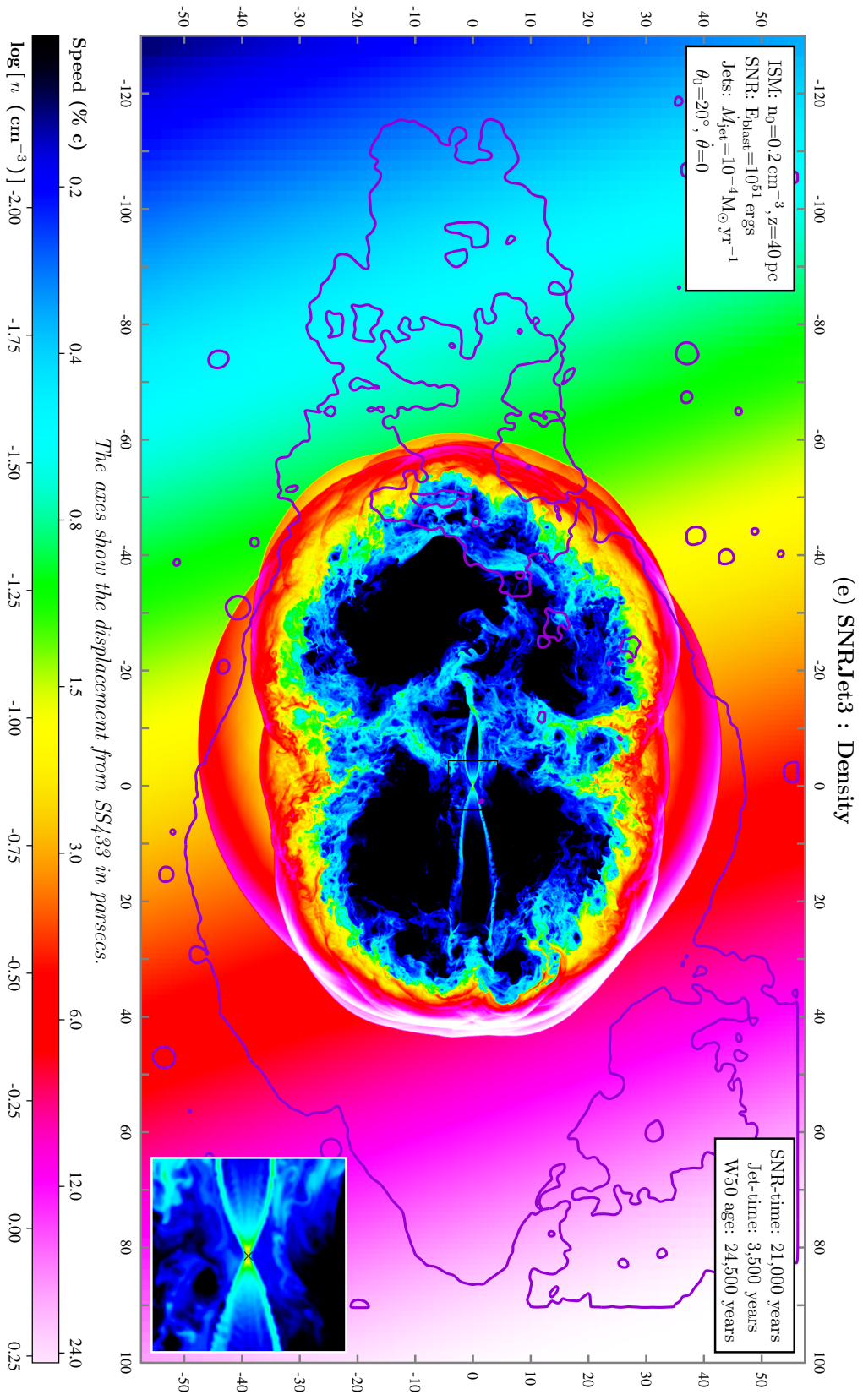
Figure B.5: This is the full size version of Figure 8.1e.

(f) **SNRJet3** : Gas speed

SNR-time: 21,000 years
Jet-time: 3,500 years
W50 age: 24,500 years

ISM: $n_0=0.2\,\mathrm{cm^{-3}}$, $z=40\,\mathrm{pc}$
SNR: $E_{\mathrm{blast}}=10^{51}$ ergs
Jets: $M_{\mathrm{jet}}=10^{-4}\mathrm{M_\odot\,yr^{-1}}$
       $\theta_0=20°$, $\dot{\theta}=0$

The axes show the displacement from SS433 in parsecs.

Speed (% c)

$\log\left[\,n\ \left(\mathbf{cm^{-3}}\right)\,\right]$
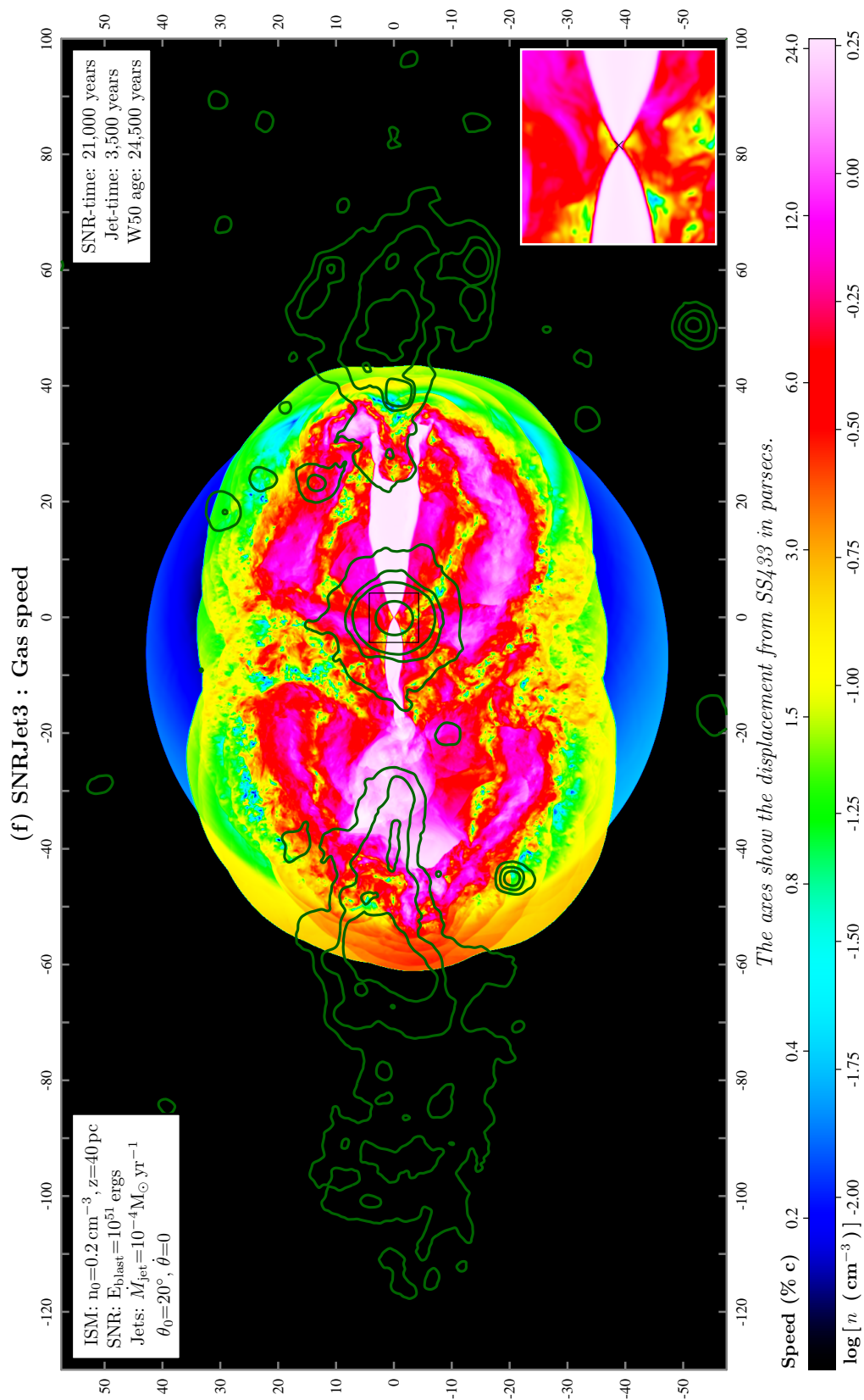
Figure B.6: This is the full size version of Figure 8.1f.

(g) **SNRJet4 : Density**

ISM: n_0=0.2 cm^{-3}, z=40 pc
SNR: E$_{blast}$=10^{51} ergs
Jets: M_{jet}=10^{-4}M$_\odot$.yr^{-1}
θ_0=0°, $\dot{\theta}$=20°/1500-yrs

SNR-time: 21,000 years
Jet-time: 4,000 years
W50 age: 25,000 years

log $[n$ (cm^{-3})]

Speed (% c)

The axes show the displacement from SS433 in parsecs.
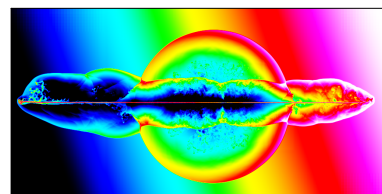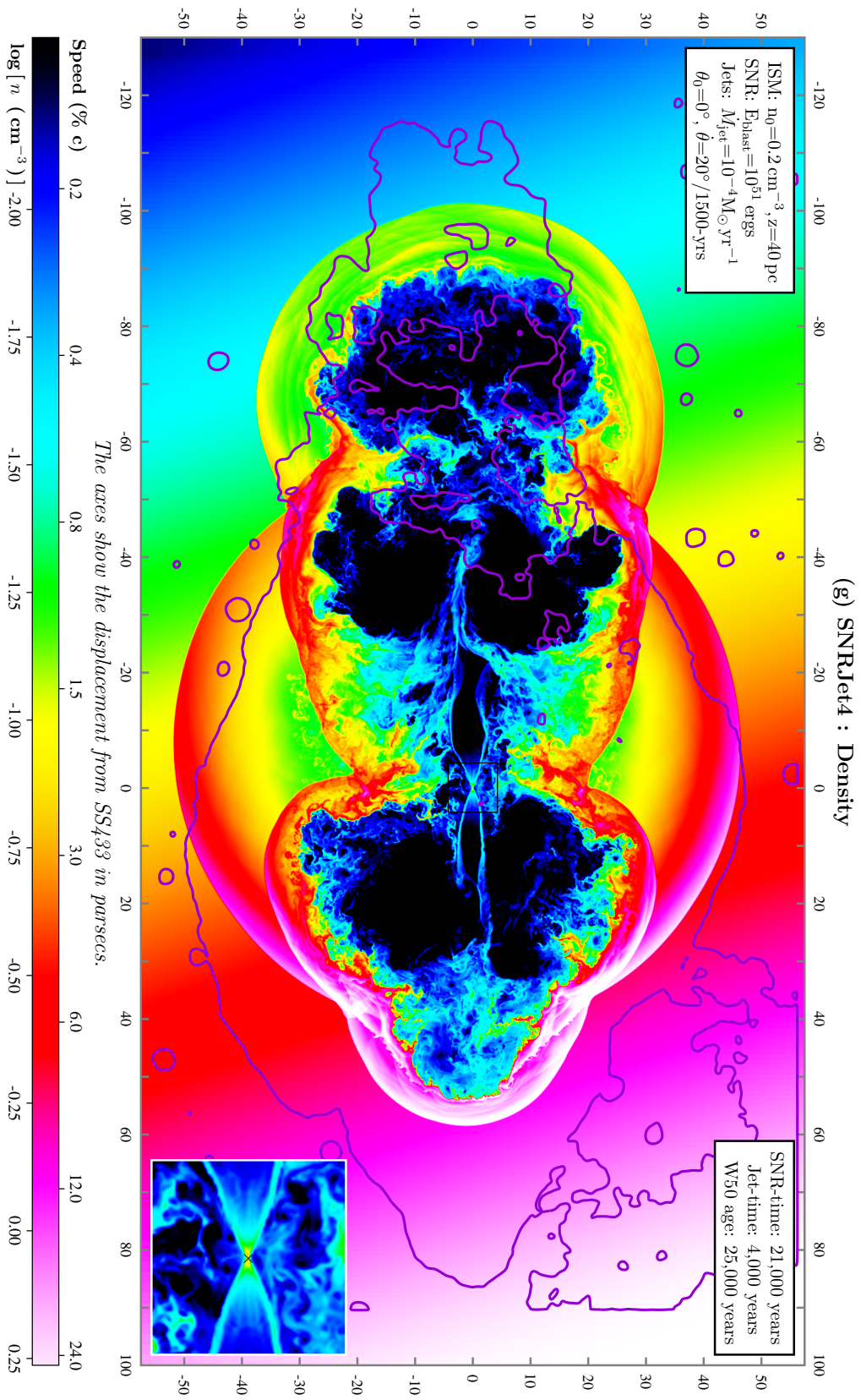
Figure B.7: This is the full size version of Figure 8.1g.

(h) **SNRJet4 : Gas speed**

SNR-time: 21,000 years
Jet-time: 4,000 years
W50 age: 25,000 years

ISM: $n_0 = 0.2\,\mathrm{cm^{-3}}$, $z = 40\,\mathrm{pc}$
SNR: $E_{blast} = 10^{51}$ ergs
Jets: $\dot{M}_{jet} = 10^{-4}\,\mathrm{M_\odot\,yr^{-1}}$
$\theta_0 = 0°$, $\dot{\theta} = 20°/1500\text{-yrs}$

The axes show the displacement from SS433 in parsecs.

Speed (% c)

$\log\left[n\;(\mathrm{cm^{-3}})\right]$
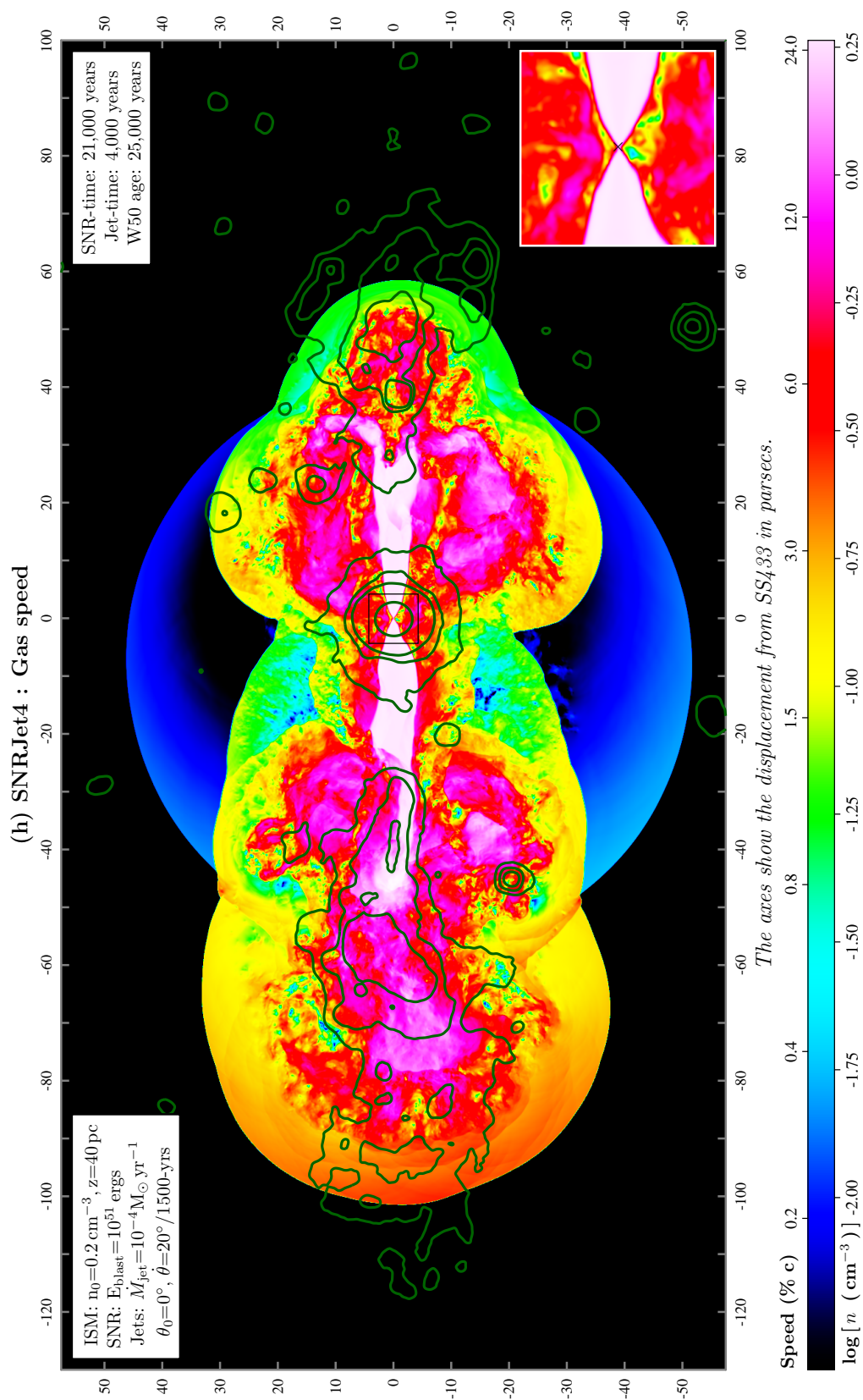
Figure B.8: This is the full size version of Figure 8.1h.

(i) SNRJet5 : Density

ISM: n_0=0.2 cm^{-3}, z=40 pc
SNR: E$_{blast}$=10^{51} ergs
Jets: M_{Jet}=10^{-4}M$_\odot$.yr^{-1}
θ_1=0°, θ_2=20°

SNR-time: 21,000 years
Jet-time: 2,300 years
W50 age: 23,300 years

The axes show the displacement from SS433 in parsecs.

Speed (% c)

log [n (cm^{-3})]

Figure B.9: This is the full size version of Figure 8.1i.

(j) SNRJet5 : Gas speed

SNR-time: 21,000 years
Jet-time: 2,300 years
W50 age: 23,300 years

ISM: n_0=0.2 cm^{-3}, z=40 pc
SNR: E_{blast}=10^{51} ergs
Jets: M_{jet}=10^{-4}M$_\odot$ yr^{-1}
θ_1=0°, θ_2=20°

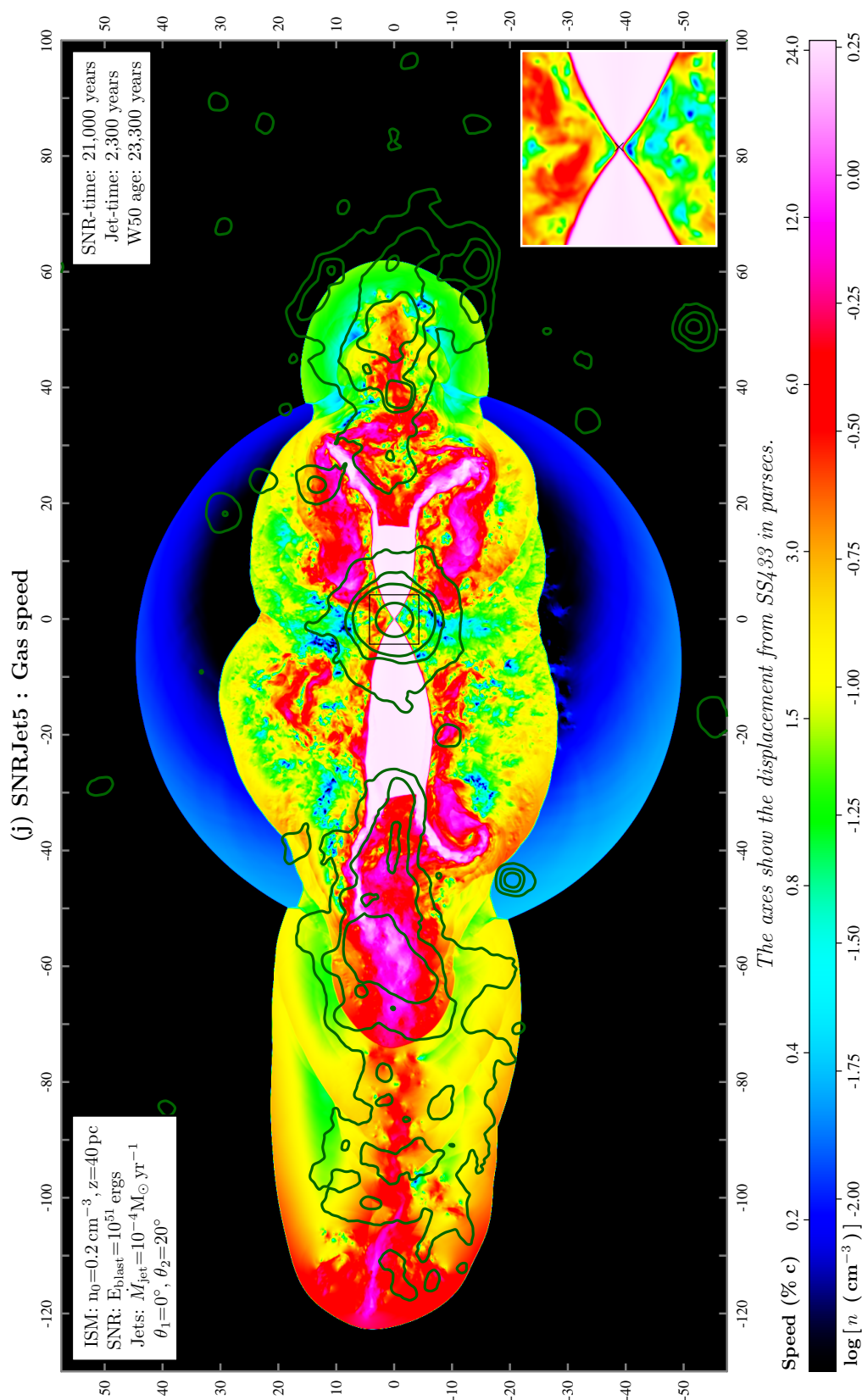*The axes show the displacement from SS433 in parsecs.*

Speed (% c)

log[n (cm^{-3})]

Figure B.10: This is the full size version of Figure 8.1j.